UNIVERSITY OF CALIFORNIA,
IRVINE

Shape and Microstructure Control in Carbon MEMS via Origami-based Fabrication and Electrospinning

DISSERTATION

submitted in partial satisfaction of the requirements
for the degree of

DOCTOR OF PHILOSOPHY

in Mechanical and Aerospace Engineering

by

Derosh George

Dissertation Committee:
Professor Marc J. Madou, Chair
Assistant Professor Edwin Peraza A. Hernandez, Co-chair
Professor Manuel Gamero
Professor Regina Ragan

2021

DEDICATION

To my parents.

TABLE OF CONTENTS

Page

LIST OF FIGURES **vi**

LIST OF TABLES **xiv**

ACKNOWLEDGMENTS **xv**

VITA **xvi**

ABSTRACT OF THE DISSERTATION **xxii**

1 Background **1**
- 1.1 Shaping of Carbon . . . 1
  - 1.1.1 Origami Fabrication Methods . . . 3
  - 1.1.2 Electrospinning Fabrication Methods . . . 32
- 1.2 Designing of Carbon Microstructure . . . 43

2 Capillary Origami-based Carbon Microfabrication **47**
- 2.1 Introduction . . . 47
- 2.2 Methodology . . . 49
  - 2.2.1 Preparation of Patterned Sheets . . . 51
  - 2.2.2 Folding of Polymer Polyhedra Using Capillary Forces . . . 52
  - 2.2.3 Fabrication of Carbon Polyhedra . . . 53
- 2.3 Results . . . 54
  - 2.3.1 Effect of Heat Treatment on the Folding Response . . . 54
  - 2.3.2 Parametric Study of Folding Deformation . . . 55
  - 2.3.3 Effect of Droplet Volume on the Final Polyhedral Shape . . . 57
  - 2.3.4 Carbon Origami . . . 58

3 Programmable Self-folding for Carbon Microfabrication **62**
- 3.1 Introduction . . . 62
- 3.2 Experimental and Computational Methods . . . 66
  - 3.2.1 Polymer Film Preparation . . . 67
  - 3.2.2 Film Patterning Using Double-exposure Photolithography . . . 69
  - 3.2.3 Self-folding Driven by Heating . . . 70
- 3.3 Results . . . 72

3.3.1 Self-folding Analysis and Characterization . . . 72
3.3.2 Origami Design . . . 87
3.3.3 Carbon Origami . . . 97

4 Comparison Study of Capillary Origami and Self-folding Origami Fabrication Methods 101
4.1 Introduction . . . 101
4.2 Origami Design . . . 102
4.3 Experimental Procedure . . . 106
4.3.1 Film Preparation . . . 106
4.3.2 Patterning . . . 108
4.3.3 Folding . . . 109
4.4 Results . . . 111

5 Nearfield Electrospinning-based Carbon Nanowriting 114
5.1 Introduction . . . 114
5.2 Methodology . . . 117
5.3 Results . . . 119
5.3.1 Parametric Study of Polymer Wire Fabrication and Patterning . . . 119
5.3.2 Carbonization of Nanowires . . . 123

6 Design of Carbon Microstructure 127
6.1 Mechanically Induced Graphitization . . . 127
6.1.1 Materials and Methods . . . 130
6.1.2 Characterization . . . 131
6.2 Chemically Induced Graphitization . . . 146
6.2.1 Materials and Methods . . . 149
6.2.2 Characterization . . . 151
6.2.3 Discussion . . . 152

7 Conclusions 153
7.1 Origami Fabrication . . . 153
7.2 Patterned Carbon Nanowires . . . 155
7.3 Microstructure Designing . . . 156

Bibliography 158

Appendix A Appendix Title 177
A.1 Nomenclature . . . 177
A.2 Capillary Origami . . . 179
A.2.1 Theoretical Modeling . . . 179
A.2.2 Effect of Heat Treatment of the Patterned Sheet on the Folding Response 184
A.2.3 Parametric Study of Folding Deformation . . . 185
A.2.4 Data Collected for the Generation of the Results . . . 186
A.2.5 Fabrication of Anchored Folded Shapes . . . 192
A.2.6 DMA Results . . . 192

A.3 Nearfield Patterning 205
A.3.1 Effect of Various Electrospinning Parameters on the Fabrication of Suspended Wires 205
A.3.2 Effect of Electric Field on the Wire Deposition on Patterned Structures 209
A.3.3 Effect of Stabilization and Pyrolysis on the Suspended Wires 209
A.3.4 Effect of Pyrolysis Temperature on the Shrinkage 210
A.3.5 Controlling the Nickel Thickness 211

LIST OF FIGURES

Page

1.1 Traditional origami (Picture credit: Curt Smith, https://bit.ly/353bCb4), wet origami (Designed by Stephan Weber, https://bit.ly/2MB460z), modular origami (Designed by Tomoko Fuse, https://bit.ly/2t5IsuC), and origamizer (Demaine and Tachi 2017 [33], licensed under Creative Commons License). 5

1.2 Bimorph approach, material gradient approach, and external field approach. 6

1.3 Bimetallic strip. 8

1.4 Implementation of bimorph approach to obtain bending using residual stress (Reproduced with permission. ©IOP Publishing. All rights reserved) (Moiseeva *et al.* 2007 [144]), swelling/shrinking (Republished with permission of the Royal Society of Chemistry; permission conveyed through Copyright Clearance Center, Inc.) (Chia Gómez *et al.* 2013 [65]), liquid crystal elastomer (Republished with permission of the Royal Society of Chemistry) (Agrawal *et al.* 2014 [1]), and shape memory polymers (Wang *et al.* 2015) [216]. 9

1.5 Working principle of liquid crystal elastomers and shape memory polymers. . 11

1.6 General folding strategies. 13

1.7 Implementation of bimorph approach to obtain folding using residual stress (Reprinted from (Bassik *et al.* 2009) [11], with the permission of AIP Publishing), swelling/shrinking (Na *et al.* 2015b) [147] (Copyright 2014 by John Wiley & Sons, Inc. Reproduced by permission of John Wiley & Sons, Inc.), liquid crystal elastomer (Yuan *et al.* 2017) [241] (Reproduced with permission from The Royal Society of Chemistry), and shape memory polymers (Teunis *et al.* 2017) [206]. 15

1.8 Implementation of material gradient approach to obtain bending using a gradient in the external field (Wang *et al.* 2016) [211], residual stress (Zhao *et al.* 2017b) [248] (Copyright 2017 by John Wiley & Sons, Inc. Reproduced by permission of John Wiley & Sons, Inc.), swelling/shrinking (Jamal *et al.* 2011a) [85] (Reproduced by permission from Macmillan Publishers Ltd: Nature Communications, copyright 2013), and shape memory polymers (Behl *et al.* 2013) [14] (Copyright 2013 by John Wiley & Sons, Inc. Reproduced by permission of John Wiley & Sons, Inc.). 17

1.9 Implementation of material gradient approach to obtain folding using residual stress (Zhao *et al.* 2017b) [248] (Copyright 2017 by John Wiley & Sons, Inc. Reproduced by permission of John Wiley & Sons, Inc.), swelling/shrinking (Jamal *et al.* 2011a) [85] (Reproduced by permission from Macmillan Publishers Ltd: Nature Communications, copyright 2013), liquid crystal elastomer (Lu *et al.* 2018) [129] (Copyright 2017 by John Wiley & Sons, Inc. Reproduced by permission of John Wiley & Sons, Inc.), and shape memory polymers (Yu *et al.* 2015) [240] (Copyright 2015, with permission from Elsevier). . . . 20
1.10 Different configurations resulting from droplet-surface interactions. 23
1.11 Implementation of external field approach to obtain bending using surface tension (Py *et al.* 2007a) [171] (Reproduced with permission, Copyright 2007 by the American Physical Society. `https://doi.org/10.1103/PhysRevLett.98.156103`), magnetic force (Hu *et al.* 2018) [80] (Reproduced by permission from Macmillan Publishers Ltd: Nature, copyright 2018), and compressive force (Yan *et al.* 2016b) [231] (Copyright 2017 by John Wiley & Sons, Inc. Reproduced by permission of John Wiley & Sons, Inc.). 24
1.12 Folding induced on nanofilms using focused ion beam. Reprinted with permission from (Si *et al.* 2014a). Copyright 2014 American Chemical Society. . 27
1.13 Implementation of external field approach to obtain folding using surface tension (George *et al.* 2019a) [60] (Copyright 2007, American Chemical Society), magnetic force (Kim *et al.* 2018) [102] (Reproduced by permission from Macmillan Publishers Ltd: Nature, copyright 2018) and compressive force (Fu *et al.* 2018) [48] (Reproduced by permission from Macmillan Publishers Ltd: Nature Materials, copyright 2018). 28
1.14 Solution electrospinning. 36
1.15 Melt electrospinning. 37
1.16 Farfield electrospinning. 38
1.17 Nearfield electrospinning. 39
1.18 Spinneret with one polymer solution (Left) and spinneret with coaxial needles that can dispense two different polymer solution for electrospinning (Right). 40
1.19 Liquid bath collector. 41
1.20 Schematic showing the process of making carbon mats using electrospinning process. 43

2.1 (a) Photolithography-based patterning of planar thin sheets used to fabricate free-standing polyhedra. (b) Capillary folding and thermally-controlled softening/hardening. The sheets are placed inside a silicone oil bath, and actuating droplets are deposited on top of them. The bath is heated to generate thermally-induced softening at the folds and allow folding. The bath is then cooled to acquire permanently folded shapes. (c) Schematic of the process at a microstructural level. (i) The degree of cross-linking in the SU8 polymer matrix is directly proportional to the exposure energy. (ii) The less cross-linked regions (the folds) are subjected to significant deformation when external forces are applied, due to the higher mobility of the partially cross-linked monomers. Deformation is made permanent by cooling and subsequently cross-linking the shape completely. 50
2.2 (a) Effect of temperature on the storage modulus of SU8 films made with different UV exposure duration. (b) Dimensions of the single-fold sheets and geometric parameters of the folded configurations. (c) Effect of exposure times on the ratio of curvature of faces κ_F to curvature of folds κ_f. A 2 mW/cm^2 UV light source is used in all cases. (d) Effect of exposure times on the folding parameter that combines fold angle and curvature ratio. 56
2.3 (a) Effect of droplet volume on the fold angle. Single-fold sheets with $L = 2$ mm are studied. (b) Effect of droplet volume on the closing of a cube. 58
2.4 (a) Platonic polyhedra obtained using the present fabrication method. The scale bars for (a) and (b) are 1.5 mm. (b) Cube with a star-shaped hole on one of its faces. (c) Carbon origami cube and dodecahedron produced from corresponding polymer shapes. 59
2.5 Schematic illustrating capillary folding of planar patterned films towards three-dimensional polyhedral shapes. 59
2.6 (a) Unfolded sheets films for dodecahedron and icosahedron with faces having patterned holes. (b) Folded dodecahedron and icosahedron from different views. All the scale bars are 1.5 mm long. 60
2.7 (a) Size comparisons of sheets before and after pyrolysis. (b) Raman spectroscopy of the carbonized SU8 origami polyhedra showing the D-peak, the G-peak and the 2D-peak. 60

3.1 Schematic summarizing the origami-based manufacturing method developed in this work. A target shape is given and is first flattened into a planar net with distinct face and fold regions using the unfolding polyhedra method. The planar net becomes the geometrical basis for the fabrication of a patterned planar film using photolithography. The film is programmed during the photolithography process to *self-fold* towards the target shape via heating. The width of the petals of the flower shown in this example is 2 mm. 67
3.2 Preparation of the SU8 photopolymer film and its supporting substrates. A middle PDMS layer is placed between the silicon wafer and the SU8 film to enable facile separation of the SU8 film. 69

3.3 Schematics and photos of the film patterning process using double-exposure photolithography: (a) Exposure steps, PEB, and development processes shown for a single flower; (b) Photolithographic masks for simultaneous fabrication of multiple samples. The width of the petals of the flowers shown in this example is 2 mm. 71
3.4 (a) Self-folding driven by heating demonstrated with a flower-like shape. The width of the flower petals is 2 mm. (b) Isometric, front, and top views of a film with a single central fold. (c) Folded films that have not undergone post-folding exposure and PEB showing no noticeable post-folding deformation with and without an applied load at room temperature. The scale bars are 1 mm long. 73
3.5 Schematic illustrating the phenomenon used to achieve self-folding of the photopolymer films. a) The SU8 film attached to the supporting structure (PDMS-coated silicon wafer) is immersed in SU8 developer solution after the double-exposure photolithography process described in Section 3.2.2. b) The developer is non-uniformly absorbed across the film, where the folds with lower crosslinking density absorb a larger amount than the faces with higher crosslinking density. The top side of the folds in direct contact with the developer solution exhibits a higher concentration than the bottom side attached to the PDMS layer. The developer removes some of the non-crosslinked polymer chains in the folds. c) The films are separated from the supporting structure. d) Self-folding is displayed by the film when the non-uniformly absorbed developer is evaporated through heating. Subsequent UV exposure and PEB completes the crosslinking process of the entire film and the folded configuration is made permanent. 75
3.6 Geometry of the fold domain studied in the analytical model. 76
3.7 (a) Illustration of the influence of fold width w on the fold angle θ for films of equal thickness h. (b) Experimental data and linear fit of fold angle θ vs. fold width w non-dimensionalized by film thickness h. (c) Contour plot of fold width w vs. film thickness h and fold angle θ generated using the proportionality constant c of the linear fit from (b) and equation (3.17). (d) Photos of folded films having the same film thickness h and different fold widths w. The scale bars represent 1 mm. 83
3.8 Fold curvature κ vs. fold width w for films of different fold widths and thicknesses. The horizontal lines represent the average curvature values for each thickness. 84
3.9 (a) Schematic and photo of a fold indicating the top radius of curvature R_t, bottom radius of curvature R_b, top fold width w_t, and bottom fold width w_b. (b)-(d) Extension ratio at the top and bottom of folds in films of different thickness h and fold widths w. 86
3.10 Experimental characterization of the exhibited fold angle θ in folds with equal width and thickness: (a) Effect of exposure energy received by the fold region; and (b) Effect of total development duration. Folds with fixed width $w = 0.55$ mm and thickness of $h = 37.7$ μm are considered. 87

3.11 Schematic illustrating the Matlab® implementation of the unfolding polyhedra method used in this work. The width of the folds is sized using equation (3.17). 89
3.12 (a) An infeasible spanning tree that contains loops and multiple pieces. (b) An infeasible spanning tree that contains no loops, but multiple pieces. (c) A feasible spanning tree that forms an origami net. However, the net is not the one corresponds to the minimum d. (d) Origami net with the smallest d of the target prism shape. 91
3.13 Cube fabricated using the presented origami-based manufacturing method. (a) Stages in the design of the planar film programmed to self-fold towards the cube when heated. The unfolding polyhedra method is used to determine the planar form of the net $\mathcal{S}_0$ starting from the polyhedral mesh $\mathcal{M}$, and double-exposure photolithography is used to pattern a photopolymer film with the geometry of the net. (b) Self-folding deformation of the net from its planar configuration towards its folded configuration $\mathcal{S}_f$. Notice the good agreement between the experimental photo and the ideal folded configuration $\mathcal{S}_f$. The scale bars represent 1.5 mm. A video showing the self-folding deformation process for this example is provided in the Supplemental Material. 92
3.14 Truncated icosahedron fabricated using the presented origami-based manufacturing method. (a) Stages in the design of the planar film programmed to self-fold towards the truncated icosahedron when heated. (b) Self-folding deformation of the net from its planar configuration towards its folded configuration $\mathcal{S}_f$. The scale bars represent 1.5 mm. 93
3.15 Four-legged platform fabricated using the presented origami-based manufacturing method. (a) Stages in the design of the planar film programmed to self-fold towards the four-legged platform when heated. (b) Self-folding deformation of the net from its planar configuration towards its folded configuration. The scale bars represent 1.5 mm. 94
3.16 Trimmed (open) torus fabricated using the presented origami-based manufacturing method. (a) Stages in the design of the planar film programmed to self-fold towards the trimmed torus when heated. (b) Self-folding deformation of the net from its planar configuration towards its folded configuration. The scale bars represent 1.5 mm. A video showing the self-folding deformation process for this example is provided in the Supplemental Material. 95
3.17 Shape accuracy a vs. film thickness h for the cube, truncated icosahedron, four-legged platform, and trimmed torus. Trimmed meshes accounting for accommodation of the smooth folds are also shown. The size of the target meshes corresponds to that of the fabricated samples shown in Figs. 3.13-3.16. The $\times$ marks the thickness at which one or more faces of the trimmed mesh are degenerated to a point or line. 98

3.18 Shape accuracy a vs. smallest edge length for the cube, truncated icosahedron, four-legged platform, and trimmed torus shapes. Trimmed target meshes are also illustrated (not shown to scale). A film thickness of 37.7 μm is used in the generation of the plots, which corresponds to the thickness used in the experimental demonstrations shown in figures 3.13-3.16. The $\times$ marks the edge lengths at which one or more faces of the trimmed mesh are degenerated to a point or line. 99
3.19 Three-dimensional carbon polyhedral shapes obtained by pyrolyzing the associated polymer shapes. The scale bars represent 1.5 mm. The photos of the polymer and carbon samples are displayed to scale, showing the decrease in overall size of the samples after pyrolysis. 100

4.1 Schematic flow of the origami-based manufacturing methods explored in this work. The methods start with a target shape model and produce the corresponding polymer polyhedra. 102
4.2 Two different *folding mechanisms* for origami structures formed by single-layer photopolymer films. In *capillary-assisted origami*, surface tension is used to trigger the folding process by placing a water droplet on the thin film. In *self-folding origami*, the folding is realized by selectively diffusing (and removing) solvent to (and from) the designated fold region. 102
4.3 Unfolding processes to generate nets for both capillary-assisted folding and self-folding. While the fold width values for the capillary-assisted folding are not dependent on the targeted fold angles, the fold widths for the self-folding method are a function of the targeted fold angles. 104
4.4 Fold angle characterization for the capillary-assisted folding method and the self-folding method. In capillary-assisted folding, the fold angle of a single fold is controlled by controlling the volume of the droplet. In the self-folding approach, the fold width and film thickness determine the fold angle. 105
4.5 Different target shapes considered as implementation examples in this work and associated nets. The sum of the distances between the centroids of the faces is minimized to obtained the most compact nets. 107
4.6 Film preparation step for capillary-assisted folding and self-folding. The photopolymer film for capillary-assisted folding is prepared on a silicon wafer, and the film for self-folding is spin-coated on a PDMS supporting structure. . . . 108
4.7 Double-exposure lithography and subsequent development in the patterning step. Double exposure is identical in both capillary-assisted folding and self-folding. Development of the films on the silicon wafer for the capillary-assisted folding is performed for an extended period to separate the patterned films from the silicon wafer. Development of the films on PDMS for self-folding is performed only for a duration recommended for the conventional lithography process. This allows the films to remain bonded to the PDMS substrate. The bottom figures show the masks for the two UV exposure steps. The first step lets UV light irradiate both folds and faces, while the second steps lets UV light irradiate only the faces to obtain higher stiffness at these regions. . . . 110

4.8 Folded shapes are achieved by placing a droplet on a softened patterned thin film in capillary-assisted folding and by heating in self-folding. 111
4.9 Simulated and fabricated pyramid, prism, and dodecahedron. Micrographs from different views are shown for capillary-assisted origami and self-folding origami. The scale bars represent 1.5 mm. 113

5.1 (a) Electromechanical spinning of polyacrylonitrile (PAN) solution onto a rotating collector to obtain patterned polymer wire deposition. (b) Pyrolysis of stabilized PAN wires inside a furnace to get pyrolytic carbon. (c) Nickel electroplating of the carbon structures to form catalytic surface for the subsequent chemical vapor deposition (CVD) of graphitic carbon. (d) chemical vapor deposition (CVD) of graphitic carbon. 118
5.2 (a) Micrograph of wires at 500 and 900 V, (b) Variation of the diameter of the fiber with applied voltage applied (The scale bar is 7 μm long), and (c) Variation of the diameter with the distance between the spinneret and the rotating collector (L). 121
5.3 (a) Various fiber profiles obtained as a function of rotational speed. (b) As a function of working distance (voltage = 1500 V). (c) i. Successfully formed suspended wires at low voltage. ii. No suspended wire formation at high voltage. (d) Wire patterns (horizontal lines) formed over carbon support structures with two microchannels (vertical lines). 122
5.4 Variation of inter-fiber spacing with (a) stage speed and (b) rotational speed of the collector. 123
5.5 (a) Patterned deposition of wires on a carbon pillar array. (b) Straightening of the wires that are coming at an angle to the array. (c) Multi-wire deposition of wires on a single column when the pillar spacing is more than the expected wire spacing. 125

6.1 (a) Stabilization process with mechanical treatment and the pyrolysis process (b) Difference in microstructure of the resulting carbon based on whether the wires are mechanically treated or not. 133
6.2 Material characterization of SAPC and untreated PAN-based CNF. High Resolution Transmission Electron Microscopy (HRTEM) of: a i) CNF and b i) SAPC microstructures. Mapping of Raman spectroscopy I_D/I_G ratio of: a ii) CNF, and b ii) SAPC. Average Raman spectrum of a iii) CNF and b iii) SAPC electrodes. Averages of over 100 collections are used to represent CNF and SAPC. ($\lambda_{excitation}$ = 532 nm) 134
6.3 X-ray Photoelectron Spectroscopy (XPS). a) XPS spectrum of the N 1s peak of SAPC. b) Table of elemental composition of the SAPC as determined by analysis of XPS spectrum. 135
6.4 Electrochemical kinetics of SAPC. Cyclic voltammograms of SAPC, CNF, and GC's electrochemical response to aqueous solution of: a) 2 M KCl and 1 mM of $K_3Fe(CN)_6$, b) 2 M KCl and 1 mM of K_3IrCl_6, and c) pH 7.4, 1 mM PBS at and 0.1 mM of dopamine at a scan rate of 100 mV/s. 136

6.5 (a) Fitting N 1s XPS peak of CNF, (b) Fitting N 1s XPS peak of mechanically treated CNF. 140
6.6 Cyclic voltammograms at 50 mV/s of (a) Mechanically treated CNF run in blank 1X PBS and in the presence of 1X PBS in the presence of 2.5 mM H_2O_2; (b). Toray, Mechanically Treated CNF, and pure PAN CNF electrodes in 1X PBS in the presence of 2.5 mM H_2O_2. 142
6.7 (a) Chronoamperometry of the Mechanically Treated CNF electrode running at -0.5V. Each addition concentration is indicated on the graph and was repeated three times after the initial indication prior to the next concentration addition. The inset is a zoomed in portion of the main graph; (b) Concentration vs Current Density data from the chronoamperometry fitted with linear regression trend line. 143
6.8 Amperometric response of the Mechanically Treated CNF at a potential of -0.5 V vs. Ag/AgCl with addition of interfering agents (1 mM H2O2, 0.15 mM AA, 1 mM Glu, 0.5 mM UA, and 1 mM H_2O_2). 145
6.9 (a) Pyrolyzed PAN wire patterns on a flat substrate. (b) Anisotropic shrinkage at the wire intersection. (c) Carbon wire bridges formed on top of a channel structure. (d) Wire of diameter less than 40 nm. 150
6.10 (a) SEM image of suspended Ni-coated pyrolyzed PAN nanowires after CVD at 1000°C. (b) Raman spectrum of suspended PAN nanowire after pyrolysis (black dotted line) and of suspended Ni-coated pyrolyzed PAN nanowire after CVD at 1000°C (Red line) (c) SEM image showing the microstructure of the electrodeposited nickel (thickness = 307.5±5.9 nm). (d) Raman spectra of graphitic layers formed on nickel layers of different thicknesses. The thicker nickel films showed a higher level of graphitization as indicated by the improved I_D (1350 cm^{-1})-to-I_G (1550 cm^{-1}) ratio. 151

LIST OF TABLES

Page

3.1 Nets for the cube, truncated icosahedron, platform, and trimmed torus determined by minimizing the sum of the distances between the centroids of each pair of faces of the net d and maximizing the shape accuracy a. 97

6.1 Electrochemical kinetics values of SAPC, CNF, and Alumina-Polished glassy carbon in different redox systems. 137
6.2 Nitrogen species based on XPS analysis. 140

ACKNOWLEDGMENTS

I want to take this opportunity to profusely thank Dr. Marc Madou and Dr. Edwin Hernandez for their continuous support and guidance over the years. I am indebted to them for their encouraging words and the infectious enthusiasm that kept me motivated during my doctoral studies. I earnestly thank Dr. Roger Lo and Dr. Maziar Ghazinejad for their invaluable advice and immense support throughout my project, even during their busy time. I would also like to extend my thanks to my fellow researchers at UCI's BioMEMS lab for making the research a delightful endeavor. Especially, Sunny Holmberg, Brandon Pollack, Lauren Cho, Kimya Pezesky, Dian Song, Yujia Liu, Alfonso Shin, Alexander Hwu, Snehan Peshin, Alexandra Perebikovsky, Dr. Lawrence Kulinsky, Tuo Zhou, Jufeng Deng, Michelle Nguyen, Juliet Nordman, Elena Helm, Nghi Nguyen, Loan Le, Jesse Mikulec, Eric Adams, Ainesh Arumugam, Mario Ramos, Ehsan Shamloo, Hamsa Gowda, and Maria Bauer. My work would not have been possible without their help and the numerous intellectually stimulating conversations we had. I would like to extend my gratitude to Dr. Manuel Gamero and Dr. Regina Ragan for agreeing to be my committee members.

Support for the electrospinning-related studies was provided by the National Science Foundation (NSF) grant #1449397. My research work here at the UCI was partially supported by the Science and Engineering Research Board (SERB), India. Moreover, I would also like to thank the UCI's Laser Spectroscopy labs and UC Irvine Materials Research Institute (IMRI) for giving access to many of the characterization tools used in this work.

I want to thank Springer Nature, the Royal Society of Chemistry, the Institute of Physics, the International Society for Optics and Photonics, the Multidisciplinary Digital Publishing Institute, and the American Society of Mechanical Engineers for giving me permission to incorporate my previously published works into this thesis.

On a more personal note, I want to thank my parents, my brothers and my sisters for their moral and emotional support. I also owe gratitude to Dr. Biny Sebastian for all the love and support, especially in the final months of the preparation of this dissertation.

VITA

Derosh George

EDUCATION

Doctor of Philosophy in Mechanical and Aerospace Engineering **2021**
University of California, Irvine *Irvine, CA*

Master of Technology in Mechanical Engineering **2013**
Indian Institute of Technology, Madras *Chennai, India*

Bachelor of Technology in Mechanical Engineering **2013**
Indian Institute of Technology, Madras *Chennai, India*

RESEARCH EXPERIENCE

Ph.D. Researcher **Sep 2016–June 2021**
University of California, Irvine *Irvine, CA*

Freeform Manufacturing Platform for Millimeter and Sub-Millimeter Carbon Structures
Supervisors: Dr. Marc J. Madou & Dr. Edwin A. Peraza Hernandez

- Devised and executed a novel 3D micromanufacturing method using programmable, thermally-triggered self-folding polymer films (First author paper)
- Created a first of its kind elastocapillary-based 3D fabrication strategy for submillimeter-sized carbon polyhedra (First author paper)
- Constructed and evaluated an electrochemically superior carbon through rational material tailoring (Co-author papers - 2)
- Led a multinational team of 11 researchers (from the USA, China, and Mexico) to develop a scalable nanomanufacturing platform for graphene-coated carbon nanowires of less than 50 nm (First author paper)

Master's and Bachelor's (Dual Degree) Researcher **Aug 2012–June 2013**
Indian Institute of Technology, Madras *Chennai, India*

Design and Optimization of Valve-less Micropump
Supervisors: Dr. Ashis Kumar Sen & Dr. Singaperumal M.

- Modeled and fabricated sub-millimeter-sized PDMS-based single and multiple inlets valveless micropumps

- Used two-way coupling simulation to study the system containing fluid, PDMS diaphragm, and piezoelectric material (Co-author papers - 2)

Junior Research Fellow **Feb 2015–Aug 2016**
Indian Institute of Technology, Madras *Chennai, India*

- Discovered a novel elastocapillary-based microfluidic liquid plug manipulation method (First author paper)
- Developed self-forming PDMS channels as an alternative for the popular paper microfluidics (Second author paper)
- Scientifically elucidated the counter-intuitive flotation of heavier droplets on lighter liquid (First author paper)
- Developed a PDMS microlens fabrication method (Second author paper)

TEACHING EXPERIENCE

Instructor - Lightweight Structures **July 2021–Sept 2021**
University of California, Irvine *Irvine, CA*

- Successfully delivered 20 lectures, organized discussions, arranged a project, and carried out many quizzes
- Incorporated video snippets, embedded quizzes, and Zoom polls to make the online course highly engaging

Teaching assistant **Mar 2018–Present**
University of California, Irvine *Irvine, CA*

- Assisted ten courses, including one graduate-level class and three upper-level undergraduate classes
- Conducted discussion sessions and office hours for classes having up to 300 students
- Courses:
  - Introduction to Computer Aided Engineering (MAE 152)
  - Introduction to Thermodynamics (MAE 91)
  - Lightweight Structures (MAE 157)
  - Engineering Analysis I (MAE 200 A)
  - Introduction to Computer Aided Design (MAE 52)
  - Theory of Machines and Mechanisms (MAE 145)
  - Mechanics of Materials (MAE 150)

PROFESSIONAL EXPERIENCE

Edison Engineer **Aug 2013- Feb 2015**
GE Power & Water, JFWTC *Bangalore, India*

- **Gas Turbine New Product Introduction Team**
  - Designed and analyzed heating and ventilation system, fire protection system, and cooling air system for 9HA GT
- **New Unit Requisition Team** Aug 2013 - Feb 2014
  - Designed piping systems for GE's unique full-speed-full-load Compressor Validation Rig (CVR)

Internship Trainee **May 2011–June 2011**
FLSmidth House *Chennai, India*

- Modeled Hydraulic Roller Press (HRP) structures for the cement processing line. Analyzed the structure using FEM and suggested significant improvements to make the design robust

AWARDS AND RECOGNITION

- Winner of ASME-SMASIS 2020 Best Student Paper competition
- Recipient of Henry Samueli Endowed Fellowship
- Recipient of SERB Fellowship for doctoral students from India
- Recipient of Merit-cum-Means scholarship for undergraduate students

OUTREACH ACTIVITIES

- Student Ambassador for National Program on Technology Enhanced Learning (NPTEL)
- Organizing Member of Tensors; an entrance exam assistance endeavor
- Collaborator: Virtual high school outreach workshop at Azusa High, a school with 97% minority enrollment

PROFESSIONAL SERVICES

- Peer reviewer for Microsystems and Nanoengineering (Nature)
- Literature survey study for Chemical Angel Network to identify surfaces ideal for continuous glucose monitoring
- Coordinator of GE Innovation Challenge 2013
- Web developer for OnMobile Global Limited and UCI BioMEMS

RESEARCH SUPERVISION

- Mentored a graduate student
  - Tuo Zhou - Patterned nanowire writing
- Mentored eight undergraduate students
  - Michelle Nguyen, Juliet Nordman, and Elena Helm - Nearfield and farfield electrospinning
  - Kimya Pezeshki - Non-spherical microparticle fabrication
  - Nghi Nguyen- Compound droplet simulation
  - Loan Le - Thin-film lithography
  - Jesse Mikulec - Theoretical study of capillary origami
  - Eric Adams - Farfield electrospinning
- Mentored a high school student
  - Ainesh Arumugam - Helped him reach state-level California Science and Engineering Fair 2018

REFEREED JOURNAL PUBLICATIONS

1. **D George**, M Madou, EA Peraza Hernandez "Programmable self-foldable films for origami-based manufacturing", Smart materials and structures. *Accepted*
2. **D George**, A Garcia, Q Pham, MR Perez, J Deng, MT Nguyen, T Zhou, SO Martinez-Chapa, Y Won, C Liu, RC Lo, R Ragan, M Madou, "Fabrication of patterned graphitized carbon wires using low voltage near-field electrospinning, pyrolysis, electrodeposition, and chemical vapor deposition", Microsystems & Nanoengineering & (1), 1-12, 2020

3. **D George**, EA Peraza Hernandez, RC Lo, M Madou "Fabrication of polymer and carbon polyhedra through controlled cross-linking and capillary deformations", Soft matter 15 (45), 9171-9177, 2019

4. RA Samy, PPA Suthanthiraraj, **D George**, R Iqbal, AK Sen "Elastocapillarity-based transport of liquids in flexible confinements and over soft substrates", Microfluidics and Nanofluidics 23 (8), 100, 2019

5. S Holmberg, M Ghazinejad, EB Cho, **D George**, B Pollack, A Perebikovsky, R Ragan, M Madou "Stress-activated pyrolytic carbon nanofibers for electrochemical platforms", Electrochimica Acta 290, 639-648, 2018

6. B Pollack, S Holmberg, **D George**, I Tran, M Madou, M Ghazinejad, "Nitrogen-rich polyacrylonitrile-based graphitic carbons for hydrogen peroxide sensing", Sensors 17 (10), 2407, 2017

7. RA Samy, **D George**, AK Sen, "Bio-inspired liquid transport via elastocapillary interaction of a thin membrane with a liquid meniscus", Soft matter 13 (38), 6858-6869, 2017

8. **D George**, S Damodara, R Iqbal, AK Sen "Flotation of denser liquid drops on lighter liquids in non-Neumann condition: Role of line tension", Langmuir 32 (40), 10276-10283, 2016

9. N Kumar, **D George**, P Sajeesh, PV Manivannan, AK Sen, "Development of a solenoid actuated planar valveless micropump with single and multiple inlet–outlet arrangements", Journal of Micromechanics and Microengineering 26 (7), 075013, 2016

10. S Damodara, **D George**, AK Sen, "Single step fabrication and characterization of PDMS micro lens and its use in optocapillary flow manipulation", Sensors and Actuators B: Chemical 227, 383-392, 2016

11. **D George**, R Anoop, AK Sen, "Elastocapillary powered manipulation of a liquid plug in a microchannel", Applied Physics Letters 107(26), 261601, 2015

12. S Singh, N Kumar, **D George**, AK Sen, "Analytical modeling, simulations and experimental studies of a PZT actuated planar valveless PDMS micropump", Sensors & Actuators A: Physical, 225, 81-94, 2015

BOOK CHAPTER

1. **D George** and M Madou, "Origami MEMS", Mechanical Sciences, Springer, 197-239

REFEREED CONFERENCE PUBLICATIONS

1. **D George**, M Madou, EA Peraza Hernandez, "Practical fabrication methods for 3D origami structures from 2D films patterned via photolithography", SPIE Advanced Lithography, Proceedings Volume 11610, Novel Patterning Technologies; 116100X, Online, 2021

2. **D George**, M Madou, EA Peraza Hernandez, "Characterization and design of programmable self-folding polymer films", Proceedings of the ASME 2020 Conference on Smart Materials, Adaptive Structures and Intelligent Systems SMASIS, Virtual, Online. September 15, 2020. V001T01A007. ASME. (**Best Student Paper Award)**

3. **D George**, M Madou, EA Peraza Hernandez, "Self-foldable single-layer photopolymer and carbon structures", Active and Passive Smart Structures and Integrated Systems IX 11376, 1137625, 2020

4. **D George**, EA Peraza Hernandez, M Madou, "Capillary folding of patterned polymer polyhedra", International Journal of Nanotechnology (IJNT), Vol. 17, No. 7/8/9/10, 2020

SKILLS

COMSOL, MATLAB, ANSYS Workbench, Fluent, CFX, SolidWorks, Python, MS Office, LaTeX
Raman Spectroscopy, SEM, XPS, AFM, Photolithography, Softlithography, DMA

ABSTRACT OF THE DISSERTATION

Shape and Microstructure Control in Carbon MEMS via Origami-based Fabrication and Electrospinning

By

Derosh George

Doctor of Philosophy in Mechanical and Aerospace Engineering

University of California, Irvine, 2021

Professor Marc J. Madou, Chair
Assistant Professor Edwin A. Peraza Hernandez, Co-Chair

Carbon possesses a distinctive ability to form chemical bonds with other carbon atoms and create unique architectures. In the last few decades, we have witnessed the discovery of different carbon systems including fullerene, nanotubes, and graphene. The versatile and diverse nature of the element can be fully exploited only if different shapes and microstructures can be manufactured, especially at the small length scales given the potential of carbon in microengineering applications. Two promising miniaturization approaches for small-scale manufacturing of carbon microelectromechanical systems are *photolithography* and *electrospinning*. However, these fabrication methods need to be further evolved to have the ability to fabricate complex three-dimensional shapes and to enable tailoring of the carbon microstructure.

The first part of this work integrates photolithography and origami design, where an assisted folding approach and a self-folding approach are devised and demonstrated as three-dimensional carbon microfabrication methods. In the *assisted folding* method, fabrication of three-dimensional polymer shapes is achieved by adjusting the material properties of photopolymer films along their planform and utilizing the enhanced surface tension effect at small length scales. Complex surface geometries with patterned facets are fabricated by implementing capillary folding on a photopatternable material. For the *self-folding method*, the

photolithography process is tailored such that developer solution is non-uniformly absorbed throughout the thickness of the fold regions. Solvent is diffused into the foldable regions of low cross-linking density during the development step of the photolithography process. The solvent concentration is non-uniform across the thickness of the folds and causes a strain gradient at these regions when the solvent is removed by heating the films, which enables self-folding. Experiments are performed to calibrate a model that relates the dimensions of the folds and their exhibited fold angle. The model is incorporated into a computational implementation of the unfolding polyhedra method, a versatile approach for origami design, that considers smoothly bent folds. This method, enhanced with the experimentally calibrated model, enables the design of planar films programmed to reliably self-fold into target three-dimensional shapes when heated. Polyhedral shapes are fabricated to demonstrate the developed method for origami-based fabrication.

In the second part of this work, the design of carbon microstructure using mechanical and chemical treatments is presented. By applying stress during carbonization, we demonstrate how to retain the alignment of Polyacrylonitrile (PAN) molecular chains achieved through electrospinning to produce a more uniformly graphitized carbon. The resulting carbon exhibits an oriented but fragmented lattice structure and are innately rich in nitrogen heteroatoms. Besides this mechanically induced graphitization, we also report a chemically induced graphitization method on patterned nanowires using a combination of low voltage electromechanical spinning and electrodeposition of nickel. This nickel-coated carbon wire structures are used as templates to selectively deposit multi layer graphene. This patterning technique offers high throughput for nano writing, which outperforms other existing nanopatterning techniques, making it a potential candidate for large-scale carbon nanomanufacturing.

Chapter 1

Background

1.1 Shaping of Carbon

Carbon rich polymer materials can retain their structural identity even after heating them at high temperature in an inert atmosphere. In the mid 1950s Redfern observed this phenomenon on a tape that he used in one of his experiments to hold some samples together in his furnace. To his surprise, the polymer tape was converted into corresponding carbon after the heat treatment. And that marks the discovery of glassy carbon. This heat treatment process to form glassy carbon is referred as pyrolysis. Back in those era, miniaturization was not common and thus the carbon structures were limited to relatively large length scales. Later, with the information technology revolution, semiconductor industry revolutionized miniaturization technology. Many fields, including microelectromechanical systems (MEMS), sensors, and the biomedical sector, adopted techniques from the semiconductor industry to achieve miniaturization. One of the most popularly used patterning technique in the semiconductor industry is photolithography. As the name indicates, it is a patterning method that involves light. The patterning method utilizes polymer resins that can be crosslinked by UV exposure

to produce patterned polymer thin films by selectively exposing the resin to UV. Luckily, some of the photocurable polymers commonplace in the MEMS fabrication have a carbon-rich backbone and hence can retain their shape post-pyrolysis. It is this property that is exploited in carbon-Microelectromechanical systems (Carbon-MEMS) to produce patterned two-dimensional carbon structures of small length scale for various applications.

The process starts by making a thin film of the photocurable carbon precursor. Silicon wafers are generally used as the supporting structures for making polymer thin films. The photocurable polymer film is selectively exposed to light to initiate chemical curing/crosslinking reaction. While some photo polymers generate new chemical bonds as a result of the exposure, there are some photosensitive polymers that experiences breakage of bonds upon irradiation. The former is categorized as the negative photoresist, whereas the latter falls under positive photoresist. Although both of these types of photocurable materials are capable of being converted into carbon, negative photoresists are predominantly used as the precursor to make patterned carbon structures. This unique way of patterning carbon was a field-transforming method since machining is unfeasible for carbon as the material is brittle in nature.

Use of a planar photocurable polymer thinfilm restricted the final patterned shapes to two-dimensional. Indeed, the quest to make more complex three-dimensional shapes remained futile additive manufacturing methods such as stereolithography and two-photon lithography capable of making millimeter and submillimeter polymer structures with complex shapes emerged. These methods use selective exposure of photocurable polymers either using a masked layer-by-layer exposure in stereolithography or using a high precision point-by-point exposure using a laser in two-photon lithography to cure the resin at required locations to create three-dimensional shapes with high accuracy. While these methods can form three-dimensional shapes having micrometer precision, the time required to fabricate such shapes, serial nature of the fabrication methods, and the exorbitant cost associated with the process

render it an unfeasible micromanufacturing method. Alternatively, if folding of the patterned two-dimensional polymer structures formed using the aforementioned photolithography method is enabled, a new three-dimensional fabrication method that resembles the traditional origami can be developed. Although there are some application specific origami fabrication attempts reported for making complex shapes using different materials, there is no such methods exists for carbon micromanufacturing. Therefore, to develop such origami-based carbon fabrication method, it is imperative to dig deeper into the reported origami microfabrication methods in other fields and learn from them.

1.1.1 Origami Fabrication Methods

Carbon structures with an extruded shapes are formed by pyrolyzing photolithographically patterned carbon-rich photopolymers as mentioned earlier. Developing a method where photolithography-based methods for making three-dimensional shapes is of importance as it would be easier to integrate such methods with the well-established integrated circuit (IC) industry-based microfabrication methods. One possible way to achieve this is by making complex three-dimensional shapes from the patterned shapes that are formed using two-dimensional fabrication methods. Origami, an artform where a single sheet of paper is folded to form intricate shapes, is a potential pathway to move from the two-dimensional nature of the photolithography to the desirable three-dimensional structures.

History of Origami

[1] Origami is an ancient Japanese art of folding a single uncut paper to form complex shapes, which date back to the 6^{th} century A. D. It was not very popular back in those days due to the

[1]Portions of this section are reprinted or adapted from [George D., Madou M.J. (2021) Origami MEMS. In: Dixit U., Dwivedy S. (eds) Mechanical Sciences. Springer, Singapore. https://doi.org/10.1007/978-981-15-5712-5_9]. Figures and texts are reprinted by permission of the Springer Nature.

high price of paper. Nevertheless, the art was sustained through the generations as a typical Japanese tradition. There are also some evidences that similar art forms existed in Europe as early as the 8^{th} century. It is not clear, however, if origami in Europe was independently developed or found its way from Japan to Europe via the famous silk road. Although the Origami artwork was practiced in various parts of the world, it was not until the 20^{th} century, during Akira Yoshizawa's time, that this art form became globalized. Yoshizawa published a system of patterns and developed a variant of origami called wet origami. Wet origami uses a dampened paper instead of a dry sheet of paper to construct more accurate non-geometric origami (Fig. 1.1). Later, Demaine and Tachi developed an algorithm to make almost any conceivable polyhedron shapes from a sheet of paper through just folding (Fig. 1.1) [33]. It is also possible to make more complex shapes through the simultaneous use of multiple sheets of papers instead of only one sheet in a technique known as modular origami (Fig. 1.1) [234]. Using traditional origami, wet origami, and modular origami, simple two-dimensional shapes are transformed into complex three-dimensional shapes [111]. Such a folding technique, from an engineer's perspective, offers some key advantages i) easy packaging and transportation due to the flat configuration, ii) high specific strength due to minimal material usage, and iii) simplicity of construction due to the absence of mechanical components. These advantages inspired engineers of the modern age to translate the origami technique to various engineering platforms, either using paper itself as the material (paper-based origami) or with the help of materials other than paper.

A sheet of paper is the raw material, and manual folding is the construction method in the paper-based origami technique. The original purpose of this type of origami was recreational. When adopted for engineering purposes, such as load-carrying applications, encapsulation and sensing, raw materials and folding strategies had to be rationally adapted for the specific application at hand [164, 87]. Before going into materials other than paper, let us briefly discuss the engineering applications of paper-based origami. For manufacturing of paper-based origami, folding methods that do not involve manual-folding become manda-

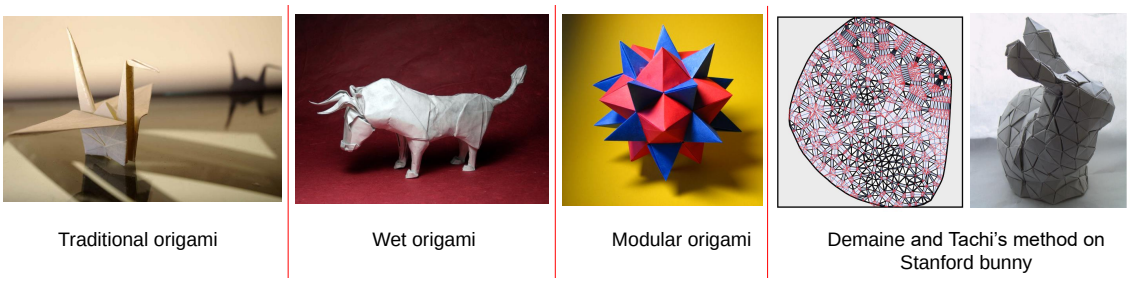

Figure 1.1: Traditional origami (Picture credit: Curt Smith, `https://bit.ly/353bCb4`), wet origami (Designed by Stephan Weber, `https://bit.ly/2MB460z`), modular origami (Designed by Tomoko Fuse, `https://bit.ly/2t5IsuC`), and origamizer (Demaine and Tachi 2017 [33], licensed under Creative Commons License).

tory. Hand-free folding of paper-based origami shapes is possible via actuation mechanisms that can be implemented on the paper through printing. For instance, folding of a paper is realized by printing a water-based ink on the paper followed by drying. Drying shrinks the paper locally and results in its folding. The dried paper is stiff enough to sustain a stable folded configuration. Such paper origami can be utilized for load carrying applications. Meanwhile, the field of paper-electronics, where paper-based electronic systems are studied, offers a host of techniques for incorporating basic electrical elements such as transistors, batteries, and actuators on a paper-based origami [109, 79, 189, 177]. Paper-based origami has also found application as an inexpensive diagnostic platform. In the year 2007, Whitesides and co-workers from Harvard University introduced a paper-based microfluidic analytic platform using a single piece of patterned paper [135]. Later the same group presented a more sophisticated form of the paper-based diagnostic platform with a stack of patterned paper layers. Eventually, integration of multi-layered paper microfluidics with the origami technique enabled single-step patterning of complex microfluidic systems [246]. This simplification also facilitated easy integration of various components, *e.g.*, a battery, into the system by bringing paper-electronics and paper microfluidics together.

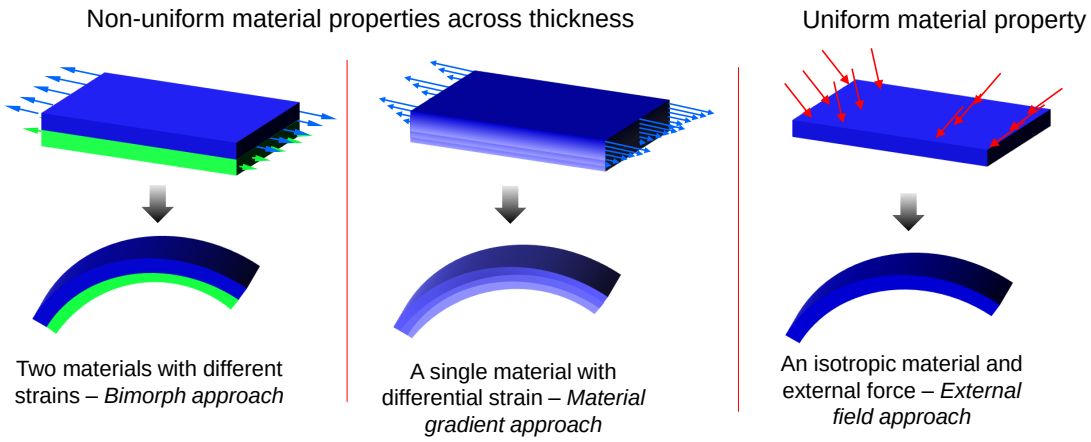

Figure 1.2: Bimorph approach, material gradient approach, and external field approach.

Folding Strategies for Origami

Here, we examine various strategies for folding sub-millimeter and sub-micron scale patterned thin sheets for origami shapes. Logical approaches to accomplish folding in the sub-millimeter regime include borrowing existing folding strategies from a larger length scale, and/or mimicking folding mechanisms found in nature. Bending and buckling tactics are adopted to transform simple two-dimensional shapes to complex three-dimensional shapes in sub-millimeter length scale. Bending of a sheet takes place when it experiences an out-of-the plane moment (Bending moment). Buckling, on the other hand, is a result of a compressive force on a slender object. Both bending and buckling on a sheet material is generally realized via two different methods: 1) by introducing a non-uniform material property across the sheet thickness followed by a trigger, or 2) by applying an external force to materials having a uniform property (Fig. 1.2). The trigger can be the mere releasing of the material from a supporting structure or the application of an external field. Generally, for the first case, a mismatch in the deformations at different locations of cross-sections along the thickness (a strain mismatch) causes bending or buckling. The required strain may be induced via swelling, shrinkage, thermal expansion, piezoelectric effect, configuration change in a liquid crystal elastomer, or a shape memory effect. In the second case, an external force prompts

bending or buckling of sheets that are isotropic in nature. Driving forces of such geometrical transformation include surface tension-based actuation, magnetic actuation, mechanical actuation, or electrical actuation. In general, bending and buckling are achieved in the sub-millimeter length scales using the following strategies (Fig. 1.2).

- By introducing different strain values on two attached sheet materials – Bimorph approach.
- By introducing differential strain across the thickness of a single material by designing different material properties across its thickness – Material gradient approach.
- By using external fields on a material with uniform properties across the thickness – External field approach. (Note: External fields may be required for the activation of both the bimorph and material gradient approaches, but the material property across the thickness is not uniform in either of them.)

Bimorph Approach

Materials often display deformation when heated. Dimensional changes generated in a material due to temperature variation are often homogeneous, leading to simple stretching or compression. However, when two such sheets (Generally, metals in the case of larger length scales) having distinct thermal expansions are bonded together (e. g. bimetallic strip), the resulting structure bends upon heating because of their strain mismatch [36]. The bending is such that it forms a convex shape towards the side of the material having a higher thermal expansion. Curvature formation by heating bimetallic strips is one of the conventional approaches for bending thin constructs at scales larger than a millimeter (Fig. 1.3). The

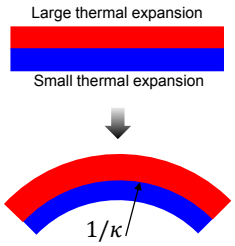

Figure 1.3: Bimetallic strip.

curvature is expressed based on Timoshenko's plate theory [202] and is given as follows.

$$\kappa = \frac{6\Delta\alpha(1+m)^2}{h[3(1+m)^2 + (1+mn)(m^2 + \frac{1}{mn})]} \tag{1.1}$$

where $\Delta\alpha$ is the difference in thermal expansion coefficients of the two materials, m is the thickness ratio between them, and n is the stiffness ratio of the two materials. Although similar bending methods using two distinct materials can be implemented for the microfabrication of bent structures, the execution of the idea at that length scale must adopt various crafty new ways. Driving forces relevant for bending sheets of micron length scales include residual stress, swelling, liquid crystal alignment, and shape memory effect. The general strategy is to attach these active materials to another inactive substance, followed by actuation/trigger (Unimorph). Alternatively, both the sheets could be active materials, as in the case of bimorphs. The term bimorph is often used as a more generalized term encompassing both uni- and bimorphs. We will be following the same convention from here onwards. The active materials either shrink or expand to causes an overall bending of the structure.

Fabrication Strategies for Curved Shapes Using Bimorph Approach

Rational exploitation of residual stress, swelling, configuration change in liquid crystal elastomer, or shape memory effect results in bent shapes (Fig. 1.4). In microfabrication, material

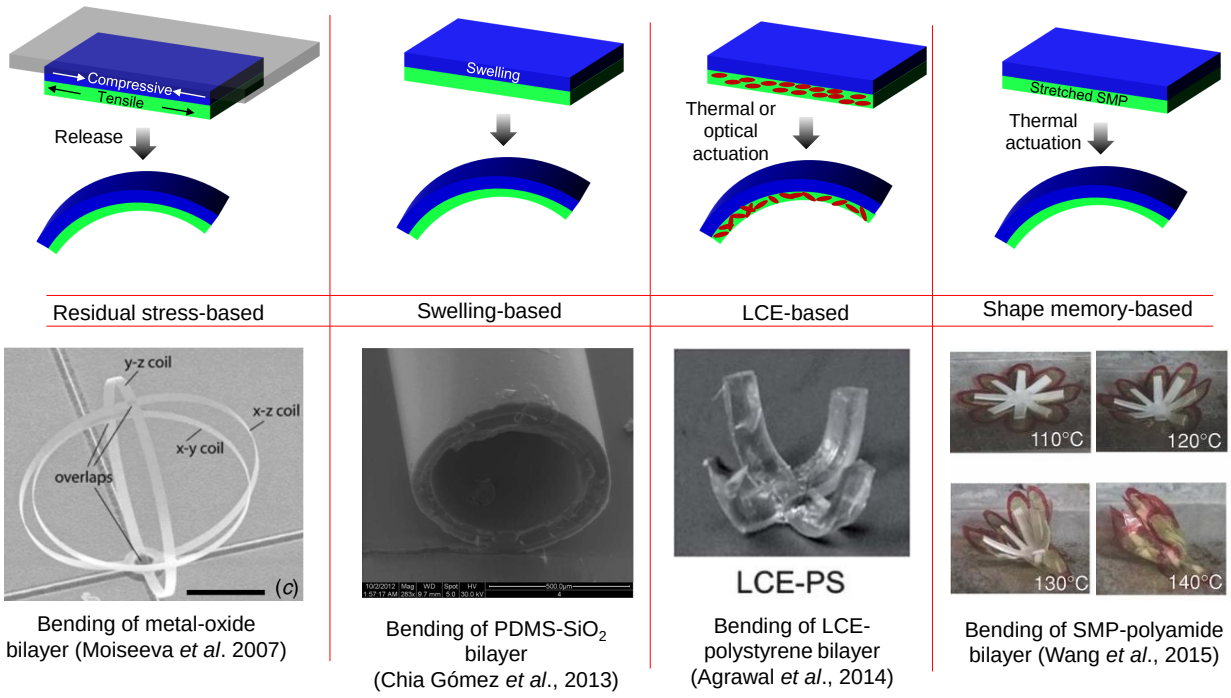

Figure 1.4: Implementation of bimorph approach to obtain bending using residual stress (Reproduced with permission. ©IOP Publishing. All rights reserved) (Moiseeva *et al.* 2007 [144]), swelling/shrinking (Republished with permission of the Royal Society of Chemistry; permission conveyed through Copyright Clearance Center, Inc.) (Chia Gómez *et al.* 2013 [65]), liquid crystal elastomer (Republished with permission of the Royal Society of Chemistry) (Agrawal *et al.* 2014 [1]), and shape memory polymers (Wang *et al.* 2015) [216].

deposition often entails compressive or tensile residual stress within the layers. This residual stress is, generally, considered detrimental for microfabrication since it acts as a bottleneck for some of the traditional fabrication processes since a large amount of such pre-stress leads to cracking of the films or even breaking of the substrate. Conversely, the same pre-stress could become a blessing and generate a bending moment capable of forming origami shapes if adjoined with another material having different internal stress. For instance, one of the ways to grow SiO_2 on silicon is by thermal oxidation. This thermal growth produces a SiO_2 layer with compressive stress. When a metal with lesser compressive stress is deposited on top of this pre-stressed SiO_2 layer, and then the bilayer is released from the silicon, the strain mismatch results in the bending of this bimorph [144]. Similarly, chromium deposition also introduces residual stress. Consequently, a bilayer of chromium (Cr) and copper (Cu) exhibits bending as soon as it is released from the supporting structure. As an extension of this bimorph approach, bending in both directions can be achieved by depositing copper and chromium in a Cr/Cu/Cr arrangement [11]. The bending direction, in this case, is dictated by the thicknesses of the patterns of the chromium layer on the top and on the bottom.

Nature presents a variety of movement mechanisms in plants that exploit swelling caused by water intake. Generally, a gradient in the solvent concentration across a cell wall leads to water intake by the cell through osmotic pressure build-up. Intake of water, in turn, leads to their swelling, and this can trigger movement in plants [97]. Among various examples from nature, one of the most studied is the bilayer design that causes the release of ripe seed from conifer cones [29]. A technique emulating such bending can be adopted for the fabrication of small origami shapes [5]. Hydrogels and certain other polymers are capable of absorbing solvents. Temporal and spatial control of the absorption and the resulting swelling of polymers enable bending and folding in those precursors [82]. Additional control over the bending or folding may be achieved by designing materials that respond to stimulations such as a change in pH, temperature, presence of enzymes, light absorption, electric field, and solvents [10, 117, 122, 204, 190].

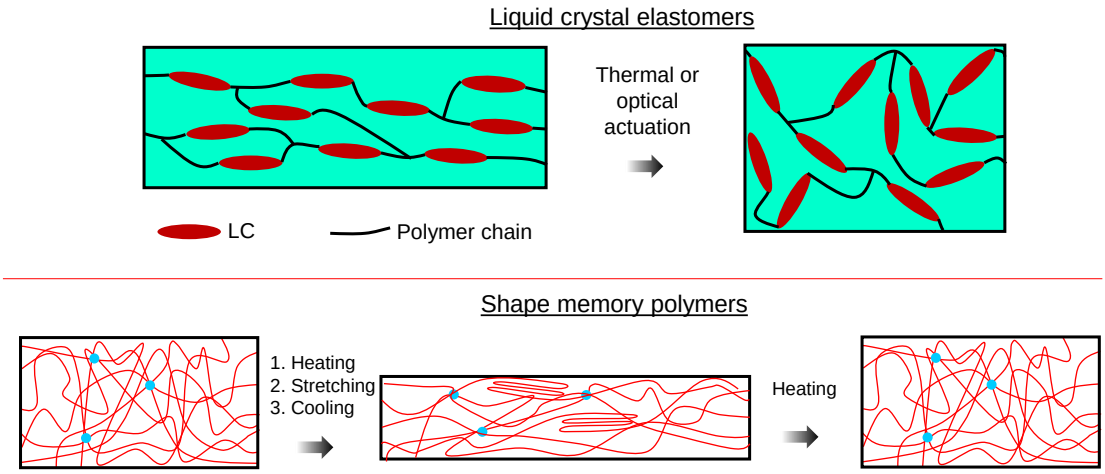

Figure 1.5: Working principle of liquid crystal elastomers and shape memory polymers.

A liquid crystalline elastomer (LCE), another type of active material, is synthesized by aligning liquid crystals (LC) inside a crosslinked polymer matrix by means of mechanical, surface, or chemical forces [152]. The aligned LCs enhance the stiffness along the length of their orientation. Conversely, when transformed into a randomly oriented configuration, the misalignment is manifested at the macroscale as a contraction of the LCE along the initial alignment direction (Fig. 1.5). This material deformation characteristic of an LCE makes it possible to fabricate three-dimensional shapes that are activated through different mechanisms. One such method utilizes a light-sensitive molecule called Azobenzene (AZ). AZ exhibits cis-trans isomerization under the influence of UV light, where trans-AZ has a rod shape and lets the LCE keeps its ordered shape, cis-AZ has a bent configuration, and its presence adversely affects the ordered structure of the LCE [114]. Disorder in an LCE, as mentioned, leads to the deformation of the material. Therefore, attaching this kind of LCE to an inactive material and then shining UV light invokes the bending of this assembly. Similar to this chemically engineered degree of crystallinity, mechanical forces can also induce alignment inside an LCE [30]. In the event of heating beyond its LC–isotropic phase transition temperature, the material loses its alignment, leading again to mechanical deformation.

Shape memory is another actuation mechanism that can be employed for bending. The shape memory effect is a material's ability to remember a configuration and return to that state upon actuation. Among various materials showing shape memory effects, shape memory alloys (SMA) and shape memory polymers (SMP) are the two major categories used in origami fabrication. SMA displays the shape memory effects because of its microstructure. For instance, NiTi, an SMA, has two stable crystal structures: austenite (stable at high temperatures) and martensite (stable at low temperatures). A deformation applied in the SMA's martensitic state is recovered upon converting it to austenite. Generally, SMAs are stretched in the martensitic state and contract when heated. This contraction results in bending in a bilayer, as depicted in Fig. 1.4. SMA increases the flexibility associated with system design since heating required for the actuation can be induced simply by applying a Joule heating current. Wireless powering with the help of an electromagnetic field is sufficient to attain the folding of centimeter-scale origami [18]. Despite these advantages, SMA is rarely used in smaller length scales due to the difficulty associated with its fabrication.

SMPs function based on an entirely different principle [173, 15, 116]. SMPs are generally amorphous polymers (polymer chains are randomly oriented) with restricted polymer chain mobility at room temperature. When they are heated above a specific transition temperature, the polymer chains attain more flexibility and are able to twist and rotate. At this stage, deformation is induced easily due to the enhanced mobility of the chains (Fig. 1.5). The polymer is then cooled down, and the deformation is temporarily locked down through physical or chemical interactions of the chains. When reheated, the original shape is recovered. Therefore, bending can be induced with such a deformed SMP that abuts an undeformed SMP sheet.

Although we mentioned various techniques where strain mismatch is used for bending, it must be noted that not any combinations of two materials that are having different strains offer a uniform bending towards one direction. A thin and stiff material on top of soft and

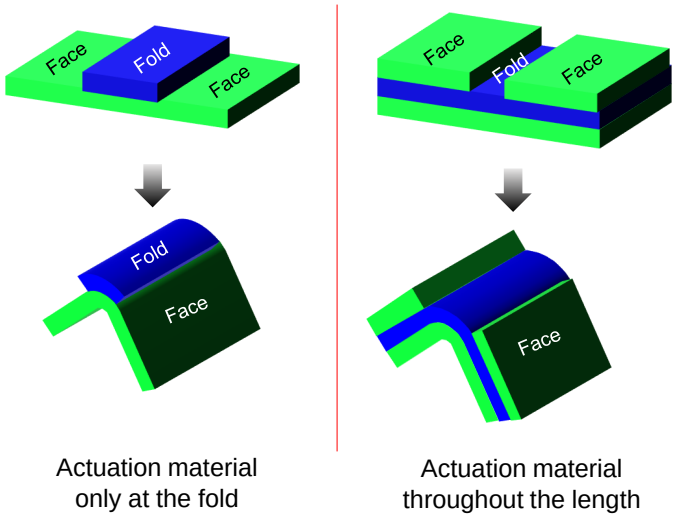

Figure 1.6: General folding strategies.

thick material can result in wrinkled shapes on the thin material [23]. Another peculiar case is when the bilayer is longitudinal rather than along thickness. The differential strain along the lateral dimension can lead to curled shapes [101, 21]. These kinds of deformations are not of interest at the moment for designing origami fabrication processes.

From Bending to Folding Using Bimorph Approach

A fold, as opposed to a bend, features a large curvature over a length that is considerably smaller than the overall size to the sheet [112]. Two typical design strategies are followed for fabricating a single fold shape and are depicted in Fig. 1.6. In the first strategy, the actuator is present only at the fold, and its deformation induces folding on the sheet assembly. The same technique can also be utilized for designing the timely folding of a bimorph. For instance, the application of a phase transforming or stiffness changing polymer at the folds of the bimorph can prevent the spontaneous folding of residual stress-based bimorphs and instead enables a controlled bending of the film driven by softening of the polymer with an appropriate trigger [10, 108]. In the second case, The actuator is present along the whole length of the sheet, but the bending is majorly focused on the fold region. Such local bending is possible by increasing the bending stiffness of the faces as shown in Fig. 1.6. A

typical example is a strip of bimorph with two rigid panels at the face regions. The bending predominantly happens at the folds since the faces are reinforced with an additional layer of material. As an extension of this folding technique, bi-directional folding (mountains and valleys) can be achieved if a soft material is sandwiched between two sheets having patterned openings on the top and bottom layers. This ability to fold in both directions allows for the fabrication of complex shapes. In one of the demonstrations by Na *et al.*, such a tri-layer design was used to make a 'crane' shape at micron length scale [148] (Fig. 1.7). The soft hydrogel sandwiched between two rigid layers had an elastic modulus two orders of magnitude less than the ones that were sandwiching it. This difference in their moduli ensured that the deformation led to folding, but not bending. It must be noted that, alternatively, a local actuation of the bimorph can also result in folding.

We mentioned earlier that bimorphs, without any other modifications, results in bending. An exception to such uniform bending is the hierarchical bending of polymer bilayers, which leads to folding [194]. Initially, when the absorption of water is activated at the edges of the bimorph, the bending occurs only at the borders of the pattern. This localized absorption and swelling lead to a tube formation at the edges. High rigidity of such tubes restricts the subsequent bending only to the intersections of those tubes. This localized bending enables folding without any additional patterning [195].

As far as the execution of the bimorph-based folding strategies is concerned, most of the examples discussed so far were based on lithography. For patterning some of the materials, we may have to rely on other techniques such as direct writing. In this technique, the volume of the target shape determines the time required for the fabrication, irrespective of whether a structure is hollow or solid. Consequently, fabrication time for a two-dimensional patterned origami precursor sheet is an order of magnitude less than the time required for the fabrication of corresponding three-dimensional shape. Therefore, folding of two-dimensional sheets is preferred over the direct writing of the corresponding three-dimensional shapes, as

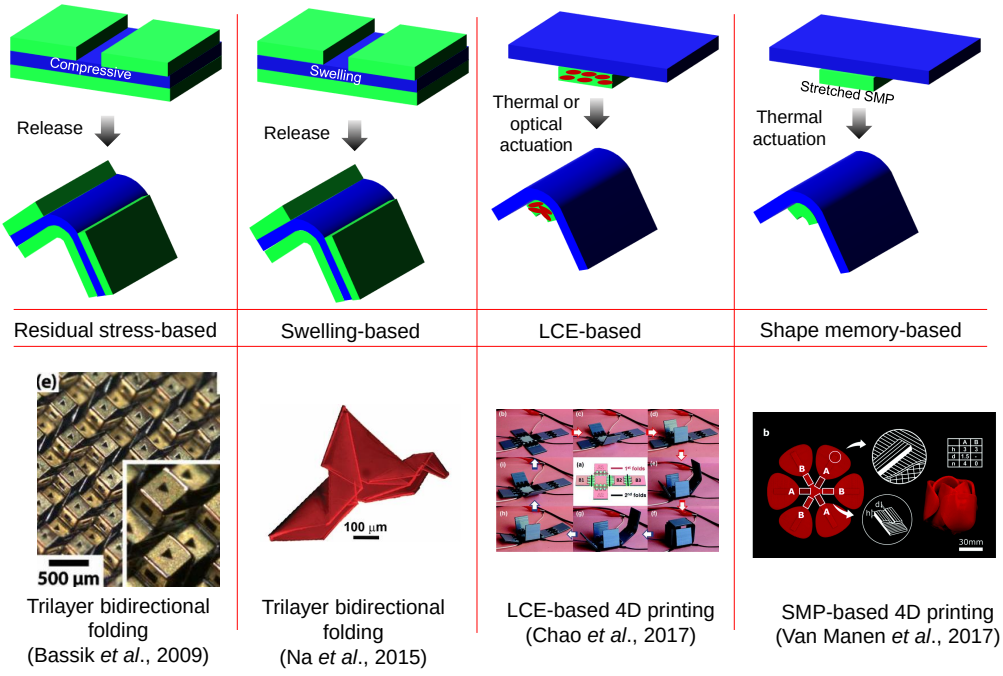

Figure 1.7: Implementation of bimorph approach to obtain folding using residual stress (Reprinted from (Bassik *et al.* 2009) [11], with the permission of AIP Publishing), swelling/shrinking (Na *et al.* 2015b) [147] (Copyright 2014 by John Wiley & Sons, Inc. Reproduced by permission of John Wiley & Sons, Inc.), liquid crystal elastomer (Yuan *et al.* 2017) [241] (Reproduced with permission from The Royal Society of Chemistry), and shape memory polymers (Teunis *et al.* 2017) [206].

far as the throughput of fabrication is concerned. Further improvements could be made by introducing 4D printing, where the morphing of the shape with respect to time is the fourth degree of freedom. This kind of morphing can reduce the production time and enables an extra degree of freedom, giving rise to free-form manufacturing. This kind of manufacturing is generally realized by incorporating active materials such as LCE and SMP in additive manufacturing through multi-material printing, followed by actuation [56].

Incorporation of the LCE into direct writing technologies was made possible with a relatively less viscous LCE ink. Low viscosity simplified the writing process as well as the required degree of molecular alignment in the resulting precursor pattern. Shear-thinning during direct writing causes the needed alignment of liquid crystals. The folding action can be initiated through Joule heating of an embedded wire inside a bimorph containing LCE [241]. Multi materials polymer 3D printers that are compatible with SMPs can fabricate foldable multi-material precursors. SMP is printed only on one side of the fold region to introduce a strain difference favorable for folding [55]. At a temperature higher than its transition temperature, the printed sheets are stretched. Then they are brought to a temperature lower than the transition temperature. When cooled, the SMP retains its original shape, but the elastomer to which it is attached does not. This difference in strain results in the bending of the sheet. When this bent shape is heated again, SMP goes back to the original shape leading to the flattening of the sheet. Printing at a temperature above the material's transition temperature can simplify the overall process even further as shown by van Manen *et al.* [207]. During the printing, the ink is extruded. This stretching is memorized by the polymer and leads to the morphing when reheated (Fig. 1.7).

Material Gradient Approach

Fabrication of bimorphs requires either multilayer photolithography or a multi-material writing, increasing the complexity of the process. Moreover, the strain mismatch that drives the morphing of the bimorph may cause occasional delamination at the interface of the two ma-

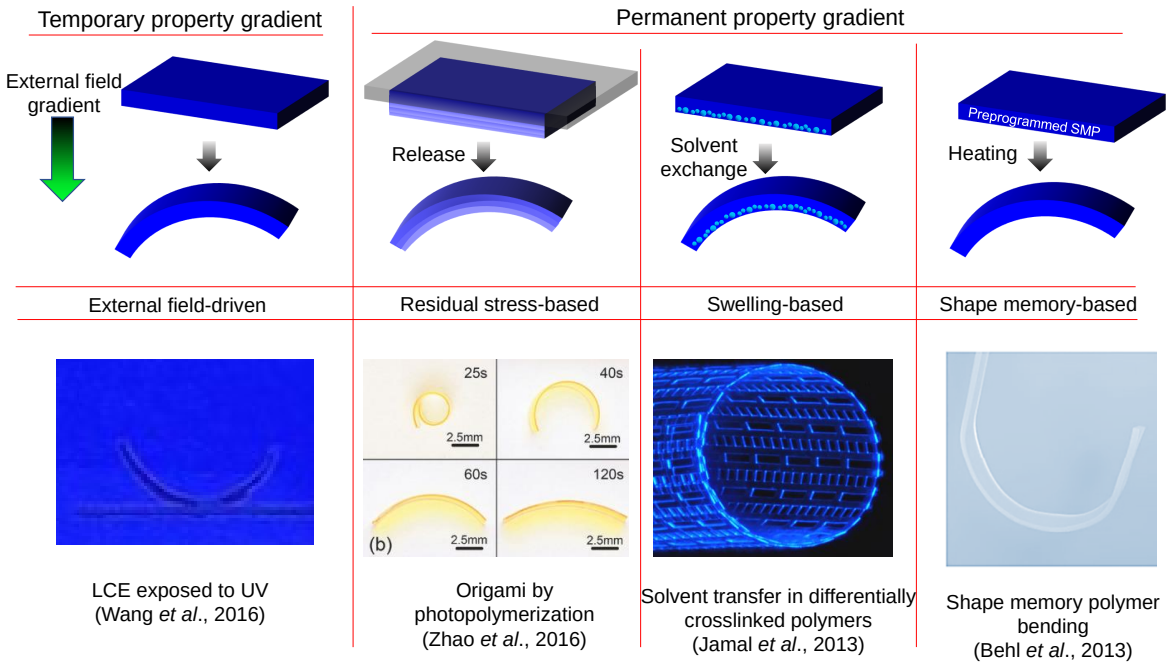

Figure 1.8: Implementation of material gradient approach to obtain bending using a gradient in the external field (Wang *et al.* 2016) [211], residual stress (Zhao *et al.* 2017b) [248] (Copyright 2017 by John Wiley & Sons, Inc. Reproduced by permission of John Wiley & Sons, Inc.), swelling/shrinking (Jamal *et al.* 2011a) [85] (Reproduced by permission from Macmillan Publishers Ltd: Nature Communications, copyright 2013), and shape memory polymers (Behl *et al.* 2013) [14] (Copyright 2013 by John Wiley & Sons, Inc. Reproduced by permission of John Wiley & Sons, Inc.).

terials. Having a smooth property gradient is the remedy for such problems that arise from a large strain mismatch (Fig. 1.8).

Fabrication Strategies for Curved Shapes Using Material Gradient Approach

Material property gradient within a sheet material can be categorized into two types; i) transient property gradient and ii) permanent property gradient. A transient property gradient is attained via reversible molecular rearrangement. An LCE sheet containing AZ upon irradiation, for instance, experiences different degrees of rearrangements at its polymer matrix across its thickness. The difference in molecular rearrangement results in a gradient in deformation with more contraction on the side closer to the light source, leading to a

bent shape. This type of tactic may be applied for swelling-based bending too [78, 69, 172]. A gradient in absorbing molecule in the medium results in a difference in the absorption across the cross-section of the sheet. However, these techniques are rarely utilized for the fabrication of complex origami shapes due to its unidirectionality[2]. Therefore, a property gradient that is permanently embedded in the material is preferred to a method that relies on an external field to achieve a transient material gradient. A permanent property gradient across the thickness of a sheet is fulfilled during its synthesis [104]. Fabrication of photopolymer sheets with varying crosslinking density is one of such synthesis methods. Photopolymers crosslinks when exposed to light. The crosslinking occurs first in the region that is closer to the light source. For explaining the process, this region is referred as the first layer, even though the crosslinking is not really a layer-by-layer process. The polymer undergoes shrinkage as a result of the crosslinking. As far as the first layer is concerned, the polymer is free to shrink in every direction. However, once a solidified layer is formed, the contraction of the subsequent layers would be constrained by the first layer. This constraint results in residual stress inside the material. The residual stress this region experiences is analogous to a stretched band. If this residual tension is released, the sheet will bend as shown in Fig. 1.7. This photopolymer-based execution of the gradient approach is known as frontal photopolymerization. It can create complex shapes having a submillimeter length scale [248]. A similar type of bending can be achieved using direct writing techniques too. Like the frontal photopolymerization-driven bending, the residual strain build-up during the writing of the second layer can lead to the bending of the film.

The degree of crosslinking across the thickness of a photopolymer reduces with the distance from the light source. This crosslinking-density gradient directly correlated to the porosity density inside its polymer matrix. Specifically, a less cross-linked SU8 sheet possesses a relatively more porosity compared to a more cross-linked sheet. Porosity in a material allows

[2]Here, external field changes the material property across the thickness unlike external field approach that we are going to discuss later, where field induces a bending moment without interfering with the material properties

for the absorption of various solvents by the substance. The more porosity that the material has, the more the absorption of solvents is. Consider a thin sheet with a crosslinking density gradient varying from a high level of crosslinking on the top to a low level of crosslinking on the bottom. If one fabricates such flat sheets with absorbed liquid (*e.g.* developer solution) inside them, the bending of the faces occurs towards the bottom surface when the solvent is removed. The cause of the bending is attributed to the shrinkage resulting from the removal of the large quantity of the solvent from the highly porous bottom surface of the sheet [85]. Please keep in mind that the reported fabrication based on this technique showed only a reversible bending of the SU8 film since nothing prevents the folded structures from going back to the original shape when placed inside the same solvent again. We will discuss a strategy to make permanent folding later in this chapter.

In the case of an SMP, the required bent shape is programmed onto a sheet by bending the film at an elevated temperature and followed by a cooling step. The sheet bends to the "memorized" shape upon heating. Unlike in the case of bimorph, where the linear deformation of the SMP bends a bilayer sheet consisting of the polymer and another material, bending is not assisted by a second material in this case.

From Bending to Folding Using Material Gradient Approach

Localized modification of material properties is easy to achieve with photopolymers by selectively illuminating the polymer sheet. In one of the methods, selective exposure concentrates the residual stress from the aforementioned sequential cross-linking to the fold region, leading to folding. Selective irradiation, in certain other photopolymer material, results in stress relaxation inside the material due to a polymer network rearrangement within it [117]. Mechanical and optical stimuli have been combined in a technique called photo-origami to exploit this stress relaxation to accomplish folding [178]. In this method, the sheets are stretched perpendicular to the length of the fold, followed by a UV exposure at the fold region. By exposing the fold region of a stretched film, localized stress relaxation can be

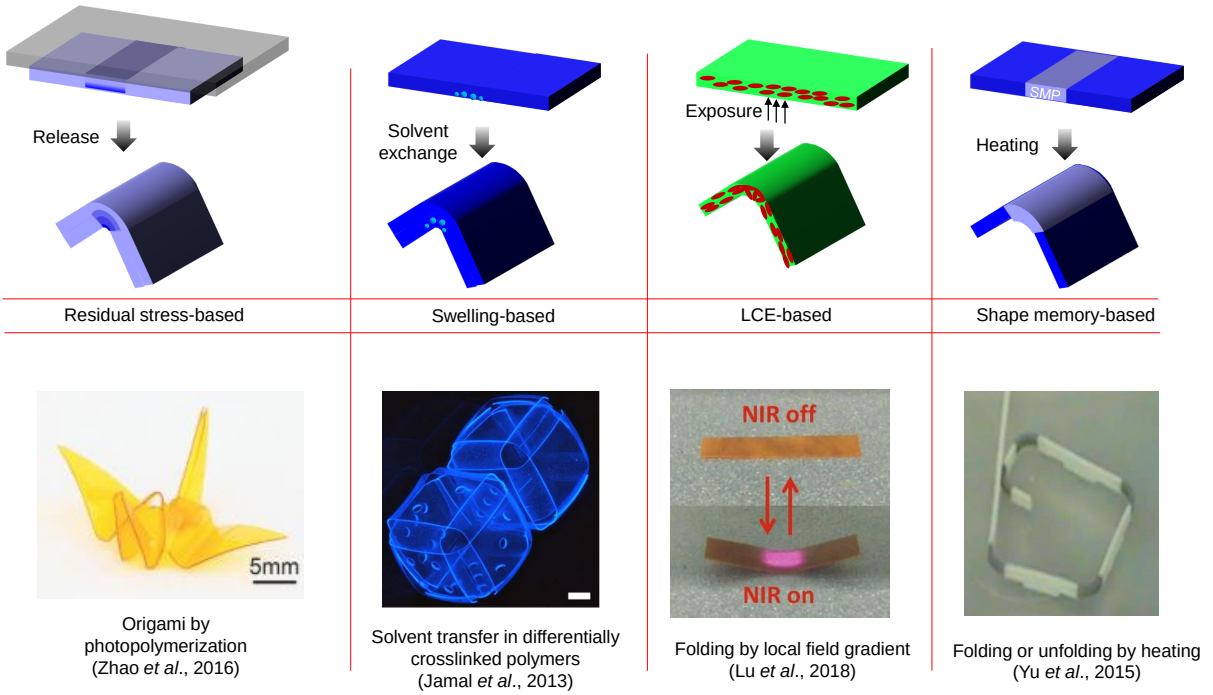

Figure 1.9: Implementation of material gradient approach to obtain folding using residual stress (Zhao *et al.* 2017b) [248] (Copyright 2017 by John Wiley & Sons, Inc. Reproduced by permission of John Wiley & Sons, Inc.), swelling/shrinking (Jamal *et al.* 2011a) [85] (Reproduced by permission from Macmillan Publishers Ltd: Nature Communications, copyright 2013), liquid crystal elastomer (Lu *et al.* 2018) [129] (Copyright 2017 by John Wiley & Sons, Inc. Reproduced by permission of John Wiley & Sons, Inc.), and shape memory polymers (Yu *et al.* 2015) [240] (Copyright 2015, with permission from Elsevier).

controlled. Exposure energy density varies across the thickness of the sheet. As a result, the irradiated side of the film experiences relatively more stress relaxation, causing local bending. The porosity density gradient that emerges from a differential crosslinking can also be focused on the fold region to achieve folding at sub-millimeter scales.

In another related light-based folding, sequential folding in mesoscale is achieved with Shrinky dinks, by printing the folds with inks of different colors followed by exposing to high-intensity light [126]. Unlike the previously mentioned photosensitive materials, here, the bending occurs due to the local heating of the material. The absorption wavelength by the ink depends on its color/absorption property. Absorption heats up the fold. Therefore, folds having different colors can be locally heated when they are exposed to the complimentary light. Shrinky dinks contract considerably upon heating because of strain release, and as a result, folding of the sheet happens. Instead of colored inks on the hinges, a graphene ink may be deposited to bend Shrinky dink material to actuate the folding with the microwave [28]. When exposed to microwave, since graphene is not transparent to microwave, the sheet is locally heated. Like the previous case, this local heating results in bending. However, the orientation of the fold with respect to the wave affects the folding of the material, limiting the versatility of the technique. In nanoscale, a focused ion beam (FIB) is used for the fabrication of folded shapes. FIB, when bombarded with the nanofilm, induces tensile or compressive stress on the film depending on the operating parameters. Gallium ion from FIB when colliding with the film can remove atoms from the gold film. The vacancies formed via this bombardment lead to grain coalescence and as a result, residual tensile stress on the top layer of the film. This leads to the bending of the thin film [192].

Heating-based folding can be induced in an LCE by locally heating the sheet beyond its transition temperature with IR irradiation. The side that is heated experiences a shrinkage due to the molecular rearrangement, leading to the bending of the LCE sheet. While folding in LCE is achieved through IR illumination of an isotropic material, an SMP-based folding

requires local preprogramming of an SMP. A direct writing technique may be employed to fabricate folds with SMP and the faces with an inactive material. By training this SMP-made fold-region, folded origami can be obtained.

External Field Approach

Here we discuss a new approach where bending of a sheet is carried out without changing its properties across the cross-section, contrasting previously discussed cases where the material properties of the sheets are tuned to induce bending. Various forces, including capillary, magnetic, and external compressive forces, can be the cause of bending in an external field approach. Since the external field approach involves different forces, it is essential to discuss them briefly before delving into the fabrication aspects of it. Capillary effects scale favorably for the micron-scale actuation. A comparison of the body forces ($\rho g l^3$) with the surface tension forces (γl), where l is the length scale, γ is the surface tension, ρ is the density, and g is the gravitational constant, reveals that the surface tension effects dominate in a smaller length scale. Therefore, surface tension can act as an actuation mechanism for micro origami fabrications. Nature takes advantage of this fact, as observed in the case of the drinking mechanisms of both Phalaropes and Hummingbirds. For a Phalarope, this heightened effect of surface tension at small scales is a way to accomplish, a gravity defying intake of prey-laden water towards its mouth. A Hummingbird's tongue exploits the surface tension to close lamellae on its tongue to entrap honey at each of its dips into honey-filled flowers. Here, the tongue closes because of the interaction between the soft lamellae and the honey. This bending phenomenon, surface tension-driven bending of the soft materials, is known as elastocapillary bending.

Droplets most often assume a spherical cap shape on a solid or a liquid surface to minimize the total surface energy. A droplet on a hard surface has three different surface energies associated with it: surface energy due to the air-liquid, solid-liquid, and solid-gas interfaces. For a droplet-surface-gas system, if the energy of liquid-gas and solid-liquid interfaces are

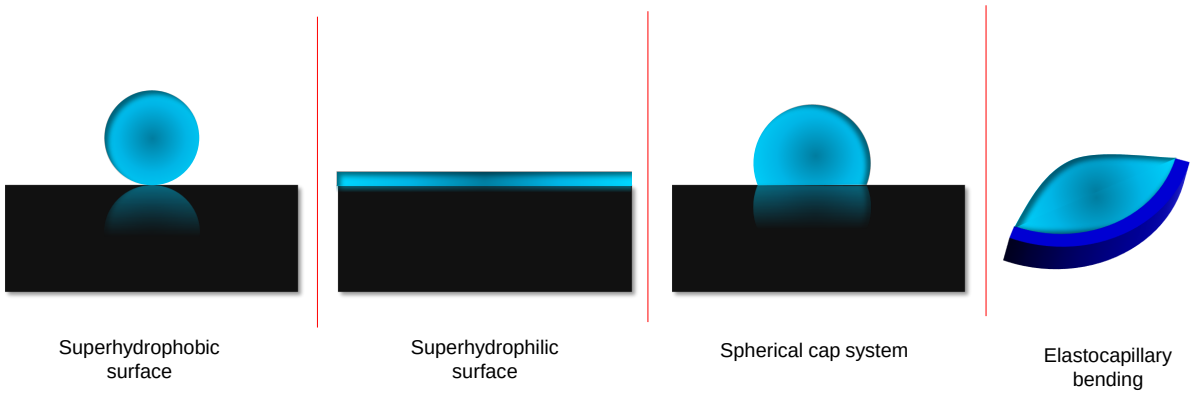

Figure 1.10: Different configurations resulting from droplet-surface interactions.

very high as compared to the other interface, the droplet forms a complete sphere to minimize the total energy. On the other hand, if the surface energy of the solid-liquid and liquid-gas is sufficiently small, the liquid spreads on the surface to avoid having the high energy offered by the solid-gas interface. In a case that is midway between these two cases, the droplet forms part of a sphere. Now imagine having a droplet on a thin sheet. The system has an extra option to wrap the sheet around the droplet to minimize the liquid-gas interfacial energy at the expense of the bending energy of the sheet. For a sufficiently thin sheet, this increase in energy is less than the reduction in surface energy. As a result, bending occurs (Figure. 1.10). Length scale below which the effect of capillary forces becomes significant is found by comparing the Laplace pressure, γ/l with the hydrostatic pressure, $\rho g l$, where l is the length scale, γ is the surface tension, ρ is the density, and g is the gravitational constant and is given by the capillary length, $l_c = \sqrt{\frac{\gamma}{\rho g}}$. For a significant bending, the curvature can be assumed to be of the order of $1/L$. Therefore, the bending energy density ($E_B = B\kappa^2/2$) scales as $Eh^3/(24(1-\mu^2)/L^2)$. The length scale at which the surface energy density of a droplet, γ, becomes significant (elastocapillary length) is then obtained by equating the bending energy density (E_B) with it and is given by elastocapillary length $L_{EC} = (\frac{Eh^3}{24(1-\mu^2)\gamma})^{\frac{1}{2}}$.

Controlled bending of a thin sheet using elastocapillary effect is achieved either with different droplet sizes or by adjusting the interfacial tensions of the sheet substrate. Droplets with

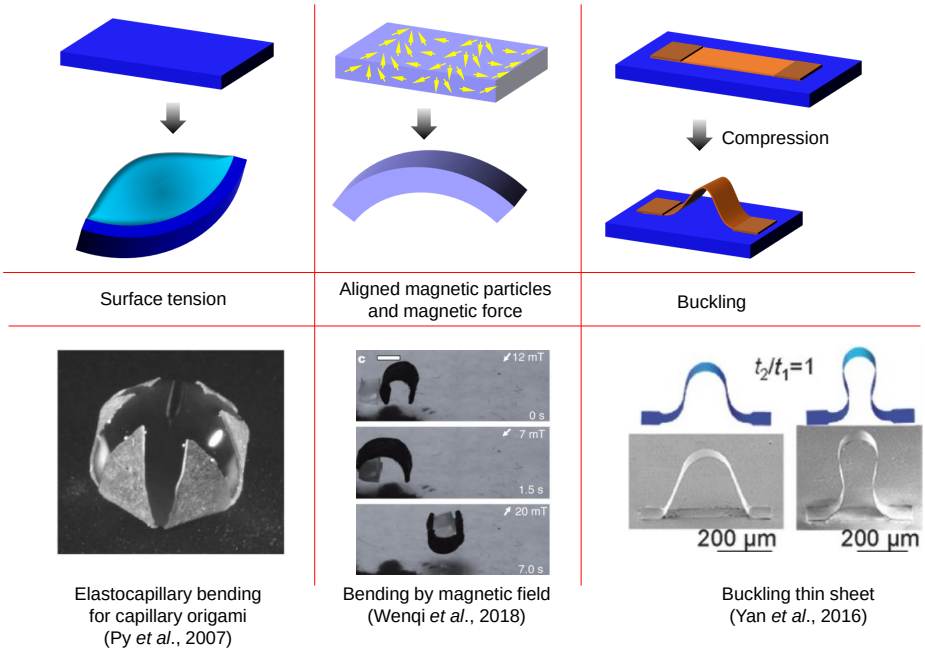

Figure 1.11: Implementation of external field approach to obtain bending using surface tension (Py *et al.* 2007a) [171] (Reproduced with permission, Copyright 2007 by the American Physical Society. `https://doi.org/10.1103/PhysRevLett.98.156103`), magnetic force (Hu *et al.* 2018) [80] (Reproduced by permission from Macmillan Publishers Ltd: Nature, copyright 2018), and compressive force (Yan *et al.* 2016b) [231] (Copyright 2017 by John Wiley & Sons, Inc. Reproduced by permission of John Wiley & Sons, Inc.).

a characteristic length too small or too big compared to the thin sheet do not bend the sheet significantly. In the case of a small droplet, energy gain would be negligible, and for a big droplet, bending of the sheet would require a significant deformation of the droplet, an energetically expensive process. Applying an electric field to the droplet changes the surface energy of the droplet. This change is manifested as change in the angle that the droplet makes with the substrate. When an electric field is applied to the droplet system, the energy associated with it is modified with additional electrostatic energy which is of the order of $\varepsilon L^2V^2/2(d+h)$, where ε is the dielectric constant, d is the insulating layer thickness, V is the voltage, h is the thickness of the sheet, and L is the length of the sheet. Comparing the electrical energy with the surface energy would give an idea about the order of magnitude of the voltage at which the contact angle is significantly affected by it and is given by $V \sim \sqrt{\gamma(d+h)/\varepsilon}$. Alternatively, the energy of the solid surface can be changed for controlling the folding angle [168, 132]. Oxygen plasma treatment is usually used for controlling the surface energy of the solid. The magnetic effect can also be utilized for causing deformation in materials. Elastomeric films embedded with magnetic particles can be magnetically controlled. An external magnetic field, B force the particles to orient along its direction [80].

Buckling occurs when a thin sheet is subjected to a compressive force. Energy density E_s of a compressed flat plate of a thickness t and a length, L is proportional to $t(\delta/L)^2$, where 2δ is the displacement by which it is compressed. Pure bending energy E_B is, on the other hand is proportional to $t^3\kappa^2$, where κ is the curvature of the flat plate. Thicker films experience a uniform compression across the cross-section of the plate. However, as the thickness reduces, the bending of the sheet becomes energetically more favorable. Therefore, thinner plates experience out of the plane buckling when compressed. In another external field approach, the cell traction force is used for folding patterned two-dimensional shapes into three-dimensional shapes.

Fabrication Strategies for Curved Shapes Using External Field Approach

Researchers from École Polytechnique, France, made complex three-dimensional shapes applying this concept by placing a drop of water on top of a soft pre-cut patterned two-dimensional polydimethylsiloxane (PDMS) sheet [171]. They used a droplet bigger than the volume of the target shape, and then the surplus water is evaporated to form completely closed 3D shapes. Until then, the capillary effect in microfabrication was purely detrimental, the one that leads to undesirable stiction in multi-layer lithography and coalescence in the case of high aspect ratio structures. The three-dimensional shapes formed using PDMS, however, was temporary. The sheets returned to their original shapes, as soon as the water droplets holding the three-dimensional shape together was evaporated. Patterning of the PDMS sheets to make two-dimensional shapes was challenging too. Moreover, the PDMS sheets had the same material property throughout their planform. Despite these shortcomings, the capillary origami method gave a new facade to one of the lithography limitations and opened a new door to three-dimensional fabrication. High elastic modulus may pose a limitation to this approach. A thinner sheet can be used to overcome the constraints posed by the high elastic modulus values of the materials. For instance, a silicon nitride with a thickness of 100 nm can be bent by the surface tension of water. Another approach to bend a high elastic modulus material is by softening it temporarily, followed by subjecting the material to capillary bending. Polymer sheets, for example, can be softened by heating them above its glass transition temperature.

Magnetic force is exploited for the reversible bending of the elastomers. The fabrication of sheets that can be controlled using an external magnet is achieved either using photolithography or using direct writing techniques. The orientation of magnetic particles determines the final folding shape of the sheet. Differently oriented magnetic particles on different faces are initially achieved by orienting the particles inside a curable silicone material using an external magnetic field followed by locking them in place by curing the silicone. A precision

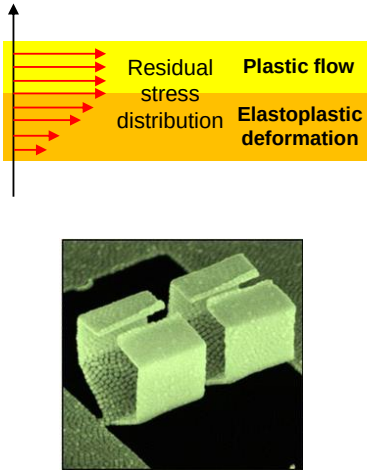

Figure 1.12: Folding induced on nanofilms using focused ion beam. Reprinted with permission from (Si *et al.* 2014a). Copyright 2014 American Chemical Society.

of 100 um is possible with photocurable silicone materials, as shown Xu *et al.* [224]. A sinusoidally arranged magnetic particles inside the sheet induces uniform bending on the sheet in a magnetic field.

Releasable multi-layered 2D precursors are buckled to form complex three-dimensional shapes. These shapes are fabricated using SOI wafers and sacrificial layers. A bonding location is designed, and multiple layers are transferred using polyvinyl alcohol onto a stretched elastomer. When the strain of the elastomer is released, the transferred structure buckles. Numerous configurations may be formed if the strain releasing sequence is controlled.

From Bending to Folding Using External Field Approach

Capillary-based folding of two-dimensional sheets made of rigid panels and flexible hinges can result in folded three-dimensional shape rather than a bent shape (Fig. 1.13). The shape obtained represents the configuration corresponding to the energy-optimized state, as explained earlier. (Therefore, the angle to which the sheet folds can be estimated by minimizing both bending and surface energies by assuming that the volume of the droplet

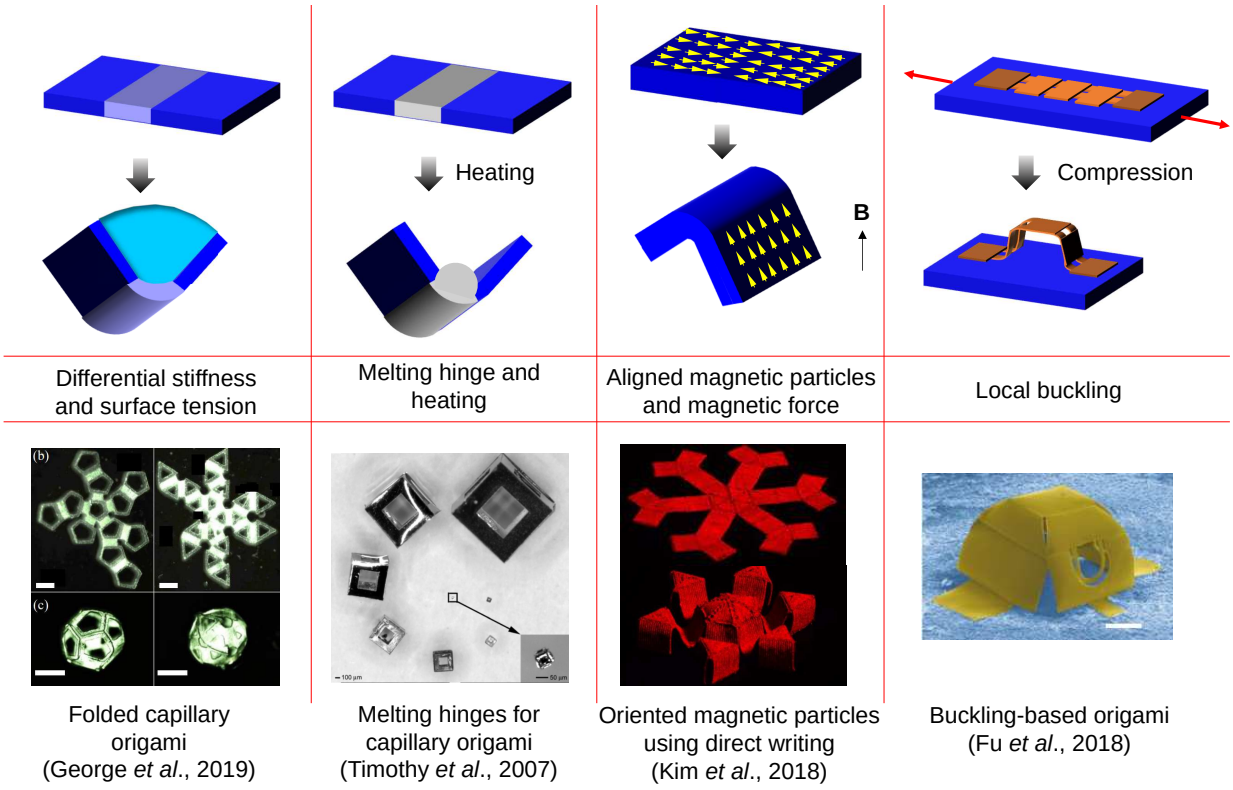

Figure 1.13: Implementation of external field approach to obtain folding using surface tension (George *et al.* 2019a) [60] (Copyright 2007, American Chemical Society), magnetic force (Kim *et al.* 2018) [102] (Reproduced by permission from Macmillan Publishers Ltd: Nature, copyright 2018) and compressive force (Fu *et al.* 2018) [48] (Reproduced by permission from Macmillan Publishers Ltd: Nature Materials, copyright 2018).

placed on the structure remains constant during the folding process [205].

Multilayer microfabrication technique can be used to make two-dimensional shapes having different materials at different locations; along the length and the thickness. Precursors can be made with high melting point rigid panels and low melting point folds. After releasing from the supporting structure, if these patterned structures are heated, the low melting point materials melt. The panels made of high melting point materials can be folded by using the surface tension of the melted hinge. Folding by a locally applied solder is an example of such a technique [67, 17]. Photolithography made local deposition of solder possible. This deposition of solder can be combined with other lithography techniques such as e-beam lithography and nanoimprint lithography to make panels with hinges in micro- and nanoscales [107]. These fabrication techniques enable the creation of smaller shapes. Moreover, the absence of any droplets at room temperature makes the fabrication process simpler. However, the materials used in this method are not ideal for most of the biological applications. Implementation of a folding procedure on polymers can overcome this shortcoming [6].

The electrostatic force drives folding action in millimeter-sized electro-origami robots [198]. Here, the folding is achieved by introducing opposite charges on each face. However, merely applying voltage is not enough to induce folding. The force which drives the folding can be improved dramatically by introducing a liquid droplet having high permittivity and high breakdown strength at the folds. The placement of liquid bead at the fold region enhances the driving force (Maxwells pressure). Moreover, an application of a high electric field is possible in this technique since the breakdown electric field increases considerably with the introduction of the liquid. Therefore, a high actuation force can be attained here, as compared to a system without any such liquid. This liquid bead prefers to be at the folds due to the electrophoretic forces generated by the high electric field there.

The integration of capillary origami to other existing MEMS components can be realized

by patterning conductive materials on top of them. Gold is considered as one of the best options for this application due to its high conductivity and low elastic modulus. The electrical connection between the faces is achieved through the gold connections that are running through the hinges [115]. The low modulus of the gold makes sure that the effect of gold on the folding is minimal. Patterned SU8 faces with latches can be fabricated using photolithography to make components that are compatible with MEMS. A hand-free bending of the faces is achieved by building conducting loops on them using gold, followed by the application of Lorentz force [183].

As far as the magnetically driven folding is concerned, a sheet where the particle orientation on adjacent faces of the origami is such that they are facing each gives rise to folding in the presence of a uniform magnetic field, as shown in Fig. 1.13. Aligned magnetic materials are achieved in a polymer matrix through a direct writing technique by sending unaligned magnetizable NdFeB particles through a magnetic field right before dispensing. In this technique, the magnetic field reorients the particles, and the rheology of the printed material keeps the aligned particle in place. The orientation of the magnetic particles with respect to the printing platform is adjusted by controlling the applied magnetic field direction and the printing direction.

Carbon MEMS Using Origami Fabrication

Carbon microparticles and micropatterns have found various applications, including sensors, flexible electronics, and photonics owing to their unique properties. Surface area, topology, and material properties of carbon influence the design and development of those types of system components. All these qualities can be controlled with the origami design techniques. Simple releasing of the two-dimensional elements from supporting structures itself increases the available surface area. Folding them and tightly packing them could further increase the available surface area in a unit volume and can create complex topologies that are otherwise difficult to achieve. Carbon also possesses excellent mechanical properties. Shapes

like Miura-ori can favorably modify overall mechanical properties even further [93, 130]. However, the carbon materials that we see in day-to-day life are not foldable. That begs the question: how can we make folded carbon shapes?

There are three significant ways to fabricate carbon-based origami.

By Folding Graphene or Graphene-based Materials

Although most of the carbon materials that we are accustomed to are brittle, carbon sheets made of single or multiple layers or atoms-single layer or multi-layer graphene- are flexible. Researchers observed sudden changes in the profiles during atomic force microscopy (AFM) scanning of functionalized graphene sheets (FGS). Such changes in the horizontal scan lines indicate the folded FGS resulting from the lateral force exerted by the AFM tip. It proves that the folding of FGS is possible with an external force. Molecular dynamics simulations show that the folding of graphene using a droplet of liquid is possible too.

A solvent exchange folding is possible with graphene. Graphene-based paper can be designed in such a way that it folds when absorbs water [146]. Fabrication of such a material is performed by locally converting graphene oxide (GO) to GO with polydopamine. When reduced, GO is converted into reduced GO (rGO) that are hydrophobic whereas GO-poly dopamine remains hydrophilic. This difference in the affinity of both material towards water leads to the local absorption of water to induce reversible bending.

By Integrating Carbon onto Other Materials

Graphene grown by chemical vapor deposition can be transferred onto SU8 by taking advantage of the adhesion force between them [35]. Polyhedral shapes containing graphene is fabricated by combining this transfer with the self-folding of differentially crosslinked SU8 that was explained earlier. This technique offers a new pathway to exploit the attractive qualities of the graphene more effectively. Earlier, we also mentioned about SiO_2 based bi-

morphs that fold due to residual stress. By including graphene also into that bimorph, a graphene origami can be developed [142].

By Converting Folded Polymer Shapes to Carbon

Polymers with carbon-rich backbones can be converted into carbon through heat treatment in an inert environment (pyrolysis). During the process, molecules other than carbon is removed, leaving the carbon behind. Interestingly, such a conversion into carbon retains the original polymer shape, but isometrically shrunken. Cellulosic paper survives pyrolysis. So does any forms that are made using cellulosic paper [84]. Therefore, structures made of carbon can be realized by pyrolyzing the paper-based origami. Although this work was focused on macro-sized carbon origami structures, the idea of forming three-dimensional carbon structures using origami was indeed an eye opener.

Our objective in this study is to develop a novel three-dimensional fabrication method where patterned two-dimensional carbonizable polymer films are folded into complex shapes. If such three-dimensional polymer shapes are possible to make, and they do not revert back to the original planar shape upon heat treatment, such fabrication route can be used for making complex three-dimensional shapes. Such an accomplishment could drive the Carbon-MEMS forward by enabling it to realize shapes that were impossible to achieve before.

1.1.2 Electrospinning Fabrication Methods

Electrospinning synthesizes nanofibers by stretching the precursor polymer solution using electric field. This synthesis method is a continuous production technique unlike the batch production that the photolithography-based carbon MEMS ensues. The phenomenon occurs when an external electrostatic force acting on the precursor polymer solution overcomes the surface tension of the polymer droplet.

History of Electrospinning

The story of electrospinning starts with electrospraying, a phenomenon where a droplet is split into tiny droplets in the presence of an electric field. It was William Gilbert in 17^{th} century that observed the phenomenon. Towards the end of 19^{th} century Lord Rayleigh systematically studied the phenomenon and theoretically predicted the formation of the electrospray. Electrospraying occurs when ionic liquid, solution containing polymers having low molecular weight, or solution having low concentration of polymer is subjected to electric field. From the electrospraying methods comes the electrosprinning for making nanofibers. When a polymer precursor of high molecular weight in volatile solvent is used for the process, the entanglement between polymer chains enables the formation of long nanowires. The volatile solvent is evaporated quickly when a low diameter wires are formed owing to the relatively large surface area to volume ratio that the wire possesses. Patents on electrospinning were filed in early 1900s, marking the starting of a new method for making extremely tiny wires from polymer solutions. Later, Geoffrey Taylor identified that the limit at which the production of nanowires/droplets occur is when the angle of the cone formed reaches below 49 degrees. In his honor, the cone formed in this process is generally known as the Taylor cone. Although the seminal work of Geoffrey Taylor on the cone jet formation happened in the 1960s, the small size of the wires prevented the field from growing as there was a lack of characterization techniques during that era. Increased use of imaging techniques such as electron microscopes revamped the research on the fields in early 2000s. This renaissance that the electrospinning saw led to its wide spread use in filters, photonic devices, electronic devices, electrochemical sensors, material strengthening processes, energy harvesting equipment, etc. While electrospraying can also be used as a machining method, in the context of carbon MEMS, electrospinning is far more relevant, and therefore, we will be focusing on the later from now on wards.

Process of Electrospinning

Electrospinning occurs when a high electric field is applied between a spinneret containing polymeric solution and a collector. Basic set-up of electrospinning is shown in Fig. 1.14. During this electrohydrodynamic process, the electrostatic repulsion of the surface charges deforms surface of the polymer solution and initiate a jet on the surface. These cone shaped instabilities are called Taylor cones. In a typical electrospinning set-up where a spinneret and the collector are ∼10 cm apart and a voltage ∼10 kV is applied, the jet ejecting from the charged polymer droplet travels in a straight line near to the cone in the region known as nearfield region. The jet gradually thins as it is accelerated by the electric field. As the formed nanowires are travelling between the droplet and the surface on to which it is collected (often referred as collectors), a combination of mechanical and electrostatic perturbations causes the wires to exhibit a whipping motion. This effect results in a random deposition of the wires on the collector. Meanwhile, the viscoelastic nature of the polymer keeps the wire from undergoing Rayleigh instability that causes it to break into droplets as in electrospraying process. Velocity of the jet in this nearfield region is estimated to be in the order of 1-10 m/s and critical length is defines as follows [74, 51]:

$$L = \frac{4kQ^3}{\pi\rho^2 I^2}\left(\frac{1}{R_0^2} - \frac{1}{r_0^2}\right), \tag{1.2}$$

where $R_0 = \frac{2\sigma Q}{\pi k\rho E}^{\frac{1}{3}}$, σ is the surface charge, Q is the flow rate, k is the electrical conductivity of the fluid, ρ is the density of the fluid, E is the strength of the electric field, I is the current passing through the jet, and r_0 is the initial radius of the jet.

This relation shows that an increase in flow rate decreases the length of the nearfield region. In this region the change in velocity of the jet gradually decreases and this leads to a whipping

motion beyond the nearfield region. It is critical to have this chaotic region to bring the radii of the wires down. Studies showed that the whipping motion causes the diameter to reduce in size in several orders of magnitude as it increases the path length. Indeed, reduction of the wire diameter from micrometers at the Taylor cone to nanometers at the collector is majorly attributed to this whipping instability. Moreover, small diameter of the wire improves the evaporation and ensures the mechanical integrity of the deposited wires. For electrospinning with bending instabilities, diameter of the spun wires, d is given by the following equation:

$$d = \left(\gamma \epsilon \frac{Q^2}{I^2} \frac{2}{\pi(2 \ln \chi - 3)} \right), \tag{1.3}$$

where γ is the surface tension, ϵ is the dielectric constant of the surrounding medium and and χ is dimensionless wavelength of the bending instability. While it is impossible to achieve a smaller wire without increasing the applied electric field, enhanced field can also cause more flow rate, leading to thicker wires.

Types of Electrospinning

Solution and Melt Electrospinning

Electrospinning process is categorized based on what is being electrospun and how the electrospinning is performed. One of such categorization is solution versus melt electrospinning. As the name indicates, in the solution electrospinning, polymer dissolved in an appropriate solvent is used. Polymer solutions can be successfully electrospun if it satisfies the following criteria:

1. They are made from polymer with large molecular weight.

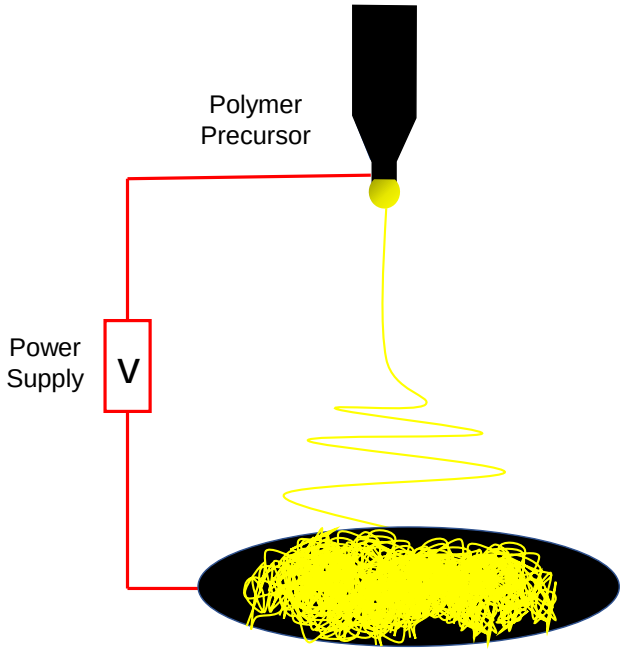

Figure 1.14: Solution electrospinning.

2. They exhibit sufficient molecular entanglement.

3. They are made using solvent that can be easily removed – Volatile solvents are generally preferred so that they evaporate quickly. Solvent exchange can also be used to remove the solvent from the wires formed.

4. They are made using a solvent solute combination with optimal solubility parameter

5. Their solute concentration is optimal – If the concentration is too low, the process results in continuous wire formation by ensuring polymer chain entanglement. In order to avoid high viscoelastic effects, the concentration should not be too high either.

6. They have optimal electrical conductivity – If the solution is not conductive at all, formation of surface charge will be difficult. Surface charges will not form if the solution is too conductive also. In fact, solutions can be made electrospinnable by adding salts during mixing or during polymerization steps.

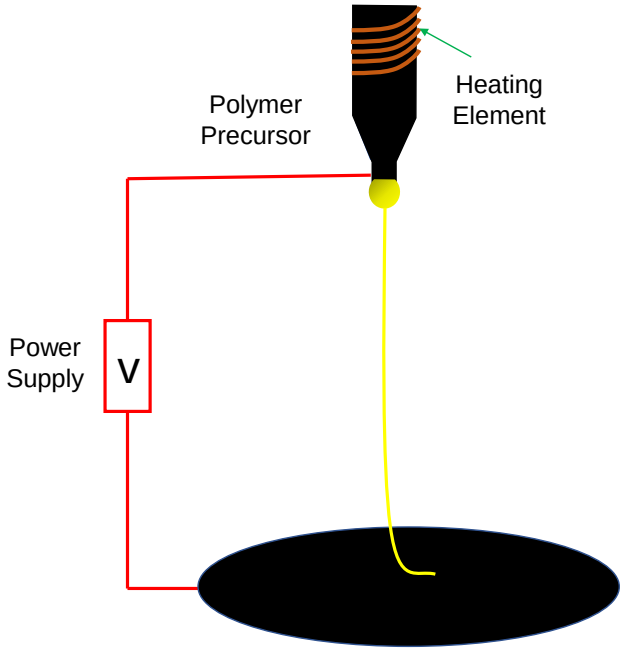

Figure 1.15: Melt electrospinning.

Melt electrospinning is another type of electrospinning where molten polymer is used instead of a polymer solution (Fig. 1.15). The need of a heating device makes the melt spinning process more complex than the solution spinning. Therefore, this method is mainly adopted if the solution spinning is not possible. Since a high temperature treatment is involved, it is also not possible to use thermoset polymers and thermally unstable polymers in this method. While the solution spinning undergoes a drying process, its melt spinning counterpart relies on solidification for continuous wire production. Melt spinning produces wires bigger than ones formed using solution spinning. The production of thicker wires in melt spinning is attributed to,

1. Rapid solidification of the melt polymer limiting the stretching
2. Suppressed whipping motion due to the low electric conductivity and high viscosity. However, electric conductivity can be increased by adding salts, and viscosity can be

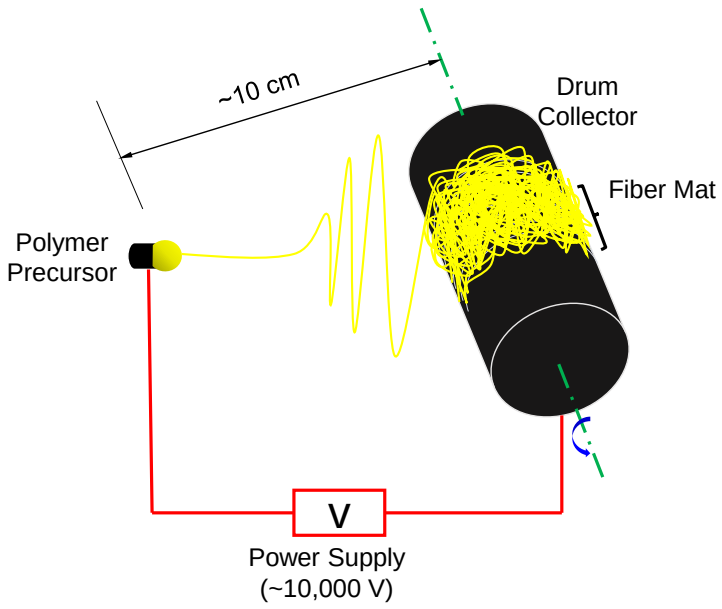

Figure 1.16: Farfield electrospinning.

reduced by using certain additives. These changes can result in reduced wire diameter.

Although the absence of the whipping motion results in the production of relatively bigger wires, it can also be seen as a blessing if the objective is to use melt spinning for controlled writing instead of random deposition.

Farfield and Nearfield Electrospinning

Based on how electrospinning is carried out, the process can also be categorized as nearfield electrospinning and farfield electropinning. In a typical electrospinning set-up where a spinneret and the collector are ∼10 cm apart and a voltage ∼10 kV is applied, the jet ejecting from the charged polymer droplet travels in a straight line near to the cone in the nearfield region and then exhibit a whipping motion, resulting in randomly deposited wires on the collector as shown in Fig. 1.16. This conventional way of electrospinning is generally known as farfield electrospinning. Due to the whipping motion of the wires produced, the control

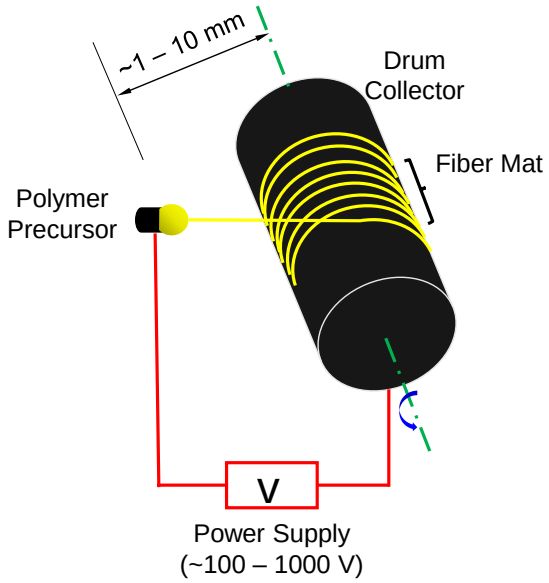

Figure 1.17: Nearfield electrospinning.

over the morphology of the electrospun wire in farfield electrospinning is limited. In order to tackle this, the nearfield region can be utilized for the deposition. Operating in nearfield region improves the controllability of the deposition process. In this electrospinnig process that is known as the nearfield electrospinning, the distance between spinneret and the collector is reduced to the order of 1 mm and the voltage applied is of the order of 100 – 1000 V as shown in Fig. 1.17. Here, by controlling the motion of either the collector or the spinneret, patterned writing of the polymer on the collector is possible. The complexity of the device is often blamed for not using this method for mass production of patterned nanowires.

Chaotic and Aligned Wire Deposition

Since the wires are preferentially deposited on a metal surface rather than on a collector surface covered with insulators, alignment of the wires can be obtained by rationally designing the collectors. Two electrodes separated by a gap as the collector ensure deposition of the

Figure 1.18: Spinneret with one polymer solution (Left) and spinneret with coaxial needles that can dispense two different polymer solution for electrospinning (Right).

wire in parallel arrangement between the electrodes. To further increase the complexity of the deposited wires, complex shaped collectors that can generate complex electric field may be used. Collector motion contributes towards the morphology of the deposited wires too. If the collector is moving with a high velocity, the deposited wires will align themselves along the direction of the velocity. If photosensitive polymer is the precursor, then the patterning of the randomly deposited wires can be done by following the photolithographic method.

Types of Spinnerets and Collectors

Different types of spinnerets and collectors are employed for electrospinning. Spinnerets can be 1) a solid pointy or planar surface, 2) a hollow droplet injecting syringe. Among hollow syringes, the needle can either be dispensing a single solution or a parallel laminar stream of multiple polymer solutions. In one of the variations, coaxial needles are used to create a

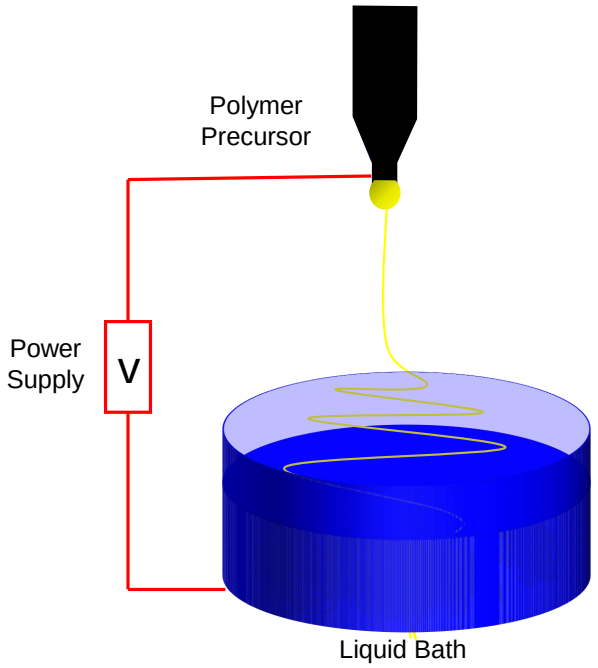

Figure 1.19: Liquid bath collector.

core-sheath configuration in the resulting wires as shown in Fig. 1.18. It is also possible to have multiple syringes to increase the throughput of the electrospinning process.

Collectors are generally conductive planar or curved surfaces. To improve the deposition footprint, an oscillating spinneret may be used. If structures are patterned on these collectors, the collected wires forms patterns on the surface owing to the disturbance in the electric field that it causes. Electricfield lines are concentrated on the pointy regions attracting the incoming wires preferentially to those regions. These topological features can be formed using the lithographic methods explained earlier in this thesis. Another way of manipulating the electicfield is by masking the collector with insulating material like tapes. Liquid baths are also used as collectors in certain cases to improve the solidification process and thus to avoid wires fusing together as shown in Fig. 1.19.

Types of Wire Materials

Electrospinning can be employed to synthesis nanowires of different materials. Metallic, ceramic, polymeric, and particle embedded wires are shown to be developed with the help of this simple method of nanowire synthesis. Among various materials, carbon is of high importance due to its multitude of applications in material science, electronics, electrical sciences, mechanical engineering, electrochemical applications, etc.

Carbon wires can be formed from carbon rich polymers. The polymers are subjected to a stabilization step followed by pyrolysis to obtain corresponding carbon structures. Polyacrylonitrile is the most commonly used precursor for carbon nanowire manufacturing. These are stabilized by heating the wires in air at 300°C for 3-6 hours. They are then heated to 1000°C in an inert atmosphere to get the PAN-derived carbon from this stabilized wires as shown in Fig. 1.20. Other polymers including lignin, polyimide, pitch, cellulose, polyvinyl alcohol, etc, have been explored as carbon precursors for nanowire production. These polymer precursors can be patterned to realize an electrospinning-based carbon-MEMS fabrication approach.

Absence of instabilities makes the near field electrospinning an attractive option for controlled deposition of polymer nanowires. Among various polymers, polyacrylonitrile (PAN) is commonly used as a precursor for making mat-like structure made of carbon nanowires. Although the fabrication of carbon mats using farfield electrospinning of PAN has been around for more than a decade now, patterned deposition of PAN remained elusive until recently. Guilia [22] demonstrated a way to make carbon wires by modifying the PAN solution by adding salt and polyethyleneoxide (PEO) to improve the spinnability in nearfield electrospinning setting. To further improve the controllability of NFES, the team here at the UCIBioMEMS developed a low voltage electromechanical spinning (EMS) method [22], which allows for yet more controlled nano writing with various polymers in NFES [81].

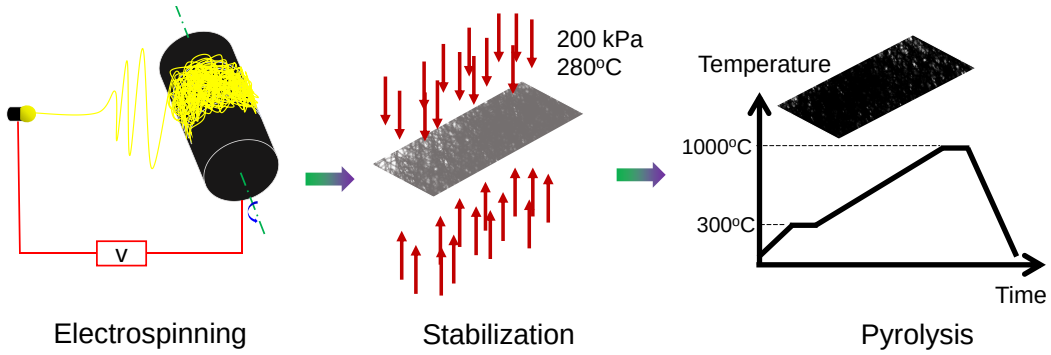

Figure 1.20: Schematic showing the process of making carbon mats using electrospinning process.

However, adding PEO, a polymer having high oxygen content, can limit the success of the carbonization of the wires thus produced. Moreover, the process struggled to reach an inter wire spacing less than 50 microns when parallel patterned wires are formed using this method. Therefore, a higher-resolution patterning method with a higher throughput of thinner fibers that is applicable to a wider variety of polymer precursors for C-MEMS and C-NEMS remains very desirable due to their advanced applications in electrochemical sensing, energy storage, and stem cell research [186].

1.2 Designing of Carbon Microstructure

Carbon possesses an extraordinary ability to form chemical bonds with numerous other elements and with itself. Owing to this unique ability, carbon continues to surprise the research community with new compounds and allotropes. Indeed, in the last few decades, we witnessed the discovery of fullerene, carbon nanotubes, and graphene. Interestingly, according

to SACADA - Samara Carbon Allotrope Database -there are more than 500 theoretically possible allotropes reported to their ever-growing list so far. Its allotropes show a wide range of mechanical, chemical, optical and electrical capability, depending on how the atoms are connected between each other. The contrasting properties of two of the most known carbon allotropes, graphite and diamond, exemplify the diversity that they have. While graphite is conductive, soft and opaque, diamond is non-conductive, hard and transparent. These kinds of dichotomy between different allotropes are not unusual for carbon. Therefore, making use of this ability of carbon to display multitude of properties by rationally tailoring its microstructure is of high importance.

The fabrication methods mentioned that involves pyrolysis (mentioned earlier) generally produces glassy carbon. In this process thermal decomposition of the polymer leads to the removal of most of the secondary atoms from the polymer, leaving a carbon structure behind. Although pyrolysis has been used to produce carbon having different morphological characteristics for decades, the underlying microstructure is yet to be completely understood. One of the initial studies was conducted using X-ray Diffraction methods by Rosalind Franklin in 1950s. In her original description of the pyrolytic carbon, she attributed the properties of the material to the porous structures that caused by the sp^3 bonds. Later in a study by Peter Harry, this idea of the non-graphitizable carbon was reshaped and the so-called porosity was identified as the fullerenic structures with sp^2 hybridization. This explanation was also consistent with the fact that sp^3 bonds are thermodynamically less stable at elevated temperatures. In fact, diamonds, an allotrope having sp^3 hybridized carbon atoms, decompose into graphite at temperatures above 1700°C. Unlike this, fullerenes are stable at such high temperatures. Although there are carbon rich polymers that can be converted into carbons that are predominantly graphitic, such polymers fail to retain the original patterns that the precursor polymer possesses. One of the reasoning given by early scientists for this incapability to retain shape is the fusion state that these graphitizable precursors are undergoing. They argue that the polymer melts when heated and the carbon atoms realign themselves

to form thermodynamically stable graphitic microstructures. This is very significant since such a process can prevent us from making patterned graphitic carbon structures using the aforementioned fabrication methods. Therefore, it is important to look into different possible routes to make patterned graphitic and/or elecrocatalytic carbon.

One way to introduce the required electrochemical properties is through mechanical activation such as polishing and fracturing. Since one of our objectives is to retain the shape, this route to improve the electrochemical performance is less feasible since these processes destroy the shape. Another pathway to enhance electrocatalytic behavior is by introducing heteroatoms in the carbon molecular matrix. Inclusion of such heteroatoms can bring the electrocatalytic behavior of glassy carbon close to its counterparts with electrochemically high performing . Such inclusions of heteroatoms can be achieved by selecting precursors containing the desired heteroatoms and retaining them during the pyrolysis process. Since pyrolysis of precursors at around 1000°C does not get rid of all the heteroatoms completely, this approach is easier to perform. It is also highly desirable to design and control the arrangement and proportion of these secondary atoms inside the carbon matrix. Along that aspect, methods to achieve different types of nitrogen inclusions inside carbon matrix is described later in this manuscript.

Properties of the carbon changes with various parameters involved in spinning process, stabilization and pyrolysis. The diameter of the wire is reported to be inversely proportional to the mechanical strength, degree of graphitization, and conductivity. Inclusion of secondary materials can also affect the properties. Secondary materials such as metal nanoparticles and carbon nanotubes have shown to augment the physical and chemical behavior of the carbon produced from pyrolysis. High temperature treatment during the stabilization step affects the final carbon product. The heat treatment enables molecular movements and rearrangements. For this reason mechanical and chemical constraints applied during this step can contribute towards the properties of the carbon wires. Finally, the pyrolysis set-

ting including the heating rate and the temperature itself affect its chemical and physical properties. For instance, at relatively lower temperature the process retains some of the heteroatoms from the polymer even after the pyrolysis process, whereas a high temperature increases the degree of graphitization and hence the conductivity. While the former is a highly sought after property by electrochemists, the low conductivity will prevent one from taking full advantage of these electrochemically promising product. Details of the characterization methods used in various studies conducted as a part of this thesis are explained in their corresponding sections.

Versatile and diverse properties of carbon can be fully exploited only if different shapes are achievable with it. Unlike its silicon counterpart, the fabrication techniques for carbon are still in its development stage. However, it is rapidly evolving with an aspiration to achieve industrial maturity. Primary routes to fabricate patterned carbon are inherently two-dimensional. This thesis addresses the difficulty to make three-dimensional carbon structures. New fabrication methods including capillary origami, self-folding origami, and electromechanical spinning are used to achieve complex morphologies. Equally important is the microstructure of the synthesized carbon. While randomness and entanglement in the precursor polymers leads to the formation of curved arrangement of carbon atoms (microstructure), producing glass-like carbon, aligned molecular chains in the precursor can lead to more organized carbon microstructure known as graphitic carbon. This method of designing/controlling the microstructure is explored in this study. Such designing capabilities could be of high interest in many areas as that would broaden the potential applications of this wonder material.

To address the requirement to make carbon structures of different shapes and microstructures, we develop 1) two new origami fabrication methods for carbon-MEMS, 2) a nearfield electrospinning-based carbon nanowire patterning method with enhanced morphology control, and 3) chemically and mechanically induced graphitization strategies for carbon-MEMS.

Chapter 2

Capillary Origami-based Carbon Microfabrication

2.1 Introduction

[1] Origami is a technique used to create three-dimensional forms from two-dimensional precursors by folding [138, 140, 143, 199]. If extended to the submillimeter scale, origami holds promise as a novel fabrication method to produce small intricate three-dimensional shapes with unique properties [176]. To generate folding in origami at the submillimeter scale, forces that scale favorably at such length domains must be considered. As length-scales become smaller, different physical forces become more or less dominant depending on their nature. Surface tension effects become much more dominant at small length-scales. For this reason, surface tension finds applications in areas such as in micro and nano fabrication and assembly. Investigations on the interactions between liquid and solid substrates reveal that

[1] Portions of this section are reprinted or adapted from [George, Derosh, Edwin A. Peraza Hernandez, Roger C. Lo, and Marc Madou. Fabrication of polymer and carbon polyhedra through controlled cross-linking and capillary deformations. Soft matter 15, no. 45 (2019), 9171-9177 https://doi.org/10.1039/C9SM01410A]

surface tension can induce deformation of soft films through a fluid-structure interaction known as elastocapillarity [99, 169, 196]. Previous works on elastocapillary-based origami [171, 169] succeeded in producing three-dimensional structures that return to their flat form when the liquid that folded them is removed [62]. While capillary origami and other reversible folding techniques such as those based on swelling [83], thermal expansion [103, 123] or shape memory [134] may lead to a wide variety of applications [42, 61, 148, 164], a folding method that allows manufacturing of permanently folded origami shapes in a batch mode would make for a powerful new fabrication method for submillimeter structures. Current elastocapillary-based submillimeter origami fabrication methods have limitations such as:

- Lack of a fabrication process for folds and faces that possess different properties such as stiffness. These differential properties are desired in origami, where theoretically the folds are expected to be flexible and the faces are required to be stiff,
- Lack of a precise batch and scalable patterning method for the initially unfolded sheets,
- Difficulty to fabricate folded structures anchored to a supporting structure,
- Inability to achieve a permanent folding deformation, and
- Inability to extend the fabrication methods to materials beyond polymers.

In this work, we develop an origami-based fabrication method for three-dimensional of millimeter and submillimeter structures through lithography, softening and hardening controlled via heat treatment, and elastocapillarity. The present study offers the following contributions:

- Localized control over the material properties of the faces and folds,
- A batch fabrication route by using photolithography,

- A fabrication method for three-dimensional shapes that can be anchored to a supporting structure,
- Permanent folding of the precursor polymer sheets by thermally controlling the degree of cross-linking and adjusting the volume of the driving liquid droplet, and
- A strategy for fabricating three-dimensional carbon shapes using pyrolysis.

2.2 Methodology

SU8, a commonly used photopolymer, is used as the base material to fabricate three-dimensional polyhedra. Using a multi-step UV exposure photolithography process, a batch fabrication of sheets with a desired fold pattern and localized compliance at the folds and faces is obtained as illustrated in Fig. 2.1 (a) (details of the experimental methods are given in the following paragraphs). Briefly, when the sheets are exposed to UV light, photoacid is generated in the SU8 matrix proportionally to the energy density of the irradiation. The post-exposure bake (PEB) causes cross-linking of the polymer at a rate proportional to the concentration of the photoacid generated in the sheet. By using lithographic photomasks with different uncovered regions, the first UV exposure is applied simultaneously to the fold and face regions while the second UV exposure is applied only at the face regions. These two steps allow us to produce less cross-linked compliant folds (where deformation is to be maximized) and more cross-linked stiff faces (where deformation is to be minimized). These characteristics are required to have better agreement with theoretical models of origami. If the two exposure energy densities are less than what is required for complete cross-linking, the patterned sheets can be released from the supporting structure.

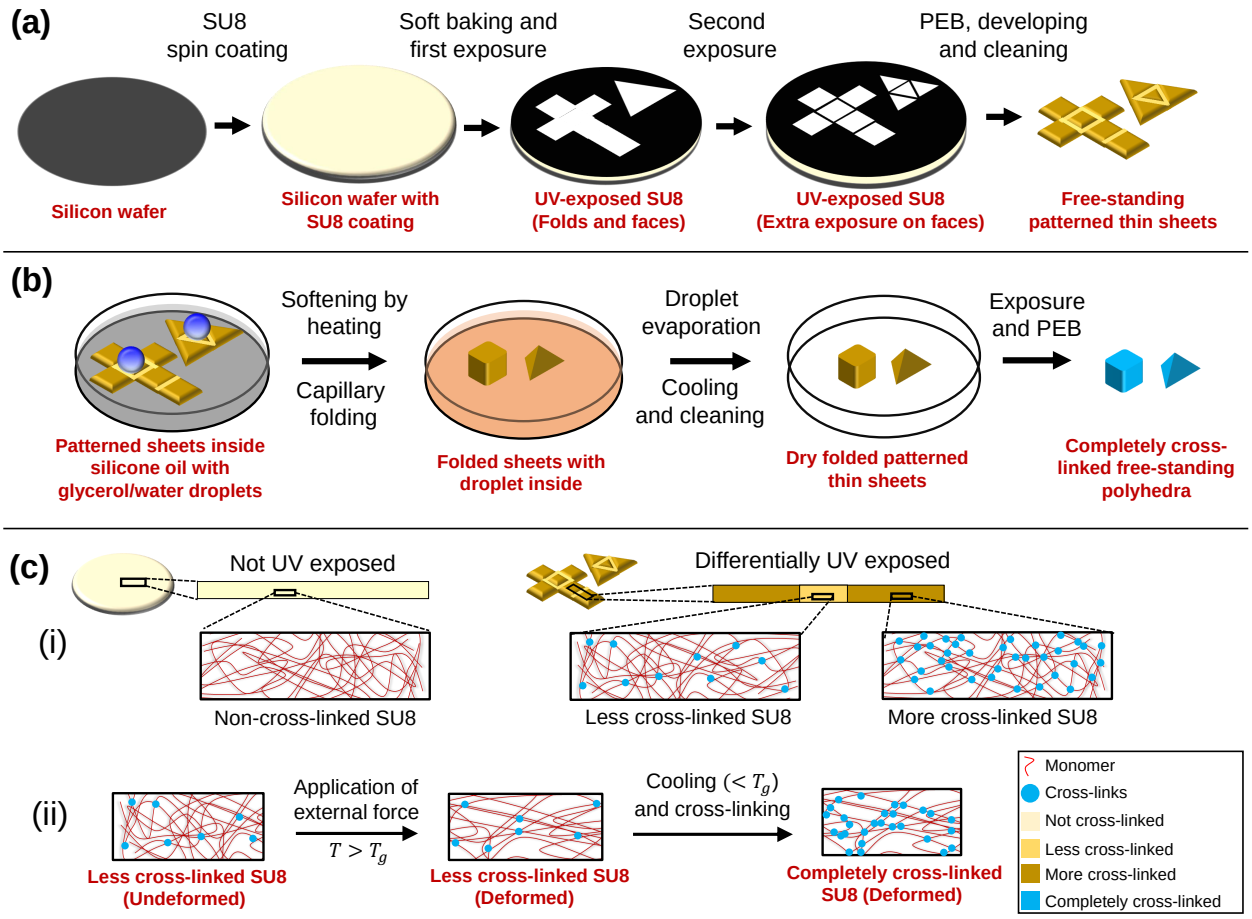

Figure 2.1: (a) Photolithography-based patterning of planar thin sheets used to fabricate free-standing polyhedra. (b) Capillary folding and thermally-controlled softening/hardening. The sheets are placed inside a silicone oil bath, and actuating droplets are deposited on top of them. The bath is heated to generate thermally-induced softening at the folds and allow folding. The bath is then cooled to acquire permanently folded shapes. (c) Schematic of the process at a microstructural level. (i) The degree of cross-linking in the SU8 polymer matrix is directly proportional to the exposure energy. (ii) The less cross-linked regions (the folds) are subjected to significant deformation when external forces are applied, due to the higher mobility of the partially cross-linked monomers. Deformation is made permanent by cooling and subsequently cross-linking the shape completely.

2.2.1 Preparation of Patterned Sheets

The patterned free-standing flat sheets used in the origami-based fabrication method are obtained using photolithography. First, SU8-2050 (MicroChem) is spin-coated on a silicon wafer at 1500 RPM and subsequently soft baked for 10 minutes. This soft baking duration is less than the recommended 20 minutes, ensuring a poor adhesion between the SU8 film and the wafer and thus facilitating the later release of the finalized patterned sheets from the wafer. After soft bake, a lithographic photomask that exposes the entire origami sheets, including folds and faces, is used to irradiate such regions for 40 seconds using a 2 mW/cm^2 UV light source. Multiple origami sheets can be created simultaneously in this step. Following the first exposure, a mask that exposes only the face regions, but not the folds, is aligned on top of the first mask to exclusively irradiate the faces for another 40 seconds using the same 2 mW/cm^2 UV light source. This gives a total exposure time of 80 seconds for the faces and 40 seconds for the folds. The difference in total exposure time is required to obtain dissimilar levels of cross-linking between the folds and faces, ensuring a folding response in good agreement with theoretical assumptions. Such assumptions require the folds to be highly flexible (less cross-linked) and the faces to be stiff (more cross-linked). The maximum exposure duration (80 seconds) is also less than the recommended period (120 seconds) for the photolithography process to prevent complete crosslinking during the Post-Exposure Baking (PEB) and therefore prevents adhesion of the sheets to the wafer. The period of the PEB is also reduced from 10 minutes (recommended period) to 5 minutes for the same reason. The patterned sheets are released from the silicon substrate after the PEB by developing using acetone or SU8 developer. The released patterned sheets are allowed to sediment in the developing liquid (acetone or SU8 developer) and are later separated from the developer by carefully draining the developer and cleaning them with isopropyl alcohol (IPA). The patterned flat sheets are recovered from the IPA mixture by drying them on a parchment paper.

Extensions of the Fabrication Method

- **Fabrication of polyhedra anchored to a substrate.** A third exposure step can be applied to create bonding between selected faces of the sheets and the silicon substrate. A mask exposing an area inside a single face of each sheet is used to irradiate these regions for additional 40 seconds using a 2 mW/cm^2 UV light source. These regions, exposed to UV light for a total of 120 seconds, are bonded to the substrate while the remainder of the sheets is not. All other fabrication steps remain the same.

- **Fabrication of polyhedra with arbitrarily shaped hole cut-outs in the faces.** Masks covering arbitrary shapes inside faces of the origami sheets are used in the two exposure steps. This leads the blocked regions to receive no UV irradiation and therefore be completely removed from the sheets during development, resulting in the arbitrary holes being created at the selected faces of the sheets.

2.2.2 Folding of Polymer Polyhedra Using Capillary Forces

The resulting free-standing patterned SU8 sheets are placed inside a silicone oil bath. Afterwards, a glycerol or water droplet is placed on top of each of the sheets. Once the droplets are placed above each patterned sheet, the oil bath is heated up to 110°C (which is above the glass transition temperature of the sheets), causing the sheets to become more compliant and be consequently folded driven by capillary forces induced by the droplets. In that way, the target polyhedral shapes are formed. The initial volume of the deposited droplets is at least 1.5 times larger than the volume of the target polyhedral shape to ensure that the droplets enter in contact with all the faces of the sheet during capillary folding. As the sheets undergo capillary folding, the droplets are gradually evaporated until their volume is reduced to approximately that of the target shape. This permitted the formation of fully closed polyhedral structures. The obtained polyhedral structures are filtered out after cool-

ing the bath down to room temperature and returning the polymer sheets to their glassy state (and thereby regain their stiffness). At room temperature, the sheets in their glassy state are permanently locked in their folded polyhedral shape.

2.2.3 Fabrication of Carbon Polyhedra

If it is desired to convert the polyhedral structures into carbon, the polymer sheets locked in their folded shape are washed with IPA and then exposed to UV light for 200 seconds using a 2 mW/cm^2 light source. This additional exposure ensures that the obtained structures are completely cross-linked and will retain their folded shape during pyrolysis. A Lindberg Blue M furnace is used to pyrolyze the polymer sheets at 900°C for one hour to obtain the final carbon structures. The structures are placed on top of a candle soot coated silicon wafer to prevent them from bonding to the substrate during the pyrolysis.

Elastocapillary bending occurs if the characteristic planform length of the sheet L is in the order of, or larger than, the elastocapillary length L_{EC} (i.e., if $L \leq L_{EC} = (Et^3/24(1-\mu^2)\gamma)^{\frac{1}{2}}$, where E, μ, and t are the Young's modulus, Poisson's ratio, and thickness of the sheet, respectively, and γ is the interfacial tension of the liquid droplet [16]). Using dimensions L= 1 mm and t = 50 μm (representative of the current study), ν= 0.5, and γ= 0.1 N/m, the previous inequality demands a Young's modulus $E \leq 14.4$ MPa. At room temperature, the differentially cross-linked SU8 sheets are at their glassy state with Young's modulus in the order of ∼2 GPa, significantly above the upper limit requirement. Thus, unstiffening of the patterned sheets is required to allow for their capillary folding into three-dimensional shapes (Figs. 2.1(b) and (c)). This unstiffening is induced by heating the sheets above their glass transition temperature Tg. By doing so, the patterned sheets reach their rubbery state and become more pliable (Fig. 2.1(d)). The faces with higher cross-linking remain stiffer than the less cross-linked folds [40]. This difference in compliance is attributed to the difference

in their molecular mobility due to the differential cross-linking achieved in the multi-step photolithography process. For the material used, softening at the folds is induced at temperatures as low as 110°C. DMA instrument limitations did not allow us to perform modulus measurements at temperatures above 90°C because of the high softening of the sheets at these temperatures. In view of this limitation, we performed curve-fitting of the obtained data from Fig. 2.2 to extrapolate the value of the storage modulus at 110°C. Details on the measurement limitations at temperatures above 90°C and on the extrapolation procedure are provided in Supplementary Document A. The extrapolated values of storage modulus at 110°C are 0.38 MPa, 0.74 MPa, 2.83 MPa, 2.87 MPa and 33.58 MPa for samples with 40 s, 60 s, 80 s, 100 s, and 180 s (completely crosslinked sample) UV exposure durations, respectively. Note that for all the samples, except the completely crosslinked one, the extrapolated modulus at 110°C is below the estimated threshold value of 14.4 MPa calculated before. The sheets regain their stiffness when they are brought back to their glassy state by cooling them to room temperature.

2.3 Results

2.3.1 Effect of Heat Treatment on the Folding Response

Folding of the thermally unstiffened sheets (with their temperature elevated to 100^oC) is triggered by placing a liquid droplet on top of them. To minimize the energy of the sheet-droplet system, i.e., the addition of the sheet strain energy and the droplet surface energy, the sheet is deformed towards a shape that aims to enclose the droplet. The obtained folded sheet accurately resembles the targeted three-dimensional origami polyhedron due to the differential compliance between folds and faces. Two additional observations were made on this process: i) In the absence of a droplet, heating the sheets does not induce discernable

folding, suggesting that cross-linking gradients across the sheet thickness caused during the photolithography process are negligible; and ii) Heating the patterned sheets for an hour or more (i.e., an extended PEB that induces a high level of cross-linking in the sheets) prior to placing a droplet on top of them results in negligible folding deformation (Supplementary Fig. A.3). The latter observation suggests that a high level of cross-linking in the sheets hinders the capillary deformation because of the resulting high stiffness.

2.3.2 Parametric Study of Folding Deformation

To select favorable exposure times for the two-step UV exposure photolithography process considering a specified sheet thickness (55 ± 3 μm here), a quantitative study on the influence of the exposure times on the resulting folded geometry was performed (Appendix Fig. A.4 and Table A.2.4 provide raw data of this study). Rectangular sheets with a single fold were analyzed. The geometry of the sheets and parameters of interest (fold angle (θ), curvatures of the faces (κ_F) and folds (κ_f)) are illustrated in Fig. 2.2 (b). Figure 2.2 (c) shows that the ratio of the curvature of the faces (κ_F) to the curvature of the fold (κ_f) decreases as the exposure time of the faces is increased with respect to that of the folds. A low value for this ratio allows for better agreement with theoretical models for origami (where faces are rigid, and folds are highly flexible).

The quality of the folding deformation of the sheets was also quantified by a folding parameter defined as $(\kappa_F/\kappa_f)(1 - \theta/\pi)$. A smaller folding parameter indicates more favorable folding deformation (with large fold angle and low face-to-fold curvature ratio). As shown in Fig. 2.2 (d), fold-face exposure times of 40-80 s and 40-100 s exhibited better folding quality as quantified by the folding parameter. Based on these results, it was opted to use exposure times of 40-80 s for all subsequent experiments. Such exposure times were selected because it was also observed that 40-100 s exposure times often led to sheet breakage at the folds

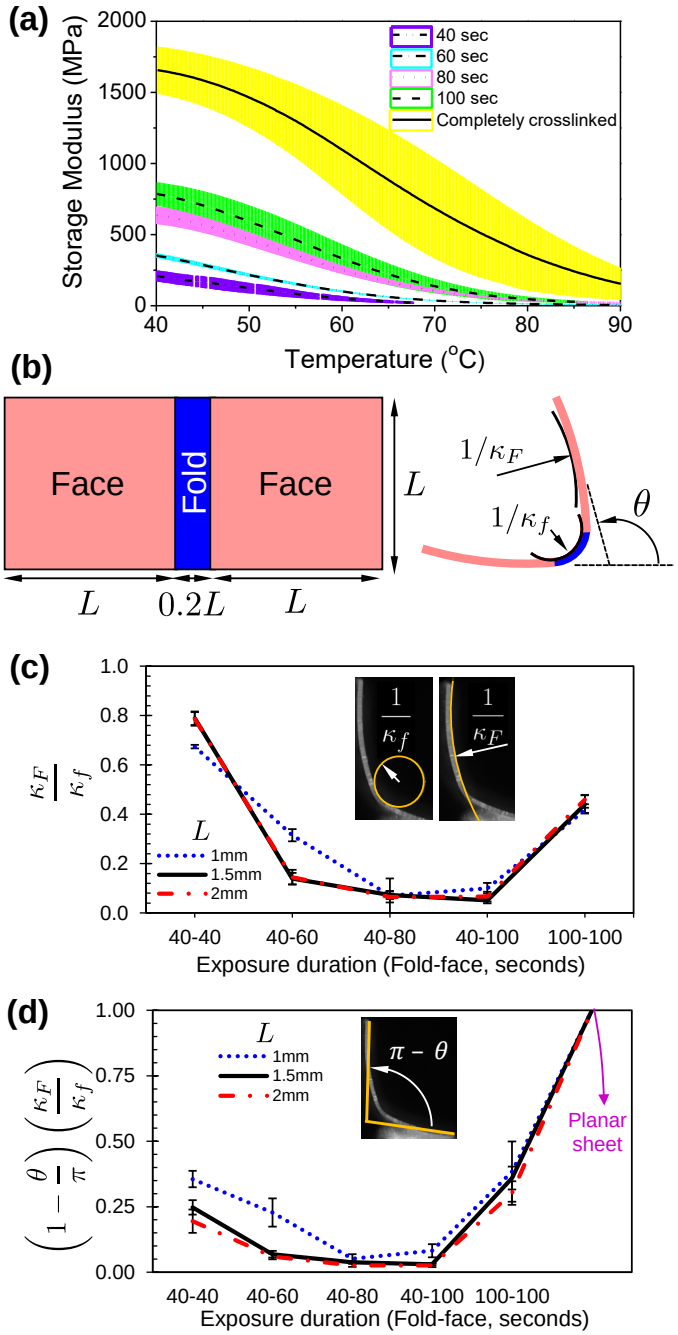

Figure 2.2: (a) Effect of temperature on the storage modulus of SU8 films made with different UV exposure duration. (b) Dimensions of the single-fold sheets and geometric parameters of the folded configurations. (c) Effect of exposure times on the ratio of curvature of faces κ_F to curvature of folds κ_f. A 2 mW/cm^2 UV light source is used in all cases. (d) Effect of exposure times on the folding parameter that combines fold angle and curvature ratio.

during the SU8 development step.

2.3.3 Effect of Droplet Volume on the Final Polyhedral Shape

The volume of the actuating droplet also affects the capillary folding deformation. To quantify this, we performed experiments on single-fold sheets and cube sheets using different droplet volumes. Figure 2.3 (a) shows fold angle vs. droplet volume for the single fold sheets. From the considered droplet volumes V_{drop}, $0.75L^3$ exhibited the largest folding angle. Droplet volumes below $0.75L^3$ produced smaller folding angles due to their lower surface energy and smaller contact area with the sheet. Droplet volumes above $0.75L^3$ also produced smaller folding angles. Although these larger droplets possess higher surface energy, the size of the droplets themselves constrain the folding deformation of the sheet.

The effect of droplet volume on the folding response is also studied by folding cube sheets (Fig. 2.3 (b)). The results show that droplet volumes larger than the target polyhedral volume do not allow the sheets to completely fold into their target closed polyhedron (Fig. 2.3 (b)). To overcome the aforementioned issues, a droplet with volume larger than the target polyhedral volume (1.5 times larger in the examples shown here) was initially deposited to ensure that the droplet comes in contact with all the faces of the sheet as it folds. Afterward, the surplus liquid is gradually removed by boiling the water droplet. This process allowed to produce fully closed origami polyhedra. The obtained polymer polyhedra showed good agreement with the anticipated polyhedral shapes with smooth folds from theoretical simulations [163] as shown in Fig. 2.4 (a). Furthermore, folded sheets with any intermediate fold angle configurations between the flat and the fully closed polyhedron configurations can be fabricated by stopping the heat application and cooling the sheet when it has reached the targeted intermediate shape.

A variation that allows for the formation of hole cut-outs at the faces of the sheets was

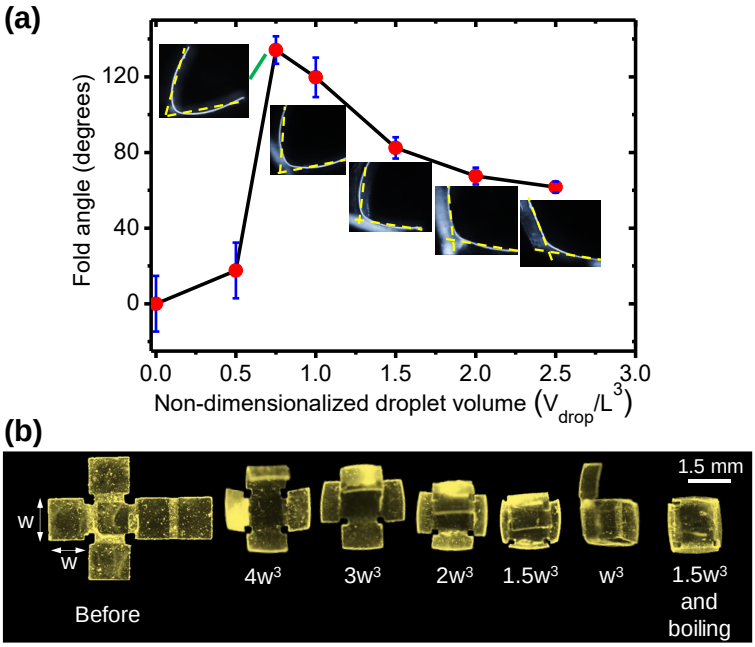

Figure 2.3: (a) Effect of droplet volume on the fold angle. Single-fold sheets with $L = 2$ mm are studied. (b) Effect of droplet volume on the closing of a cube.

also explored as shown in Fig. 2.5. Hole cut-outs on the faces are introduced by using lithographic photomasks that do not expose the cut-out regions to the UV irradiation at any step. When folded, the sheets having faces with hole cut-outs can form three-dimensional structures with patterned walls (Fig. 2.6). Additionally, the precursor sheets can be kept anchored to the supporting structure by introducing a third exposure to the anchor region (see Appendix Fig. A.5).

2.3.4 Carbon Origami

Structures formed by completely cross-linked SU8, a polymer with high carbon content, can be converted into corresponding isometrically shrunken carbon shapes through pyrolysis [215]. To demonstrate this, folded polyhedra are first subjected to flood exposure to complete the cross-linking at the folds and the faces. This complete cross-linking ensures that the

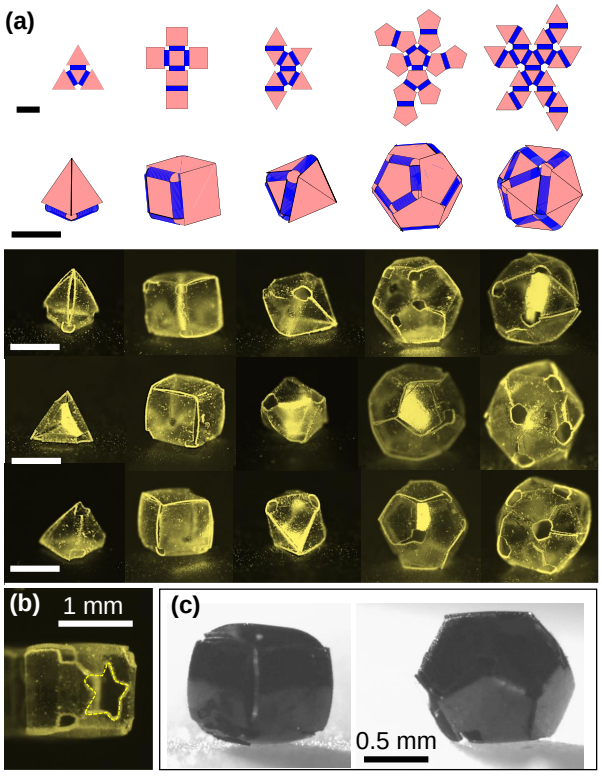

Figure 2.4: (a) Platonic polyhedra obtained using the present fabrication method. The scale bars for (a) and (b) are 1.5 mm. (b) Cube with a star-shaped hole on one of its faces. (c) Carbon origami cube and dodecahedron produced from corresponding polymer shapes.

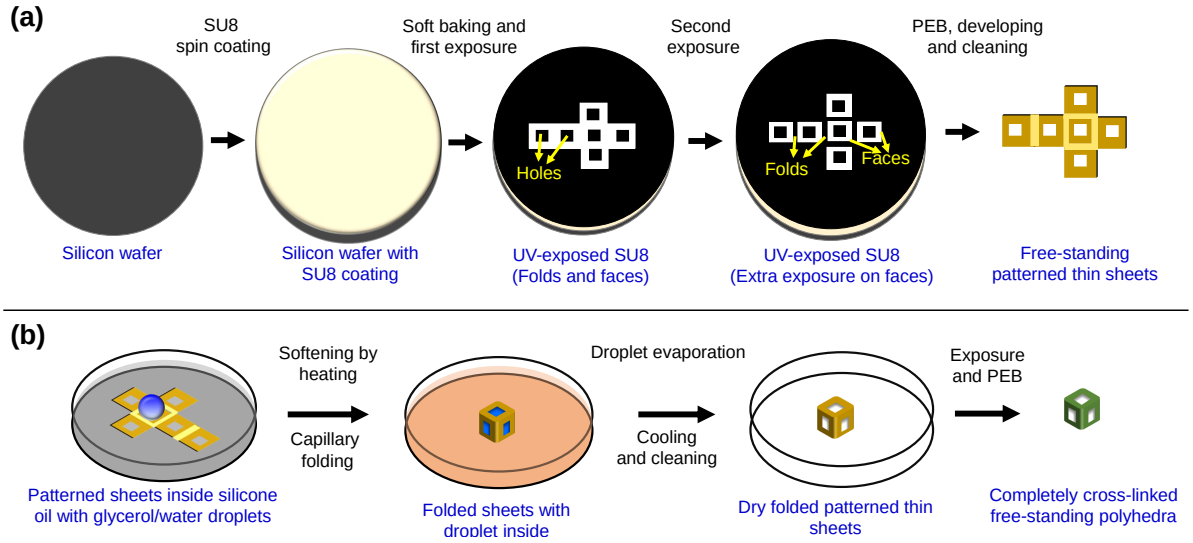

Figure 2.5: Schematic illustrating capillary folding of planar patterned films towards three-dimensional polyhedral shapes.

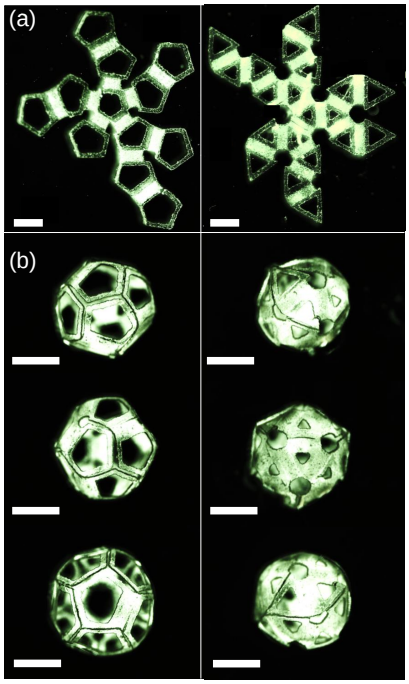

Figure 2.6: (a) Unfolded sheets films for dodecahedron and icosahedron with faces having patterned holes. (b) Folded dodecahedron and icosahedron from different views. All the scale bars are 1.5 mm long.

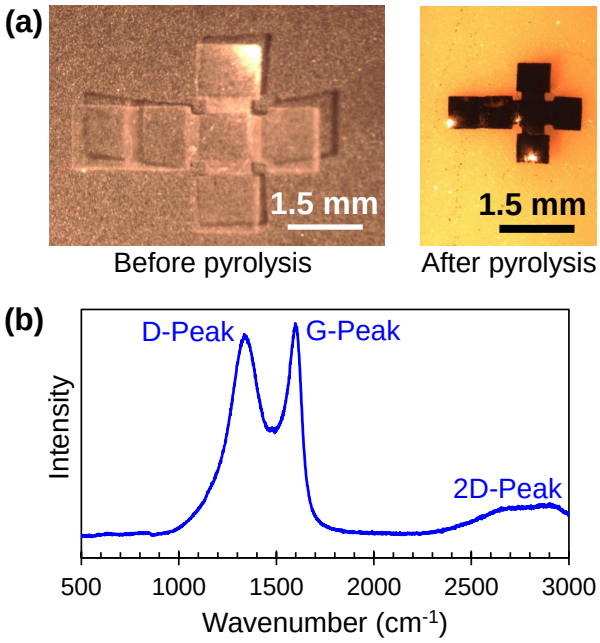

Figure 2.7: (a) Size comparisons of sheets before and after pyrolysis. (b) Raman spectroscopy of the carbonized SU8 origami polyhedra showing the D-peak, the G-peak and the 2D-peak.

folded shapes obtained using capillary origami retain their form during pyrolysis. Results of carbonized shapes obtained from corresponding polymer shapes are shown in Fig. 2.3 (d). The original polymer polyhedral shapes were preserved in the corresponding carbon shapes. Comparison of the sizes of the polymer shapes before and after pyrolysis show that the polymer origami structures were shrunk isometrically by about 57% of their original size when converted into carbon (Fig. 2.7 (a)). The microstructural characterization of the carbon polyhedra obtained from the polymer polyhedra was performed using Raman spectroscopy (Fig. 2.7 (b)). The ratio of the intensities of the D-peak (at 1350 cm^{-1}) to that of the G-peak (at 1550 cm^{-1}) obtained here is 1.03, and the ratio of the 2D-peak (2690 cm^{-1}) to the G-peak intensity is 0.12. These ratios indicate the formation of carbon structures that are glassy in nature. These carbon shapes can be metalized using techniques such as electroless deposition and electroplating to create origami structures formed by different materials [95]

Chapter 3

Programmable Self-folding for Carbon Microfabrication

3.1 Introduction

[1] To enable manufacturing at the small scales (millimeter and below), researchers have gathered inspiration from miniaturization approaches employed in distinct areas, for example, in the semiconductor industry [145, 131]. A promising miniaturization approach from this industry that has enabled small-scale manufacturing is photolithography [131, 167, 249]. One of the limitations of conventional photolithography, which is broadly used to manufacture two-dimensional architectures, is the difficulty to fabricate three-dimensional shapes. Due to this limitation, three-dimensional extensions of traditional photolithography such as

[1] Portions of this section are reprinted or adapted from [George, Derosh, Marc J. Madou, and Edwin A. Peraza Hernandez."Programmable self-foldable films for origami-based manufacturing." Smart Materials and Structures 30, no. 2 (2020): 025012 https://doi.org/10.1088/1361-665X/abd004] and [George, Derosh, Marc Madou, and Edwin A. Peraza Hernandez. "Characterization and Design of Programmable Self-Folding Polymer Films." In ASME 2020 Conference on Smart Materials, Adaptive Structures and Intelligent Systems. American Society of Mechanical Engineers Digital Collection, 2020 https://doi.org/10.1115/SMASIS2020-2286

multilayer lithography and two-photon lithography have gained interest [236, 235, 200, 139]. However, these techniques are complex for implementation in freeform manufacturing and time-consuming. Therefore, an alternative method based on photolithography that can address the shortcomings of existing platforms is of interest.

If the detailed two-dimensional architectures created from conventional photolithography could be folded in a controlled manner, then origami principles can be applied to extend photolithography to the manufacturing of three-dimensional shapes. Origami uses folding to transform two-dimensional sheets into three-dimensional structures, and is being explored in various other fields as the enabler of new manufacturing methods [92, 34, 106, 181]. These explorations are due to mathematical and computational advances in the design of origami structures which have expanded the spectrum of shapes that can be created using folding to intricate constructions such as freeform polyhedra, complex robotic frames, among others [33, 110, 153, 157, 37, 220, 160].

Folding deformations for potential origami-based manufacturing can be implemented at large length scales through the application of external forces [7], or by self-folding using smart materials such as shape memory alloys [203, 113], shape memory polymers (SMP) [87, 55], dielectric and magnetoactive elastomers [245, 2], among other material options [165]. Folding at smaller length scales brings significant complications since external forces may not be practically applied in a precise manner to obtain the desired folds. Embedding smart materials to the sheets is a viable folding approach at such length scales. While most smart material-based origami fabrication methods are confined to length scales larger than a millimeter, there are some exceptions. Ge *et al.* [55] and Yuan *et al.* [241] employed a 3D printing technique to include SMP wires embedded in origami films. Although the incorporation of SMP in 3D printing enables the origami-based fabrication processes, the size scaling is limited by the printer resolution [241]. In another smart material-based origami method, Felton *et al.* [39] used seven layers of three different materials to achieve folding in small

length scales. Different folds in these programmable self-folding composite origami sheets could be simultaneously folded through uniform heating. Alternatively, these sheets could be sequentially folded with the use of Joule heating. Sequential folding improves the versatility of the fabrication method by enabling the creation of a wider range of target shapes. Liu *et al.* [127] utilized the shape memory effect of pre-strained polymer films with ink-colored folds to achieve optically-controlled sequential folding of the films. This approach used a combination of the wavelength of the light used for exposure and the color of the ink that defined the individual folds to achieve sequential folding. The absorption of the light by the colored folds heated the films locally, leading to local self-folding through strain relief.

Folding can also be achieved at the millimeter and sub-millimeter length scales using other approaches [82]: By inducing buckling [91, 193], by applying a magnetic field on magnetically responsive sheets [225], by using surface tension [60, 155], or by heating sheets with non-uniform thermal expansion properties [241, 49, 68, 118, 242, 4]. Buckling-induced folding can be achieved in planar sheets by selectively bonding them to a stretched supporting substrate at localized regions. In that approach, compressive forces obtained from the shrinkage of the substrate are used to buckle the sheets and enable folding [92]. Therefore, free-standing structures cannot be formed using this approach. Free-standing folded shapes enabled by buckling can be obtained by incorporating active materials in the laminated films [87, 30]. In ref. [87], when SMP sheets are bonded in a bi-morph configuration to slender polymer films and the SMP is subsequently shrunk by heating, the thin polymer films are reported to be delaminated from the SMP and buckled, thereby forming free-standing, folded shapes. In magnetically-induced folding, a uniform magnetic field is applied on patterned planar sheets containing a distribution of oriented magnetic particles to form three-dimensional shapes. These sheets having oriented magnetic particles require highly specialized fabrication platforms, rather than simple conventional photolithography. Folding driven by surface tension can be implemented by depositing droplets on patterned sheets fabricated using simple photolithography processes [60]. However, droplet-assisted folding has size scaling challenges

and may only produce shapes topologically equivalent to spheres. Folding induced by applying heat to sheets with non-uniform thermal expansion properties across their thickness is generally obtained by using laminated sheets such as bi-morphs [12, 190, 195]. These bi-morphs demand multi-material and multilayer fabrication techniques. Tuning the thermal expansion properties of a single-layered sheet across its thickness is more compatible with low-cost, conventional photolithography than bi-morphs and is explored herein.

Various properties of photopolymers depend on their crosslinking density. This dependency can be exploited to achieve designed spatial distributions of material properties in photopolymer films. Jamal *et al.* [86] successfully achieved differential porosity density in photopolymer sheets by manipulating their crosslink density. They utilized the porosity distribution of the thin film to obtain folding by implementing the solvent transfer approach [86]. However, fold angle control and permanent folding were not trivial with this method. In a related study, Zhao *et al.* [248] used photopolymerization to create folded structures with characteristic length scales of 5 mm from planar sheets, albeit assisted by hand. An entirely hands-free folding technique is necessary to successfully enable manufacturing of freeform shapes and miniaturization to smaller scales.

This chapter presents a manufacturing method for three-dimensional shapes of millimeter and sub-millimeter characteristic lengths based on programmable self-folding behavior of thin films. Photolithography techniques are used to fabricate the films and engineer their self-folding response. The main steps of the end-to-end manufacturing method are illustrated in figure 3.1. The method begins with a three-dimensional target shape that is mathematically represented as a polyhedral mesh. The *unfolding polyhedra method* [163] is employed to flatten the polyhedral mesh into a planar form denoted as the *net* [180]. The net is comprised of *face* and *fold* regions. Photolithography is used to pattern a planar polymer film using the geometry of the determined net. Double-exposure photolithography is employed to create films with flexible folds of low crosslinking density and stiff faces of high

crosslinking density. This difference in stiffness between the folds and the faces allows for good agreement with computational design of origami structures that assumes flexible folds and rigid faces. The development process performed after UV exposure is carried out by immersing the films in developer solution. The fold regions experience higher absorption of developer solution due to their lower crosslinking density as compared to the faces. Within each fold, a higher concentration of developer is present on the side of the film that came in direct contact with the developer. When the films are heated, the absorbed developer is evaporated causing inhomogeneous strains across the thickness of the folds and generating self-folding. Programming of precise fold angles is achieved by adjusting the dimensions of the fold regions based on experimentally calibrated relations. The main contributions of this work that enable such an origami-based manufacturing method are summarized as follows:

- A photolithography process for the fabrication of polymer films with thermally induced self-folding behavior is devised by tuning the exposure energy distribution of the films and their development process
- A strategy to predict and program the folding behavior of the fabricated films is realized by proposing and experimentally calibrating a relation between the dimensions of the folds and the fold angle they achieve when heated
- An end-to-end freeform manufacturing method is developed by integrating the unfolding polyhedra method in the design of films programmed to self-fold towards a target shape when heated

3.2 Experimental and Computational Methods

This section presents the experimental and computational approaches employed in the development of the origami-based manufacturing method. Sections 3.2.1, 3.2.2, and 3.2.3 re-

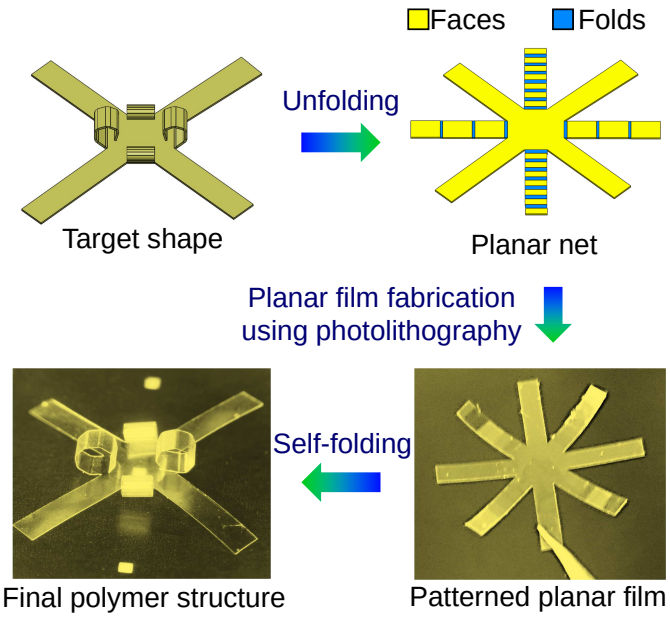

Figure 3.1: Schematic summarizing the origami-based manufacturing method developed in this work. A target shape is given and is first flattened into a planar net with distinct face and fold regions using the unfolding polyhedra method. The planar net becomes the geometrical basis for the fabrication of a patterned planar film using photolithography. The film is programmed during the photolithography process to *self-fold* towards the target shape via heating. The width of the petals of the flower shown in this example is 2 mm.

spectively describe the experimental procedures associated with the preparation, patterning, and self-folding of the photopolymer films used in the fabrication of the freeform polyhedral shapes. Section 3.3.1 presents the experimental approaches used to characterize and model the folding response of the fabricated films. Finally, Section 3.3.2 describes the integration of experimental calibration and modeling results with the unfolding polyhedra method to enable the design of films that are programmed to self-fold towards target polyhedral shapes.

3.2.1 Polymer Film Preparation

The polymer films studied in this work are composed of the negative tone photoresist SU8. This photoresist exhibits strong adhesion with silicon substrates, a desirable quality in traditional photolithography where the fabricated films are required to remain attached to their

substrate. However, here the patterned polymer films need to be removed from their substrate for subsequent folding towards their three-dimensional target shape and hence weak adhesion between the films and the substrate is required. For this reason, the silicon wafer (University wafers, USA) is coated with polydimethysiloxane (PDMS), a polymer that adheres weakly with SU8, prior to the deposition of SU8 as illustrated in Fig. 3.2.

The PDMS coating is made by first mixing ten parts of PDMS monomer (Dow corning, USA) with one part of crosslinking agent (Dow corning, USA). The mixing introduces bubbles in the solution. Accordingly, the mixture is degassed inside a vacuum oven at room temperature for 15 minutes to remove all the bubbles. This homogeneous mixture of the monomer and the curing agent is spin-coated on the silicon wafer at 500 RPM. The PDMS-coated silicon wafer is thermally cured by heating it on a hot plate at 80°C for 10 minutes. A uniform layer of SU8 2025 (KayakuAM Inc., USA) is formed on top of the PDMS-coated silicon wafer through spin coating. The thickness of both PDMS and SU8 films is characterized by using a Nikon Eclipse LV100 microscope fitted with a SPOT RT sCMOS camera. The thickness of the films at different locations is measured by comparing their images against a picture of a scale using ImageJ software. Due to the compliance of the PDMS film, a supporting structure is needed to record the image of the film along its thickness dimension. Accordingly, to characterize the thickness of the PDMS film, a secondary thick PDMS sheet is produced by curing the mixture inside a glass container. The PDMS film is transferred on to the thick PDMS sheet, and the bilayer is sliced into thin pieces. Then, images of the sliced pieces are taken using the microscope and analyzed. The PDMS film thickness is found to be 126±2.0 μm. Auxiliary supporting structures are not required to characterize the thickness of the SU8 films due to their higher stiffness. In this work, the SU8 is spin-coated at 2000 RPM, 2500 RPM, and 3000 RPM to obtain films with thicknesses of 33.9±1.0 μm, 37.7±1.0 μm, and 44.0±1.0 μm, respectively. The formed SU8 film is soft baked at 50°C for 1 hour to solidify it by removing the solvent. The SU8 film at this stage is non-crosslinked.

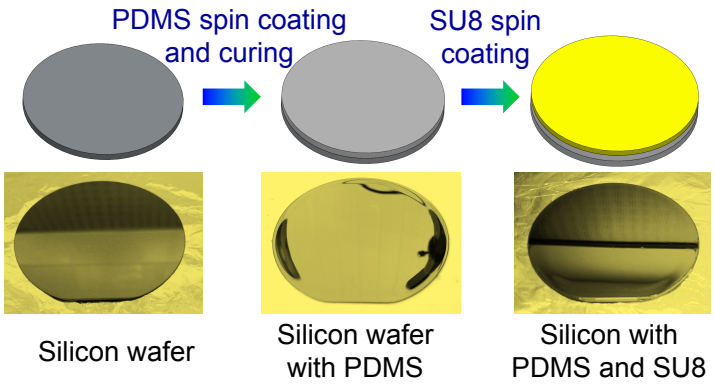

Figure 3.2: Preparation of the SU8 photopolymer film and its supporting substrates. A middle PDMS layer is placed between the silicon wafer and the SU8 film to enable facile separation of the SU8 film.

3.2.2 Film Patterning Using Double-exposure Photolithography

After production of the non-crosslinked, uniform SU8 films, they are patterned with the desired fold and face regions using double-exposure photolithography. The crosslinking density of the SU8 photopolymer increases upon UV exposure, and it is used to control the spatial distribution of material properties in the films. This is carried out by modulating the intensity of the UV light source and/or the local duration of exposure. In this work, a two-step UV exposure process involving two photolithographic masks is used to pattern the SU8 films. During the first exposure step, *both faces and folds* are irradiated for 40 seconds using a UV light source with an intensity of 2 mW/cm^2, as shown in Fig. 3.3 (a). This is achieved by using a mask that only allows UV light to pass on the face and fold regions. In the second exposure step, *only the face regions* are exposed to UV light with an intensity of 2 mW/cm^2 for 40 seconds. This is achieved by using a mask that only allows UV light to pass on the face regions. In total, the face regions are exposed to UV light of 2 mW/cm^2 intensity for 80 seconds, and the fold regions are exposed to UV light of 2 mW/cm^2 intensity for 40 seconds.

When the films are subjected to post-exposure baking (PEB), the face regions that were irradiated by UV light for the longer duration of 80 seconds crosslink more, whereas the

fold regions exposed only for 40 seconds crosslink relatively less. The PEB is performed by placing the film and substrate on a hot plate at 95°C for 12 minutes. The modulus of elasticity of SU8 is directly proportional to its crosslinking density[2]. Therefore, the face regions are stiffer than the fold regions. This difference in stiffness between the folds and the faces allows for good agreement with the assumption of flexible folds and rigid faces made in computational design of origami structures.

Next, the non-uniformly crosslinked film is treated with SU8 developer solution for two minutes. The SU8 developer removes non-crosslinked regions of the SU8 film. The fold regions that have lower crosslinking density than the faces absorb a higher amount of developer, while the face regions absorb negligible developer concentrations due to their higher crosslinking density. Within each fold region, the concentration of the developer is higher on the side that is in direct contact with the developer solution, creating a gradient of developer concentration across the thickness. Figure 3.3 (b) shows that the complete patterning process can be simultaneously performed on various samples, making the entire patterning process favorable for fast production of multiple samples.

3.2.3 Self-folding Driven by Heating

The patterned films that have folds with a gradient of developer concentration across their thickness are subjected to uniform heating to induce folding, as illustrated in figure 3.4. The patterned films are first carefully removed from the PDMS-coated silicon wafer using a razor blade one hour after the development step. The free-standing patterned films are uniformly heated by placing them inside an oil bath at 80°C. Heating softens the folds further [60] and evaporates the developer absorbed within them. The removal of the non-uniformly absorbed developer in the folds results in a gradient of strains across their thickness. This causes

[2]The reader is referred to ref. [60] for characterization data of the modulus of elasticity of SU8 as a function of UV exposure duration.

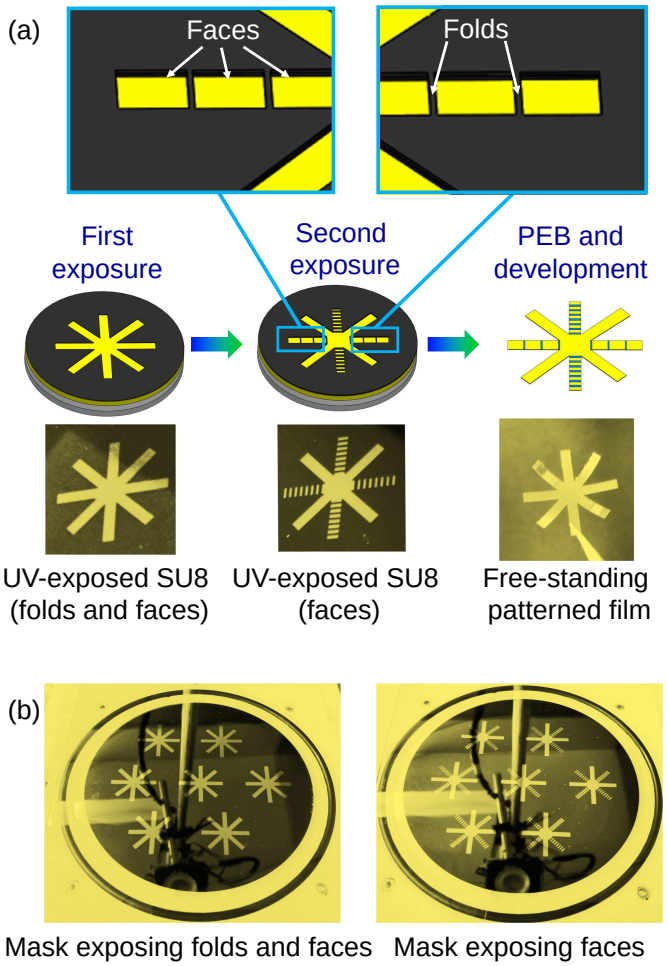

Figure 3.3: Schematics and photos of the film patterning process using double-exposure photolithography: (a) Exposure steps, PEB, and development processes shown for a single flower; (b) Photolithographic masks for simultaneous fabrication of multiple samples. The width of the petals of the flowers shown in this example is 2 mm.

localized bending at these regions and creates self-folding motion of the films. It is observed that the more exposed face regions exhibit negligible deformation during this motion, as depicted in Fig. 3.4(b). To verify this observation, a comparison of the dimensions of the faces of the folded sample against the face dimensions of the photolithographic mask is performed. This comparison confirmed that the faces do not undergo discernible deformation during the folding process. After the films are folded, the oil bath is cooled to room temperature to harden the folded films. These folded films are removed from the oil bath and washed with isopropyl alcohol. The folded films are then exposed to UV light for 200 seconds

and subsequently heated at 50°C for 12 hours to completely saturate their crosslinking density, both at face and fold regions. The post-folding UV exposure and PEB ensure that the folded films are less sensitive to temperature changes due to the saturation of their crosslinking density. It is noted, however, that the films can retain their folded shape at room temperature even without this post-folding UV exposure and PEB. Fig. 3.4 (c) shows two folded films that are not subjected to post-folding UV exposure and PEB, and it is observed that they retain their folded shape at room temperature and display no noticeable deformation even when an object of 50 mg is placed on top of them.

3.3 Results

3.3.1 Self-folding Analysis and Characterization

To achieve predictable folding deformation in the patterned films produced using the processes described in Sections 3.2.1-3.2.3, the behavior of their folds must be characterized and analyzed. The phenomenon that allows for thermally driven self-folding of the patterned films is illustrated in Fig. 3.5. The films patterned using the double-exposure photolithography process presented in Section 3.2.2 contain folds of lower crosslinking density and faces of higher crosslinking density. The more crosslinked face regions exhibit negligible absorption of the developer solution during the development process. In contrast, the less crosslinked fold regions undergo a high rate of developer absorption. The absorbed developer removes the non-crosslinked polymer chains from the polymer matrix within the folds, leaving voids filled with the developer [149]. Since the diffusion of developer occurs between the solution and only one side of the folds, a higher concentration of these voids filled with developer is expected to be present towards that side as illustrated in Fig. 3.5 (b). When the films are detached from the supporting structure, the developer inside the voids keeps the films

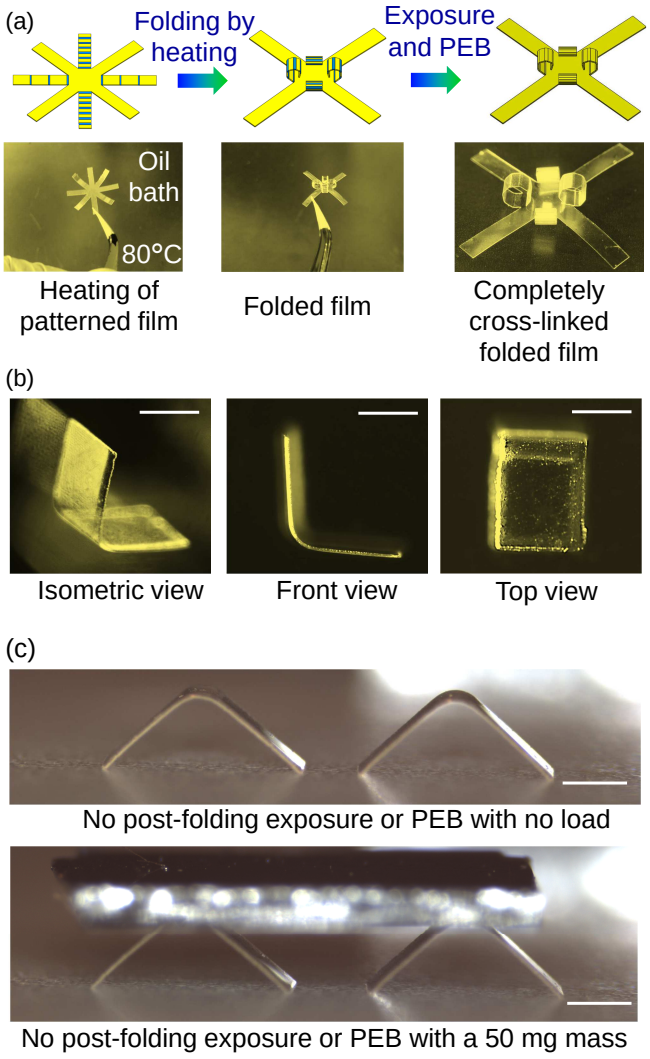

Figure 3.4: (a) Self-folding driven by heating demonstrated with a flower-like shape. The width of the flower petals is 2 mm. (b) Isometric, front, and top views of a film with a single central fold. (c) Folded films that have not undergone post-folding exposure and PEB showing no noticeable post-folding deformation with and without an applied load at room temperature. The scale bars are 1 mm long.

in their planar form as shown schematically in Fig. 3.5 (c). When the films are heated as described in Section 3.2.3, the developer is removed from the voids through evaporation. This causes the voids to collapse which leads to localized compressive strains [149]. The non-homogeneous concentration of developer at the folds leads to non-uniform compressive strains across their thickness, where the top side having higher developer concentration than the bottom side shrinks by a larger amount. This causes local bending (folding) at the fold

regions as illustrated in Fig. 3.5 (d).

A simple analytical model describing the deformation of the folds is derived to support the understanding of the folding response. The list of symbols used in the derivation of the model is provided in A.1. The physical domain of the analytical model consists of the single fold region shown in Fig. 3.6. The fold region has width w, length b, and thickness h. The coordinate along the thickness of the fold is denoted as $z \in [-\frac{h}{2}, \frac{h}{2}]$ where $z = \frac{h}{2}$ corresponds to the top side of the fold in contact with the developer solution and $z = -\frac{h}{2}$ corresponds to the bottom side attached to the supporting structure. The fold exhibits a fold angle θ when heated.

Considering the large ratio of the planform dimensions of the folds relative to their thickness, diffusion of the developer into the fold is modeled as one-dimensional and along the thickness direction. Accordingly, the diffusion equation governing the developer concentration field $c(z,t)$ is written as follows:

$$\frac{\partial c(z,t)}{\partial t} = D\frac{\partial^2 c(z,t)}{\partial z^2}, \tag{3.1}$$

where t and D are the time and the diffusion coefficient, respectively. The time dependence in equation (3.1) is removed by assuming that a steady state concentration field has been achieved when the films are removed from the substrate. This is justifiable because the considered film thicknesses are in the order of tens of microns and the films are removed from the substrate one hour after the development step. The steady state form of equation (3.1)

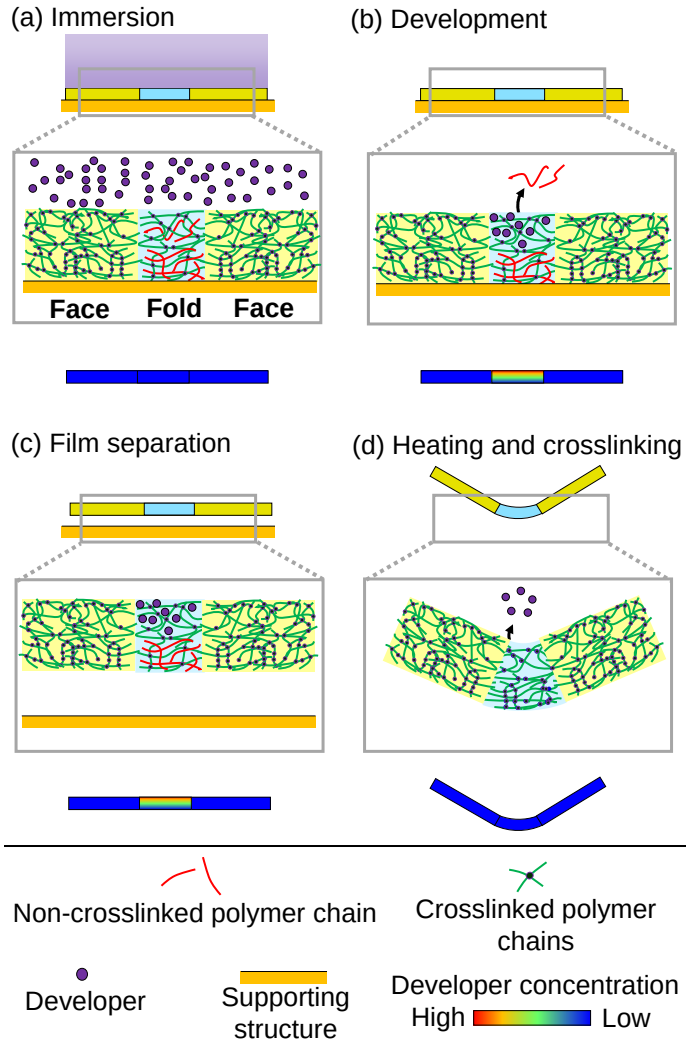

Figure 3.5: Schematic illustrating the phenomenon used to achieve self-folding of the photopolymer films. a) The SU8 film attached to the supporting structure (PDMS-coated silicon wafer) is immersed in SU8 developer solution after the double-exposure photolithography process described in Section 3.2.2. b) The developer is non-uniformly absorbed across the film, where the folds with lower crosslinking density absorb a larger amount than the faces with higher crosslinking density. The top side of the folds in direct contact with the developer solution exhibits a higher concentration than the bottom side attached to the PDMS layer. The developer removes some of the non-crosslinked polymer chains in the folds. c) The films are separated from the supporting structure. d) Self-folding is displayed by the film when the non-uniformly absorbed developer is evaporated through heating. Subsequent UV exposure and PEB completes the crosslinking process of the entire film and the folded configuration is made permanent.

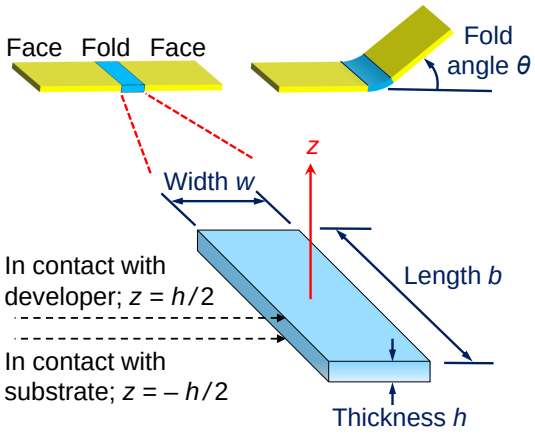

Figure 3.6: Geometry of the fold domain studied in the analytical model.

is written as:

$$D\frac{\partial^2 c(z)}{\partial z^2} = 0. \tag{3.2}$$

The mathematical form of the concentration field $c(z)$ is determined by solving equation (3.2) and is given as follows:

$$c(z) = C_{c0} + C_{c1}z, \tag{3.3}$$

where C_{c0} and C_{c1} are the constant and linear coefficients of the concentration field. As equation (3.3) indicates, the fold may exhibit a non-homogeneous concentration field of developer across the thickness direction z. When the absorbed developer is removed via heating as illustrated in Fig. 3.5 (d), shrinkage occurs across the fold thickness proportionally to the developer concentration. Accordingly, the inelastic (actuation) strain field exhibited by the folds during heating, denoted by $\varepsilon_a(z)$, is assumed to have the same form of the

concentration field from equation (3.3):

$$\varepsilon_a(z) = C_{\varepsilon 0} + C_{\varepsilon 1} z, \tag{3.4}$$

where $C_{\varepsilon 0}$ and $C_{\varepsilon 1}$ are the constant and linear coefficients of the actuation strain field. As indicated in Fig. 3.6, the side of the fold that is attached to the PDMS substrate during development is located at $z = -\frac{h}{2}$ and the side that is in direct contact with the developer is located at $z = \frac{h}{2}$. It is assumed that the absorption of developer at the side in contact with the PDMS substrate is negligible and thus a zero actuation strain condition is assumed at $z = -\frac{h}{2}$. Also, a maximum actuation strain magnitude denoted by ε_A is assumed at $z = \frac{h}{2}$. These two end conditions are written as follows:

$$\begin{aligned} \varepsilon_a\left(-\tfrac{h}{2}\right) &= 0, \\ \varepsilon_a\left(\tfrac{h}{2}\right) &= -\varepsilon_A. \end{aligned} \tag{3.5}$$

Here, ε_A is assumed positive and hence it appears a negative sign in equation (3.5). The coefficients $C_{\varepsilon 0}$ and $C_{\varepsilon 1}$ are determined by applying the end conditions in equation (3.5) to the actuation strain field in equation (3.4):

$$\begin{aligned} C_{\varepsilon 0} &= -\frac{\varepsilon_A}{2}, \\ C_{\varepsilon 1} &= -\frac{\varepsilon_A}{h}. \end{aligned} \tag{3.6}$$

Substituting the previous result into equation (3.4) provides the following actuation strain field:

$$\varepsilon_a(z) = -\varepsilon_A \left(\frac{1}{2} + \frac{z}{h} \right). \tag{3.7}$$

The total strain field in the folds corresponds to the addition of the elastic strain field $\varepsilon_e(z)$ and the actuation strain field $\varepsilon_a(z)$. Assuming Euler-Bernoulli beam theory and neglecting extension of the mid-surface of the fold, the total strain is given by $-z\kappa$, where κ is the curvature of the film. Accordingly, the equation relating the total strain and its elastic and actuation contributions is written as:

$$-z\kappa = \varepsilon_e(z) + \varepsilon_a(z), \tag{3.8}$$

and the elastic strain field $\varepsilon_e(z)$ is determined as follows:

$$\begin{aligned} \varepsilon_e(z) &= -z\kappa - \varepsilon_a(z) \\ &= -z\kappa + \varepsilon_A \left(\frac{1}{2} + \frac{z}{h} \right). \end{aligned} \tag{3.9}$$

Assuming a constant Young's modulus at the folds denoted by E, the stress field $\sigma(z)$ is the

product of E and the elastic strain field:

$$\begin{aligned} \sigma(z) &= E\varepsilon_e(z) \\ &= -zE\kappa + E\varepsilon_A\left(\frac{1}{2}+\frac{z}{h}\right). \end{aligned} \tag{3.10}$$

The external moment m applied to the fold is neglected because the forces exerted by the viscosity of the surrounding fluid and gravity are minimal due to the small size of the films. A detailed study to evaluate the assumption that the material has a constant Young's modulus is recommended as a future work since the polymer materials often shows viscoelastic behavior. Using this assumption and Euler-Bernoulli beam theory, the following equation of moment equilibrium is obtained:

$$-b\int_{\frac{-h}{2}}^{\frac{h}{2}} \sigma(z)\, z\, \mathrm{d}z \;=\; m \;=\; 0. \tag{3.11}$$

The following expressions are obtained by substituting $\sigma(z)$ from equation (3.10) into equation (3.11) and integrating over the thickness of the film:

$$\begin{aligned} 0 &= b\int_{\frac{-h}{2}}^{\frac{h}{2}} \left(-z^2E\kappa + E\varepsilon_A\left(\frac{z}{2}+\frac{z^2}{h}\right)\right)\mathrm{d}z \\ &= bE\left(-\frac{\kappa h^3}{12}+\frac{\varepsilon_A h^2}{12}\right). \end{aligned} \tag{3.12}$$

The previous equation is solved for curvature κ and the following is obtained:

$$\kappa = \frac{\varepsilon_A}{h}. \tag{3.13}$$

The radius of curvature R is the reciprocal of the curvature. Thus:

$$R \;=\; \frac{1}{\kappa} \;=\; \frac{h}{\varepsilon_A}. \tag{3.14}$$

The expression relating the fold angle θ with the dimensions of the fold and ε_A is obtained by using the relation between arc-length and radius of curvature as follows:

$$w = \theta R \quad \rightarrow \quad \theta = \frac{w}{R}, \tag{3.15}$$

and therefore using equation (3.14):

$$\theta = \varepsilon_A \frac{w}{h}. \tag{3.16}$$

The analytical derivation which arrives to equation (3.16) suggests a linear relation between θ and $\frac{w}{h}$, where the physical meaning of the slope in this relation corresponds to the maximum actuation strain attained during self-folding ε_A. For a fixed film thickness h and an assumed

fixed value of ε_A, the fold angle θ achieved by the folds is directly proportional to the fold width w, as illustrated by the schematics of Fig. 3.7 (a).

Experimental characterization of the relation between the fold angle attained by the folds and their size dimensions is performed by fabricating patterned films with a single fold such as those illustrated in figure 3.7(a). Films with different values of thickness h and width w are studied. Five samples for each combination of h and w are fabricated and tested. The fold angles are measured from side-view pictures of the films taken after folding. Values of thickness h of 33.9±1.0 μm, 37.7±1.0 μm, and 44.0±1.0 μm, and widths w ranging from 225 μm to 825 μm are considered. Figure 3.7(b) shows the results of fold angle θ vs. $\frac{w}{h}$ for all the combinations of fold width w and film thickness h. For a fixed proportionality constant c, the fold angle θ achieved by the folds is observed to be linearly related to the width of the folds non-dimensionalized by the film thickness (w/h) as follows:

$$\theta = c\frac{w}{h}. \tag{3.17}$$

Figure 3.7(b) shows a linear fit generated considering all the data points. The linear fit is constrained to pass to through the point ($\frac{w}{h} = 0, \theta = 0$). Good agreement is observed between the linear fit and the data points, and the linear fit has a R-squared value of 0.992. The linear fit has a slope of 6.68 deg/(mm/mm), which is equivalent to 0.117 rad/(mm/mm). This slope corresponds to the proportionality constant c in equation (3.17). The error bars represent one standard deviation considering the fold angles measured from the five samples for each data point. Figure 3.7(c) shows a contour plot of fold width w vs. film thickness h and fold angle θ generated using the slope of the linear fit from figure 3.7(b) and equation (3.17). Such information can be used to determine the width w required for a fold to achieve a target fold angle θ for a given film thickness h. By doing so for each fold in the film,

it would be "programmed" to self-fold in an accurate manner towards an intended shape. Similar relations between fold angle and fold dimensions have been used in the design of shape memory polymer-based [203, 54, 161, 3] and shape memory alloy-based self-folding structures [181, 158, 159]. Equation (3.17) along with the value of c from the experimental data are employed in the subsequent section to devise a design approach for the self-folding films based on computational origami.

Figure 3.7(d) shows side view micrographs used in the measurement of the fold angle. It is observed in these micrographs that the curvature of the folds is constrained to the plane of folding. This behavior is also observed in figure 3.4(b). The folds and faces are distinguished by blue and yellow shades. As can be qualitatively observed in this figure, the radius of curvature R of the folds is nearly identical across different samples with the same thickness and different fold widths. The curvature of the folds κ is determined from the micrographs of the folded films. To this end, the top and the bottom edges of the folds in the pictures are fitted with circles to find the top radius of curvature R_t and bottom radius of curvature R_b, respectively. The average of these two radii of curvature is assumed to be the effective radius of curvature of the fold R:

$$R = \frac{R_t + R_b}{2}, \tag{3.18}$$

and the curvature κ is the reciprocal of the radius of curvature R:

$$\kappa = \frac{1}{R}. \tag{3.19}$$

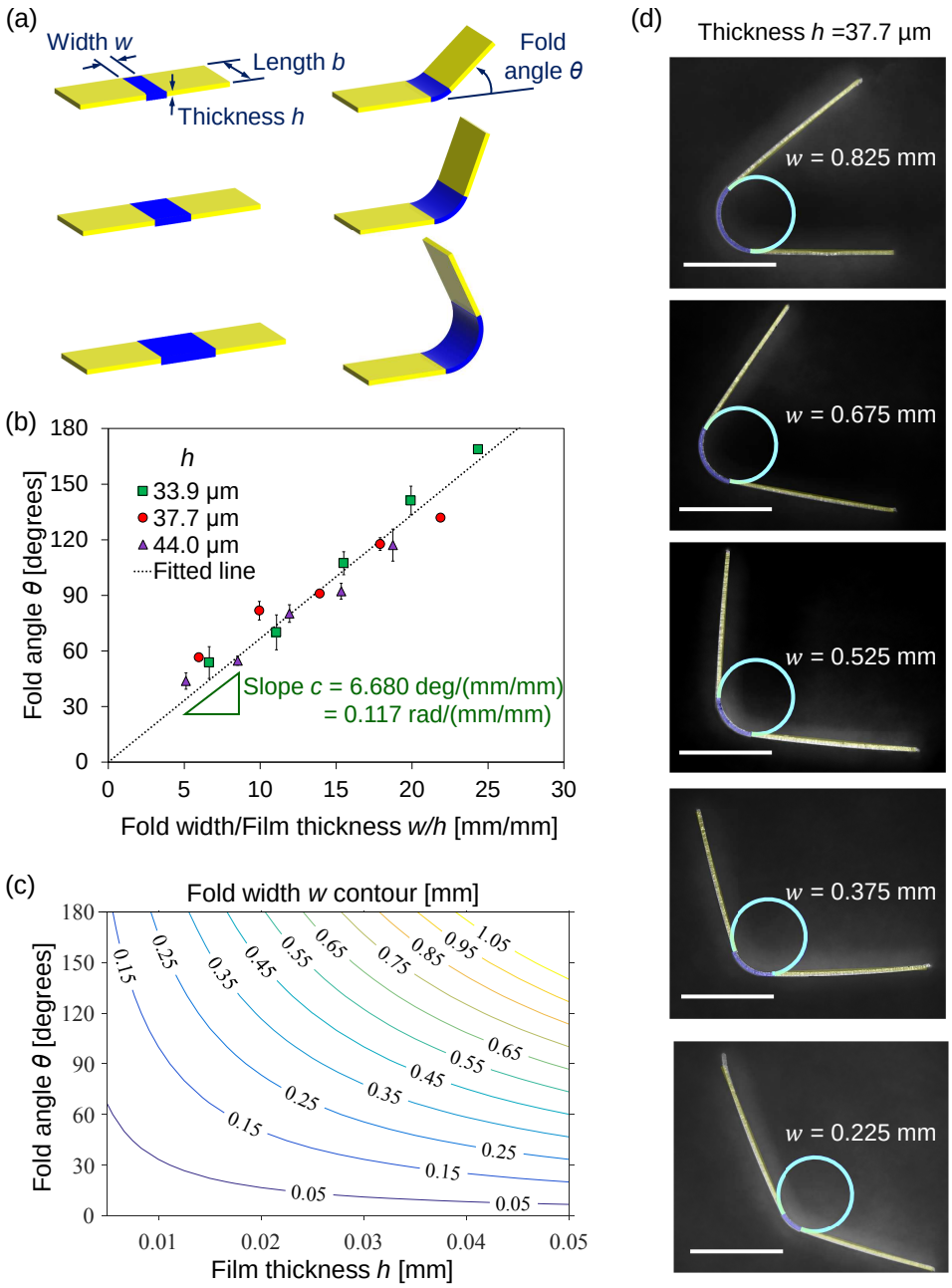

Figure 3.7: (a) Illustration of the influence of fold width w on the fold angle θ for films of equal thickness h. (b) Experimental data and linear fit of fold angle θ vs. fold width w non-dimensionalized by film thickness h. (c) Contour plot of fold width w vs. film thickness h and fold angle θ generated using the proportionality constant c of the linear fit from (b) and equation (3.17). (d) Photos of folded films having the same film thickness h and different fold widths w. The scale bars represent 1 mm.

The measured curvatures are plotted against the fold widths w of the samples in figure 3.8.

The plot shows that the curvature of the folds is relatively constant across samples with the

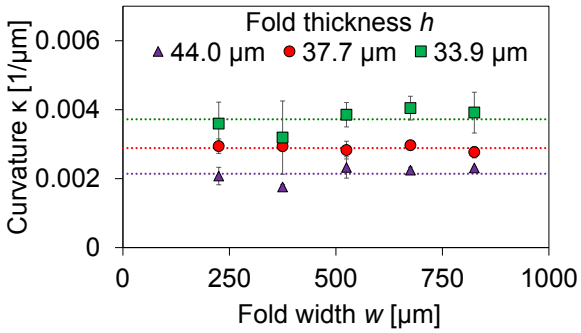

Figure 3.8: Fold curvature κ vs. fold width w for films of different fold widths and thicknesses. The horizontal lines represent the average curvature values for each thickness.

same thickness values.

Fold widths of the top side w_t and bottom side w_b of the folded fold regions are determined as shown in figure 3.9(a) to evaluate the extension or contraction behavior that leads to folding. During folding, w_t and w_b take different values than the originally designed fold width w. Using the measurements of w_t and w_b, the extension ratios at the top side λ_t and bottom side λ_b of the fold regions are calculated as follows:

$$\lambda_t = \frac{w_t - w}{w}, \tag{3.20}$$

and

$$\lambda_b = \frac{w_b - w}{w}. \tag{3.21}$$

The results of the determined top and bottom extension ratios provided in figure 3.9(b)-3.9(d) show that the top side of the fold regions that comes in direct contact with the developer solution has a lower extension ratio than the bottom side for all cases. The extension ratio values for both the top and bottom sides of the fold regions increase as the thickness of the

films h increases, and generally decrease as the width of the folds w increases.

According to the study by Jamal *et al.* [86], the UV exposure during the photolithography process can cause a gradient in the crosslinking density throughout the film thickness, with a relatively higher crosslinking density at the side directly exposed to the UV source. Although the influence of UV exposure time on the resulting crosslinking density distribution and the influence of this distribution on the self-folding behavior are not each separately studied in this work, experiments are performed herein to directly characterize the influence of exposure time on the self-folding behavior. Since the developer absorption is another major contributing factor to the self-folding behavior, the effect of development duration on the fold angles exhibited by the folds is also characterized.

For the characterization of the influence of UV exposure, folds with fixed width $w = 0.55$ mm and thickness of $h = 37.7$ μm are considered. A UV light source having an intensity of 2 mW/cm^2 is used. The exposure duration is varied between 40 seconds to 80 seconds so that the energy received by the fold region is ranging from 80 mJ/cm^2 to 160 mJ/cm^2. Exposure energies below this range result in breakage of the folds during the development step and are therefore not considered for the study. The results show that an exposure energy value of 80 mJ/cm^2 provides the highest fold angle θ among all the cases considered, as illustrated in figure 3.10(a). Higher values of exposure energy result in an abrupt decrease of the exhibited fold angle. This is because higher exposure energies create higher crosslinking density at the folds, which decreases the amount of solvent they absorb during development.

The characterization of the influence of the development duration on the exhibited fold angles is performed by testing development periods from two minutes to six minutes and the results are shown in figure 3.10(b). Folds with fixed width $w = 0.55$ mm and thickness of $h = 37.7$ μm are again considered. The folds developed for three minutes exhibit slightly larger fold angles compared to those developed for two minutes (the development duration used in all other experiments in this chapter). Treatment with the developer for longer than

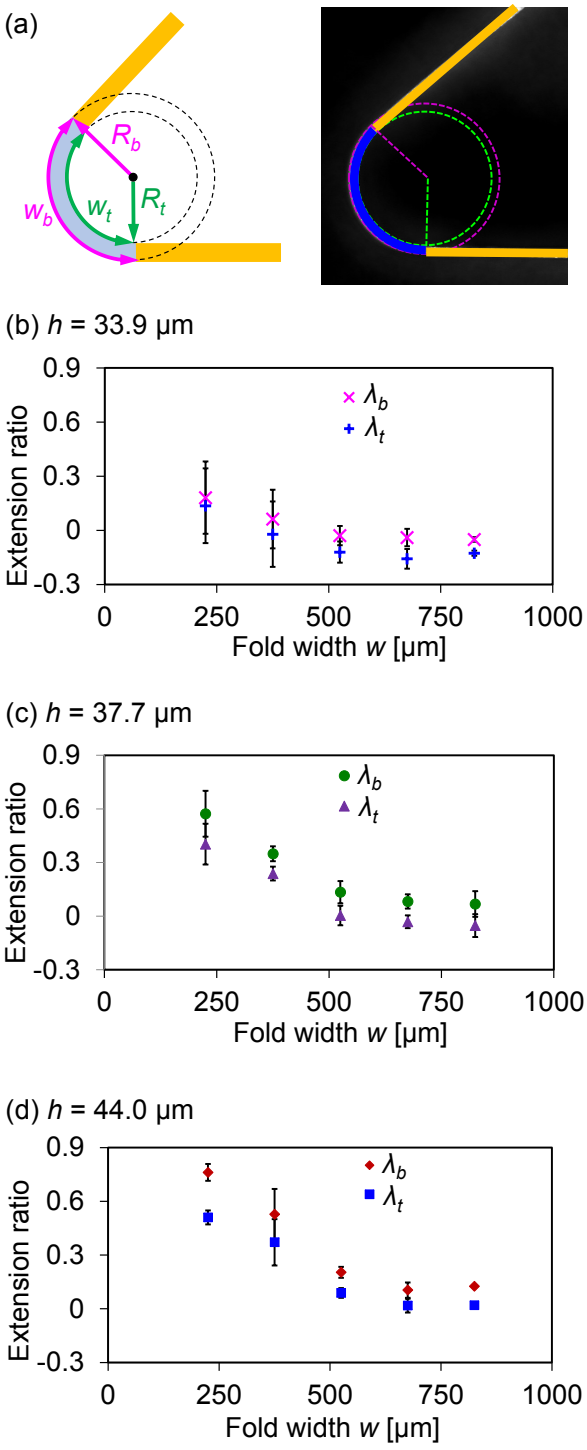

Figure 3.9: (a) Schematic and photo of a fold indicating the top radius of curvature R_t, bottom radius of curvature R_b, top fold width w_t, and bottom fold width w_b. (b)-(d) Extension ratio at the top and bottom of folds in films of different thickness h and fold widths w.

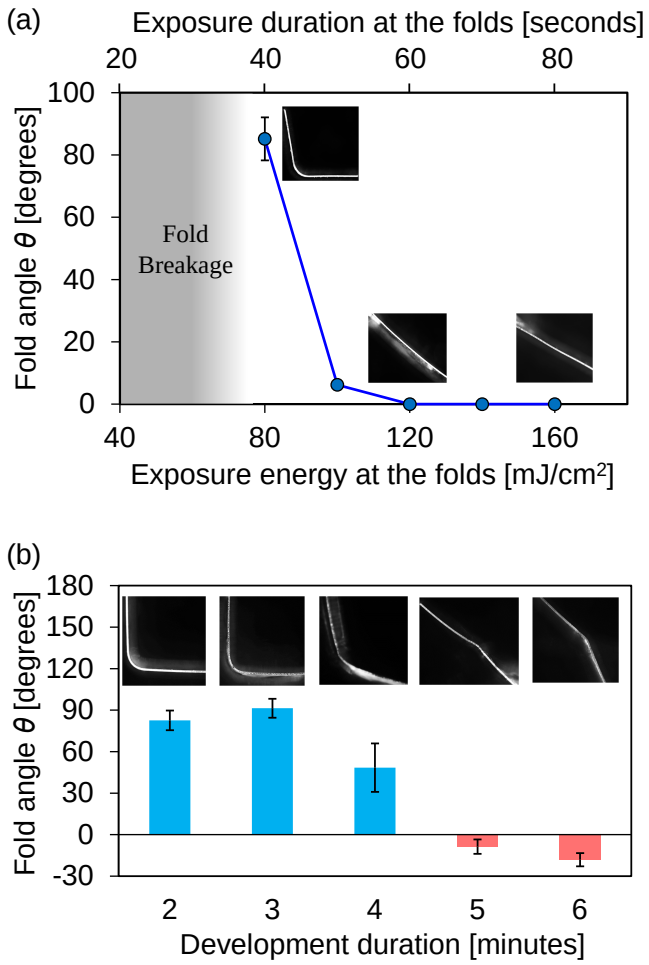

Figure 3.10: Experimental characterization of the exhibited fold angle θ in folds with equal width and thickness: (a) Effect of exposure energy received by the fold region; and (b) Effect of total development duration. Folds with fixed width $w = 0.55$ mm and thickness of $h = 37.7$ μm are considered.

three minutes causes the values of the exhibited fold angle to decrease and to eventually reach negative values, meaning folding in the opposite direction.

3.3.2 Origami Design

Computational origami is leveraged in this work to enable the design of films that are *programmed* to self-fold towards target shapes. To this end, the experimentally calibrated relation between the response fold angle and the fold dimensions in equation (3.17) is inte-

grated with the *unfolding polyhedra method* [180, 162, 221, 32]. A `Matlab`® implementation of the unfolding polyhedra method that considers smooth folds, such as those exhibited by the self-folding films as shown in figure 3.7, is employed in this work [163]. The progression stages of the unfolding polyhedra method are illustrated in figure 3.11. To implement the method, the target shape is provided as a three-dimensional polyhedral mesh denoted by $\mathcal{M} \subset \mathbb{R}^3$. The unfolding polyhedra method proceeds with the creation of a spanning tree [166], which is a branched path on $\mathcal{M}$ that passes through each face of $\mathcal{M}$ and does not contain loops. The spanning tree passes through each face of $\mathcal{M}$ only once. The edges of $\mathcal{M}$ that are not crossed by the spanning tree are assigned as cuts while those crossed by the spanning tree are assigned as the fold locations.

Since the folds exhibited by the films are smoothly bent regions rather than creases, the mesh is virtually *trimmed* at the fold locations to accommodate the fold regions [163]. The *trimmed mesh* is denoted as $\mathcal{M}_{\#} \subset \mathcal{M}$. The trimming process uses the values of the fold widths, which are calculated using equation (3.17) and the required value of the fold angle at each of the edges designated as folds. The planar configuration $\mathcal{S}_0$ of the *net*, which is the origami sheet that can be folded towards the target shape, is determined by flattening $\mathcal{M}_{\#}$ along the fold locations and placing the fold regions with their required width at these locations as shown in figure 3.11. Photolithographic masks for the double-exposure photolithography process described in Section 3.2.2 are designed based on the geometry of the planar net. These masks allow for the production of films with the layout of folds and faces required such that they self-fold towards the target shape when heated.

A given target mesh $\mathcal{M}$ can have multiple feasible nets. In general, a net can be defined by the set of cuts applied to $\mathcal{M}$ in order to flatten it into the net $\mathcal{S}_0$. Using such an approach, the net selected for experimental fabrication is determined in this work by solving the following

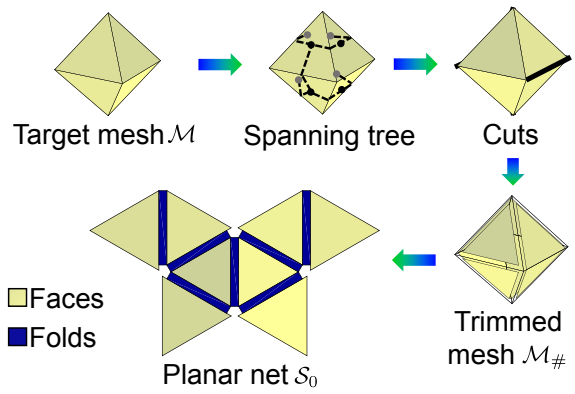

Figure 3.11: Schematic illustrating the `Matlab`® implementation of the unfolding polyhedra method used in this work. The width of the folds is sized using equation (3.17).

optimization problem:

$$\begin{aligned} \text{Find:} \quad & \mathbf{e} \\ \text{That minimize:} \quad & f \\ \text{Subject to:} \quad & e_i \in \{0,1\}, \\ & \mathcal{S}_0 \text{ is single connected shape} \\ & \mathcal{S}_0 \text{ does not contain overlapping faces or folds} \end{aligned} \tag{3.22}$$

where $\mathbf{e}$ is a vector containing the fold and cut assignments of each interior edge of $\mathcal{M}$ and f is the objective function. Each component of $\mathbf{e}$, denoted by e_i, can take a value of 0 (if interior edge i is a fold) or 1 (if interior edge i is a cut). The obtained net should be formed by a single piece that does not contain overlapping faces, as shown in Fig. 3.12. Constraints that enforce such characteristics are included in the optimization problem. The objective function f employed in this work corresponds to the sum of the distances between the centroids of each pair of faces in the net, denoted by d:

$$f = d. \tag{3.23}$$

If d is minimized (Example is shown in Fig. 3.12), it is expected that the determined net would be compact such that multiple nets can be sketched together in a single photolithographic mask and be simultaneously fabricated. Also, it is expected that minimizing d would reduce the errors arising from the variability in the exhibited fold angles (since long branches in the nets that often lead to shape inaccuracies would be avoided). The optimization problem in equation (3.22) is solved using the genetic algorithm solver `ga` built-in in `Matlab`. Implementation examples of this process are presented in the subsequent section.

Structures with target shapes of different geometries and potential functionalities are fabricated to demonstrate the manufacturing method outlined in the previous section. The fabrication of a cube, a truncated icosahedron, a platform, and a trimmed torus are considered. A film thickness of 37.7 μm is used in all the examples. One of the main potential applications of origami shapes at millimeter and sub-millimeter length scales is entrapment of particles or substances [43]. Figure 3.13 displays the fabrication stages of a closed shape, a cube, using the current fabrication method. Figure 3.13(a) shows the target polyhedral mesh $\mathcal{M}$, the edges that are cut for deployment of the mesh into a planar form, the trimmed mesh $\mathcal{M}_{\#}$ showing the regions of $\mathcal{M}$ that are removed to accommodate the folds, and the planar net $\mathcal{S}_0$. Figure 3.13(a) also shows the produced planar film with the geometry of the net. Figure 3.13(b) illustrates the self-folding deformation of the net from its planar configuration towards its folded configuration $\mathcal{S}_f$, and provides a photo of the self-folding film in its folded form. All the five folds in the net for the cube are folded to 90° to form the cube shape, which shows that the design approach presented in Section 3.3.2 is effective. There is good agreement between the experimental photo and the ideal folded configuration $\mathcal{S}_f$. In figure 3.14, the fabrication of a truncated icosahedron having similar potential functionalities is presented. The truncated icosahedron shape is clearly more complicated than the cube shape, requiring an accurate self-folding process. In comparison to the 6 squared faces in a cube, a truncated icosahedron has 12 regular pentagonal faces and 20 regular hexagonal faces. With the presented manufacturing method, fabrication of a truncated icosahedron and

a cube follow identical steps, irrespective of the differences in complexities in their ultimate shapes.

In addition to closed shapes, the presented manufacturing method can also be employed in the production of open shapes with various potential functionalities. Figure 3.15 shows

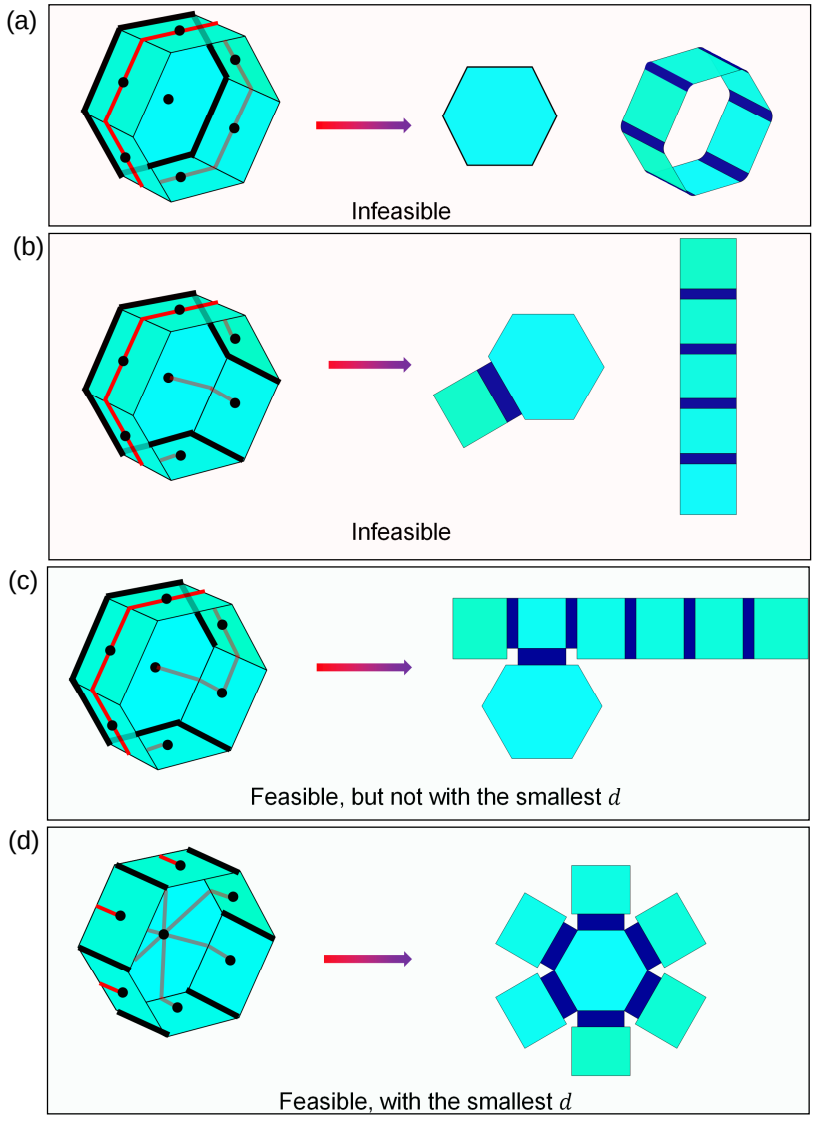

Figure 3.12: (a) An infeasible spanning tree that contains loops and multiple pieces. (b) An infeasible spanning tree that contains no loops, but multiple pieces. (c) A feasible spanning tree that forms an origami net. However, the net is not the one corresponds to the minimum d. (d) Origami net with the smallest d of the target prism shape.

different stages in the design and fabrication of a four-legged platform. Just as in the examples showing closed shapes, good agreement is observed between the ideal folded net $\mathcal{S}_f$ and the shapes observed in the photos of the samples for the four-legged platform.

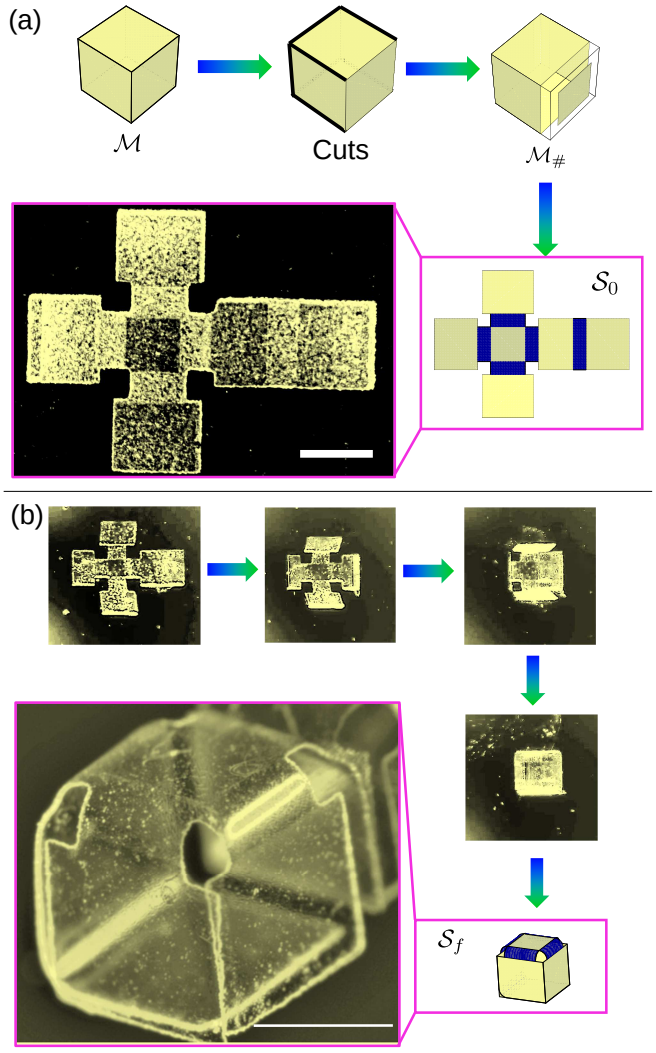

Figure 3.13: Cube fabricated using the presented origami-based manufacturing method. (a) Stages in the design of the planar film programmed to self-fold towards the cube when heated. The unfolding polyhedra method is used to determine the planar form of the net $\mathcal{S}_0$ starting from the polyhedral mesh $\mathcal{M}$, and double-exposure photolithography is used to pattern a photopolymer film with the geometry of the net. (b) Self-folding deformation of the net from its planar configuration towards its folded configuration $\mathcal{S}_f$. Notice the good agreement between the experimental photo and the ideal folded configuration $\mathcal{S}_f$. The scale bars represent 1.5 mm. A video showing the self-folding deformation process for this example is provided in the Supplemental Material.

The presented heat-assisted self-folding of programmable polymer films allows for controlled folding through the range of fold angles of $[0°, 180°]$ as shown in figure 3.7(b). This range of fold angles allows for the creation of convex shapes. Suggested future work includes the exploration of techniques that allow for the extension of this method to include folds in the range $[-180°, 0°)$. Nevertheless, there are exceptions of non-convex shapes which can be created using the method at its present state by appropriately making cuts on the edges of the target mesh $\mathcal{M}$ that would require a fold angle outside of the range $[0°, 180°]$. This is

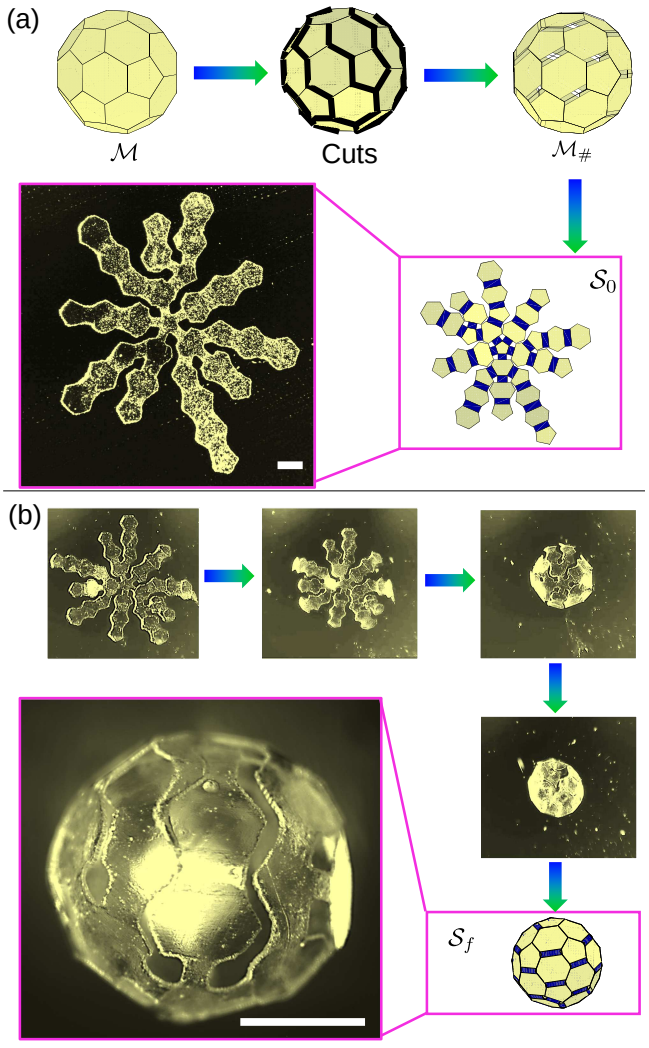

Figure 3.14: Truncated icosahedron fabricated using the presented origami-based manufacturing method. (a) Stages in the design of the planar film programmed to self-fold towards the truncated icosahedron when heated. (b) Self-folding deformation of the net from its planar configuration towards its folded configuration $\mathcal{S}_f$. The scale bars represent 1.5 mm.

demonstrated through the application of the present method to the trimmed torus shown in figure 3.16. Cuts made on the target mesh of the trimmed torus included all the edges that required fold angles outside of the range $[0°, 180°]$.

Scaling the present manufacturing method in terms of size requires further investigation to establish its feasible size domain. Preliminary computational evaluations of the scaling effects of the film thickness and target shape size are performed by extrapolating the experimental

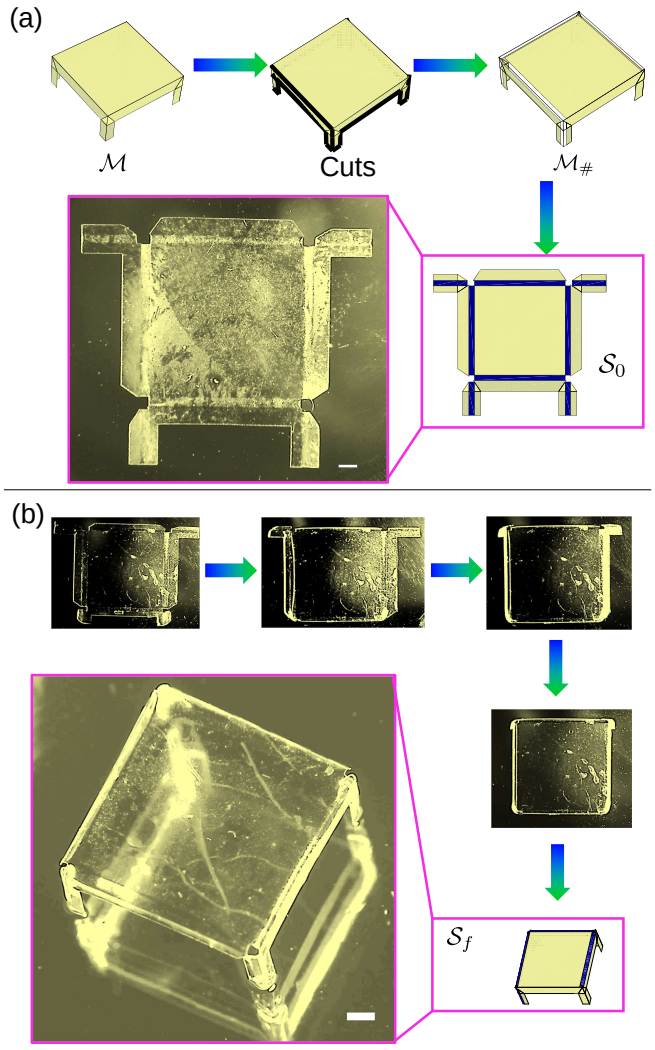

Figure 3.15: Four-legged platform fabricated using the presented origami-based manufacturing method. (a) Stages in the design of the planar film programmed to self-fold towards the four-legged platform when heated. (b) Self-folding deformation of the net from its planar configuration towards its folded configuration. The scale bars represent 1.5 mm.

data presented in Section 3.3.1 and the results from the fabrication examples of this section. Since the shapes obtained using the manufacturing method involve smooth folds, as opposed to conventional creased folds, the polymer shapes deviate from the original target shapes that contain shape edges. This deviation can be quantified using shape accuracy a defined as the ratio of the surface area of the trimmed mesh $\mathcal{M}_{\#}$ to the surface area of the original

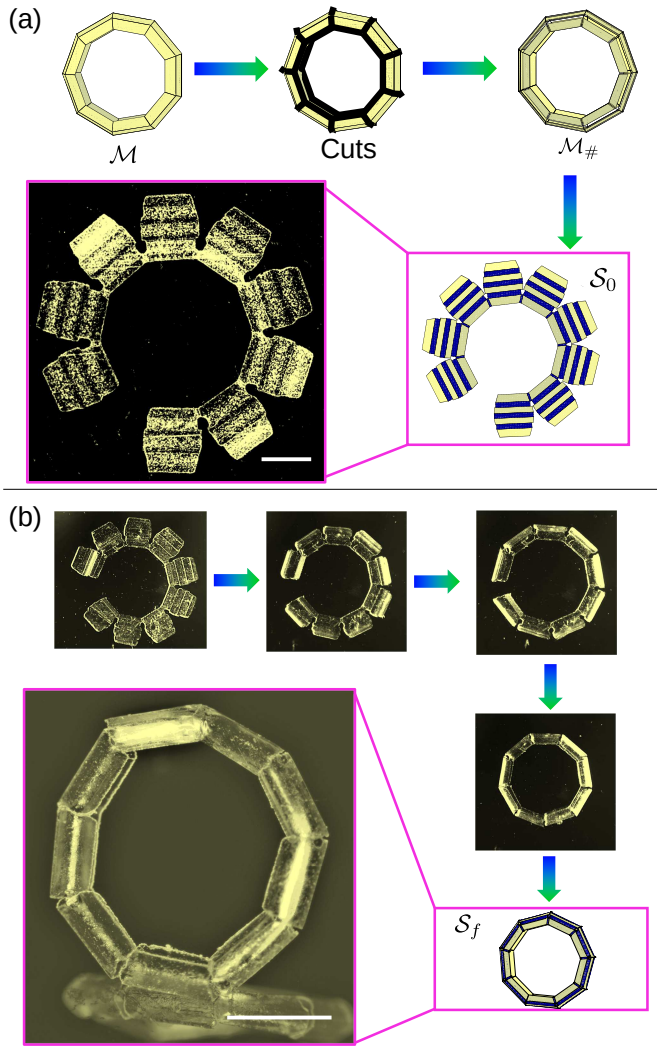

Figure 3.16: Trimmed (open) torus fabricated using the presented origami-based manufacturing method. (a) Stages in the design of the planar film programmed to self-fold towards the trimmed torus when heated. (b) Self-folding deformation of the net from its planar configuration towards its folded configuration. The scale bars represent 1.5 mm. A video showing the self-folding deformation process for this example is provided in the Supplemental Material.

target mesh $\mathcal{M}$:

$$a = \frac{\text{Area}(\mathcal{M}_{\#})}{\text{Area}(\mathcal{M})}. \tag{3.24}$$

For the scaling analysis, nets obtained by maximizing the accuracy of the target shape a are considered (*i.e.,* $f = -a$ in equation (3.22)), in addition to the nets determined by minimizing the sum of the distances between the centroids of each pair of faces in the net d (*i.e.,* $f = d$ in equation (3.22)). The nets for the four shapes considered in this section associated with each objective function are shown in Table 3.1. With the exception of the cube, all shapes displayed different optimal nets based on the two considered optimization criteria. Figure 3.17 shows plots of accuracy vs. film thickness for target shapes of fixed sizes. As expected, the nets optimized for maximum shape accuracy a showed higher accuracy values than the ones optimized for minimum d, except for the cube where the nets obtained from the two optimization criteria are equal. The reduction in accuracy displayed in the plots with the thickness of the film is due to the increase in the fold width obtained from equation (3.17). Increasing the film thickness eventually results in an increase of the fold sizes that ultimately ends shrinking the faces down to a line or a point. These bounds are indicated with a "$\times$" symbol in the plots. Figure 3.18 shows the effects of scaling the target shape while keeping the film thickness fixed. The plots are generated assuming a film thickness of 37.7 μm, which is the same as that used in the fabrication examples in this section. Because the fold angle is not a function of the size scale of the target shape, the fold widths remain constant even when the size of the target shape is reduced, leading to inaccuracies as smaller target shapes are sought. Similar to figure 3.17, the "$\times$" symbol marks the target shape sizes for which one or more of the faces are degenerated to a point or line, thereby resulting in shapes with different topology than the target shape.

Table 3.1: Nets for the cube, truncated icosahedron, platform, and trimmed torus determined by minimizing the sum of the distances between the centroids of each pair of faces of the net d and maximizing the shape accuracy a.

	Cube	Truncated icosahedron	Platform	Trimmed torus
Minimum centroidal distance d	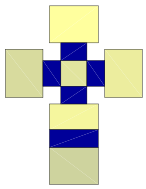	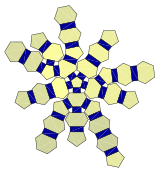	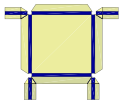	
Maximum accuracy a	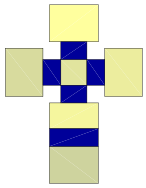	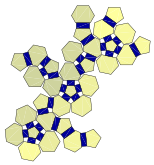	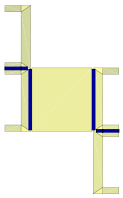	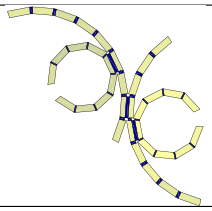

The presented manufacturing method based on programmable, self-foldable polymer films could complement 3D printing of millimeter and sub-millimeter shapes in some instances including the fabrication thin-walled hollow constructions. Thin-walled hollow structures often demand the use of excessive support structures to avoid a potential collapse of the shape during 3D printing. The use of support structures not only affects the pre-processing and the material usage, but it also necessitates a time-consuming post-processing step to bring the structure to the target shape. An origami-based manufacturing method can produce thin-walled, hollow three-dimensional shapes without the use of supporting structures. The absence of additional material makes it a cost-effective alternative to the conventional 3D printing approach in cases where thin-walled shapes need to be fabricated.

3.3.3 Carbon Origami

The presented fabrication methods used only a single-layer of photopolymer to achieve the three-dimensional polyhedral shapes. Here, SU8, a polymer with a carbon-rich backbone, facilitated the folding-based fabrication. Such carbon-rich materials enable the conversion

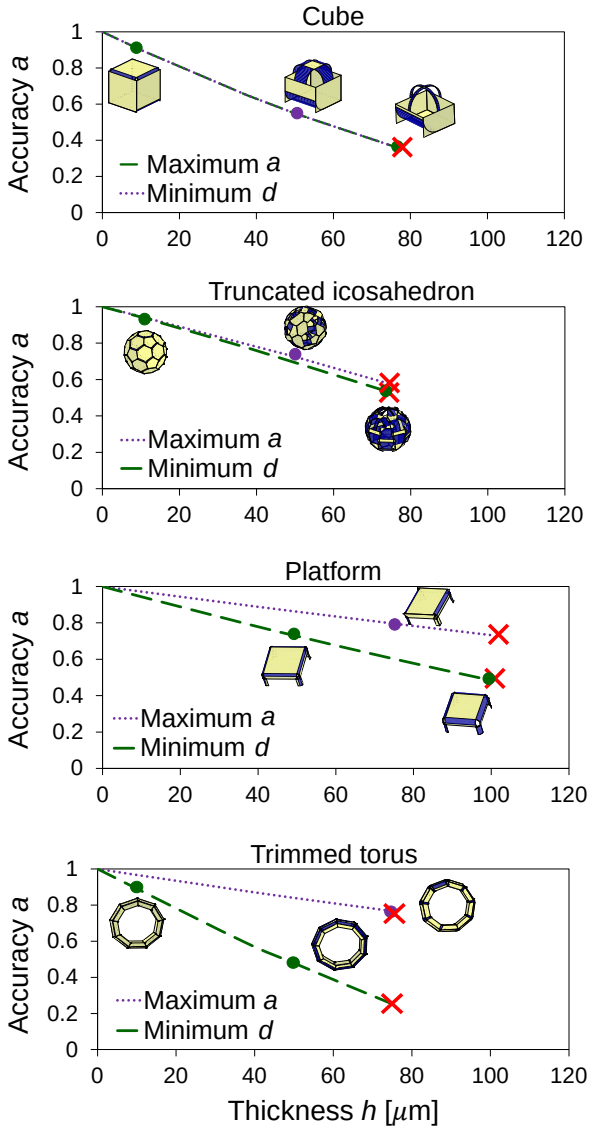

Figure 3.17: Shape accuracy a vs. film thickness h for the cube, truncated icosahedron, four-legged platform, and trimmed torus. Trimmed meshes accounting for accommodation of the smooth folds are also shown. The size of the target meshes corresponds to that of the fabricated samples shown in Figs. 3.13-3.16. The $\times$ marks the thickness at which one or more faces of the trimmed mesh are degenerated to a point or line.

of the polymer to their corresponding carbon shapes without losing their shape accuracy. The carbon-rich three-dimensional shapes created using the origami fabrication method are successfully converted into carbon by heating them in an inert environment at 1000°C inside a quartz tube. The resulted carbon shapes are visually identical yet shrunken versions of the shape of the corresponding three-dimensional polymer precursors, as shown in Fig. 3.19.

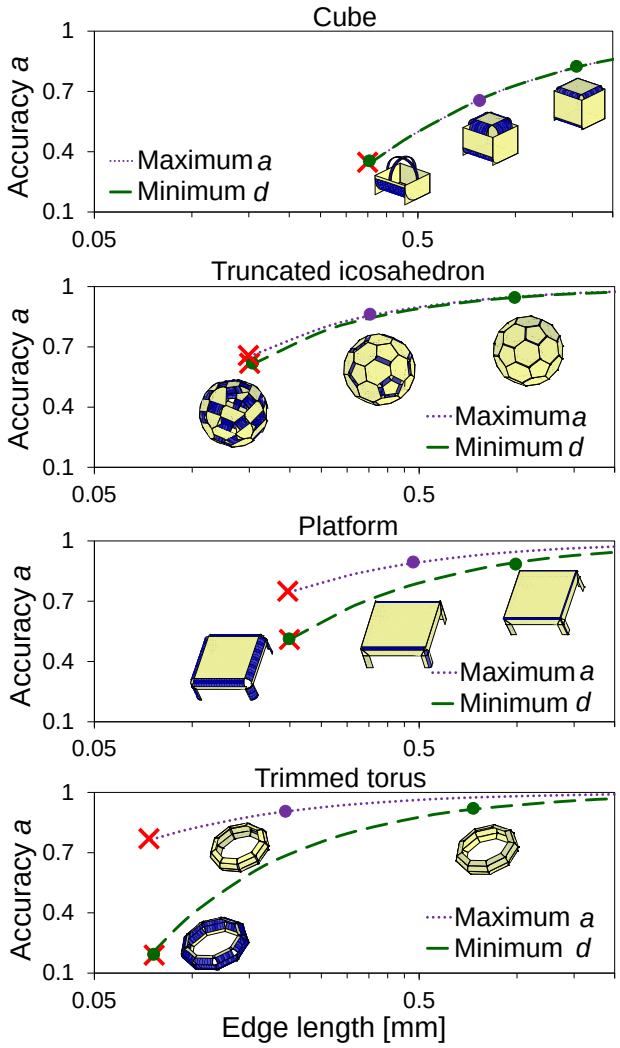

Figure 3.18: Shape accuracy a vs. smallest edge length for the cube, truncated icosahedron, four-legged platform, and trimmed torus shapes. Trimmed target meshes are also illustrated (not shown to scale). A film thickness of 37.7 μm is used in the generation of the plots, which corresponds to the thickness used in the experimental demonstrations shown in figures 3.13-3.16. The $\times$ marks the edge lengths at which one or more faces of the trimmed mesh are degenerated to a point or line.

Many of the potential applications of the polyhedral shapes that can be fabricated using the present manufacturing method, however, have different material requirements. Coating of the carbon structures with a desired metal via electroless plating [41, 26, 119] can allow for further extension of the present method into metallic polyhedral structures.

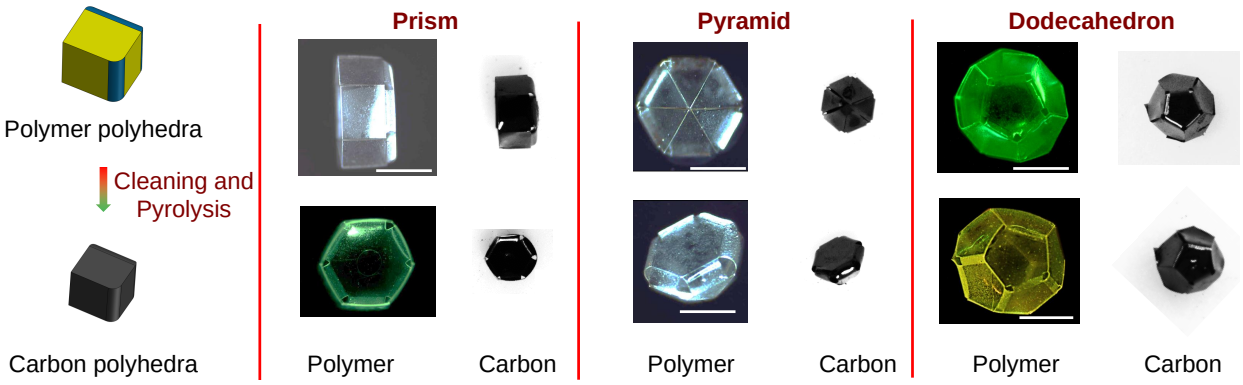

Figure 3.19: Three-dimensional carbon polyhedral shapes obtained by pyrolyzing the associated polymer shapes. The scale bars represent 1.5 mm. The photos of the polymer and carbon samples are displayed to scale, showing the decrease in overall size of the samples after pyrolysis.

Chapter 4

Comparison Study of Capillary Origami and Self-folding Origami Fabrication Methods

4.1 Introduction

[1]The capillary-assisted folding and the diffusion-based self-folding can be achieved using patterned single layer photopolymer with rationally tailored material properties. In this study, these two methods involving similar photolithographic fabrication methods are compared and contrasted through a host of experiments. The main goal of the study is to devise fabrication methods that can create polymer shapes starting from a computational target shape, as shown in Fig. 4.1. The remainder of this chapter is structured as follows: Section 4.2 delineates the origami-based design of the polymer films for origami manufacturing, Sec-

[1]Portions of this section are reprinted or adapted from [Derosh George, Marc J. Madou, Edwin A. Peraza Hernandez, "Practical fabrication methods for 3D origami structures from 2D films patterned via photolithography," Proc. SPIE 11610, Novel Patterning Technologies 2021, 116100X (22 February 2021); https://doi.org/10.1117/12.25829734]

tion 4.3 explains the experimental procedures followed to fabricate capillary-assisted origami and self-folding origami, and Section 4.4 provides examples of employing capillary-assisted and self-folding origami methods for fabricating three-dimensional polymer and carbon structures.

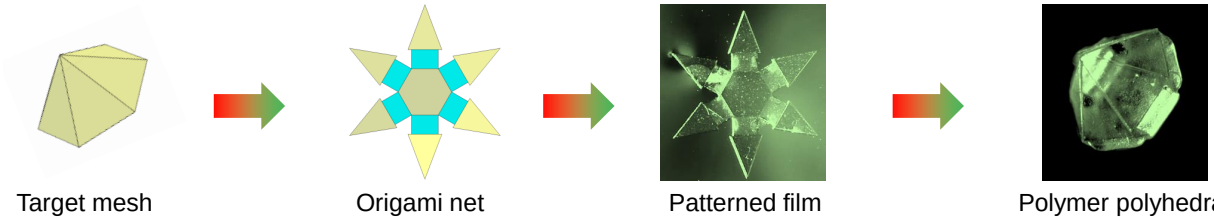

Figure 4.1: Schematic flow of the origami-based manufacturing methods explored in this work. The methods start with a target shape model and produce the corresponding polymer polyhedra.

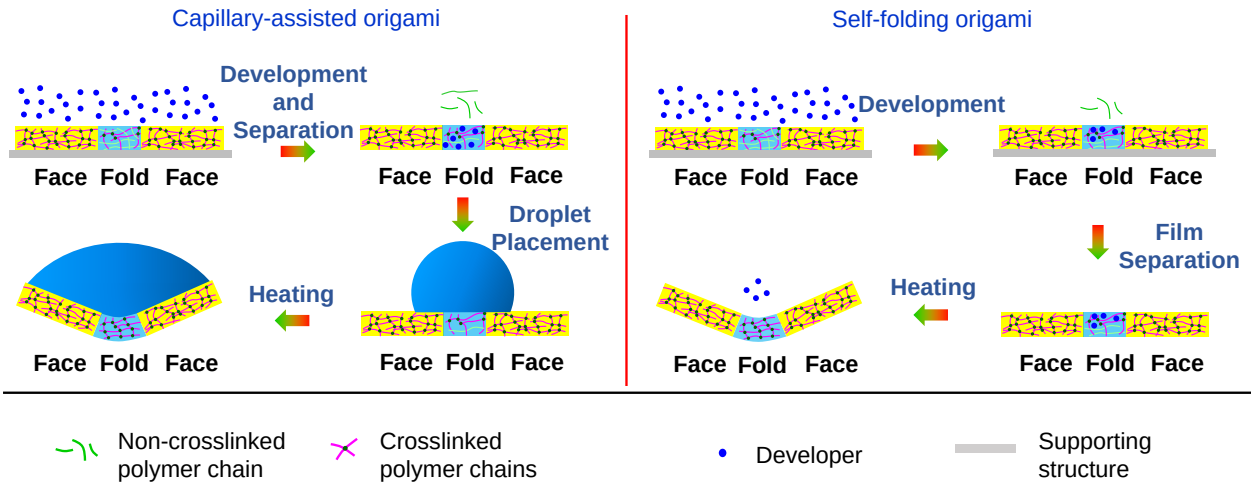

Figure 4.2: Two different *folding mechanisms* for origami structures formed by single-layer photopolymer films. In *capillary-assisted origami*, surface tension is used to trigger the folding process by placing a water droplet on the thin film. In *self-folding origami*, the folding is realized by selectively diffusing (and removing) solvent to (and from) the designated fold region.

4.2 Origami Design

The two primary ways to fold thin films explored herein are by exerting an external force or by inducing an internal strain gradient via mass transport. Favorable scaling of the sur-

face tension with the reduction in characteristic length is utilized to drive the folding in the capillary-assisted folding and achieve three-dimensional shapes at millimeter and sub-millimeter length scales. A soft film with uniform thickness and material properties will undergo a uniform bending under the influence of a droplet. However, to accomplish folding instead of a uniform bending of the film, the fold regions are deliberately made more compliant than the face regions. When an external force is applied on such films having relatively compliant fold regions and stiffer face regions, the deformations resulting from the force will be concentrated on the weaker fold regions, emulating a typical folding process as depicted in Fig. 4.2.

On the other hand, to induce self-folding, selective diffusion of a chemical and its subsequent removal is employed as shown in Fig. 4.2. Specifically, when the developer solution is diffused into the partially crosslinked regions of the film (folds), it removes the non-crosslinked polymer chains from the film, forming voids [149]. Heating of the film leads to the removal of the trapped developer, and subsequent collapse of the voids that manifests as deformation. Since a large concentration of voids is present on the side that was in direct contact with the developer solution, more shrinkage is expected to occur on that side, leading to a strain gradient that produces bending.

Implementing the two aforementioned types of strategies on a single layer of carbon-rich polymer would enable a successful transformation of these three-dimensional shapes into corresponding carbon structures. A photopolymer is chosen to precisely control the crosslinking density and the shape across the planform. Overall, the objective of this study is to devise an origami-based three-dimensional fabrication method that reaches the target polymer polyhedra shape from the corresponding computational model. Here the process starts with three-dimensional meshes of the target shape. Initially, these three-dimensional models need to be unfolded into their corresponding two-dimensional nets, as shown in Fig. 4.3. The cuts at various corners are made such that an unfolded two-dimensional shape is formed from

the target mesh. Although the fold width does not affect the fold angle in capillary-assisted folding, there should be a compliant fold region with a finite length to emulate the desired sharp bending behavior at the fold region. The predetermined fold width is incorporated in the design by trimming the mesh at the fold regions. The nets resulting from these processes have folds (shown in light blue) that connect the faces (shown in yellow). A similar unfolding approach is followed for designing the self-folding net from the target mesh. Unlike capillary-assisted folding, the fold widths are a function of the targeted fold angle at each fold for the self-folding method.

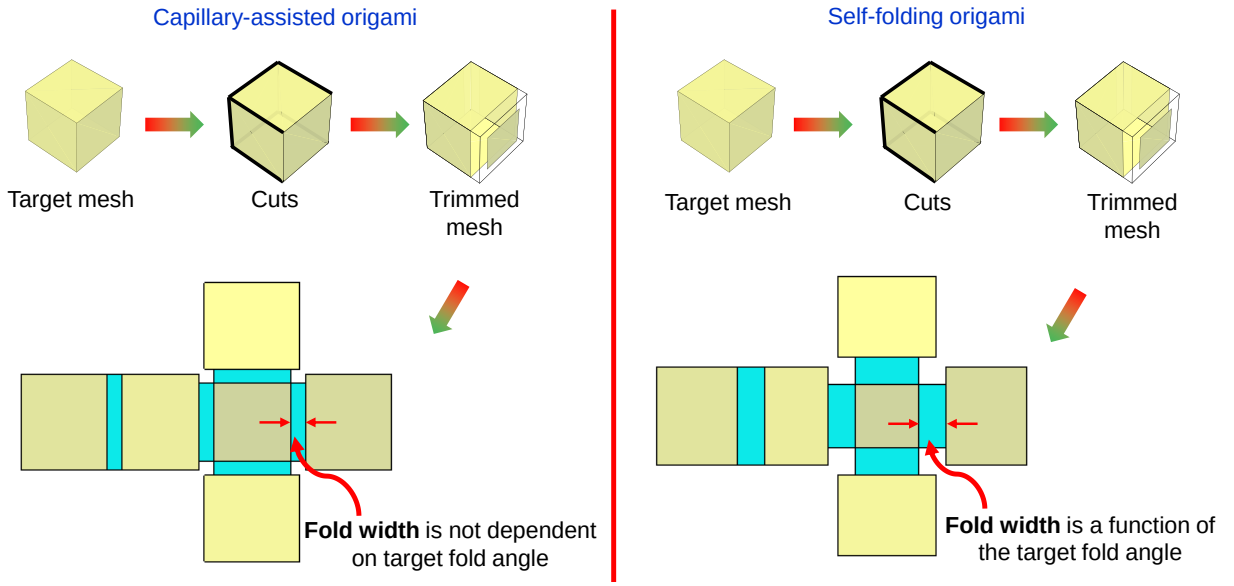

Figure 4.3: Unfolding processes to generate nets for both capillary-assisted folding and self-folding. While the fold width values for the capillary-assisted folding are not dependent on the targeted fold angles, the fold widths for the self-folding method are a function of the targeted fold angles.

To devise a manufacturing method, precise control over the folding deformation is required. For capillary-assisted folding, predictable folding of a single fold film is possible by modulating the droplet volume placed over the film through controlled evaporation [58]. The fold angle characterization is performed using single-fold films. The results showed a sudden increase followed by a steady decrease in fold angle as the volume of the droplet used for the folding process increases, as shown in Fig. 4.4. The initial increase is observed for low

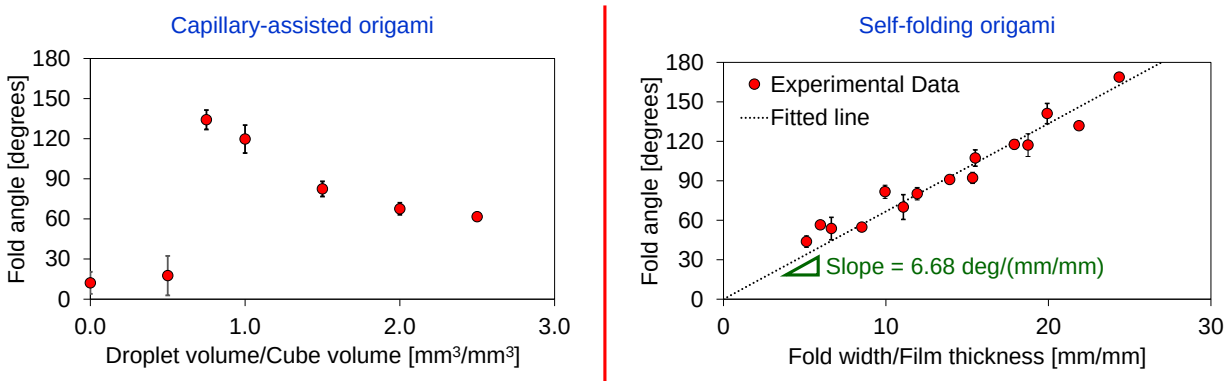

Figure 4.4: Fold angle characterization for the capillary-assisted folding method and the self-folding method. In capillary-assisted folding, the fold angle of a single fold is controlled by controlling the volume of the droplet. In the self-folding approach, the fold width and film thickness determine the fold angle.

volume droplets, in which case the volume is too small to induce a significant bending moment on the film. The sudden decline in the fold angle near the non-dimensionalized volume of about 1 makes the controlled folding of shapes with high fold angles difficult to achieve. This limitation can be removed by placing a large droplet that is large enough to reach the edges and then removing the excess volume. The need to use excess volume makes the fold angle control by controlling the droplet volume a less effective method, limiting the range of shapes that can be formed using capillary-assisted folding.

For the self-folding method, the fold angle is observed to be a function of different parameters, including film thickness, fold width, exposure duration, and development duration. In this study, film thickness and fold width are varied to evaluate their effect on the fold angle exhibited; the remaining parameters are kept unchanged. The results showed that fold angle is linearly dependent on the ratio of the fold width and the film thickness. This relation is crucial since that enables precise control over each individual fold angle by programming the thin film during the fabrication process.

A polyhedron can be unfolded into different net shapes [162, 163], and therefore, it is essential to choose a net that is feasible for the two folding approaches presented herein. Each fold has a fold width that corresponds to the target fold angle it will attain when the self-folding

approach is implemented. Consequently, the shape of the original net that fold into the target shape is not going to play a vital role in the outcome of the folding process. However, it would be better to use the most compact net shape for folding in capillary-assisted folding since the droplets driving the folding have a spherical-cap shape. Nets optimized for minimum distance between the faces make the most compact unfolded shapes, ideal for the capillary-assisted folding. The optimization is carried out by obtaining the distance between each face and then minimizing the sum of all such distances for the shape by using a genetic algorithm, where the design variables correspond to the assignment of each edge in the target shape as fold or as a cut [59]. Figure 4.5 shows that the compactness of the net increases as the optimization progresses. The same optimized net shapes are also used for the self-folding process to be consistent across the folding processes. The details of the fabrication process are provided in the following section.

4.3 Experimental Procedure

4.3.1 Film Preparation

SU8, a photopolymer that exhibits an increase in cross-linking density upon UV irradiation, is used to fabricate the three-dimensional shapes through folding. The first step of the fabrication process is the preparation of the thin film, illustrated in Fig. 4.6. The thin film is made by spin-coating the photopolymer on a supporting structure. A silicon wafer is used as the supporting material for making the patterned thin film used for the capillary-assisted folding. Silicon, as compared to its oxide counterpart, forms a weaker bond with SU8. This weak bonding would be a bane since the removal of the patterned film from the supporting structure is needed to get free-standing pattern films that can be folded into three-dimensional shapes. SU8 2025 is spin-coated at 900 RPM to obtain a uniform film

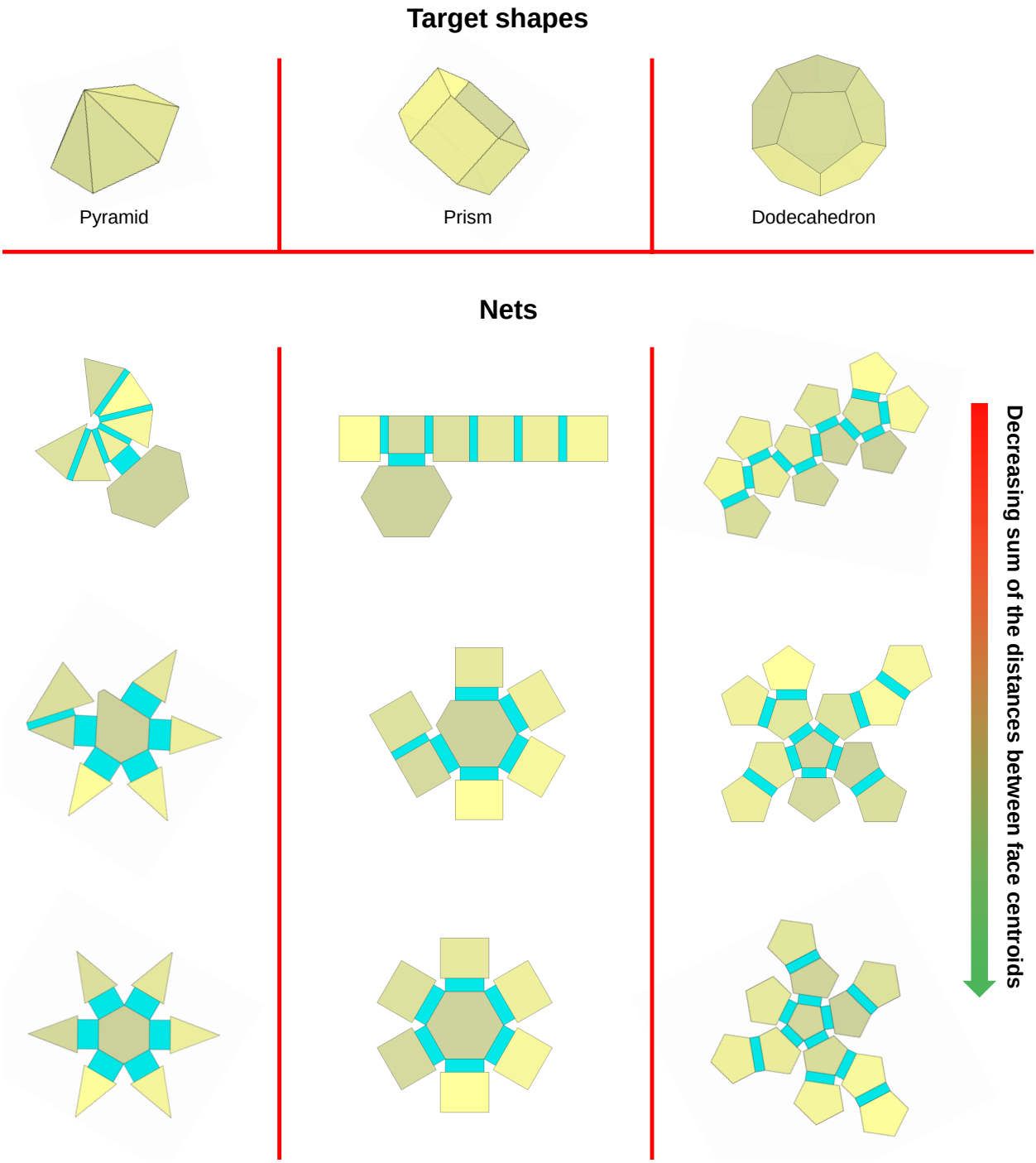

Figure 4.5: Different target shapes considered as implementation examples in this work and associated nets. The sum of the distances between the centroids of the faces is minimized to obtained the most compact nets.

with thickness of 55 μm.

A different approach is followed for self-folding origami method. Instead of a silicon support structure, a PDMS-coated support structure is used for the self-folding experiments. First, PDMS monomer and its curing agent are mixed in 10:1 ratio. Trapped bubbles formed from this mixing are removed from the PDMS mixture by placing it inside a vacuum chamber for 15 minutes. The bubble-free PDMS is spin-coated on top of a silicon/silicon dioxide wafer at 500 RPM and then cured on top of a hot plate at 80°C for 10 minutes. SU8 is spin-coated on top of this PDMS covered silicon/silicon dioxide wafer at 2500 RPM to obtain a film thickness of about 35 μm.

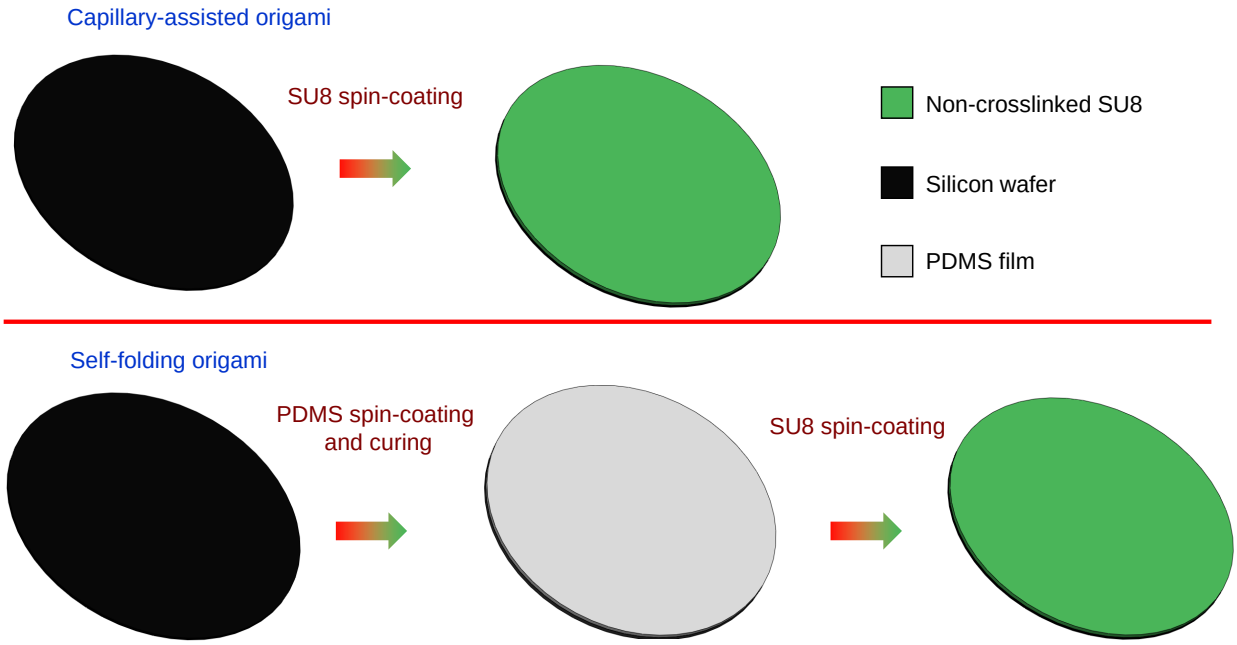

Figure 4.6: Film preparation step for capillary-assisted folding and self-folding. The photopolymer film for capillary-assisted folding is prepared on a silicon wafer, and the film for self-folding is spin-coated on a PDMS supporting structure.

4.3.2 Patterning

After the SU8 thin film is spin-coated on top of the supporting structure, double-exposure photolithography is performed to increase the cross-linking density of the film at selected locations, as illustrated in Fig. 4.7. During the first exposure, both the fold and the face

regions are exposed to UV light for 40 seconds. In the second exposure, only the face regions are exposed to UV light for an additional duration of 40 seconds. This additional exposure at the face regions enables the formation of more cross-linked regions during the subsequent post-exposure baking step. Post-exposure baking is performed at 95°C for 10 minutes.

In the case of capillary-assisted folding, the silicon wafer with the SU8 film is developed using either acetone or SU8 developer after post-exposure baking. Unlike the traditional developing step, the development is performed for an extended period. The extended development lasts until the patterned films are completely detached from the supporting structure. These free-standing films are collected, washed in an IPA bath, and then dried to perform the subsequent folding step.

For the self-folding approach, once the thin film is formed on top of the PDMS substrate, it is subjected to the same double-exposure used for the capillary-assisted folding that formed a highly crosslinked face region and a less-crosslinked fold region. However, in the self-folding method, the development step is different from the previously mentioned extended development. Here, the development is performed for only 2 minutes. Unlike the extended development, the short development does not remove the patterned film from the supporting structure.

4.3.3 Folding

In capillary-assisted origami, the free-standing planar patterned films are placed inside a hot oil bath to soften them by bringing them closer to their glass transition temperature. A water droplet is placed on top of the films to induce folding, as shown in Fig. 4.8. Heating of the film causes softening. The face regions remain stiffer than the fold regions since the face regions have a higher crosslinking density. A droplet having a volume 1.5 times that of the target shape is used to fold these planar films. The excess water volume is removed by

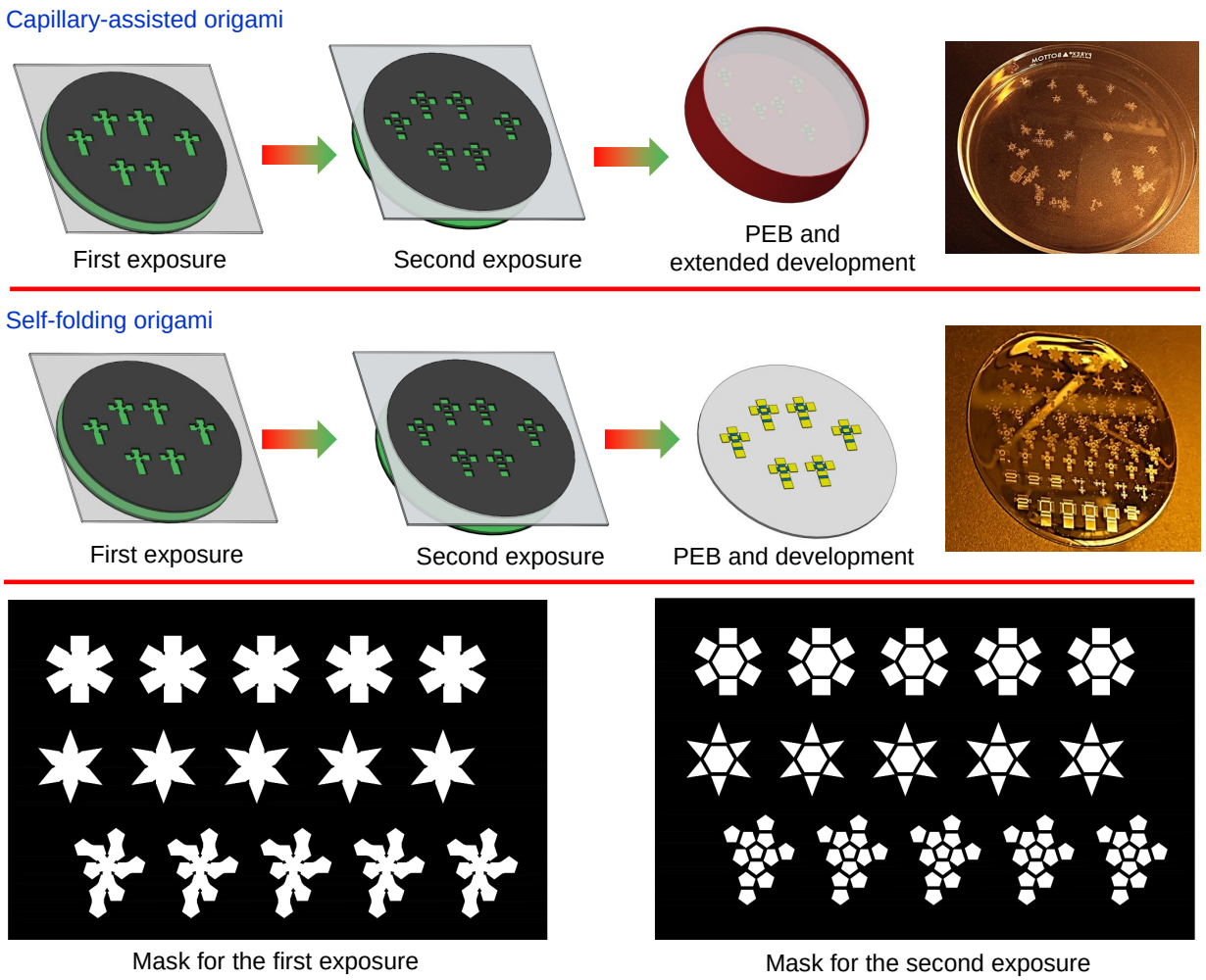

Figure 4.7: Double-exposure lithography and subsequent development in the patterning step. Double exposure is identical in both capillary-assisted folding and self-folding. Development of the films on the silicon wafer for the capillary-assisted folding is performed for an extended period to separate the patterned films from the silicon wafer. Development of the films on PDMS for self-folding is performed only for a duration recommended for the conventional lithography process. This allows the films to remain bonded to the PDMS substrate. The bottom figures show the masks for the two UV exposure steps. The first step lets UV light irradiate both folds and faces, while the second steps lets UV light irradiate only the faces to obtain higher stiffness at these regions.

letting it boil over time. For this reason, the oil bath is set at 105°C. Once the film is folded to its intended shape, the oil bath is cooled to room temperature. Cooling helps to keep the folded target since the stiffness of the polymer film increases as temperature decreases [60]. Additional UV exposure is performed after removing the three-dimensional folded films from the oil and cleaning, to ensure that the fold regions are completely cross-linked.

For the self-folding approach, the patterned films are attached to the PDMS substrate, instead of free-standing, after the development step. These patterned films are carefully removed from the PDMS substrate by using a razor blade. Folding is performed inside an oil bath that is set at 80°C, where the developer transport phenomenon illustrated in Fig. 4.2 induces self-folding. The cleaning and the subsequent UV exposure steps are identical to those of the capillary-assisted fabrication method.

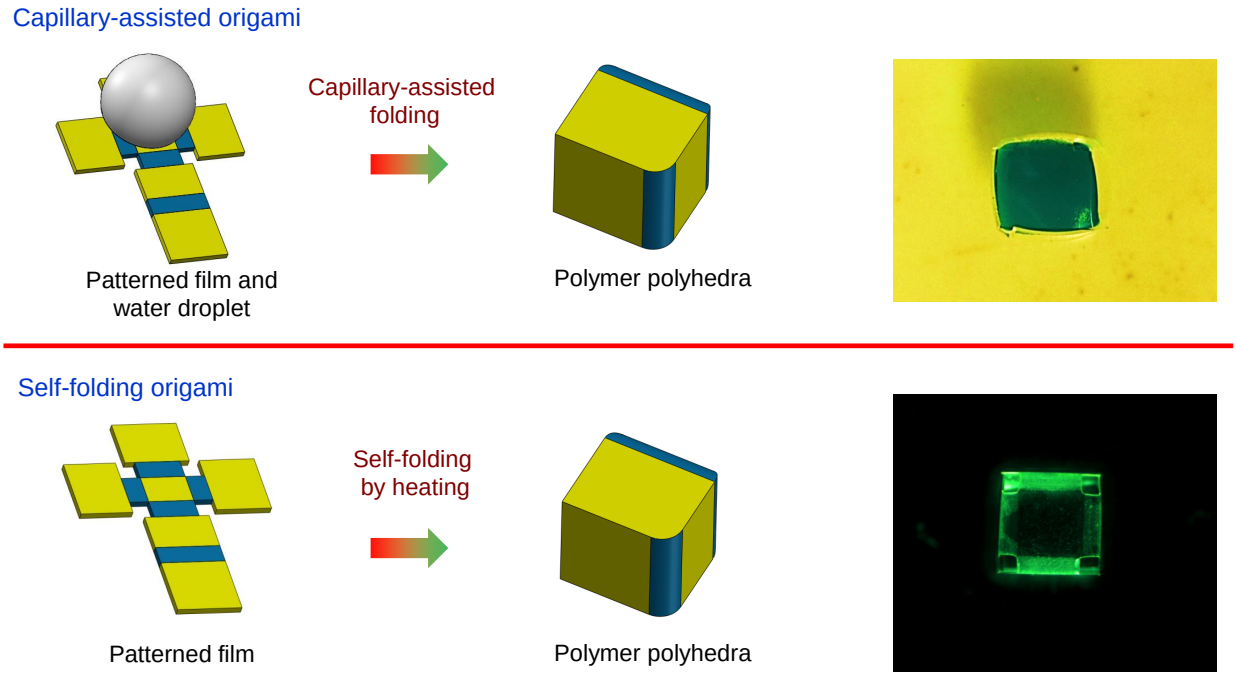

Figure 4.8: Folded shapes are achieved by placing a droplet on a softened patterned thin film in capillary-assisted folding and by heating in self-folding.

4.4 Results

Two-dimensional nets are fabricated by using masks made from the optimized net shapes shown at the bottom of Fig. 4.5. The predicted shape from the computational model and the fabricated three-dimensional shapes matched reasonably well in all three cases, as shown in Fig. 4.9. The three-dimensional shapes are made either by heating these nets or by placing droplets on them after softening, as explained earlier. A pyramid, a prism, and a

dodecahedron are used to demonstrate and compare the two folding processes, as illustrated in Fig. 4.9. Nets with identical fold widths are used in all three of the capillary-assisted folding demonstrations since the fold angle does not depend on the fold width.

Unlike the capillary driven folding, the fold angles exhibited at the individual depend on their dimensions as captured in Fig. 4.4. Therefore, the fold widths used for these three shapes need to be different in the three self-folding demonstrations. The pyramid shape requires fold angles of about 135°. Such large fold angles necessitate a relatively wider fold width for the self-folding compared to the nets used for the capillary-assisted folding. The hexagonal prism is formed by folding the six identical lateral faces to an angle of 90°, a value less than what is required for the pyramid, leading to relatively smaller fold widths for the prism. The dodecahedron has the smallest required fold angles and therefore its net for self-folding origami has the smallest fold widths.

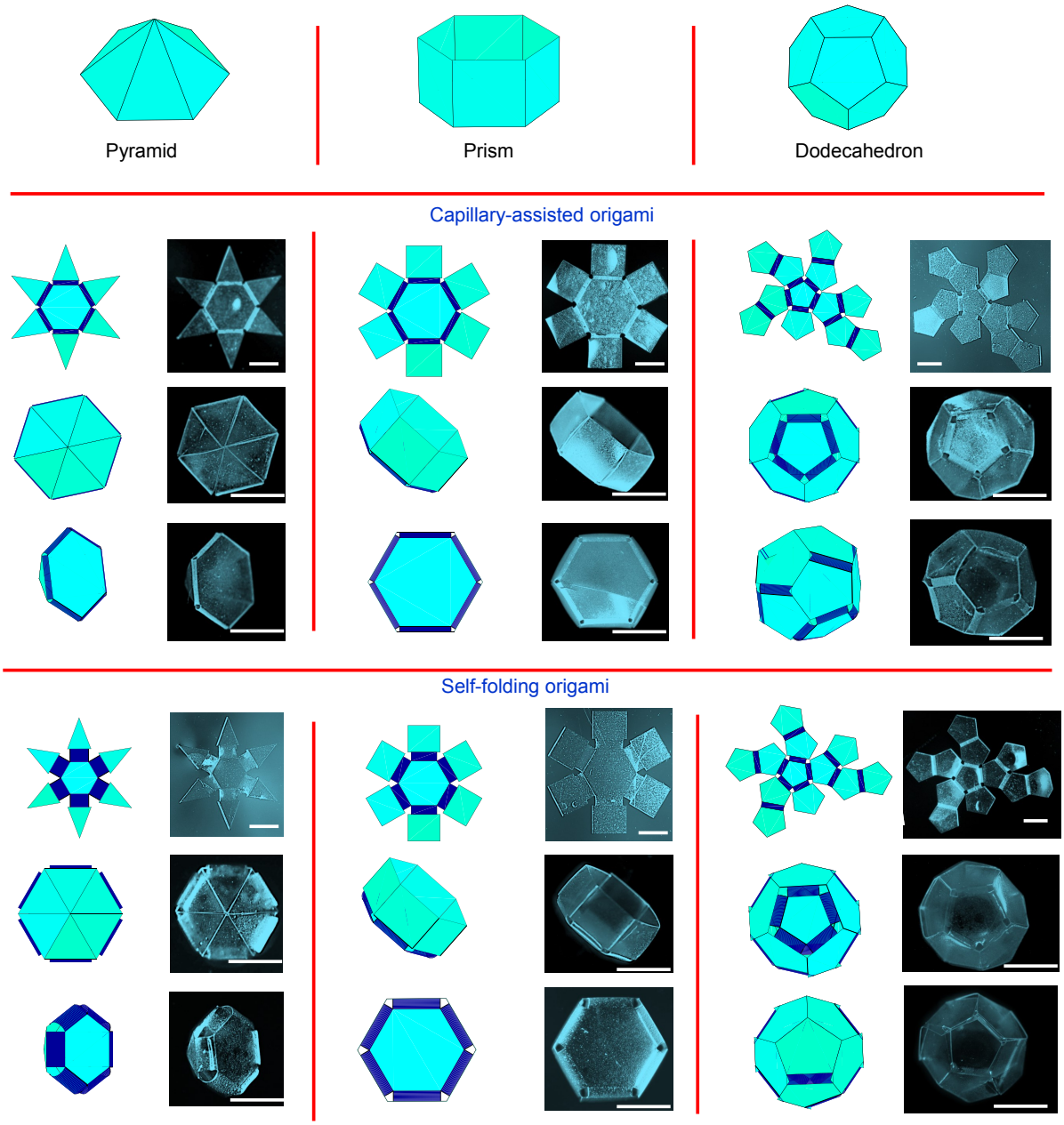

Figure 4.9: Simulated and fabricated pyramid, prism, and dodecahedron. Micrographs from different views are shown for capillary-assisted origami and self-folding origami. The scale bars represent 1.5 mm.

Chapter 5

Nearfield Electrospinning-based Carbon Nanowriting

5.1 Introduction

[1] Among various shapes, micro- and nanowires have gained unprecedented attention from the research community owing to their applications in fields, such as photonics [232], electronics [141], energy harvesting [154], and metamaterials citebauer2016approaching. A study showed that fabrication of wires having structural uniformity could result in low-loss photonic wires for waveguiding[69]. Using a layer-by-layer assembly of nanowires, fabrication of multi-nanowire field effect transistors (FETs) can be realized [88]. Assembly of inorganic nanowires may be used for the fabrication of flexible electronics [128]. In another reported case, it has been shown that conversion of mechanical energy to electrical energy is possible using an array of zinc oxide nanowires [251]. Mechanical metamaterials made of polymer

[1]Portions of this section are reprinted or adapted from [George, D., Garcia, A., Pham, Q. et al. Fabrication of patterned graphitized carbon wires using low voltage near-field electrospinning, pyrolysis, electrodeposition, and chemical vapor deposition. Microsyst Nanoeng 6, 7 (2020). https://doi.org/10.1038/s41378-019-0117-7]

can be transformed to carbon to enhance its mechanical properties[13]. Apart from these general applications of nanowires, aligned and suspended carbon wires have shown to have applications as strain sensors, temperature sensors and gas sensors[209] and expected to have potential applications in far-field thermal emitters [8]. However, their potential use in next-generation products remains limited by the low throughput, high complexity, small working area, and the expense of the equipment involved in current fabrication techniques.

Far-field and near-field electrospinning, on the other hand, have the potential to become scalable nanomanufacturing methods for nanowire structures owing to their simplicity, affordability, and versatility. While far-field electrospinning (FFES) utilizes the regime where bending instabilities generate randomly oriented nanofiber mats, near-field electrospinning (NFES) exploits the regime where the bending instabilities are minimal thus allowing for precise patterning applications [197]. To further improve the controllability of NFES, our team developed a low voltage electromechanical spinning (EMS) method[22], which allows for yet more controlled nano writing with various polymers in NFES [81]. However, a yet higher-resolution patterning method with a higher throughput of thinner fibers that is applicable to a wider variety of polymer precursors for C-MEMS and C-NEMS remains very desirable. Improving the throughput of the NFES will help in the manufacture of new classes of well-defined polymer and carbon micro/nanostructures for advanced applications in electrochemical sensing, energy storage, and stem cell research [186, 98, 76, 127, 121, 213]).

Fiber patterning using NFES involves two main steps i.e., jet initiation and controlled fiber deposition. In the presence of an electric field E, jet initiation occurs at the surface of a liquid droplet with diameter a and surface tension γ, when the electrostatic pressure ($\sim \epsilon_o E^2$) is comparable to the capillary pressure ($\sim \gamma/a$), where ϵ_o is the permittivity of free space. Therefore, in order to overcome the surface tension of the liquid droplet to form a Taylor cone on the droplet, an electric field $E \sim V/L \sim \sqrt{\gamma/(\epsilon_o a)} \sim 10^6$ V/m, considering typical values $\gamma \sim 0.1$ Nm, $a \sim 0.01$ m and $\epsilon_o = 8.85 \times 10^{-12}$ F/m needs to be applied, where L

is the distance between the droplet and the collector and V is the voltage applied across L. At a low voltage, fibers can be extruded out of the droplet by bringing it close to the collector, while for a case with a relatively large L, a higher voltage is needed to be applied to initiate the electrospinning. Once a continuous fiber jet is obtained, the relative motion of the spinneret and the collector is used to control the deposition of fibers.

NFES is carried out in the straight jet regime, where electrically driven bending instabilities caused by the lateral perturbations are absent, to provide better control over the nanowire deposition. In this regime, where electrically driven instabilities are absent, mechanical instabilities such as buckling could still be present. The deposition process in this regime is analogous to lowering an elastic rope onto a surface, a process that is accompanied by buckling and subsequently coiling of the rope [70]. To avoid this buckling and thus to obtain straight wires, the distance L has to be small and the collector velocity must be more than or equal to the jet velocity. For a liquid of conductivity κ_p and density ρ, the jet velocity, v_{jet}, is reported to be $(\frac{\kappa_p \gamma \pi}{\epsilon_o \rho})^{\frac{1}{3}} \frac{1}{f^2}$, where f is the nondimensionalized radius of the jet [52]. From this expression for the jet velocity, it is observed that smaller fibers are generated with higher velocity due to its inverse square relationship with the fiber radius. This high velocity poses a significant challenge when trying to obtain straight and controlled writing of smaller fibers, which requires the collector to be mounted onto an expensive high-precision high-speed linear stage. We overcame this hurdle by translating this demanding linear motion into a rotational motion ω and by stepping the position of the fiber jet to obtain aligned nanofibers on a collector of radius R.

The rotational motion is mainly used here to uncoil the fibers, not to thin the fibers. The rotational motion can improve the inter-fiber spacing for high-resolution nanopatterning. In this set-up, the resolution (Δx) of the nanopatterning is a function of both linear velocity

of the spinneret (v) and the rotational speed of the collector (ω) as given in Eq. (5.1):

$$\Delta x = v/\omega. \tag{5.1}$$

5.2 Methodology

The electrospinning solution (11% PAN) was prepared by dissolving PAN (150,000 mw, Sigma Aldrich, St. Louis, MO) in dimethylformamide (DMF) by stirring at 50°C for 24 hours. The solution was drawn into a 1 mL syringe with a 30-gauge stainless steel needle. The tip of the needle was fitted with a polytetrafluoroethylene (PTFE) tube to avoid wetting the outside of the stainless-steel tip. The syringe was then attached to a syringe pump. A linear stage with a Prior III controller was used to move the dispensing system at various linear speeds, ranging from 30 to 2400 μm/s. A DC voltage range between 100-1500 V was applied to the tip of the dispensing needle using a high voltage source which is grounded to the rotating collector (300 - 2000 RPM) (Fig. 5.1(a)). The distance between the spinneret and rotating collector was varied between 0.7 and 10 mm. Either bare silicon substrates or silicon substrates with patterned carbon structures were secured with conductive carbon tape into designated grooves in the rotating drum. A microscope equipped with a camera was used to visually monitor the needle-to-collector distance, the jet initiation, and the stability of the Taylor cone. The fiber jet was first initiated by varying the working distance (Supporting Document 1). Aligned nanofibers were obtained by moving the syringe pump parallel to the axis of the drum rotation. Experiments were carried out varying the linear speed of the spinneret and the rotational speed of the collector to find the correlation between these two parameters and the inter-fiber spacing.

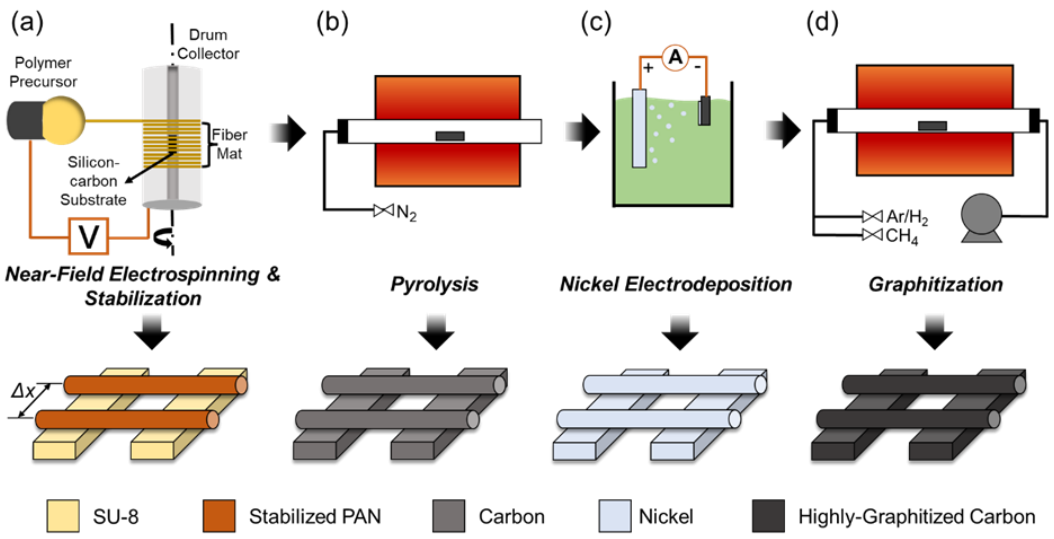

Figure 5.1: (a) Electromechanical spinning of polyacrylonitrile (PAN) solution onto a rotating collector to obtain patterned polymer wire deposition. (b) Pyrolysis of stabilized PAN wires inside a furnace to get pyrolytic carbon. (c) Nickel electroplating of the carbon structures to form catalytic surface for the subsequent chemical vapor deposition (CVD) of graphitic carbon. (d) chemical vapor deposition (CVD) of graphitic carbon.

The patterned PAN fibers obtained by this technique were pyrolyzed to produce carbon fibers. The wires on the silicon substrates were first stabilized at 270°C for 6 hours to ensure high carbon content after pyrolysis. Following the stabilization, a Lindberg Blue M furnace was used for pyrolyzing the nanowires at 1000°C, under an inert atmosphere, to produce carbon nanofibers (Fig. 5.1(b)). The resulting carbon nanowires were then compared with PAN nanowires under SEM (Tescan GAIA3) to study the shrinkage caused by pyrolysis. A carbon support structure with a channel width of 40 μm on a silicon dioxide coated Si wafer was used as the collector substrate to fabricate suspended PAN nanowires. This support structure was obtained by pyrolyzing the corresponding SU8 photolithographic pattern. The suspended PAN fibers were then pyrolyzed as described earlier.

5.3 Results

5.3.1 Parametric Study of Polymer Wire Fabrication and Patterning

Wires were initiated by applying a voltage between a polymer droplet and a rotating collector and then bringing the droplet sufficiently close to the collector. Once a steady Taylor cone was established, the distance between the spinneret and the rotating collector was adjusted to the desired working distance. The effect of voltage on the diameter of the fibers was investigated by fabricating fibers at voltages ranging from 400 V to 900 V. This range chosen here for PAN falls within other reported near field electrospinning voltages for polymers (0.2 kV to 12 kV)[228]. As shown in Fig. 5.2(a) and (b), the experimental results demonstrate good agreement with the predicted trend that the diameter increases with applied voltage. The fiber diameter showed an inverse dependency on the working distance between the spinneret and the collector (Fig. 5.2(c)). In this near field electrospinning setup, the larger

wires are obtained by applying higher voltages but those often come with variations in diameter along the length of the wire (inset in Fig. 5.2(b)). This inconsistency in the wire diameter is due to an insufficient rate of solvent evaporation from these wires during the transit from the spinneret to the collector.

A time scale evaluation of the jet travel time and the evaporation rate gives one an insight into how important it is to work in the low voltage regime to obtain uniform wires. The jet travel time to obtain straight wires scales as $\sim L/R\omega \sim (10^{-3})/(10^{-1})(10) = 10^{-3}$ s, whereas the evaporation time scales as $\sim r^2/D$ which is approximately equal to 10^{-1} s for the relatively bigger fibers obtained at higher voltages. Therefore, in order to obtain solid and uniform wires, either the wires must be small (diameter $\sim$ 100 nm) or the distance between the spinneret and collector should be far enough for the solvent to fully evaporate. However, electrospinning at a distance of about 20 mm (voltage = 1,500 V) results in the formation of coiled fibers (Fig. 5.3) with the current EMS setup and when PAN is used. The formation of these coiled wires is attributed to the higher velocity of the fibers relative to the collector [191] and thus exhibit a higher probability of deviation from a straight path [175]. As depicted in Fig. 5.3(a) and (b), a shorter spinneret-to-collector distance and/or a faster collector rotational speed must be used to achieve straight patterns. Therefore, a shorter working distance with low voltage electrospinning is suggested to obtain patterned deposition of small wires with consistent diameter on a flat substrate. These observations on the straightness of the wires and their uniformity of diameter confirm that the low voltage EMS with a rotating collector is ideal to form straight PAN nanowires for nanomanufacturing. Additionally, low voltage electrospinning allows for the deposition of suspended wires across support structures due to the increased strength resulting from better solvent evaporation and thus solidification for suspended structures (Fig. 5.3(c) i). However, at relatively high-voltages, the wires fall into the trenches (Fig. 5.3(c) ii). Therefore, the enhanced diffusion-based solvent evaporation rate of the wires formed using electromechanical spinning enables the patterning of suspended wires over channels as shown in Fig. 5.3(d). To further verify

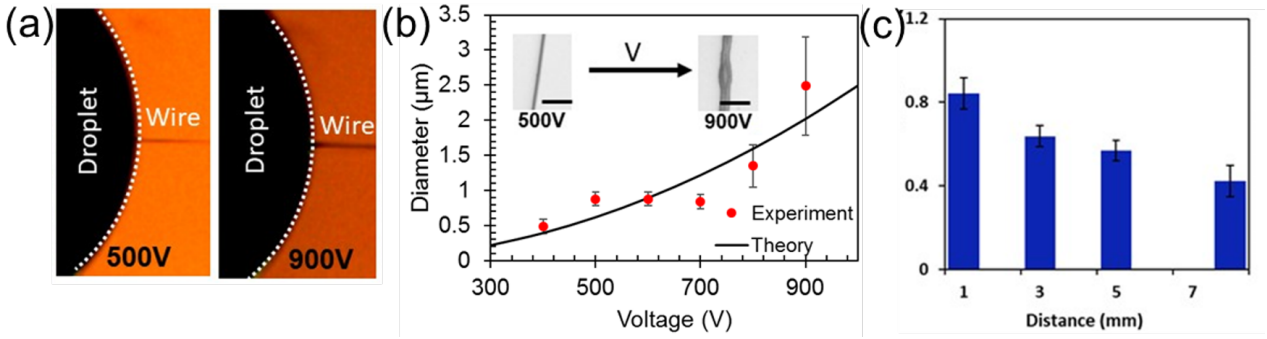

Figure 5.2: (a) Micrograph of wires at 500 and 900 V, (b) Variation of the diameter of the fiber with applied voltage applied (The scale bar is 7 μm long), and (c) Variation of the diameter with the distance between the spinneret and the rotating collector (L).

the prediction, experiments with different concentrations of polymer solutions was performed (7%, 9%, 11%, 13%, and 15%). It has been observed that at high concentrations (>13% w/w), suspended wires can be formed even at high voltages (>900 V) as opposed to lower concentrations (Fig. A.21). However, high concentration results in larger diameter wires and hence are not considered for the fabrication of carbon nanowires. Polymer wires suspended across a large gap can be achieved at low voltage (Fig. A.22).

As shown in Fig. 5.4(a), the inter-fiber spacing increases linearly with the linear speed of the spinneret, which agrees well with the predictions from Eq. (5.1). Moreover, the resolution of the patterns (Δx) consistently improved with increasing rotational speed (Fig. 5.4(b)) until Δx reached 7.9±2.3 μm (Fig. 5.4(a)). Our attempts to produce patterns with a resolution of less than 7 μm resulted in uneven inter-fiber spacing with the smallest Δx less than 1 μm (Fig. 5.4(b)). The irregularity of spacing distribution may be attributed to either the rotational imbalance of the collector or the air disturbance caused by the collector rotation.

Improved alignment and better patterning can be attained by actively directing the incoming fibers to desired locations. Previous studies have shown that a concentrated electric field produced by sharp locations on the substrate can be used for guiding the fibers [238]. Here,

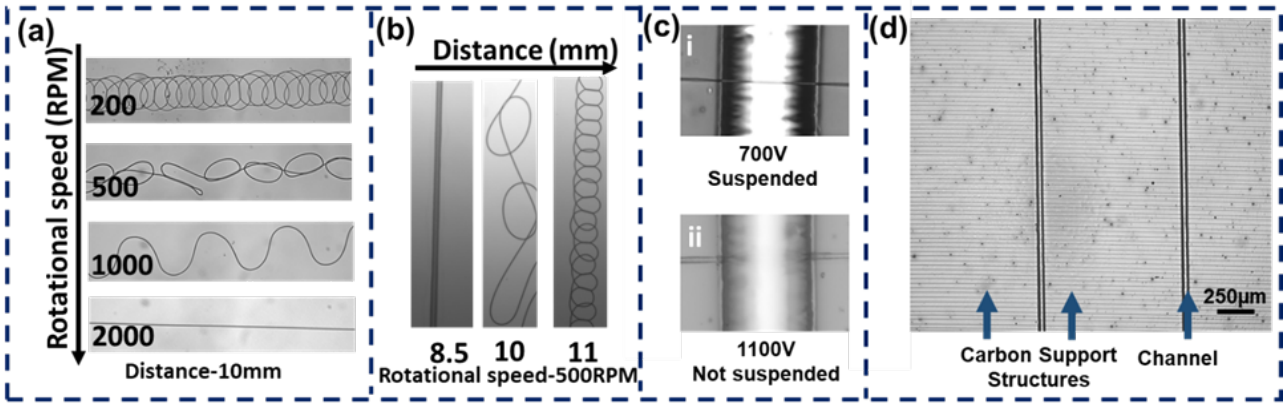

Figure 5.3: (a) Various fiber profiles obtained as a function of rotational speed. (b) As a function of working distance (voltage = 1500 V). (c) i. Successfully formed suspended wires at low voltage. ii. No suspended wire formation at high voltage. (d) Wire patterns (horizontal lines) formed over carbon support structures with two microchannels (vertical lines).

we used patterned carbon pillars on a silicon substrate for collecting the wires. The results show that the pillars attracted the wires towards them, giving rise to highly ordered suspended wires on the pillars. Experiments were performed with pillars having cylindrical and square cross-sections. A preferential deposition on the edge of the pillars was observed (Figs. 5.5 and A.24). The observed preferential deposition was corroborated by the isocurves from the simulation results showing the electric field (Fig. A.24). Additionally, prior research on the pyrolysis shrinkage by Martinez et. al. showed that the structures may form sharp edges after pyrolysis [150]. Those sharp edges could have further enhanced a favored deposition on the edges due to the concentrated electric field at that region. Electric field simulations carried out with COMSOL Multiphysics showed a concentrated electric field near the edges of the pillars (Fig. A.24). The required spacing between the wires can be obtained using Eq. (5.1), which should equate to the distance between the pillars. Executing NFES produces suspended wires across all the pillars with predetermined inter-fiber spacing mediated by the pillar arrays (Fig. 5.5(a)). It is interesting to note that the attraction of the pillars is dominant enough to ensure that the wires are laid down exactly on the pillars even if the

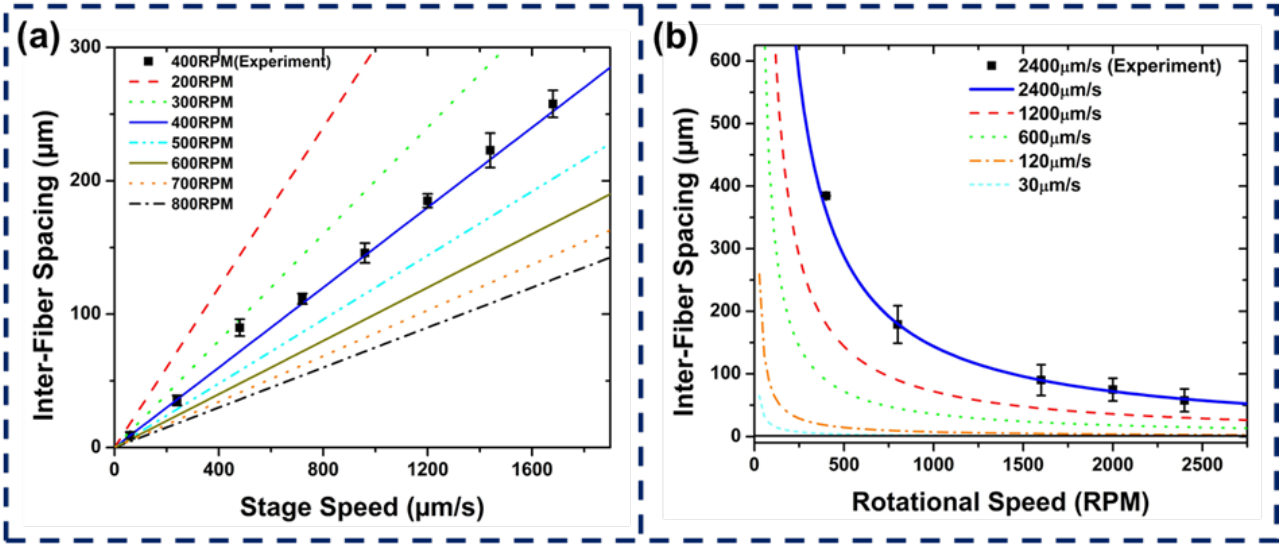

Figure 5.4: Variation of inter-fiber spacing with (a) stage speed and (b) rotational speed of the collector.

incoming wires are slightly offset by a small angle to the pillar array, correcting the error on its own, as shown in Fig. 5.5(b). An inter-fiber spacing lower than the pillar spacing resulted in pairing of wires in a regular interval (Fig. 5.5(c)).

5.3.2 Carbonization of Nanowires

The studies showed 87% survival of suspended wires on 7 μm deep channels having width less than 40 μm for submicron wires (Table. A.3). The polymer wires undergo shrinkage during pyrolysis to get sub 50 nm carbon wires. An isometric shrinkage is expected for a free-standing polymer structure when subjected to pyrolysis. Here the wires are having different mechanical constraints depending on whether it is suspended or on a planar surface. Accordingly, different amount of shrinkage-anisotropic shrinkage- can happen to the wires. A detailed study was performed to quantify the shrinkage of the wire that are suspended and on a surface. Wires were pyrolyzed at 600°C, 700°C, 800°C, 900°C and 1000°C to find the effect of the temperature on the shrinkage. Results showed an increasing trend in the

percentage of shrinkage from 47.7% for the wires pyrolyzed at 600°C to a 74.6% shrinkage for 1000°C for the wires on surface (Fig. A.26). This shrinkage is small as compared to the suspended part of the wires. Percentage of shrinkage for the suspended region ranged from 58.2% to 88.6% for a pyrolysis temperature range from 600°C to 1000°C (Fig. A.25).

Pyrolysis was shown to shrink the fibers uniformly when they are in parallel, but when multiple layers are deposited on top of each other (i.e., crisscross patterns in Fig. 6.9(a)), the top fiber shrank nonuniformly at the intersections, as represented in Fig. 6.9(b). For a wire which is in contact with the surface, the shrinkage will be mainly along the height since the bottom of the wire is constrained by the contact that it has with the surface. For a wire which is suspended between two structures, the wire shrinks radially. These differences in shrinkage is the reason for the peculiar shrinkage at the intersection since the wire is in a suspended state on either side immediately to the first wire. The suspended polymer fibers were converted to carbon nanowires by pyrolysis and retained their shape to form bridges across the carbon support structures (Fig. 6.9(c)). It is worth noting that the supporting structures used here to suspend the wires are carbonized SU8 in order to avoid breaking the wires due to structural shrinkage during the pyrolysis. Wires smaller than 40nm were formed due to the combined effect of low-voltage nearfield electrospinning and the shrinkage (Fig. 6.9(d)).

The carbon nanowires were characterized with a Renishaw InVia Raman microscope to check the intensities of D (I_D), G (I_G), and 2D (I_{2D}) peaks at 1350 cm^{-1}, and 1550 cm^{-1}, and 2690 cm^{-1}, respectively. The ratio of I_D to I_G was observed to be 1 and the ratio of I_{2D} to I_G 0.14. These ratios along with the large width of the 2D peak indicate the formation of turbostratic carbon, as reported in previous studies (58).

A major challenge with prior electromechanical spinning-based nano writing on flat collectors is the lag in patterning transition when changing patterning directions [20]. With the typical back-and-forth motion on a linear stage to create parallel patterns, the surface placement of

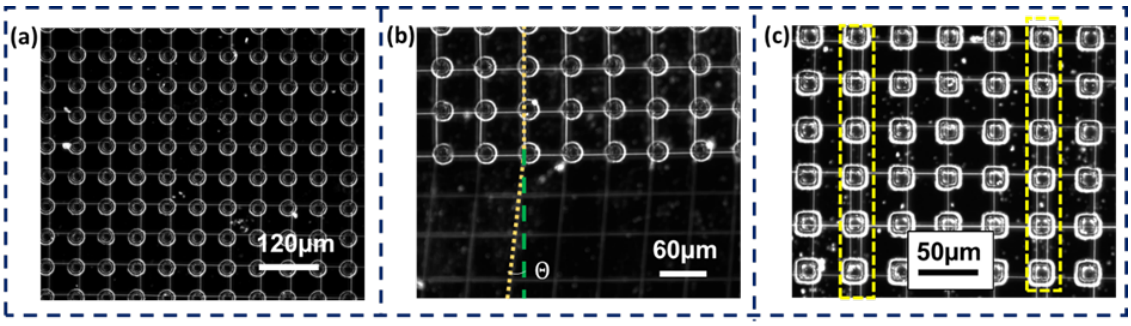

Figure 5.5: (a) Patterned deposition of wires on a carbon pillar array. (b) Straightening of the wires that are coming at an angle to the array. (c) Multi-wire deposition of wires on a single column when the pillar spacing is more than the expected wire spacing.

the extruded fiber lags behind the spinneret as it moves and changes directions. Such spatial and temporal lagging in patterning often causes the deposited fibers to overlap and to change diameter, making it difficult to obtain high-resolution writing. The use of a rotating collector overcomes these challenges by avoiding the abrupt directional changes (i.e., back-and-forth motion) and the lagging velocity between the spinneret and the collector (Supporting Document 2). Additionally, compared to a linear stage, the throughput using a rotating collector can be significantly enhanced by enlarging the diameter of the collector, making it viable for large-scale nanomanufacturing. The presented electromechanical spinning-based nano writing method can attain highly accurate patterned deposition by controlling the rotational and the linear speeds.

The throughput using NFES was significantly increased in comparison to two-photon lithography and other laser-based nano writing techniques, which offers a maximum throughput of about 5,000 μm/s [45]. For instance, the present NFES method allows writing patterns at a resolution (Δx) of 8 μm at a throughput of 1 m/s, which is two orders of magnitude higher than other existing nanopatterning approaches. According to the predictive model (Eq. (5.1)), a highly coveted 1 μm spacing should be achieved with a combination of a low stage speed ($\sim$20 μm/s) and a high rotational speed ($\sim$1,200 RPM) if the aforementioned irregularities are managed. Such high throughput fabrication of patterned carbon wires is

highly desired as there is lack of a nanomanufacturing system having control over micro and macro shapes for carbon [209], especially for shapes having dimensions less than 50 nm. Carbon nanowires, both aligned and suspended wires, have shown to have applications as strain sensors (aligned carbon wires), temperature sensors (suspended wires) and gas sensors (suspended wires) [209]. Apart from these carbon specific applications, nanowriting of polymer wires also shown to be suitable for the fabrication of nanochannels, enhanced solid electrolyte, light emitting wires and nano resonators [9, 105, 127, 174].

Additionally, the patterning method described here may be extended to other polymers to obtain carbon patterns having different properties. The suspended carbon nanowires described here offer a unique advantage for producing graphitic carbon wires of different properties, because it is possible to tune the resultant nanowires by controlling the diameter of the template nanowire, the thickness of the electro deposited metal catalyst and growth time.

While the presented carbon nanowire fabrication technique has various aforementioned advantages, it is worth mentioning that the technique has various shortcomings too. This technique limits the fabrication to straight and aligned polymer and carbon wires. Though it is possible to electrospin suspended wires across a large distance, the fabrication of suspended carbon wires is restricted by the geometric parameters. This limitation is due to the transformations that they undergo in the subsequent steps. In the current study, a diameter-to-channel width ratio of ~ 1000 was obtained. Fabrication of smaller carbon wires is difficult since the polymer wire diameter in the current technique was limited by the low stability of the Taylor cone at low voltages.

Chapter 6

Design of Carbon Microstructure

6.1 Mechanically Induced Graphitization

[1] Polymers are generally categorized as amorphous and semi-crystalline polymers. Amorphous polymers have oriented molecular chains whereas semi-crystalline polymers have relatively organized and tightly packed molecular chains. Due to the difference in the arrangement of the polymer chains, these two types of polymers behave differently under heat. While amorphous polymers exhibit a glass transition temperature, semi crystalline polymers have a melting point. Since amorphous carbon does not undergo melting, it can be converted into corresponding isometrically shrunk carbon shapes, given the polymer is 'carbon-rich.' On the other hand, having a melting point prevents most of the semi-crystalline polymers from keeping the shape intact during the pyrolysis.

[1] Portions of this section are reprinted or adapted from [Holmberg, Sunshine, Maziar Ghazinejad, EunByul Cho, Derosh George, Brandon Pollack, Alexandra Perebikovsky, Regina Ragan, and Marc Madou. "Stress-activated pyrolytic carbon nanofibers for electrochemical platforms." Electrochimica Acta 290 (2018): 639-648. https://doi.org/10.1016/j.electacta.2018.09.013] and [Pollack, Brandon; Holmberg, Sunshine; George, Derosh; Tran, Ich; Madou, Marc; Ghazinejad, Maziar. 2017. "Nitrogen-Rich Polyacrylonitrile-Based Graphitic Carbons for Hydrogen Peroxide Sensing" Sensors 17, no. 10: 2407. https://doi.org/10.3390/s17102407]

Carbon shapes that are formed from amorphous polymer are often fall under the category of glass-like carbon/glassy carbon. These glass-like carbons contain curved carbon microstructures known as fullerenic carbon. Formation of this arrangement of carbon atoms (microstructure) is often attributed to the randomness and entanglement in the precursor polymers. Conversely, having aligned molecular chains in the precursor can lead to more organized carbon microstructure known as graphitic carbon. This method of making graphitic shapes could be of high interest in many areas. However, preserving the shape and the chain alignment simultaneously is challenging (due to the melting behavior of the semi-crystalline polymers), yet plausible.

Polyacylonitrile, unlike SU8 is a semi-crystalline polymer and has shown to have the capability to retain the shape during pyrolysis, given that the heating rate is below 40°oC/min. Although pyrolysis of PAN leads to some graphitic regions in the carbon obtained, it still majorly gives a non-graphitic carbon. however, the semi-crystalline nature of the polymer makes it easier to mechanically align the molecular chains and thereby controlling the microstructure of the resulting carbon. It has been observed that an application of shear force on the polymer solution can result in the alignment of molecular chains. The alignment of PAN molecular chains under such shear force results in an improved degree of graphitization on the surface of extruded wires as presented by numerous literature. However, this graphitization is limited to a small layer on the surface of the wire. One way to overcome this challenge is to make the wires small enough that the molecular alignment will be present across the diameter of the wire.

As mentioned earlier, the electrostatic force creates the ejection of nanowires from the polymer droplet. During the propulsion of the fiber, at the Taylor cone the polymer solution is accelerated from its stationary stage to the jet velocity in a short distance and time. This sudden change in velocity at the solution-air interface is exerting a shear strong enough to align the molecular chain at the interface. Rather than aligning of the molecular chain only during

the electrospinning step, and this is distributed between all the three steps – electrospinning, stabilization, and pyrolysis – to get improved results. We hypothesized that the alignment occurring during the electrospinning need to be supplemented with mechanical stresses in the subsequent steps for it to be preserved and carried on to the final carbon formed from it. Moreover, the existing strategies used in industries include an additional stretching step during the stabilization step of the polymer to improve the properties even further. Keeping these points in mind, two different experiments were carried out: 1) by applying an additional tensile stress during stabilization, 2) by applying a compressive stress during the stabilization step. The resulting carbon showed improved graphitization compared to the ones that did not undergo any such additional steps. Although improved graphitization was observed, characterization of the carbon using Raman spectroscopy showed that the improvement is insignificant. Although electrospun wires results in smaller wires than the extrusion method (<500 nm), perhaps the molecular alignment in the core region of the wires is insignificant, and that may have led to the insubstantial improvement in the graphitization.

The graphitization of the carbon throughout the cross section of the wire, instead of just at the outer surface, can be achieved by dispersing carbon nano tubes (CNT) in the PAN precursor. This modification should be done in addition to applying mechanical stresses during the stabilization process. The presence of CNT induces additional shear forces in the core region since it experiences a dielectrophoretic force against the flow due to the surrounding electricfield. This additional shear force ensures that the molecular chain in the core regions are aligned as well, leading to a better degree of graphitization as shown in Fig. 6.1. As mentioned earlier, mechanical stress should be applied during the stabilization step to ensure the retention of the molecular alignment during this step of the carbonization process. During the stabilization, PAN molecular chains undergoes cyclization where the neighboring nitrile groups (-CN) react with each other to form pyridine-like cycles. Upon pyrolysis, these straightened, cyclized polymer chains forms graphitic carbon. In the absence of mechanical stress, it is highly likely that the long chain molecules will curl and the wound

polymer chain leads to fullerenic carbon upon pyrolysis.

6.1.1 Materials and Methods

Electrospinning

Polyacrylonitrile (PAN) (Sigma Aldrich) with a molecular weight of 150,000 g/mol, N,N-dimethylformamide (DMF) (Sigma Aldrich) and multi-walled carbon nanotubes (MWCNT) (Sigma Aldrich) were used to obtain pure PAN mats and PAN-CNT mats via electrospinning. To obtain a solution with a final concentration of 8% PAN for electrospinning, PAN powder was dissolved in DMF. The mixture of PAN and DMF was stirred for 24 hours at 40o C to ensure homogeneity. Solution for preparing PAN-CNT mats was obtained by dispersing MWCNT into DMF by ultrasonicating the mixture for 1 hour. This mixture was then stirred for 24 hours to avoid agglomeration of MWCNT. PAN was then added to the mixture and stirred for another 24 hours to obtain a final solution containing 1% MWCNT and 8% PAN. The pure PAN and PAN-CNT mats were electrospun by applying a potential of 1.6kV between a continuously dispensing syringe (0.25 mL/hr) and a rotating, metallic drum collector (rotating at 500 RPM). The mats were removed from the drum after electrospinning for 4hrs.

Mechanical Treatment and Stabilization

Prior to stabilization, PAN-CNT mats were mechanically rolled using a Dayton roller press to further align the carbon molecular chains. These PAN-CNT mats were then compressed to 200 kPa and stabilized at 280°C for 6 hours to obtain mechanically treated PAN-CNT mats, the precursor to SAPC as shown in Fig 6.1. Pure PAN mats underwent no mechanical treatment and were stabilized at 280°C immediately following electrospinning.

Carbonization

The mats were pyrolyzed in an inert, nitrogen gas environment (flow rate of 9000 sccm) inside a Lindberg Blue M tube furnace. To increase graphitization and prevent nanoporosity of the carbon, a two-step pyrolysis process was used. The mats were first heated to 300°C at a rate of 4.5°C/min and kept at this temperature for an hour. The temperature was then increased to 1000°C at 2.5°C/min and held at this value for an hour before cooling down to the ambient temperature.

6.1.2 Characterization

High Resolution Transmission Electron Microscopy (HRTEM) allowed us to visually study the correlation between the synthesis method and the carbon's microstructure. Fig. 6.2a and b demonstrate the microstructures of untreated PAN-based pyrolytic carbon nanofibers (PNF) and stress activated PAN-based carbon nanofibers (SAPC), respectively. A quick examination of the HRTEM micrographs reveals a remarkable improvement in ordering of pyrolytic carbon when it is produced from stress-aligned polymer chains. As can be seen in Fig. 6.2 b i, the mechanically treated carbon displays relatively aligned carbon planes with wavy fringes. By contrast, the micrograph of PNF in Fig. 6.2 a i shows far less distinctive features with more circular, cage-like microstructures commonly seen in amorphous or glass-like carbons [72, 73]. Additionally, the oriented, but short and wavy fringes of SAPC display a graphitized structure with a high quantity of edge planes.

Raman Spectroscopy allows for quantifying the degree and uniformity of graphitization of the material. Averaged Raman spectra and Raman maps were determined based on 100 spectra collected across 5 μm $\times$ 5 μm areas of the PNF mats (Fig. 6.2 aii and 6.2 bii). The quality of graphitization can be evaluated by the ratio of the D peak intensity, centered between 1300 and 1400 cm^{-1}, to that of the G peak, located between 1560 and 1600 cm^{-1}. The G peak

is related to the in-plane bond stretching motion of pairs of sp^2-hybridized carbon atoms and the D peak is related to the disorder and deviation from perfect graphitic structure [44]. Hence, the lower the D to G ratio (I_D/I_G), the higher the level of graphitization within the carbon. Lorentzian curve fitting [179] was employed to decompose the Raman spectra to its constituent peaks, including D and G peaks. Analysis of the resolved Raman peaks suggest a substantial enhancement in the graphitization of PAN-based carbon after stress-induced molecular alignment, with the average I_D/I_G dropping from 1.47 to 0.90. Furthermore, this enhancement in graphitization of SAPC electrodes is prevalent throughout the nanofibers mats, as corroborated by the uniform Raman mapping of the resulting carbon. This uniform graphitization also translates to notably higher conductivity in PAN-based carbon fabrics [63].

To investigate the presence of heterogeneous atoms and the composition of the PAN-based carbons, we employed X-ray Photoelectron Spectroscopy (XPS). The XPS data reveals the presence of nitrogen and oxygen in the pyrolytic carbon, with a composition breakdown of 94.5±0.1 at% carbon, 4.4±0.5 at.% nitrogen and 1±0.3 at.% oxygen (Fig. 6.3 a) and b). Using Lorentzian curve fitting to deconvolute the nitrogen peak, N 1s, a rather unique distribution of nitrogen groups is found, comprised of 19.2% pyridinic, 57.0% graphitic, and a negligible amount of pyrrolic nitrogen atoms in the synthesized carbon fibers [222, 120]. The detected nitrogen heteroatoms originate from the nitrogen-rich PAN precursors that endured the low-temperature pyrolysis. The breakdown of the nitrogen heteroatoms in the synthesized carbon is of particular interest for its electrochemical performance [212]. It is important to note that the nitrogen heteroatoms are inherent in the as-pyrolyzed carbon, and no additional post-synthesis process, such as doping, has to be applied.

Accordingly, to probe our new carbon material for different electrochemical behaviors, we study its electrochemical response in three different redox systems: potassium hexachloroiridate $[IrCl_6]^{2-/3-}$ (surface insensitive), potassium ferricyanide $[Fe(CN)_6]^{3-/4-}$ (surface sensitive),

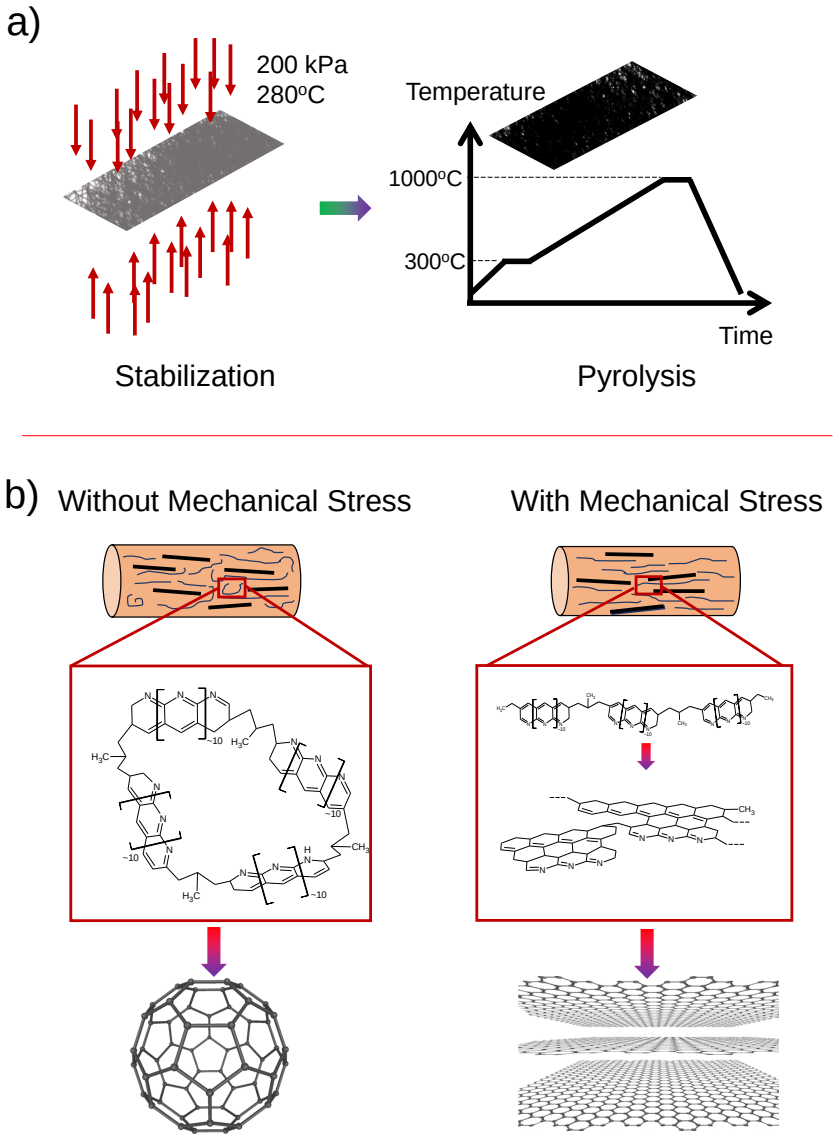

Figure 6.1: (a) Stabilization process with mechanical treatment and the pyrolysis process (b) Difference in microstructure of the resulting carbon based on whether the wires are mechanically treated or not.

and dopamine (adsorption surface sensitive) [137, 19, 89]. For conducting the electrochemical characterization, the carbon mats produced though pyrolysis were cut into smaller pieces (about 3 × 10 mm). Carbon electrodes were fabricated by connecting a thin copper wire to the mat using conductive carbon paste (Structure Probe, Inc.). Polydimethylsiloxane

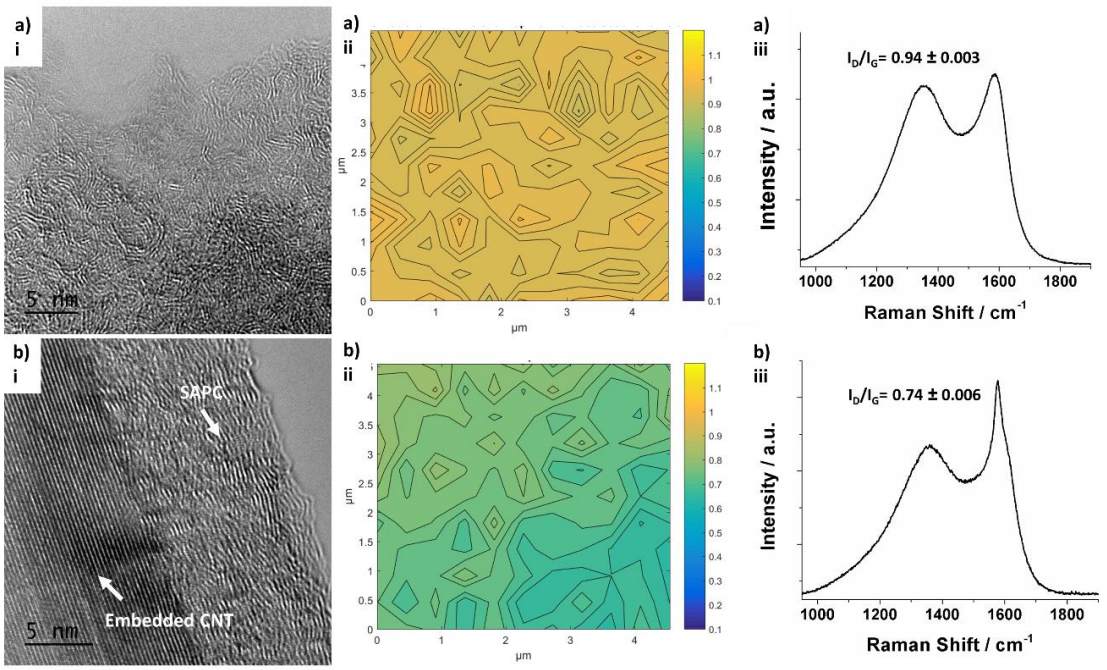

Figure 6.2: Material characterization of SAPC and untreated PAN-based CNF. High Resolution Transmission Electron Microscopy (HRTEM) of: a i) CNF and b i) SAPC microstructures. Mapping of Raman spectroscopy I_D/I_G ratio of: a ii) CNF, and b ii) SAPC. Average Raman spectrum of a iii) CNF and b iii) SAPC electrodes. Averages of over 100 collections are used to represent CNF and SAPC. ($\lambda_{excitation}$ = 532 nm)

(PDMS) (Dow Corning Corporation) was used to secure the electrode onto a 15 × 20 mm glass slide. Electrochemical tests were carried out using a Princeton Applied Research VersaSTAT 4 Potentiostat. The electroactive surface area of the sample was calculated using electrochemical impedance spectroscopy (EIS). EIS was performed in a blank electrolyte solution of 1 × Phosphate Buffered Saline (PBS) at a frequency of 10,000 Hz to 0.1 Hz. An equivalent circuit was used to fit the resultant Nyquist plot data. The electroactive surface area was determined using equation (2)

$$A_{act} = I_c/(C_{dl}v) \tag{6.1}$$

(2) where the double-layer specific capacitance, C_{dl}, was determined by normalizing the capacitance value of the equivalent circuit by that of the geometric surface area of the electrode.

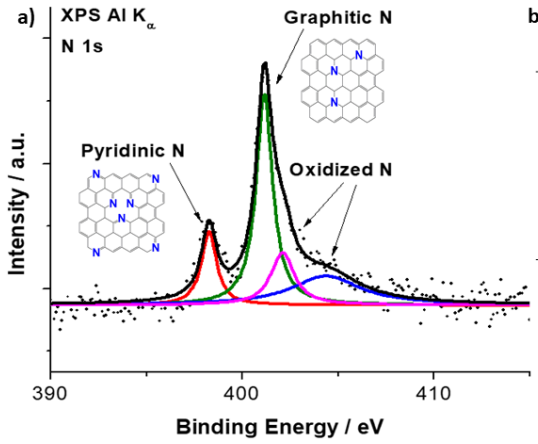

b)

Elements		at. % in gCNF
Carbon		94.5
Oxygen		1
Nitrogen		4.4
Components	**Binding Energy (eV)**	**at. % in Nitrogen**
Pyridinic N	398.5	19.21
Pyrrolic N	400.1	~0
Graphitic N	401.3	56.97
Oxidized N	405.0 & 402.6	13.97& 9.85

Figure 6.3: X-ray Photoelectron Spectroscopy (XPS). a) XPS spectrum of the N 1s peak of SAPC. b) Table of elemental composition of the SAPC as determined by analysis of XPS spectrum.

The scan rate (V/s), v, and the double-layer charging current, I_c, were obtained using cyclic voltammetry (CV). Cyclic voltammograms in these solutions allowed us to investigate the electrochemical kinetics of four different electrode materials (PNF, SAPC, polished Glassy Carbon, and MWCNT) by determining the heterogeneous electron transfer rate (k^o_{app}), the ratio between the reduction and oxidation current peaks (I_{red}/I_{ox}), and the linearity between the current peaks and the square root of the scan rate. Fig. 6.4 summarize the results.

The k^o_{app} values shown in the electrochemical kinetics table in Table 6.1 are determined using the Nicholson method, which assumes the behavior of the carbon electrodes is comparable to that of 2D planar electrodes. The validity of this assumption is seen in the collected voltammograms in Fig. 6.4, which demonstrate a linear relation between the square root of the scan rate and the peak current density [19, 151]. To study the three different carbon electrodes systematically, we first analyze their electrochemical behavior within each aqueous redox probe, and then compare their varying performances across the different probes.

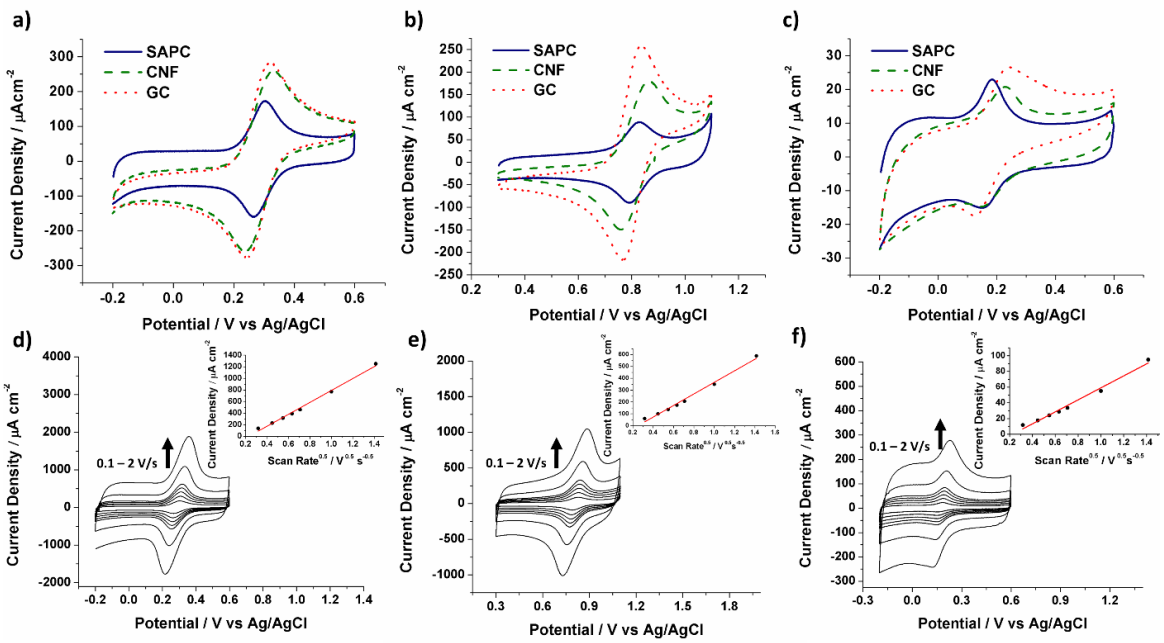

Figure 6.4: Electrochemical kinetics of SAPC. Cyclic voltammograms of SAPC, CNF, and GC's electrochemical response to aqueous solution of: a) 2 M KCl and 1 mM of $K_3Fe(CN)_6$, b) 2 M KCl and 1 mM of K_3IrCl_6, and c) pH 7.4, 1 mM PBS at and 0.1 mM of dopamine at a scan rate of 100 mV/s.

As mentioned earlier, potassium $[IrCl_6]^{2-/3-}$ is an outer-sphere redox probe. Due to the tunneling of electrons through the electrode surface, the response of carbon electrodes in $[IrCl_6]^{2-/3-}$ is more susceptible to the underlying carbon microstructure and is insensitive to the defects and interactions occurring on the surface [137]. Thus, potassium $[IrCl_6]^{2-/3-}$ is a suitable electrochemical probe for structural analysis of our pyrolytic carbon fibers. As seen in Table, SAPC exhibits an electron transfer rate (k^o_{app}) that is nearly 8 times greater than that of PNF (0.0461 cm s^{-1} vs. 0.00586 cm s^{-1}), and nearly two times greater than that of alumina-polished glassy carbon (0.0461 cm s^{-1} vs. 0.0232 cm s^{-1}), a standard activated carbon electrode used here as a control. The enhanced kinetics of SAPC in $[IrCl_6]^{2-/3-}$ underlines the high proportion of disorders in the form of edge sites within the structure of the SAPC electrodes. As predicted for surface insensitive analytes, microstructural defects do more to improve electrochemical kinetics than simple mechanical roughening of the electrode surface.

	CNF	SAPC	Alumina-Polished Glassy Carbon
$[Fe(CN)_6]^{3-/4-}$			
k_o^{app} (cm/s)	0.00795	0.114	0.0135
I_{red}/I_{ox}	0.99	0.99	0.99
$[IrCl_6]^{3-/4-}$			
k_o^{app} (cm/s)	0.00586	0.0461	0.0232
I_{red}/I_{ox}	0.99	0.99	0.99

Table 6.1: Electrochemical kinetics values of SAPC, CNF, and Alumina-Polished glassy carbon in different redox systems.

To investigate the effects of surface interactions and defects on the three pyrolytic carbons, we use $[Fe(CN)_6]^{3-/4-}$, a benchmark inner-sphere redox probe with high kinetic sensitivity to the state of electrode surfaces [10,11,34]. Here, the electron transport kinetics show a similar upward trend, with SAPC electrodes exhibiting k^o_{app} values 14 times greater than PNF electrodes (0.114 cm s^{-1} vs. 0.00795 cms^{-1}) and 10 times greater than alumina-polished glassy carbons (0.114 cm s^{-1} vs. 0.0135 cms^{-1}). The higher k^o_{app} values determined in $[Fe(CN)_6]^{3-/4-}$ (compared to that of $[IrCl_6]^{2-/3-}$) points to the effectiveness of our carbon synthesis method in boosting surface features of SAPC, i.e., edge planes and other electroactive sites. Indeed, HRTEM characterization of the carbon electrode surface corroborates this electrochemical deduction (Fig. 6.2) [63]. The improved surface kinetics of SAPC over that of mechanically roughened glassy carbon is due to the stable and persistent nature of the energy states in the surface sites of SAPC. The coarse nature of the mechanical abrasion used to polish glassy carbon electrodes produces defects that are electrochemically unstable and transient [24, 210]. On the other hand, the surface states of SAPC electrodes are forged at the elevated temperatures of the pyrolysis process and are therefore more resistant to passivation. This phenomenon is discussed further in the stability analysis of the electrodes.

As an extension of what we discussed before about the remarkable performance of the graphitic carbon as an electrode for electrochemical testing, a Hydrogen peroxide (H_2O_2) sensor using the graphitic carbon is demonstrated as a potential application in this report. (H_2O_2) is a common byproduct of many biochemical reactions and is therefore a

common analyte used to indirectly detect cellular signaling, aging mechanism, and various oxidases, such as glucose oxidase, NADPH oxidase, urate oxidase, and lactate oxidase [71, 64, 217, 201, 247, 57]. Though its major application lies in biosensing, its detection is of high importance in various other fields including textile industry, the food industry, and paper manufacturing as well [46]. Consequently, the detection of H_2O_2 is a major field of research for many sensing related applications.

Various techniques have been employed to achieve sensing of H_2O_2 such as fluorescence, colorimetric, and electrochemical methods [71, 64, 217]. Among these, electrochemical detection, in general, has the reputation of having high sensitivity, selectivity, and affordability. However, early experiments of H_2O_2 sensing used noble metals, such as platinum and gold as catalytic surface for attaining high sensitivity, making the electrochemical detection of H_2O_2 an expensive option [233, 53, 94]. This has eventually led to the use of various carbon allotropes, such as pure graphene, carbon nanotubes, and graphite for this purpose, which not only circumvents the use of expensive noble metals but also allows for a non-enzymatic method of sensing [90, 214, 243, 244]. Despite the advantages, the performances of these carbon allotropes are not on par with the existing sensors with noble elements. The main challenges in the area of carbon based H_2O_2 sensors include slow kinetics and interferences from species, such as ascorbic acid and uric acid, which prompts studies geared toward enhancing carbon catalytic performance [25].

In recent years, studies on the incorporation of heteroatoms into the carbon lattice have gained attention for its promise to enhance the catalysis of the modified carbon. The insertion of heteroatoms into the carbon matrices can tailor the electro-catalytic activity of the material to either enhance or diminish its electrons density. P-type graphene showed enhanced capability to oxidize, whereas the presence of n-type showed improved reduction capacity in various carbon allotropes [201, 247, 57]. The reducing nature of n-type carbon material, such as NRGC, is found to be highly advantageous in various applications, such

as fuel cell and biosensors [38, 124, 75, 125]. In particular, characterization of electrochemistry of nitrogen-rich graphitic carbons (NRGC) have revealed their potential as catalysts for various analytes such as hydrogen peroxide, ascorbic acid, dopamine, and uric acid [184]. Furthermore, NRGC's enhanced electrocatalysis has been demonstrated to allow for the simultaneous detection of these analytes within the same solution [187]. Specifically, NRGC's capacity for H_2O_2 reduction reaction is used as one of the standard measure of its catalytic performance [184].

It has been reported that the presence of pyridinic-N and graphitic-N enhances the catalytic behavior as it provides extra electron density to the graphitic basal plane [230]. The electron affinity possessed by nitrogen atoms causes a positive charge enhancement in the adjacent carbon atoms in the basal plane. This thought to be an adsorption enhancer in graphitic carbon [218]. This, consequently, aids the electrochemical reduction reaction. Moreover, a side-on adsorption of H_2O_2 (Yeager model) is made possible through this N-doping, making its o-o bond relatively weaker as compared to an edge-on adsorption, which in turn enables easier hydrogen peroxide reduction [227, 66].

A high degree of graphitization with graphitic edges can also contribute towards an improved electrochemical performance. Hence, an increase in the proportion of graphitic-N in the carbon structure is advantageous. Graphitic-N has a higher thermal stability as compared to the other types of nitrogen present in the material. Therefore, higher relative concentrations of graphitic nitrogen are generally observed at higher pyrolysis temperatures [250]. It is important to note that the overall nitrogen content within the pyrolytic carbon decreases as the pyrolysis temperature increases. Consequently, we have two competing factors that influence the overall quantity of graphitic nitrogen in the pyrolytic carbon structure. Here, the application of mechanical treatment in the fabrication of carbon with relatively low-temperature pyrolysis has resulted in nitrogen content as high as 4.4%, of which 57% is graphitic nitrogen. The corresponding spectra are given in Fig. 6.5 and Table 6.2.

Component (BE)	at.% in CNF	at.% in Mechanically Treated CNF
Pyridinic-N (398.5 eV)	24.14	19.21
Pyrrolic-N (400.1 eV)	35.29	∼0
Graphitic-N (401.3 eV)	30.58	56.97
Oxidized-N (405 eV & 402.6 eV)	9.99 & 0	13.97 & 9.85

Table 6.2: Nitrogen species based on XPS analysis.

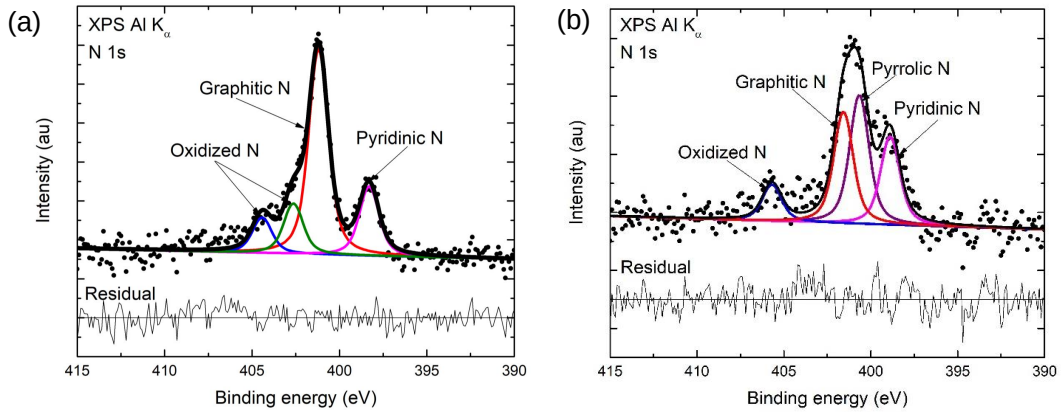

Figure 6.5: (a) Fitting N 1s XPS peak of CNF, (b) Fitting N 1s XPS peak of mechanically treated CNF.

It has been shown that N-doped graphene sheets have higher electrocatalytic capacity for H_2O_2 reduction as compared to that of pure graphene [184]. This phenomenon is attributed to the presence of pyridinic-N and graphitic-N sites, which assist H_2O_2 reduction by weakening the o-o bond [218]. Additionally, it is expected that graphitic carbon structures with edge planes would demonstrate higher electrocatalytic activity as compared to amorphous carbons. In the previous characterizations, we demonstrated that our mechanically treated CNFs is inherently rich in graphitic edge planes, and possess high concentrations of pyridinic and graphitic nitrogen atoms. Thus, we anticipate that the synthesized carbons exhibit high propensity for H_2O_2 sensing owing to enhanced electrocatalytic reduction of hydrogen peroxide.

Electrochemical Impedance Spectroscopy (EIS) was performed on the carbon electrodes in a blank solution of 1×PBS (pH 7.4) to determine the electrochemically active surface areas. The double layer capacitance (C_{dl}) was determined from fitting the equivalent circuit model to the Nyquist plots [27]. The active surface area (A_{act}) of the electrode was calculated using Equation (1) [31]:

$$A_{act} = \frac{I_c}{C_{dl} v} \tag{6.2}$$

Here, C_{dl} is the double-layer specific capacitance (μF/cm^2) and the scan rate is given as v (V/s). I_c is the double layer charging current, acquired from cyclic voltammetry. The determined active surface areas were used to normalize the current responses for all of the electrochemical tests.

Cyclic Voltammetry allows us to investigate the aptitude of mechanically treated CNFs for H_2O_2 reduction. In Figure 6.6, there are two sets of representative Cyclic Voltammograms (CV) which were run at 50 mV/s in 1×PBS (pH 7.4) with 2.5 mM of H_2O_2. All of the voltages are compared against Ag/AgCl. Figure 6.6 (a) shows a comparison of the CVs of mechanically treated CNF in 1X PBS with and without the presence of 2.5 mM of H_2O_2. With the addition of the H_2O_2, there is a clear increase in the current response, exhibiting a 300 μA increase at -0.5 V vs. Ag/AgCl. Furthermore, the treated CNFs exhibit an onset potential of -0.1 V vs. Ag/AgCl, comparable to other nitrogen-doped graphene based sensors [25]. It is worth noting that there is a peak seen in plain 1X PBS of mechanically treated CNF, which could be a result of residual amounts of oxygen being reduced. This response will be further investigated in future works.

The CVs of mechanically treated CNF is compared with that of the electrodes made from

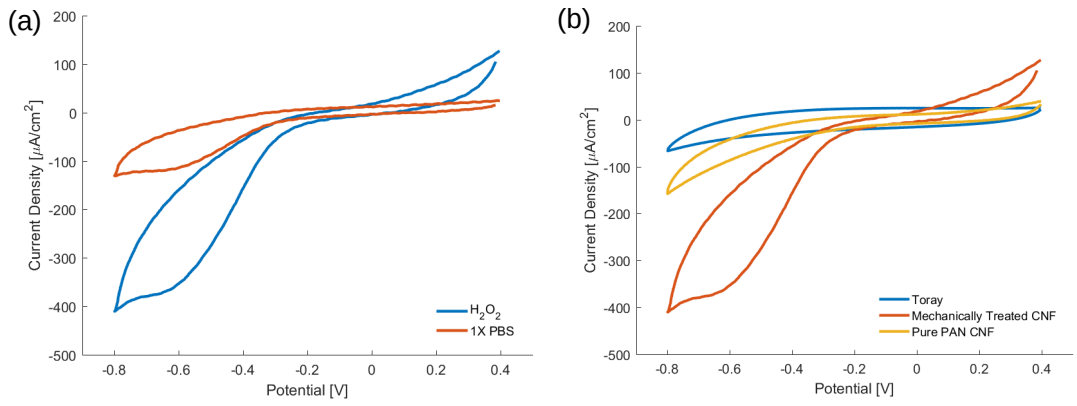

Figure 6.6: Cyclic voltammograms at 50 mV/s of (a) Mechanically treated CNF run in blank 1X PBS and in the presence of 1X PBS in the presence of 2.5 mM H_2O_2; (b). Toray, Mechanically Treated CNF, and pure PAN CNF electrodes in 1X PBS in the presence of 2.5 mM H_2O_2.

Toray (a type of commercially available graphitic fiber), and untreated pure PAN based CNF (Figure 6.6 (b). Toray exhibited no noticeable increase in current response after the addition of hydrogen peroxide, indicating little to no electrocatalysis of hydrogen peroxide reduction. Between pure PAN CNFs and treated PAN CNFs electrodes, treated PAN CNF electrodes demonstrated much larger current response with the addition of hydrogen peroxide.

The reported electrochemical results echo previous studies on NRGC electrocatalysis of hydrogen peroxide. As seen from the XPS data, pure PAN CNF contains small amounts of pyridinic-N and graphitic-N, which contributes to its reduction of hydrogen peroxide. Toray, on the other hand contains no nitrogen groups due to the high temperatures used for its synthesis and therefore has no reduction of hydrogen peroxide. Between treated and untreated CNFs, the much larger current response to hydrogen peroxide could be largely attributed to the higher graphitization seen in the treated CNFs, which is known to contribute to enhance electron transfer efficiencies.

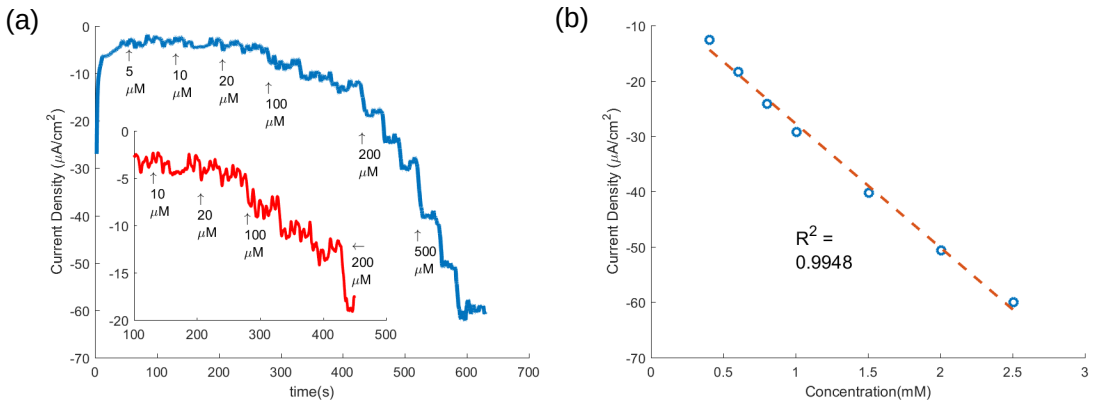

Figure 6.7: (a) Chronoamperometry of the Mechanically Treated CNF electrode running at -0.5V. Each addition concentration is indicated on the graph and was repeated three times after the initial indication prior to the next concentration addition. The inset is a zoomed in portion of the main graph; (b) Concentration vs Current Density data from the chronoamperometry fitted with linear regression trend line.

Chronoamperometry (CA) allows us to determine the sensitivity and limit of detection (LOD) of mechanically treated CNF as H_2O_2 sensor as seen by the representative CA graph in Fig. 6.7 (a). The CA were performed at -0.5 V vs. Ag/AgCl, the typical potential at which the current density peaks for the treated PAN electrodes. During the CA, the current was allowed to stabilize before each subsequent additions of hydrogen peroxide and the concentration versus the current density was then extracted from the CA and plotted in Fig. 6.7 (b).

From this Fig 6.7 (b), the sensitivity was calculated by the linear regression equation:

$$I = -2.54C - 0.604 \tag{6.3}$$

where C is the concentration in mM and I is the current density in μA cm^{-2}. Here, the

slope, and thus sensitivity, is 2.54 μA cm^{-2} mM^{-1} with a correlation coefficient (R2) of 0.9948. The LOD was then calculated by Equation (3), where a signal to noise ratio of 3 (S/N = 3) was used [133].

$$LOD = \frac{3\sigma}{S} \tag{6.4}$$

The standard deviation, σ, was taken from the stable signal of a blank solution and S is the linear regression equation's slope. The LOD was calculated to be 0.609 μM. An average response time of 4.6 s was observed after each addition.

In addition, CA was used to investigate the selectivity of the hydrogen peroxide reduction in the presence of other analytes, namely, Ascorbic Acid (AA), Uric Acid (UA), and Glucose (Glu). Figure 6.8 demonstrates the representative graph of CA with the resulting current responses after additions of 1 mM H_2O_2, 0.15 mM AA, 1 mM Glu, 0.5 mM UA, and a second 1 mM H_2O_2 at the indicated times. The results indicate that at the working potential of -0.5 V there was little to no response from any of the tested interfering agents, while there was still a noticeable response from the addition of H_2O_2. This signifies the high selectivity of the treated PAN electrodes to hydrogen peroxide reduction.

A number of works have reported application of different forms of carbon allotropes as a basis for H_2O_2 sensing with platforms such as nitrogen doped carbon nanotubes [226], graphene platinum nanocomposites [223], and nitrogen-doped graphene nanoribbons [188]. Such studies have resulted in sensitivities ranging between 0.967-154.78 μA mM^{-1}, and LODs of 0.15 to 90 μM [188, 156]. In comparison, the mechanically treated CNF sensors produce a sensitivity of 2.87 μA mM^{-1} when multiplied by active surface area. The acquired sensitivity suggests that, in spite of their facile synthesis route, the electrocatalytic performance of mechanically treated CNF sensors is comparable to that of the graphene-based sensors with more complex synthesis routes. Furthermore, the mechanically treated CNF demonstrated

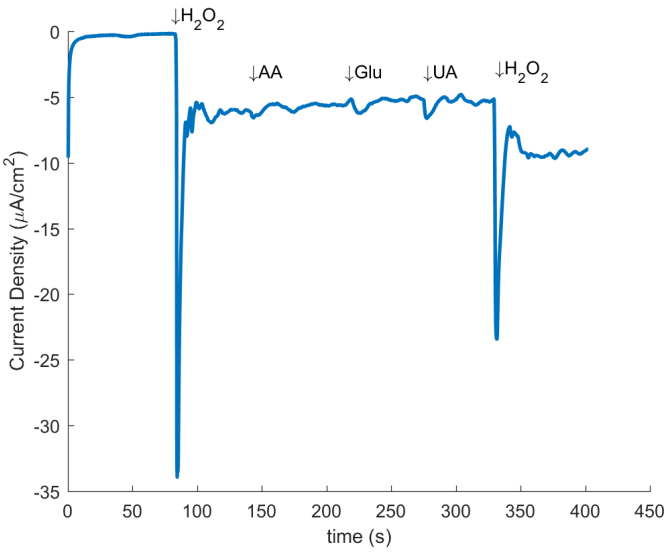

Figure 6.8: Amperometric response of the Mechanically Treated CNF at a potential of -0.5 V vs. Ag/AgCl with addition of interfering agents (1 mM H2O2, 0.15 mM AA, 1 mM Glu, 0.5 mM UA, and 1 mM H_2O_2).

high selectivity towards H_2O_2 in the presence of the common interfering analytes: Glu, AA and UA. It is important to note that the H_2O_2 sensors were developed from as-pyrolyzed CNFs without additional processing. Refinement of the presented synthesis method will potentially yield additional enhancement in both the carbon graphitization degree and the quantity of nitrogen groups to further reduce the LOD, and augment the sensitivity of the electrodes.

Nitrogen-rich graphitic carbons (NRGC) are emerging as an attractive platform for sensing devices. In particular, the presence of graphitic and pyridinic nitrogen in NRGC can enhance the catalytic behavior as it increases electron density of the graphitic basal planes. Accordingly, NRGCs have shown the capability of reducing substrates, such as H_2O_2, and have shown promise as potential alternatives to expensive metal-based catalysts such as gold. However, current methodologies for their synthesis such as nitrogen plasma bombardment, could damage the surface and morphology of the carbon structure. Here, we demonstrate

an alternative synthesis method with which pyrolyzed graphitic substrates possessing N-C bonds can be produced in a single, facile pyrolysis step. Through the application of electrospinning technique, polymer fibers mats consisting of polyacrylonitrile (PAN) infused with carbon nanotubes (CNT) are produced and mechanically treated prior to their pyrolysis. The resulting pyrolytic carbon microstructure possesses a considerable increase in graphitization as demonstrated by its characterization using Raman spectroscopy, Transmission Electron Microscopy (TEM), and X-ray photoelectron spectroscopy (XPS). Furthermore, XPS analysis of the chemical constituents of the resulting carbon shows a high percentage of pyridinic-N and graphitic-N, which would enhance the reduction of hydrogen peroxide. Consistently, the mechanically treated CNFs showed a significant increase in the current response to hydrogen peroxide compared to untreated fiber mats as well as PAN based Toray. The treated carbon nanofiber mats were then characterized for their hydrogen peroxide sensing capability and demonstrated a sensitivity of 2.24 μA mM^{-1} and an LOD of 0.609 μM. The reported results suggest that, despite their facile fabrication, the hydrogen peroxide sensors developed from mechanically treated CNFs compare favorably to sophisticated nitrogen-doped graphene sensors. Thus, this report points to a cost-effective and scalable strategy for synthesizing nitrogen-rich graphitic carbons for hydrogen peroxide sensing.

6.2 Chemically Induced Graphitization

Graphene, a material made of a single layer of sp^2 hybridized carbon atoms, has been at the center of the carbon research in the last decade. Its synthesis by Andre Geim and Konstantin Novoselov in 2004 using mechanical exfoliation was a turning point in the history of carbon research. From then onwards, research in various fields, including electronics, electrochemistry, optics, themoscience, etc saw a renaissance owing to graphene's high specific surface area, Youngs modulus, thermal conductivity, transparency, and chemical stability.

The original fabrication method was a top-down method where the single atom layer is made through mechanical exfoliation of graphite. Other exfoliation methods including liquid phase exfoliation and arc discharge. Alternatively, bottom-up technique such as chemical vapor deposition and epitaxial growth by using gaseous carbon containing sources were also developed to synthesis graphene. These chemical methods have seen an increased popularity due to its ability to directly synthesis the graphene on a surface. Moreover, the study by Li et. al. (Electrochemistry of individual monolayer graphene sheets) showed that the I_{2d}/I_g ratio of the CVD grown graphene is higher than the one formed from mechanical exfoliation, pointing towards a superior graphene. In CVD method, hydrocarbon gases are used as the carbon sources to synthesis graphene. Either copper or nickel initiates the catalytic conversion of the carbon into single or multi-layer graphene.

Graphitized carbon has become a preferred material for numerous applications because of its superior physicochemical properties, such as mechanical strength [229, 47], electrochemical activity [77], and exceptional thermal and electrical conductivities [182]. More specifically, carbon-based micro/nanopatterns are important for developing electrochemical sensors, transparent conductors, flexible electronics, photonic crystals and supercapacitors [50, 96, 239, 100]. Techniques including patterning photoresist followed by pyrolysis (C-MEMS and C-NEMS), ozone assisted etching and self assembly are used to fabricate patterned carbon structures [219, 239]. However, one of the most common types of carbon patterning where pyrolysis of a polymer carbon precursor is used (i.e. C-MEMS and C-NEMS), typically results in non-graphitizable carbon [208]. Despite its innate non-graphitic properties, a recent study has revealed that the glassy carbon derived from some of the carbon precursors has the ability to transform into "glassy graphene" using the material itself as a template [237]. chemical vapor deposition (CVD) of carbon on a patterned nickel template remains one of the most popular ways to fabricate patterned graphitized structures because of the better understanding of the underlying chemistry of the growth process [100, 170, 212]. However, this patterning technique has not reached its fullest potential due

to the lack of a scalable and affordable micro/nanopatterning technique to achieve patterned nickel structures.

Apart from their potential use as a carbon source to synthesize patterned graphitized carbon structures, carbon patterns are involved in a myriad of applications, including microneedles, stem cell scaffolds, and gas sensing platforms [186]. Patterned precursor polymers shrink isometrically to the final carbon structures after undergoing pyrolysis. Taking advantage of this isometric transformation, carbon structures of various shapes are made by patterning photopolymers using any type of lithography followed by pyrolysis. Other methods including micro-transfer molding and micro/nano writing have been reported for patterning polymer precursors for making carbon structures. However, among the various explored shapes, producing three dimensional structures including suspended structures remains a challenging task. Far field electrospinning-based suspended wire deposition onto a patterned surface is reported earlier [185]. However, the morphology of the deposited wires is restricted by the design of the collector. Recent studies have pursued the rational creation of complex multi-dimensional carbon shapes in order to further expand the applications of structurally designed carbon-based materials. Structures made using two-photon lithography is converted to carbon through pyrolysis to obtain carbon structures having sub-micron dimensions. Various other works on photolithography-based fabrication managed to make controlled patterns of wires with submicron dimensions [105, 136]. However, a technique for controlled high throughput fabrication of carbon wires in nanometer regime (<100 nm) with intended morphology is yet to be developed and is required to exploit the full potential of the carbon nanostructures.

6.2.1 Materials and Methods

In order to increase the degree of graphitization of the wires, a nickel catalyst was relied on. Ni was uniformly electrodeposited onto the suspended PAN derived carbon fibers using an effective current density of 0.3 mA/cm^2 for 5 min, with a three-electrode setup in an aqueous solution of 1M $NiSO_4$ + 0.2M $NiCl_2$ + 0.6M H_3BO_3 (Fig. 5.1(c)). A nickel plate and the suspended carbon fiber sample served as the counter and working electrode, respectively, and were maintained at a separation distance of $\sim$ 2 cm while the Ag/AgCl served as a reference electrode. Clipping the electrode onto the carbon channel allowed the current to conduct through all the connected nanowires in parallel. The nickel-coated nanowires were then gently rinsed in DI water and dried on a hot plate at 70°C. The nickel-coated nanowires were then loaded into a 1 in Lindberg Blue M quartz tube furnace and evacuated to a pressure of approximately 10^{-2} torr in a reducing environment of 100 SCCM Ar/H_2 (5%). The furnace was purged under vacuum/gas for 1 hour at ambient temperature and, ramped to 1000°C at a rate of 30°C/min and held there for 1 hour. After 1 hour, 0.8 SCCM of CH_4 was introduced for a growth period of 2 min. The samples were quickly cooled by opening the furnace clamshell and exposing the tube to ambient temperature whilst under reducing environment to obtain graphitized carbon patterns

The thickness of the deposited nickel was controlled by the duration of the deposition (Fig. A.26). Nickel films with thickness range varying from 70 nm to 310 nm were made in the current study for evaluating the effect of thickness in the subsequent graphitization step. The degree of graphitization of the resulting deposition was evaluated using Raman spectroscopy. It has been observed that the samples with thickness more than $\approx$100 nm showed considerably better degree of graphitization in comparison to the graphite formed on thinner nickel films.

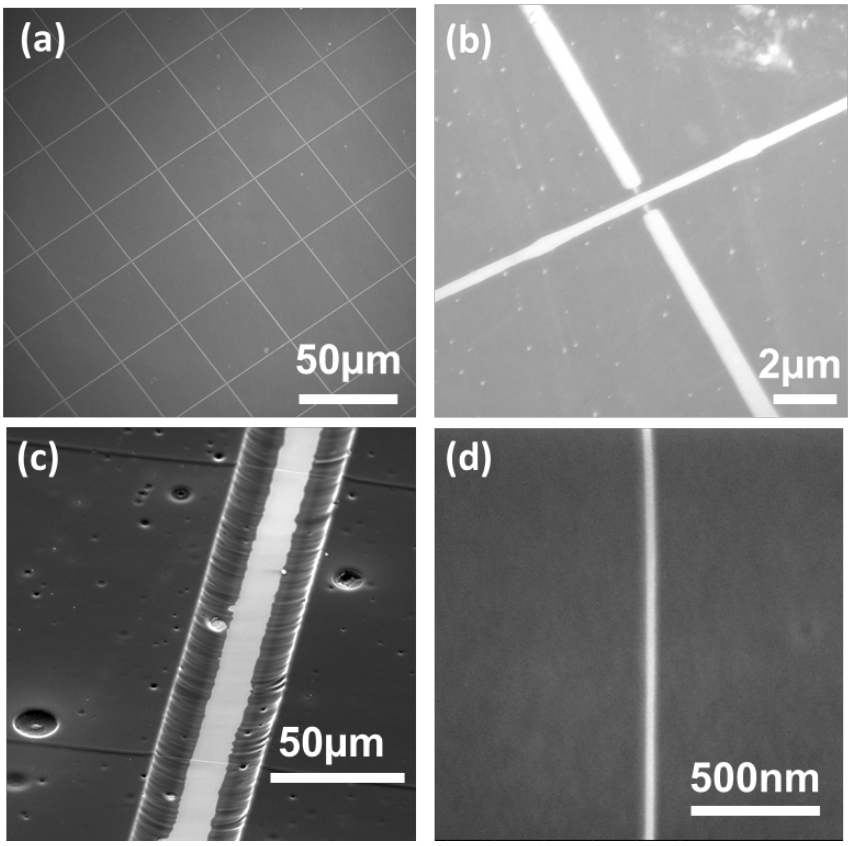

Figure 6.9: (a) Pyrolyzed PAN wire patterns on a flat substrate. (b) Anisotropic shrinkage at the wire intersection. (c) Carbon wire bridges formed on top of a channel structure. (d) Wire of diameter less than 40 nm.

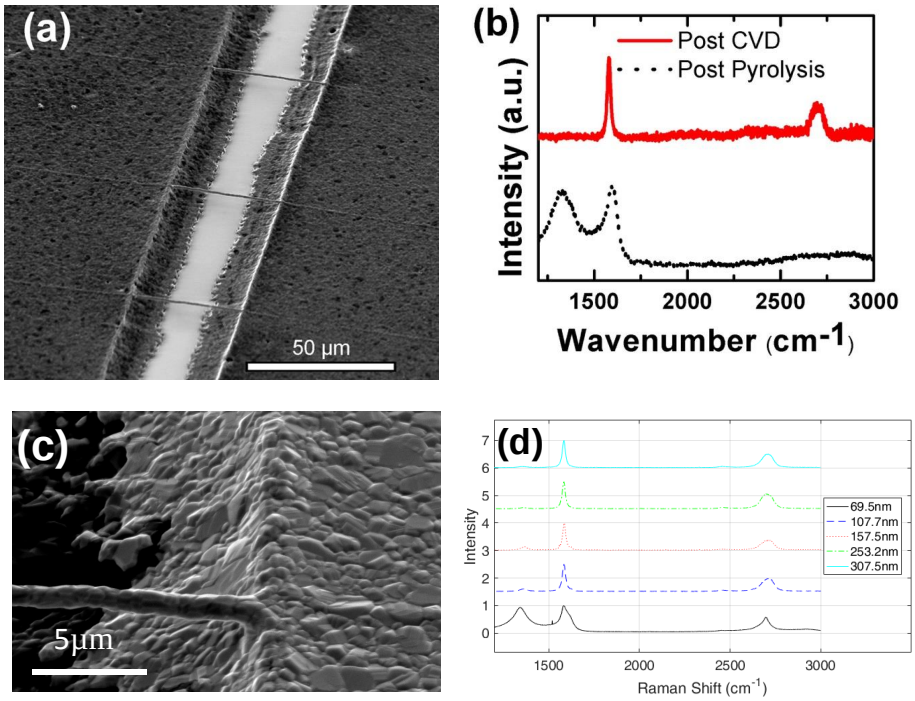

Figure 6.10: (a) SEM image of suspended Ni-coated pyrolyzed PAN nanowires after CVD at 1000°C. (b) Raman spectrum of suspended PAN nanowire after pyrolysis (black dotted line) and of suspended Ni-coated pyrolyzed PAN nanowire after CVD at 1000°C (Red line) (c) SEM image showing the microstructure of the electrodeposited nickel (thickness = 307.5±5.9 nm). (d) Raman spectra of graphitic layers formed on nickel layers of different thicknesses. The thicker nickel films showed a higher level of graphitization as indicated by the improved I_D (1350 cm^{-1})-to-I_G (1550 cm^{-1}) ratio.

6.2.2 Characterization

Raman spectra of the nanowires after pyrolysis and after CVD are shown in Fig. 6.10. The spectra indicate that CVD at 1,050°C for 2 min is sufficient to induce highly graphitized carbon with a ratio of I_{2D} to I_G of ~ 0.4. Here, the symmetric shape of I_{2D} does not indicate the presence of graphite, which is typically identified with a "shoulder". As the I_{2D}/I_G ratio is low, it is not possible to determine the number of graphene layers, but the Raman spectrum here suggests a material more similar to multilayer graphene than graphite.

6.2.3 Discussion

Nickel and copper are the two most widely used catalytic materials for the synthesis of graphene/graphite using CVD. Nickel forms graphite through a precipitation process of 'soaked-carbon' due to its high carbon solubility, whereas copper forms graphitic carbon (majorly single-layer graphene) through adsorption process. The carbon solubility of nickel increases with temperature. The high-temperature step is used to "soak" the nickel with enough carbon atoms to form interconnected graphitic layers, which can inherit the shape of the original nickel structure, after cool-down. The cool-down step brings simultaneous segregation and precipitation, where the carbon atoms form coherent films. The electrodeposition of nickel was employed here for the goal of developing a low-cost and high-throughput fabrication method for graphitized carbon patterns. The growth of the graphitic film is affected by the microstructure of the nickel film. The surface of the electrodeposited nickel optically appears smooth and mirror-like on the contact pads. Closer examination using SEM reveals roughness attributed by the deposited nickel nanocrystals (Fig. 6.10 (c)). The heating during the graphitization process results in the modification of the nickel surface to predominantly Ni$<$ 111 $>$, the preferred orientation for the graphite growth [3], facilitating graphitization on the deposited film. The thicknesses of the nickel films should also be controlled to produce an appropriate amount of diffused carbon, which leads to the formation of graphitic carbon wires. Experiments were performed to study the electrodeposition process and the effect of the electrodeposited nickel film thickness on the graphitization. The thickness of the deposited nickel was controlled by the duration of the deposition (Fig. A.26). Nickel films with thickness ranging from 70 nm to 310 nm were made in the current study to investigate the effect of thickness in the subsequent graphitization step. The degree of graphitization of the resulting deposition was evaluated using Raman spectroscopy. It has been observed that the samples with thickness more than $\sim$ 100 nm showed considerably better degree of graphitization in comparison to the graphite formed on thinner nickel films (Fig. 6.10 (d)).

Chapter 7

Conclusions

7.1 Origami Fabrication

Two origami-based manufacturing methods were presented in this study, a *capillary-assisted* origami fabrication method and a diffusion-based *self-folding* method. The capillary-assisted folding exploited the heightened effect of surface forces at small length scales to achieve folding, whereas the self-folding is realized by engineering a heat-triggered strain gradient across the thickness of a photopolymer at the fold locations. In capillary-based origami, folds and faces with different localized stiffness can be created using a single-layer photopolymer and by modulating the energy applied in different UV exposure steps. The employed actuation mechanism is based on a combination capillary forces and controlled thermal softening/stiffening. The process allows for the creation of origami structures that are permanently locked in their target polyhedral shape. Since the procedure is based on photolithography, it is a batch process that is scalable in terms of size and number of the simultaneously fabricated structures. Arbitrarily-shaped hole cut-outs at the faces can also be introduced in the photolithography process. Furthermore, the polymer polyhedra can be converted to carbon

through pyrolysis. These carbon polyhedra open a plethora of routes to make submillimeter structures with different material and surface properties.

The second folding method, where no droplets were involved, was enabled through the fabrication, characterization, and design of self-foldable photopolymer films that were *programmed* to morph into a target polyhedral shape driven by thermal stimulus. Double-exposure photolithography was used to create the planar films with the required outline and fold pattern, where stiff face regions of high crosslinking density and compliant fold regions of low crosslinking density were synthesized. The thermal stimulus was applied by submerging the planar films into a heated fluid and did not require localized application of heat, making the method favorable for manufacturing at small scales. Furthermore, the photolithography process and thermally driven self-folding of the films can be performed on multiple samples simultaneously, making the manufacturing method attractive for batch production. The novelty of this work is summarized by the following experimental and computational contributions:

- A double-exposure photolithography process that creates patterned films with localized folds of lower stiffness and faces of higher stiffness was devised. The non-homogeneous concentration of developer solution exhibited in the folds during the development step was exploited to obtain self-folding at these regions when they are heated and the absorbed developer evaporates. The relation between the size dimensions of the folds and their achieved fold angle was experimentally characterized.

- An end-to-end origami-based manufacturing method was created by integrating the experimental characterization results and an origami design method. Specifically, the *unfolding polyhedra method* for origami with smooth folds (such as those exhibited by the fabricated films) was implemented to enable the design of the shape and fold pattern of the planar films that allow them to accurately self-fold into their target polyhedral form.

Only a single layer of carbon-rich photopolymer was used in both cases, making the manufacturing processes very practical. Moreover, using only a single photopolymer rich in carbon also enabled the conversion of the polymer shapes to the corresponding three-dimensional carbon shapes. Potential applications of the manufacturing method include packaging of micro-systems, fabrication of stages for MEMS and other microsystems, and entrapment of particles of millimeter and sub-millimeter sizes. Suggested future work includes the exploration of experimental approaches that enable bi-directional folding, which will expand the spectrum of target shapes that can be fabricated using this manufacturing method. Additionally, different photopolymers should be investigated with the aim of finding candidates that can be self-folded at temperatures closer to body temperature, which will make the present manufacturing method suitable for biomedical applications such as drug encapsulation and delivery.

7.2 Patterned Carbon Nanowires

We demonstrated a high-throughput and scalable EMS technique with a rotating collector which provides simplified and improved control over the nanowire straightness, diameter, and inter-fiber spacing. A simplified model that accounts for various electrospinning parameters was employed to predict the spacing of nanowires and to control their diameter. The polymer wire patterns obtained using the technique was successfully converted into pyrolytic carbon structures. The new patterning process is capable of producing carbon nanowires of diameter as small as 37.15 ± 1.5 nm and inter-fiber spacing of $7.9\pm$ 2.3 μm with a throughput that outperforms other existing nanopatterning techniques. These dimensions may be further improved by optimizing fabrication parameters based on the above-mentioned predictive models. The proposed technique is also capable of producing suspended wires at a writing speed as high as 1 m/s. The capability to form bridges between structures and the ability to

direct them to desired locations using pre-patterned structures further broadens the potential use of this high-throughput wire deposition method.

7.3 Microstructure Designing

Using a stress-induced process, we demonstrated how realignment of PAN molecular chains produces a uniformly graphitized carbon. The resulting carbon exhibit an oriented but fragmented lattice structure, as visualized by HRTEM imaging. Further material characterization with XPS indicates that the stress activated pyrolytic carbon is innately rich in nitrogen heteroatoms. The presence of these chemical and structural disorders in the SAPC prompted us to perform a comprehensive electrochemical study with surface insensitive (potassium hexachloroiridate), and surface sensitive (potassium ferricyanide) electrochemical kinetics show that SAPC's heterogenous electron transfer rate is 5 to 14 times higher than that of standard pyrolytic PAN carbons and 2 to 10 times higher than polished commercial glassy carbon in both the surface insensitive and sensitive redox probes. The results underline the correlation between the enhanced sensitivity of SAPC towards surface sensitive species and the numerous graphitic edges and nitrogen heteroatoms present in the carbon lattice. The presence of these "defects" is associated with the quantity of the electroactive sites on the carbon electrodes. It is important to note that the mere presence of heterogeneous atoms and edge planes in carbon structure does not constitute enhanced electrochemical behavior, since their effect could be countered by a low-degree of graphitization in the resulting carbon. The results reported here suggest that a key concept in carbon's electrochemistry is the right amount of select "disorders" within a generally "ordered" framework. The former increases the localized DOS around the E° of the redox systems of interest, facilitating heterogeneous electron transfer, and the latter enhances electron transport within the carbon electrode. The introduced stress-activation route harnesses the versatility of carbon by producing a

graphitic framework, which features heteroatoms and structural disorders that are tuned for electrochemical performance. The mechanically treated CNFs showed a significant increase in the current response to hydrogen peroxide compared to untreated fiber mats as well as PAN based Toray. The treated carbon nanofiber mats were then characterized for their hydrogen peroxide sensing capability and demonstrated a sensitivity of 24.5 μA mM^{-1} and an LOD of 69.12 μM. The reported results suggest that, despite their facile fabrication, the hydrogen peroxide sensors developed from mechanically treated CNFs compare favorably to sophisticated nitrogen-doped graphene sensors.

The work on producing chemically induced graphitization on nanowires showed a high throughput fabrication technique for PAN-derived pyrolytic carbon nanowires and graphitic nanowires, providing a major contribution to the field of carbon MEMS. The control over the morphology of the wires, majorly diameter, was studied in detail by evaluating various parameters of the nearfield electrospinning as well as the pyrolysis. Though the controlled writing of various polymers was studied by various groups before, a study based on the controlled writing of PAN using nearfield electrospinning and its conversion into carbon nanowires are seldom studied. Specifically, pyrolytic carbon nanowires with sub 50 nm are rarely reported. We also demonstrated a cost-effective way to convert these PAN-derived carbon to graphitic carbon by exploiting the conductive nature of the carbon structures, widening the applications even further. Experiments were performed to study the electrodeposition process and the effect of the electrodeposited nickel film thickness on the graphitization. The thickness of the deposited nickel was controlled by the duration of the deposition. Nickel films with thickness ranging from 70 nm to 310 nm were made in the current study to investigate the effect of thickness in the subsequent graphitization step. The degree of graphitization of the resulting deposition was evaluated using Raman spectroscopy. It has been observed that the samples with thickness more than $\sim$100 nm showed considerably better degree of graphitization in comparison to the graphite formed on thinner nickel films.

Bibliography

[1] A. Agrawal, T. Yun, S. L. Pesek, W. G. Chapman, and R. Verduzco. Shape-responsive liquid crystal elastomer bilayers. *Soft Matter*, 10(9):1411–1415, 2014.

[2] S. Ahmed, Z. Ounaies, and M. Frecker. Investigating the performance and properties of dielectric elastomer actuators as a potential means to actuate origami structures. *Smart Materials and Structures*, 23(9):094003, 2014.

[3] B. An, S. Miyashita, A. Ong, M. T. Tolley, M. L. Demaine, E. D. Demaine, R. J. Wood, and D. Rus. An end-to-end approach to self-folding origami structures. *IEEE Transactions on Robotics*, 34(6):1409–1424, 2018.

[4] N. An, M. Li, and J. Zhou. Predicting origami-inspired programmable self-folding of hydrogel trilayers. *Smart Materials and Structures*, 25(11):11LT02, 2016.

[5] C. M. Andres, J. Zhu, T. Shyu, C. Flynn, and N. A. Kotov. Shape-morphing nanocomposite origami. *Langmuir*, 30(19):5378–5385, 2014.

[6] A. Azam, K. E. Laflin, M. Jamal, R. Fernandes, and D. H. Gracias. Self-folding micropatterned polymeric containers. *Biomed Microdevices*, 13:51–58, 2011.

[7] D. J. Balkcom and M. T. Mason. Robotic origami folding. *The International Journal of Robotics Research*, 27(5):613–627, 2008.

[8] D. G. Baranov, Y. Xiao, I. A. Nechepurenko, A. Krasnok, A. Alù, and M. A. Kats. Nanophotonic engineering of far-field thermal emitters. *Nature Materials*, 2019.

[9] L. Baraton, Z. He, C. S. Lee, J.-L. Maurice, C. S. Cojocaru, A.-F. Gourgues-Lorenzon, Y. H. Lee, and D. Pribat. Synthesis of few-layered graphene by ion implantation of carbon in nickel thin films. *Nanotechnology*, 22(8):085601, 2011.

[10] N. Bassik, B. T. Abebe, K. E. Laflin, and D. H. Gracias. Photolithographically patterned smart hydrogel based bilayer actuators. *Polymer*, 51(26):6093–6098, 2010.

[11] N. Bassik, G. M. Stern, and D. H. Gracias. Microassembly based on hands free origami with bidirectional curvature. *Applied Physics Letters*, 95(9):1–4, 2009.

[12] N. Bassik, G. M. Stern, and D. H. Gracias. Microassembly based on hands free origami with bidirectional curvature. *Applied Physics Letters*, 95(9):091901, 2009.

[13] J. Bauer, A. Schroer, R. Schwaiger, and O. Kraft. Approaching theoretical strength in glassy carbon nanolattices. *Nature materials*, 15(4):438–443, 2016.

[14] M. Behl, K. Kratz, J. Zotzmann, U. Nöchel, and A. Lendlein. Reversible bidirectional shape-memory polymers. *Advanced materials*, 25(32):4466–4469, 2013.

[15] M. Behl, M. Y. Razzaq, and A. Lendlein. Multifunctional shape-memory polymers. *Advanced materials*, 22(31):3388–3410, 2010.

[16] J. Bico, B. Roman, L. Moulin, and A. Boudaoud. Adhesion: elastocapillary coalescence in wet hair. *Nature*, 432(7018):690, 2004.

[17] M. Boncheva, D. a. Bruzewicz, and G. M. Whitesides. Millimeter-scale self-assembly and its applications. *Pure and Applied Chemistry*, 75(5):621–630, 2003.

[18] M. Boyvat, J.-S. Koh, and R. J. Wood. Addressable wireless actuation for multijoint folding robots and devices. *Science Robotics*, 2(8), 2017.

[19] D. A. Brownson, D. K. Kampouris, and C. E. Banks. Graphene electrochemistry: fundamental concepts through to prominent applications. *Chemical Society Reviews*, 41(21):6944–6976, 2012.

[20] D. A. Brownson, S. A. Varey, F. Hussain, S. J. Haigh, and C. E. Banks. Electrochemical properties of CVD grown pristine graphene: Monolayer- vs. quasi-graphene. *Nanoscale*, 6(3):1607–1621, 2014.

[21] M. Byun, C. D. Santangelo, and R. C. Hayward. Swelling-driven rolling and anisotropic expansion of striped gel sheets. *Soft Matter*, 9(34):8264–8273, 2013.

[22] G. Canton, L. Kulinsk, M. Technology, and G. Canton. Electro-Mechanical Spinning : A New Manufacturing Technique for MicrolNano-Fabrication of Carbon Fibers. *IEEE International Symposium on Advanced Packaging Materials*, 4(Paper 9):230–239, 2013.

[23] D. Chen, J. Yoon, D. Chandra, A. J. Crosby, and R. C. Hayward. Stimuli-responsive buckling mechanics of polymer films. *Journal of Polymer Science Part B: Polymer Physics*, 52(22):1441–1461, 2014.

[24] Q. Chen and G. M. Swain. Structural characterization, electrochemical reactivity, and response stability of hydrogenated glassy carbon electrodes. *Langmuir*, 14(24):7017–7026, 1998.

[25] W. Chen, S. Cai, Q.-Q. Ren, W. Wen, and Y.-D. Zhao. Recent advances in electrochemical sensing for hydrogen peroxide: a review. *Analyst*, 137(1):49–58, 2012.

[26] X. Chen, J. Xia, J. Peng, W. Li, and S. Xie. Carbon-nanotube metal-matrix composites prepared by electroless plating. *Composites Science and Technology*, 60(2):301–306, 2000.

[27] L. Cheng, X.-L. Li, H.-J. Liu, H.-M. Xiong, P.-W. Zhang, and Y.-Y. Xia. Carbon-coated li4ti5o12 as a high rate electrode material for li-ion intercalation. *Journal of the Electrochemical Society*, 154(7):A692, 2007.

[28] D. Davis, R. Mailen, J. Genzer, and M. D. Dickey. Self-folding of polymer sheets using microwaves and graphene ink. *RSC Advances*, 5(108):89254–89261, 2015.

[29] C. Dawson, J. F. Vincent, and A.-M. Rocca. How pine cones open. *Nature*, 390(6661):668–668, 1997.

[30] L. T. De Haan, C. Sánchez-Somolinos, C. M. W. Bastiaansen, A. P. H. J. Schenning, and D. J. Broer. Engineering of complex order and the macroscopic deformation of liquid crystal polymer networks. *Angewandte Chemie - International Edition*, 51(50):12469–12472, 2012.

[31] M. De Leo, A. Kuhn, and P. Ugo. 3d-ensembles of gold nanowires: preparation, characterization and electroanalytical peculiarities. *Electroanalysis: An International Journal Devoted to Fundamental and Practical Aspects of Electroanalysis*, 19(2-3):227–236, 2007.

[32] E. D. Demaine. Folding and unfolding linkages, paper, and polyhedra. In *Japanese Conference on Discrete and Computational Geometry*, pages 113–124. Springer, 2000.

[33] E. D. Demaine and T. Tachi. Origamizer: A practical algorithm for folding any polyhedron. In *33rd International Symposium on Computational Geometry (SoCG 2017)*. Schloss Dagstuhl-Leibniz-Zentrum fuer Informatik, 2017.

[34] D. Deng and Y. Chen. Origami-based self-folding structure design and fabrication using projection based stereolithography. *Journal of Mechanical Design*, 137(2), 2015.

[35] T. Deng, C. Yoon, Q. Jin, M. Li, Z. Liu, and D. H. Gracias. Self-folding graphene-polymer bilayers. *Applied Physics Letters*, 106(20), 2015.

[36] M. L. Dunn, Y. Zhang, and V. M. Bright. Deformation and structural stability of layered plate microstructures subjected to thermal loading. *Journal of Microelectromechanical Systems*, 11(4):372–384, 2002.

[37] T. A. Evans, R. J. Lang, S. P. Magleby, and L. L. Howell. Rigidly foldable origami gadgets and tessellations. *Royal Society Open Science*, 2(9):150067, 2015.

[38] S. N. Faisal, E. Haque, N. Noorbehesht, W. Zhang, A. T. Harris, T. L. Church, and A. I. Minett. Pyridinic and graphitic nitrogen-rich graphene for high-performance supercapacitors and metal-free bifunctional electrocatalysts for orr and oer. *RSC advances*, 7(29):17950–17958, 2017.

[39] S. Felton, K. Becker, D. Aukes, and R. Wood. Self-folding with shape memory composites at the millimeter scale. *Journal of Micromechanics and Microengineering*, 25(8):085004, 2015.

[40] R. Feng and R. J. Farris. Investigation of thermal and mechanical properties of SU8 negative photoresist coatings. *Journal of Micromechanics and Microengineering*, 13(1):80–88, 2003.

[41] Y. Feng and H. Yuan. Electroless plating of carbon nanotubes with silver. *Journal of Materials Science*, 39(9):3241–3243, 2004.

[42] R. Fernandes and D. H. Gracias. Self-folding polymeric containers for encapsulation and delivery of drugs. *Advanced Drug Delivery Reviews*, 64(14):1579–1589, 2012.

[43] R. Fernandes and D. H. Gracias. Self-folding polymeric containers for encapsulation and delivery of drugs. *Advanced Drug Delivery Reviews*, 64(14):1579–1589, 2012.

[44] A. C. Ferrari. Raman spectroscopy of graphene and graphite: Disorder, electron–phonon coupling, doping and nonadiabatic effects. *Solid state communications*, 143(1-2):47–57, 2007.

[45] A. C. Ferrari, J. C. Meyer, V. Scardaci, C. Casiraghi, M. Lazzeri, F. Mauri, S. Piscanec, D. Jiang, K. S. Novoselov, S. Roth, and A. K. Geim. Raman spectrum of graphene and graphene layers. *Physical Review Letters*, 97(18):1–4, 2006.

[46] J. L. Fierro, J. M. Campos-martin, and G. Blanco-brieva. Hydrogen peroxide synthesis: An outlook beyond the anthraquinone process angewandte. *Angewandte Chemie-International Edition*, 45:6962–6984, 2006.

[47] I. W. Frank, D. M. Tanenbaum, A. M. van der Zande, and P. L. McEuen. Mechanical properties of suspended graphene sheets. *Journal of Vacuum Science & Technology B: Microelectronics and Nanometer Structures*, 25(6):2558, 2007.

[48] H. Fu, K. Nan, W. Bai, W. Huang, K. Bai, L. Lu, C. Zhou, Y. Liu, F. Liu, J. Wang, M. Han, Z. Yan, H. Luan, Y. Zhang, Y. Zhang, J. Zhao, X. Cheng, M. Li, J. W. Lee, Y. Liu, D. Fang, X. Li, Y. Huang, Y. Zhang, and J. A. Rogers. Morphable 3D mesostructures and microelectronic devices by multistable buckling mechanics. *Nature Materials*, 17(3):268–276, 2018.

[49] K. Fuchi, T. H. Ware, P. R. Buskohl, G. W. Reich, R. A. Vaia, T. J. White, and J. J. Joo. Topology optimization for the design of folding liquid crystal elastomer actuators. *Soft Matter*, 11(37):7288–7295, 2015.

[50] N. Fukaya, D. Y. Kim, S. Kishimoto, S. Noda, and Y. Ohno. One-step sub-10 μm patterning of carbon-nanotube thin films for transparent conductor applications. *ACS Nano*, 8(4):3285–3293, 2014.

[51] A. M. Gañán-Calvo. Cone-jet analytical extension of taylor's electrostatic solution and the asymptotic universal scaling laws in electrospraying. *Physical review letters*, 79(2):217, 1997.

[52] A. M. Gañán-Calvo, N. Rebollo-Muñoz, and J. M. Montanero. The minimum or natural rate of flow and droplet size ejected by Taylor cone-jets: Physical symmetries and scaling laws. *New Journal of Physics*, 15, 2013.

[53] X. Gao, S. He, C. Zhang, C. Du, X. Chen, W. Xing, S. Chen, A. Clayborne, and W. Chen. Single crystal sub-nanometer sized cu6 (sr) 6 clusters: Structure, photophysical properties, and electrochemical sensing. *Advanced science*, 3(12):1600126, 2016.

[54] M. R. Garza, E. A. Peraza-Hernandez, and D. J. Hartl. Self-folding origami surfaces of non-zero Gaussian curvature. In *Proceedings of SPIE Smart Structures/NDE, Behavior and Mechanics of Multifunctional Materials XIII*, volume 10968, page 109680R. International Society for Optics and Photonics, 2019.

[55] Q. Ge, C. K. Dunn, H. J. Qi, and M. L. Dunn. Active origami by 4D printing. *Smart Materials and Structures*, 23(9), 2014.

[56] Q. Ge, H. J. Qi, and M. L. Dunn. Active materials by four-dimension printing. *Applied Physics Letters*, 103(13):131901, 2013.

[57] D. Geng, Y. Chen, Y. Chen, Y. Li, R. Li, X. Sun, S. Ye, and S. Knights. High oxygen-reduction activity and durability of nitrogen-doped graphene. *Energy & Environmental Science*, 4(3):760–764, 2011.

[58] D. George, E. A. P. Hernandez, R. C. Lo, and M. Madou. Fabrication of polymer and carbon polyhedra through controlled cross-linking and capillary deformations. *Soft matter*, 15(45):9171–9177, 2019.

[59] D. George, M. J. Madou, and E. A. Peraza Hernandez. Programmable self-foldable films for origami-based manufacturing. *Smart Materials and Structures*, 30(2):025012, 2020.

[60] D. George, E. A. Peraza Hernandez, R. C. Lo, and M. Madou. Fabrication of polymer and carbon polyhedra through controlled cross-linking and capillary deformations. *Soft Matter*, 15(1):9171–9177, 2019.

[61] D. George, A. Rajappan, and A. K. Sen. Elastocapillary powered manipulation of liquid plug in microchannels. *Applied Physics Letters*, 107(May):261601, 2015.

[62] N. R. Geraldi, F. F. Ouali, R. H. Morris, G. McHale, and M. I. Newton. Capillary origami and superhydrophobic membrane surfaces. *Applied Physics Letters*, 102(21), 2013.

[63] M. Ghazinejad, S. Holmberg, O. Pilloni, L. Oropeza-Ramos, and M. Madou. Graphitizing non-graphitizable carbons by stress-induced routes. *Scientific reports*, 7(1):1–10, 2017.

[64] A. Gomes, E. Fernandes, and J. L. Lima. Fluorescence probes used for detection of reactive oxygen species. *Journal of biochemical and biophysical methods*, 65(2-3):45–80, 2005.

[65] L. P. C. Gómez, P. Bollgruen, A. I. Egunov, D. Mager, F. Malloggi, J. G. Korvink, and V. A. Luchnikov. Vapour processed self-rolled poly (dimethylsiloxane) microcapillaries form microfluidic devices with engineered inner surface. *Lab on a Chip*, 13(19):3827–3831, 2013.

[66] K. Gong, F. Du, Z. Xia, M. Durstock, and L. Dai. Nitrogen-doped carbon nanotube arrays with high electrocatalytic activity for oxygen reduction. *science*, 323(5915):760–764, 2009.

[67] D. H. Gracias, V. Kavthekar, J. C. Love, K. E. Paul, and G. M. Whitesides. Fabrication of micrometer-scale, patterned polyhedra by self-assembly. *Advanced Materials*, 14(3):235–238, 2002.

[68] J. Guan, H. He, D. J. Hansford, and L. J. Lee. Self-folding of three-dimensional hydrogel microstructures. *The Journal of Physical Chemistry B*, 109(49):23134–23137, 2005.

[69] X. Guo, Y. Ying, and L. Tong. Photonic nanowires: From subwavelength waveguides to optical sensors. *Accounts of Chemical Research*, 47(2):656–666, 2014.

[70] M. Habibi, N. Ribe, and D. Bonn. Coiling of elastic ropes. *Physical review letters*, 99(15):154302, 2007.

[71] S. Hanaoka, J.-M. Lin, and M. Yamada. Chemiluminescent flow sensor for h2o2 based on the decomposition of h2o2 catalyzed by cobalt (ii)-ethanolamine complex immobilized on resin. *Analytica Chimica Acta*, 426(1):57–64, 2001.

[72] P. Harris. Fullerene-related structure of commercial glassy carbons. *Philosophical Magazine*, 84(29):3159–3167, 2004.

[73] P. J. Harris. Structure of non-graphitising carbons. *International Materials Reviews*, 42(5):206–218, 1997.

[74] J.-H. He, Y. Wu, and W.-W. Zuo. Critical length of straight jet in electrospinning. *Polymer*, 46(26):12637–12640, 2005.

[75] S. He, B. Zhang, M. Liu, and W. Chen. Non-enzymatic hydrogen peroxide electrochemical sensor based on a three-dimensional mno 2 nanosheets/carbon foam composite. *RSC Advances*, 4(90):49315–49323, 2014.

[76] J. Heo, D. Shim, G. T. Teixidor, S. Oh, M. Madou, and H. Shin. Carbon interdigitated array nanoelectrodes for electrochemical applications. *Journal of the Electrochemical Society*, 158(3):J76, 2011.

[77] S. Holmberg, M. Ghazinejad, E. B. Cho, D. George, B. Pollack, A. Perebikovsky, R. Ragan, and M. Madou. Stress-activated pyrolytic carbon nanofibers for electrochemical platforms. *Electrochimica Acta*, 290:639–648, 2018.

[78] D. P. Holmes, M. Roché, T. Sinha, and H. A. Stone. Bending and twisting of soft materials by non-homogenous swelling. *Soft Matter*, 7(11):5188–5193, 2011.

[79] L. Hu, J. W. Choi, Y. Yang, S. Jeong, F. La Mantia, L.-F. Cui, and Y. Cui. Highly conductive paper for energy-storage devices. *Proceedings of the National Academy of Sciences*, 106(51):21490–21494, 2009.

[80] N. Hu, M. Sun, X. Lin, C. Gao, B. Zhang, C. Zheng, H. Xie, and Q. He. Self-Propelled Rolled-Up Polyelectrolyte Multilayer Microrockets. *Advanced Functional Materials*, 28(25):1–9, 2018.

[81] Y. Huang, Y. Duan, Y. Ding, N. Bu, Y. Pan, N. Lu, and Z. Yin. Versatile, kinetically controlled, high precision electrohydrodynamic writing of micro/nanofibers. *Scientific Reports*, 4:1–9, 2014.

[82] L. Ionov. Soft microorigami: self-folding polymer films. *Soft Matter*, 7(15):6786–6791, 2011.

[83] L. Ionov. Biomimetic hydrogel-based actuating systems. *Advanced Functional Materials*, 23(36):4555–4570, 2013.

[84] M. Islam, J. Flach, and R. Martinez-Duarte. Carbon origami: A method to fabricate lightweight carbon cellular materials. *Carbon*, 133:140–149, 2018.

[85] M. Jamal, A. M. Zarafshar, and D. H. Gracias. Differentially photo-crosslinked polymers enable self-assembling microfluidics. *Nature communications*, 2(1):1–6, 2011.

[86] M. Jamal, A. M. Zarafshar, and D. H. Gracias. Differentially photo-crosslinked polymers enable self-assembling microfluidics. *Nature Communications*, 2:527, 2013.

[87] S. Janbaz, R. Hedayati, and A. Zadpoor. Programming the shape-shifting of flat soft matter: from self-rolling/self-twisting materials to self-folding origami. *Materials Horizons*, 3(6):536–547, 2016.

[88] A. Javey, S. Nam, R. S. Friedman, H. Yan, and C. M. Lieber. Layer-by-layer assembly of nanowires for three-dimensional, multifunctional electronics. *Nano Letters*, 7(3):773–777, 2007.

[89] X. Ji, C. E. Banks, A. Crossley, and R. G. Compton. Oxygenated edge plane sites slow the electron transfer of the ferro-/ferricyanide redox couple at graphite electrodes. *ChemPhysChem*, 7(6):1337–1344, 2006.

[90] B.-B. Jiang, X.-W. Wei, F.-H. Wu, K.-L. Wu, L. Chen, G.-Z. Yuan, C. Dong, and Y. Ye. A non-enzymatic hydrogen peroxide sensor based on a glassy carbon electrode modified with cuprous oxide and nitrogen-doped graphene in a nafion matrix. *Microchimica Acta*, 181(11-12):1463–1470, 2014.

[91] H. Jiang, Y. Sun, J. A. Rogers, and Y. Huang. Mechanics of precisely controlled thin film buckling on elastomeric substrate. *Applied Physics Letters*, 90(13):133119, 2007.

[92] H. Jiang, H. Yu, G. Konjevod, and Y. Xu. Origami enabled manufacturing systems and methods, July 11 2017. US Patent 9,706,646.

[93] S. JL, E. AA, M. L, H. RC, H. T, S. CD, and C. I. Using origami design principles to fold reprogrammable mechanical metamaterials. *Science*, 345(6197):647–650, 2014.

[94] J. Ju and W. Chen. In situ growth of surfactant-free gold nanoparticles on nitrogen-doped graphene quantum dots for electrochemical detection of hydrogen peroxide in biological environments. *Analytical chemistry*, 87(3):1903–1910, 2015.

[95] N. C. Judd. Electroless deposition of copper and nickel on carbon fibres. *Composites*, 1(6):345, 1970.

[96] K. Kempa, B. Kimball, J. Rybczynski, Z. P. Huang, P. F. Wu, D. Steeves, M. Sennett, M. Giersig, D. V. Rao, D. L. Carnahan, D. Z. Wang, J. Y. Lao, W. Z. Li, and Z. F. Ren. Photonic crystals based on periodic arrays of aligned carbon nanotubes. *Nano Letters*, 3(1):13–18, 2003.

[97] R. Kempaiah and Z. Nie. From nature to synthetic systems: Shape transformation in soft materials. *Journal of Materials Chemistry B*, 2(17):2357–2368, 2014.

[98] D. Kim, B. Pramanick, A. Salazar, I.-W. Tcho, M. J. Madou, E. S. Jung, Y.-K. Choi, and H. Hwang. 3d carbon electrode based triboelectric nanogenerator. *Advanced Materials Technologies*, 1(8):1600160, 2016.

[99] H.-Y. Kim and L. Mahadevan. Capillary rise between elastic sheets. *Journal of Fluid Mechanics*, 548(-1):141, 2006.

[100] K. S. Kim, Y. Zhao, H. Jang, S. Y. Lee, J. M. Kim, K. S. Kim, J. H. Ahn, P. Kim, J. Y. Choi, and B. H. Hong. Large-scale pattern growth of graphene films for stretchable transparent electrodes. *Nature*, 457(7230):706–710, 2009.

[101] W. Kim, F. Peaudecerf, M. W. Baldwin, and J. W. Bush. The hummingbird's tongue: a self-assembling capillary syphon. *Proceedings of the Royal Society B: Biological Sciences*, 279(1749):4990–4996, 2012.

[102] Y. Kim, H. Yuk, R. Zhao, S. A. Chester, and X. Zhao. Printing ferromagnetic domains for untethered fast-transforming soft materials. *Nature*, 558(7709):274–279, 2018.

[103] K. Kobayashi, S. H. Oh, C. K. Yoon, and D. H. Gracias. Multitemperature Responsive Self-Folding Soft Biomimetic Structures. *Macromolecular Rapid Communications*, 39(4):1–7, 2018.

[104] I. Y. Konotop, I. R. Nasimova, M. V. Tamm, N. G. Rambidi, and A. R. Khokhlov. Novel ph-responsive hydrogels with gradient charge distribution. *Soft Matter*, 6(8):1632–1634, 2010.

[105] M. Kurek, F. K. Larsen, P. E. Larsen, S. Schmid, A. Boisen, and S. S. Keller. Nanomechanical pyrolytic carbon resonators: Novel fabrication method and characterization of mechanical properties. *Sensors (Switzerland)*, 16(7), 2016.

[106] K. Kuribayashi, K. Tsuchiya, Z. You, D. Tomus, M. Umemoto, T. Ito, and M. Sasaki. Self-deployable origami stent grafts as a biomedical application of Ni-rich TiNi shape memory alloy foil. *Materials Science and Engineering: A*, 419(1-2):131–137, 2006.

[107] H. R. Kwag, J.-H. Cho, S.-Y. Park, J. Park, and D. H. Gracias. Self-folding nanostructures with imprint patterned surfaces (SNIPS). *Faraday Discussions*, 191:61–71, 2016.

[108] K. E. Laflin, C. J. Morris, T. Muqeem, and D. H. Gracias. Laser triggered sequential folding of microstructures. *Applied Physics Letters*, 101(13):131901, 2012.

[109] B. Lamprecht, R. Thünauer, M. Ostermann, G. Jakopic, and G. Leising. Organic photodiodes on newspaper. *physica status solidi (a)*, 202(5):R50–R52, 2005.

[110] R. J. Lang. A computational algorithm for origami design. In *Proceedings of the Twelfth Annual Symposium on Computational Geometry*, pages 98–105, 1996.

[111] J. Lang Robert. Origami design secrets: Mathematical methods for an ancient art, sec. ed. *AK Peters*, 2011.

[112] C. Lauff, T. W. Simpson, M. Frecker, Z. Ounaies, S. Ahmed, P. von Lockette, R. Strzelec, R. Sheridan, and J.-M. Lien. Differentiating bending from folding in origami engineering using active materials. In *ASME 2014 international design engineering technical conferences and computers and information in engineering conference*. American Society of Mechanical Engineers Digital Collection, 2014.

[113] D.-Y. Lee, G.-P. Jung, M.-K. Sin, S.-H. Ahn, and K.-J. Cho. Deformable wheel robot based on origami structure. In *2013 IEEE International Conference on Robotics and Automation*, pages 5612–5617. IEEE, 2013.

[114] K. M. Lee, M. L. Smith, H. Koerner, N. Tabiryan, R. A. Vaia, T. J. Bunning, and T. J. White. Photodriven, flexural–torsional oscillation of glassy azobenzene liquid crystal polymer networks. *Advanced Functional Materials*, 21(15):2913–2918, 2011.

[115] A. Legrain, J. W. Berenschot, N. R. Tas, and L. Abelmann. Capillary origami of micro-machined micro-objects: Bi-layer conductive hinges. *Microelectronic Engineering*, 140:60–66, 2015.

[116] A. Lendlein and O. E. Gould. Reprogrammable recovery and actuation behaviour of shape-memory polymers. *Nature Reviews Materials*, 4(2):116–133, 2019.

[117] A. Lendlein, H. Jiang, O. Jünger, and R. Langer. Light-induced shape-memory polymers. *Nature*, 434(7035):879–882, 2005.

[118] T. G. Leong, C. L. Randall, B. R. Benson, N. Bassik, G. M. Stern, and D. H. Gracias. Tetherless thermobiochemically actuated microgrippers. *Proceedings of the National Academy of Sciences of the United States of America*, 106(3):703–708, 2009.

[119] Q. Li, S. Fan, W. Han, C. Sun, and W. Liang. Coating of carbon nanotube with nickel by electroless plating method. *Japanese Journal of Applied Physics-Part 2 Letters*, 36(4):501–503, 1997.

[120] S.-M. Li, S.-Y. Yang, Y.-S. Wang, C.-H. Lien, H.-W. Tien, S.-T. Hsiao, W.-H. Liao, H.-P. Tsai, C.-L. Chang, C.-C. M. Ma, et al. Controllable synthesis of nitrogen-doped graphene and its effect on the simultaneous electrochemical determination of ascorbic acid, dopamine, and uric acid. *Carbon*, 59:418–429, 2013.

[121] Y. Lim, J.-I. Heo, M. Madou, and H. Shin. Monolithic carbon structures including suspended single nanowires and nanomeshes as a sensor platform. *Nanoscale research letters*, 8(1):1–9, 2013.

[122] F. Liu and M. W. Urban. Recent advances and challenges in designing stimuli-responsive polymers. *Progress in polymer science*, 35(1-2):3–23, 2010.

[123] J. L. Liu and X. Q. Feng. On elastocapillarity: A review. *Acta Mechanica Sinica/Lixue Xuebao*, 28(4):928–940, 2012.

[124] M. Liu, S. He, and W. Chen. Co 3 o 4 nanowires supported on 3d n-doped carbon foam as an electrochemical sensing platform for efficient h 2 o 2 detection. *Nanoscale*, 6(20):11769–11776, 2014.

[125] M. Liu, R. Liu, and W. Chen. Graphene wrapped cu2o nanocubes: non-enzymatic electrochemical sensors for the detection of glucose and hydrogen peroxide with enhanced stability. *Biosensors and Bioelectronics*, 45:206–212, 2013.

[126] Y. Liu, J. K. Boyles, J. Genzer, and M. D. Dickey. Self-folding of polymer sheets using local light absorption. *Soft matter*, 8(6):1764–1769, 2012.

[127] Y. Liu, B. Shaw, M. D. Dickey, and J. Genzer. Sequential self-folding of polymer sheets. *Science Advances*, 3(3):1–8, 2017.

[128] Z. Liu, J. Xu, D. Chen, and G. Shen. Flexible electronics based on inorganic nanowires. *Chemical Society Reviews*, 44(1):161–192, 2015.

[129] X. Lu, H. Zhang, G. Fei, B. Yu, X. Tong, H. Xia, and Y. Zhao. Liquid-crystalline dynamic networks doped with gold nanorods showing enhanced photocontrol of actuation. *Advanced Materials*, 30(14):1706597, 2018.

[130] C. Lv, D. Krishnaraju, G. Konjevod, H. Yu, and H. Jiang. Origami based mechanical metamaterials. *Scientific Reports*, 4, 2014.

[131] M. J. Madou. *Fundamentals of Microfabrication: The Science of Miniaturization*. CRC press, 2018.

[132] S. Manakasettharn, J. Ashley Taylor, and T. N. Krupenkin. Bio-inspired artificial iridophores based on capillary origami: Fabrication and device characterization. *Applied Physics Letters*, 99(14):2012–2015, 2011.

[133] X. Mao, X. Yang, G. C. Rutledge, and T. Alan Hatton. Ultra-wide-range electrochemical sensing using continuous electrospun carbon nanofibers with high densities of states. *ACS applied materials & interfaces*, 6(5):3394–3405, 2014.

[134] Y. Mao, K. Yu, M. S. Isakov, J. Wu, M. L. Dunn, and H. Jerry Qi. Sequential Self-Folding Structures by 3D Printed Digital Shape Memory Polymers. *Scientific Reports*, 5:1–12, 2015.

[135] A. W. Martinez, S. T. Phillips, M. J. Butte, and G. M. Whitesides. Supporting information for patterned paper as a platform for inexpensive, low volume, portable bioassays, 2007.

[136] R. Martinez-Duarte. SU-8 photolithography as a toolbox for carbon MEMS. *Micromachines*, 5(3):766–782, 2014.

[137] R. L. McCreery. Advanced carbon electrode materials for molecular electrochemistry. *Chemical reviews*, 108(7):2646–2687, 2008.

[138] T. McGuire, M. Hirsch, M. Parsons, S. Leake, and J. Straub. A CubeSat deployable solar panel system. *Energy Harvesting and Storage: Materials, Devices, and Applications VII*, 9865(May):98650C, 2016.

[139] F. P. Melchels, J. Feijen, and D. W. Grijpma. A review on stereolithography and its applications in biomedical engineering. *Biomaterials*, 31(24):6121–6130, 2010.

[140] M. M. Mikulas, R. S. Pappa, J. Warren, and G. Rose. Telescoping Solar Array Concept for Achieving High Packaging Efficiency. *AIAA SciTech Forum*, 2nd AIAA S(January 5-9):1–21, 2015.

[141] S. Min, T. Kim, B. Kim, H. Cho, Y. Noh, H. Yang, J. Cho, and T. Lee. Large-scale organic nanowire lithography and electronics. nat commun 4: 1773, 2013.

[142] M. Z. Miskin, K. J. Dorsey, B. Bircan, Y. Han, D. A. Muller, P. L. McEuen, and I. Cohen. Graphene-based bimorphs for micron-sized, autonomous origami machines. *Proceedings of the National Academy of Sciences*, 115(3):466–470, 2018.

[143] S. Miyashita, S. Guitron, S. Li, and D. Rus. Robotic metamorphosis by origami exoskeletons. *Science Robotics*, 2(10):1–7, 2017.

[144] E. Moiseeva, Y. M. Senousy, S. McNamara, and C. K. Harnett. Single-mask microfabrication of three-dimensional objects from strained bimorphs. *Journal of Micromechanics and Microengineering*, 17(9), 2007.

[145] W. M. Moreau. *Semiconductor Lithography: Principles, Practices, and Materials*. Springer Science & Business Media, 2012.

[146] J. Mu, C. Hou, H. Wang, Y. Li, Q. Zhang, and M. Zhu. Origami-inspired active graphene-based paper for programmable instant self-folding walking devices. *Science advances*, 1(10):e1500533, 2015.

[147] J. H. Na, A. A. Evans, J. Bae, M. C. Chiappelli, C. D. Santangelo, R. J. Lang, T. C. Hull, and R. C. Hayward. Programming reversibly self-folding origami with micropatterned photo-crosslinkable polymer trilayers. *Advanced Materials*, 27(1):79–85, 2015.

[148] J. H. Na, A. A. Evans, J. Bae, M. C. Chiappelli, C. D. Santangelo, R. J. Lang, T. C. Hull, and R. C. Hayward. Programming reversibly self-folding origami with micropatterned photo-crosslinkable polymer trilayers. *Advanced Materials*, 27(1):79–85, 2015.

[149] S. Nandi and H. H. Winter. Swelling behavior of partially cross-linked polymers: A ternary system. *Macromolecules*, 38:4447–4455, 2005.

[150] R. Natu, M. Islam, J. Gilmore, and R. Martinez-Duarte. Shrinkage of SU-8 microstructures during carbonization. *Journal of Analytical and Applied Pyrolysis*, 131(November 2017):17–27, 2018.

[151] R. S. Nicholson. Theory and application of cyclic voltammetry for measurement of electrode reaction kinetics. *Analytical chemistry*, 37(11):1351–1355, 1965.

[152] C. Ohm, M. Brehmer, and R. Zentel. Liquid crystalline elastomers as actuators and sensors. *Advanced Materials*, 22(31):3366–3387, 2010.

[153] C. D. Onal, R. J. Wood, and D. Rus. Towards printable robotics: Origami-inspired planar fabrication of three-dimensional mechanisms. In *2011 IEEE International Conference on Robotics and Automation*, pages 4608–4613. IEEE, 2011.

[154] C.-T. Pan, C.-K. Yen, S.-Y. Wang, Y.-C. Lai, L. Lin, J. Huang, and S.-W. Kuo. Near-field electrospinning enhances the energy harvesting of hollow pvdf piezoelectric fibers. *Rsc Advances*, 5(103):85073–85081, 2015.

[155] S. Pandey, M. Ewing, A. Kunas, N. Nguyen, D. H. Gracias, and G. Menon. Algorithmic design of self-folding polyhedra. *Proceedings of the National Academy of Sciences*, 108(50):19885–19890, 2011.

[156] V. Penmatsa, H. Kawarada, and C. Wang. Fabrication of carbon nanostructures using photo-nanoimprint lithography and pyrolysis. *Journal of Micromechanics and Microengineering*, 22(4):045024, 2012.

[157] E. Peraza Hernandez, D. Hartl, and D. Lagoudas. Design and simulation of origami structures with smooth folds. *Proceedings of the Royal Society A: Mathematical, Physical and Engineering Sciences*, 473(2200):20160716, 2017.

[158] E. Peraza Hernandez, D. J. Hartl, and D. C. Lagoudas. Modeling and design of shape memory alloy-based origami structures with smooth folds. In *25th AIAA/AHS Adaptive Structures Conference*, page 1875, 2017.

[159] E. A. Peraza Hernandez, D. J. Hartl, and D. C. Lagoudas. Analysis and design of an active self-folding antenna. In *International Design Engineering Technical Conferences and Computers and Information in Engineering Conference*, volume 58189, page V05BT08A049. American Society of Mechanical Engineers, 2017.

[160] E. A. Peraza Hernandez, D. J. Hartl, and D. C. Lagoudas. Introduction to active origami structures. In *Active Origami*, pages 1–53. Springer, 2019.

[161] E. A. Peraza Hernandez, D. J. Hartl, and D. C. Lagoudas. Structural mechanics and design of active origami structures. In *Active Origami*, pages 331–409. Springer, 2019.

[162] E. A. Peraza Hernandez, D. J. Hartl, and D. C. Lagoudas. Unfolding polyhedra method for the design of origami structures with creased folds. In *Active Origami*, pages 111–155. Springer, 2019.

[163] E. A. Peraza Hernandez, D. J. Hartl, and D. C. Lagoudas. Unfolding polyhedra method for the design of origami structures with smooth folds. In *Active Origami*, pages 269–292. Springer, 2019.

[164] E. A. Peraza-Hernandez, D. J. Hartl, R. J. Malak, and D. C. Lagoudas. Origami-inspired active structures: A synthesis and review. *Smart Materials and Structures*, 23(9), 2014.

[165] E. A. Peraza Hernandez, D. J. Hartl, R. J. Malak Jr, and D. C. Lagoudas. Origami-inspired active structures: A synthesis and review. *Smart Materials and Structures*, 094001(23):1–28, 2014.

[166] E. A. Peraza Hernandez, S. Hu, H. W. Kung, D. Hartl, and E. Akleman. Towards building smart self-folding structures. *Computers & Graphics*, 37(6):730–742, 2013.

[167] A. Pimpin and W. Srituravanich. Review on micro-and nanolithography techniques and their applications. *Engineering Journal*, 16(1):37–56, 2012.

[168] M. Pineirua, J. Bico, and B. Roman. Capillary origami controlled by an electric field. *Soft Matter*, 6(18):4491–4496, 2010.

[169] M. Piñeirua, J. Bico, and B. Roman. Capillary origami controlled by an electric field. *Soft Matter*, 6:4491, 2010.

[170] J. Plutnar, M. Pumera, and Z. Sofer. The chemistry of CVD graphene. *Journal of Materials Chemistry C*, 6(23):6082–6101, 2018.

[171] C. Py, P. Reverdy, L. Doppler, J. Bico, B. Roman, and C. N. Baroud. Capillary origami: Spontaneous wrapping of a droplet with an elastic sheet. *Physical Review Letters*, 98(15):2–5, 2007.

[172] A. Rath, S. Mathesan, and P. Ghosh. Folding behavior and molecular mechanism of cross-linked biopolymer film in response to water. *Soft Matter*, 12(45):9210–9222, 2016.

[173] D. Ratna and J. Karger-Kocsis. Recent advances in shape memory polymers and composites: a review. *Journal of Materials Science*, 43(1):254–269, 2008.

[174] A. Reina, X. Jia, J. Ho, D. Nezich, H. Son, V. Bulovic, M. S. Dresselhaus, and J. Kong. Large area, few-layer graphene films on arbitrary substrates by chemical vapor deposition. *Nano letters*, 9(1):30–35, 2009.

[175] D. H. Reneker, A. L. Yarin, H. Fong, and S. Koombhongse. Bending instability of electrically charged liquid jets of polymer solutions in electrospinning. *Journal of Applied Physics*, 87(9 I):4531–4547, 2000.

[176] J. Rogers, Y. Huang, O. G. Schmidt, and D. H. Gracias. Origami MEMS and NEMS. *MRS Bulletin*, 41(2):123–129, 2016.

[177] J. P. Rojas, D. Conchouso, A. Arevalo, D. Singh, I. G. Foulds, and M. M. Hussain. Paper-based origami flexible and foldable thermoelectric nanogenerator. *Nano Energy*, 31(October 2016):296–301, 2017.

[178] J. Ryu, M. D'Amato, X. Cui, K. N. Long, H. Jerry Qi, and M. L. Dunn. Photo-origami-Bending and folding polymers with light. *Applied Physics Letters*, 100(16), 2012.

[179] A. Sadezky, H. Muckenhuber, H. Grothe, R. Niessner, and U. Pöschl. Raman microspectroscopy of soot and related carbonaceous materials: spectral analysis and structural information. *Carbon*, 43(8):1731–1742, 2005.

[180] W. Schlickenrieder. Nets of polyhedra, 1997.

[181] D. M. Sessions, J. T. Ruff, F. A. Espinal, G. H. Huff, S. S. Jape, E. Peraza-Hernandez, D. C. Lagoudas, D. J. Hartl, and B. Borges. Folding, tessellation, and deployment of an origami-inspired active-material-enabled self-folding reflector antenna. In *2018 IEEE International Symposium on Antennas and Propagation & USNC/URSI National Radio Science Meeting*, pages 929–930. IEEE, 2018.

[182] M. Sevilla and A. B. Fuertes. Catalytic graphitization of templated mesoporous carbons. *Carbon*, 44(3):468–474, 2006.

[183] N. S. Shaar, G. Barbastathis, and C. Livermore. Integrated Folding, Alignment, and Latching for Reconfigurable Origami Microelectromechanical Systems. *Journal of Microelectromechanical Systems*, 24(4):1043–1051, 2015.

[184] Y. Shao, S. Zhang, M. H. Engelhard, G. Li, G. Shao, Y. Wang, J. Liu, I. A. Aksay, and Y. Lin. Nitrogen-doped graphene and its electrochemical applications. *Journal of Materials Chemistry*, 20(35):7491–7496, 2010.

[185] C. S. Sharma, H. Katepalli, A. Sharma, and M. Madou. Fabrication and electrical conductivity of suspended carbon nanofiber arrays. *Carbon*, 49(5):1727–1732, 2011.

[186] S. Sharma and M. Madou. Review article: A new approach to gas sensing with nanotechnology. *Philosophical Transactions of the Royal Society A: Mathematical, Physical and Engineering Sciences*, 370(1967):2448–2473, 2012.

[187] Z.-H. Sheng, X.-Q. Zheng, J.-Y. Xu, W.-J. Bao, F.-B. Wang, and X.-H. Xia. Electrochemical sensor based on nitrogen doped graphene: simultaneous determination of ascorbic acid, dopamine and uric acid. *Biosensors and Bioelectronics*, 34(1):125–131, 2012.

[188] L. Shi, X. Niu, T. Liu, H. Zhao, and M. Lan. Electrocatalytic sensing of hydrogen peroxide using a screen printed carbon electrode modified with nitrogen-doped graphene nanoribbons. *Microchimica Acta*, 182(15):2485–2493, 2015.

[189] H. Shigemune, S. Maeda, Y. Hara, N. Hosoya, and S. Hashimoto. Origami robot: a self-folding paper robot with an electrothermal actuator created by printing. *IEEE/ASME Transactions on Mechatronics*, 21(6):2746–2754, 2016.

[190] T. S. Shim, S.-H. Kim, C.-J. Heo, H. C. Jeon, and S.-M. Yang. Controlled origami folding of hydrogel bilayers with sustained reversibility for robust microcarriers. *Angewandte Chemie International Edition*, 51(6):1420–1423, 2012.

[191] D. Shin, J. Kim, and J. Chang. Experimental study on jet impact speed in near-field electrospinning for precise patterning of nanofiber. *Journal of Manufacturing Processes*, 36(October):231–237, 2018.

[192] K. J. Si, D. Sikdar, Y. Chen, F. Eftekhari, Z. Xu, Y. Tang, W. Xiong, P. Guo, S. Zhang, Y. Lu, et al. Giant plasmene nanosheets, nanoribbons, and origami. *ACS nano*, 8(11):11086–11093, 2014.

[193] J. Song, H. Jiang, W. Choi, D.-Y. Khang, Y. Huang, and J. A. Rogers. An analytical study of two-dimensional buckling of thin films on compliant substrates. *Journal of Applied Physics*, 103(1):014303, 2008.

[194] G. Stoychev, N. Puretskiy, and L. Ionov. Self-folding all-polymer thermoresponsive microcapsules. *Soft Matter*, 7(7):3277–3279, 2011.

[195] G. Stoychev, S. Zakharchenko, S. Turcaud, J. W. Dunlop, and L. Ionov. Shape-programmed folding of stimuli-responsive polymer bilayers. *ACS nano*, 6(5):3925–3934, 2012.

[196] R. W. Style and E. R. Dufresne. Static wetting on deformable substrates, from liquids to soft solids. *Soft Matter*, 8:7177, 2012.

[197] Y. Sun, W. M. Choi, H. Jiang, Y. Y. Huang, and J. A. Rogers. Controlled buckling of semiconductor nanoribbons for stretchable electronics. *Nature nanotechnology*, 1(3):201–207, 2006.

[198] M. Taghavi, T. Helps, and J. Rossiter. Electro-ribbon actuators and electro-origami robots. *Science Robotics*, 3(25), 2018.

[199] R. Tang, H. Huang, H. Tu, H. Liang, M. Liang, Z. Song, Y. Xu, H. Jiang, and H. Yu. Origami-enabled deformable silicon solar cells. *Applied Physics Letters*, 104(8), 2014.

[200] S. Thian, Y. Tang, J. Fuh, Y. Wong, L. Lu, and H. Loh. Micro-rapid-prototyping via multi-layered photo-lithography. *The International Journal of Advanced Manufacturing Technology*, 29(9-10):1026–1032, 2006.

[201] H. Tian, L. Wang, Z. Sofer, M. Pumera, and A. Bonanni. Doped graphene for dna analysis: The electrochemical signal is strongly influenced by the kind of dopant and the nucleobase structure. *Scientific reports*, 6(1):1–10, 2016.

[202] S. Timoshenko. Analysis of bi-metal thermostats. *Josa*, 11(3):233–255, 1925.

[203] M. T. Tolley, S. M. Felton, S. Miyashita, D. Aukes, D. Rus, and R. J. Wood. Self-folding origami: shape memory composites activated by uniform heating. *Smart Materials and Structures*, 23(9):094006, 2014.

[204] I. Tomatsu, K. Peng, and A. Kros. Photoresponsive hydrogels for biomedical applications. *Advanced drug delivery reviews*, 63(14-15):1257–1266, 2011.

[205] J. W. Van Honschoten, J. W. Berenschot, T. Onda??uhu, R. G. P. Sanders, J. Sundaram, M. Elwenspoek, and N. R. Tas. Elastocapillary fabrication of three-dimensional microstructures. *Applied Physics Letters*, 97(1), 2010.

[206] T. Van Manen, S. Janbaz, and A. A. Zadpoor. Programming 2D/3D shape-shifting with hobbyist 3D printers. *Materials Horizons*, 4(6):1064–1069, 2017.

[207] T. van Manen, S. Janbaz, and A. A. Zadpoor. Programming the shape-shifting of flat soft matter. *Materials Today*, 21(2):144–163, 2018.

[208] C. Wang and M. Madou. From MEMS to NEMS with carbon. *Biosensors and Bioelectronics*, 20(10):2181–2187, apr 2005.

[209] C. Wang, K. Xia, H. Wang, X. Liang, Z. Yin, and Y. Zhang. Advanced Carbon for Flexible and Wearable Electronics. *Advanced Materials*, 31(9):1–37, 2019.

[210] J. Wang and T. Peng. Enhanced stability of glassy carbon detectors following a simple electrochemical pretreatment. *Analytical chemistry*, 58(8):1787–1790, 1986.

[211] M. Wang, B.-P. Lin, and H. Yang. A plant tendril mimic soft actuator with phototunable bending and chiral twisting motion modes. *Nature communications*, 7(1):1–8, 2016.

[212] R. Wang, Y. Hao, Z. Wang, H. Gong, and J. T. Thong. Large-diameter graphene nanotubes synthesized using Ni nanowire templates. *Nano Letters*, 10(12):4844–4850, 2010.

[213] X. Wang and C. S. Ozkan. Multisegment nanowire sensors for the detection of DNA molecules. *Nano Letters*, 8(2):398–404, 2008.

[214] X. Wang, G. Sun, P. Routh, D.-H. Kim, W. Huang, and P. Chen. Heteroatom-doped graphene materials: syntheses, properties and applications. *Chemical Society Reviews*, 43(20):7067–7098, 2014.

[215] X. Wang, G. Zheng, L. Xu, W. Cheng, B. Xu, Y. Huang, and D. Sun. Fabrication of nanochannels via near-field electrospinning. *Applied Physics A: Materials Science and Processing*, 108(4):825–828, 2012.

[216] Y. Wang, C. Dhong, and J. Frechette. Out-of-Contact Elastohydrodynamic Deformation due to Lubrication Forces. *Physical Review Letters*, 115(24):1–5, 2015.

[217] S. Watabe, Y. Sakamoto, M. Morikawa, R. Okada, T. Miura, and E. Ito. Highly sensitive determination of hydrogen peroxide and glucose by fluorescence correlation spectroscopy. *PLoS One*, 6(8):e22955, 2011.

[218] P. Wu, P. Du, H. Zhang, and C. Cai. Microscopic effects of the bonding configuration of nitrogen-doped graphene on its reactivity toward hydrogen peroxide reduction reaction. *Physical Chemistry Chemical Physics*, 15(18):6920–6928, 2013.

[219] Y. Wu, H. Tao, S. Su, H. Yue, H. Li, Z. Zhang, Z. Ni, and X. Chen. Patterning Graphene Film by Magnetic-Assisted UV Ozonation. *Scientific Reports*, 7(March):1–9, 2017.

[220] Z. Xi, Y.-h. Kim, Y. J. Kim, and J.-M. Lien. Learning to segment and unfold polyhedral mesh from failures. *Computers & Graphics*, 58:139–149, 2016.

[221] Z. Xi and J.-M. Lien. Continuous unfolding of polyhedra-a motion planning approach. In *2015 IEEE/RSJ International Conference on Intelligent Robots and Systems (IROS)*, pages 3249–3254. IEEE, 2015.

[222] T. Xing, Y. Zheng, L. H. Li, B. C. Cowie, D. Gunzelmann, S. Z. Qiao, S. Huang, and Y. Chen. Observation of active sites for oxygen reduction reaction on nitrogen-doped multilayer graphene. *Acs Nano*, 8(7):6856–6862, 2014.

[223] F. Xu, M. Deng, G. Li, S. Chen, and L. Wang. Electrochemical behavior of cuprous oxide–reduced graphene oxide nanocomposites and their application in nonenzymatic hydrogen peroxide sensing. *Electrochimica Acta*, 88:59–65, 2013.

[224] T. Xu, J. Zhang, M. Salehizadeh, O. Onaizah, and E. Diller. Millimeter-scale flexible robots with programmable three-dimensional magnetization and motions. *Science Robotics*, 4(29):eaav4494, 2019.

[225] T. Xu, J. Zhang, M. Salehizadeh, O. Onaizah, and E. Diller. Millimeter-scale flexible robots with programmable three-dimensional magnetization and motions. *Science Robotics*, 4(29), 2019.

[226] X. Xu, S. Jiang, Z. Hu, and S. Liu. Nitrogen-doped carbon nanotubes: high electrocatalytic activity toward the oxidation of hydrogen peroxide and its application for biosensing. *Acs Nano*, 4(7):4292–4298, 2010.

[227] Z. Xu, H. Li, B. Yin, Y. Shu, X. Zhao, D. Zhang, K. Li, X. Hou, J. Lu, et al. N-doped graphene analogue synthesized by pyrolysis of metal tetrapyridinoporphyrazine with high and stable catalytic activity for oxygen reduction. *RSC advances*, 3(24):9344–9351, 2013.

[228] J. Xue, T. Wu, Y. Dai, and Y. Xia. Electrospinning and electrospun nanofibers: Methods, materials, and applications. *Chemical Reviews*, 119(8):5298–5415, 2019.

[229] L. Xue, Z. Zhu, L. Fan, F. Liu, and H. Wang. Effect of microstructure on the mechanical properties of PAN-based carbon fibers during high-temperature graphitization. *Journal of Materials Science*, 43(12):4316–4322, 2008.

[230] R. Yadav and C. Dixit. Synthesis, characterization and prospective applications of nitrogen-doped graphene: A short review. *Journal of Science: Advanced Materials and Devices*, 2(2):141–149, 2017.

[231] Z. Yan, F. Zhang, J. Wang, F. Liu, X. Guo, K. Nan, Q. Lin, M. Gao, D. Xiao, Y. Shi, et al. Controlled mechanical buckling for origami-inspired construction of 3d microstructures in advanced materials. *Advanced functional materials*, 26(16):2629–2639, 2016.

[232] H. Yang, C. R. Lightner, and L. Dong. Light-emitting coaxial nanofibers. *ACS nano*, 6(1):622–628, 2012.

[233] M. Yang, F. Qu, Y. Lu, Y. He, G. Shen, and R. Yu. Platinum nanowire nanoelectrode array for the fabrication of biosensors. *Biomaterials*, 27(35):5944–5950, 2006.

[234] Y. Yang and Z. You. Geometry of transformable metamaterials inspired by modular origami. *Journal of Mechanisms and Robotics*, 10(2), 2018.

[235] P. Yao, G. J. Schneider, B. Miao, J. Murakowski, D. W. Prather, E. D. Wetzel, and D. J. O'Brien. Multilayer three-dimensional photolithography with traditional planar method. *Applied Physics Letters*, 85(17):3920–3922, 2004.

[236] P. Yao, G. J. Schneider, D. W. Prather, E. D. Wetzel, and D. J. O'Brien. Fabrication of three-dimensional photonic crystals with multilayer photolithography. *Opt. Express*, 13(7):2370–2376, Apr 2005.

[237] Q. Yi, G. Zou, M. H. Rummeli, J. Wu, J. Jian, X. Dai, H. Wang, Z. Qian, H. Liu, and Y. Cao. Ultra-smooth glassy graphene thin films for flexible transparent circuits. *Science Advances*, 2(11):e1601574, 2016.

[238] X. You, C. Ye, and P. Guo. Electric field manipulation for deposition control in near-field electrospinning. *Journal of Manufacturing Processes*, 30:431–438, 2017.

[239] D. Yu and L. Dai. Self-assembled graphene/carbon nanotube hybrid films for supercapacitors. *Journal of Physical Chemistry Letters*, 1(2):467–470, 2010.

[240] K. Yu, A. Ritchie, Y. Mao, M. L. Dunn, and H. J. Qi. Controlled sequential shape changing components by 3d printing of shape memory polymer multimaterials. *Procedia Iutam*, 12:193–203, 2015.

[241] C. Yuan, D. J. Roach, C. K. Dunn, Q. Mu, X. Kuang, C. M. Yakacki, T. J. Wang, K. Yu, and H. J. Qi. 3D printed reversible shape changing soft actuators assisted by liquid crystal elastomers. *Soft Matter*, 13(33):5558–5568, 2017.

[242] S. Zeng, Y. Gao, Y. Feng, H. Zheng, H. Qiu, and J. Tan. Programming the deformation of a temperature-driven bilayer structure in 4d printing. *Smart Materials and Structures*, 28(10):105031, 2019.

[243] C. Zhang, L. Li, J. Ju, and W. Chen. Electrochemical sensor based on graphene-supported tin oxide nanoclusters for nonenzymatic detection of hydrogen peroxide. *Electrochimica Acta*, 210:181–189, 2016.

[244] R. Zhang and W. Chen. Fe3c-functionalized 3d nitrogen-doped carbon structures for electrochemical detection of hydrogen peroxide. *Science Bulletin*, 60(5):522–531, 2015.

[245] W. Zhang, S. Ahmed, S. Masters, Z. Ounaies, and M. Frecker. Finite element analysis of electroactive polymer and magnetoactive elastomer based actuation for origami-inspired folding. In *Smart Materials, Adaptive Structures and Intelligent Systems*, volume 50480, page V001T01A001. American Society of Mechanical Engineers, 2016.

[246] X. Zhang, J. Li, C. Chen, B. Lou, L. Zhang, and E. Wang. A self-powered microfluidic origami electrochemiluminescence biosensing platform. *Chemical Communications*, 49(37):3866–3868, 2013.

[247] Y. Zhang, J. Ge, L. Wang, D. Wang, F. Ding, X. Tao, and W. Chen. Manageable n-doped graphene for high performance oxygen reduction reaction. *Scientific reports*, 3(1):1–8, 2013.

[248] Z. Zhao, J. Wu, X. Mu, H. Chen, H. J. Qi, and D. Fang. Origami by frontal photopolymerization. *Science Advances*, 3(4):1–8, 2017.

[249] Y. Zhong, S. Lundemo, and E. W. Jager. Development of polypyrrole based solid-state on-chip microactuators using photolithography. *Smart Materials and Structures*, 27(7):074006, 2018.

[250] Q. Zhu, S. Money, A. Russell, and K. Thomas. Determination of the fate of nitrogen functionality in carbonaceous materials during pyrolysis and combustion using x-ray absorption near edge structure spectroscopy. *Langmuir*, 13(7):2149–2157, 1997.

[251] W. Z.L. and S. J. Piezoelectric nanogenerators based on zinc oxide nanowire arrays. *Science*, 312(5771):242–246, 2006.

Appendix A

Appendix Title

A.1 Nomenclature

b	Fold length
$c(z)$	Steady state concentration field of developer along the film thickness direction z
$c(z,t)$	Transient concentration field of developer along the film thickness direction z at time t
C_{ci}	$i \in \{0,1\}$; Coefficients of the polynomial describing the developer concentration field
$C_{\varepsilon i}$	$i \in \{0,1\}$; Coefficients of the polynomial describing the inelastic (actuation) strain field
D	Diffusion coefficient
E	Young's modulus of the fold
h	Film thickness
m	Moment
$\mathcal{M}$	$\subset \mathbb{R}^3$; Target mesh

$\mathcal{M}_{\#}$	$\subset \mathcal{M}$; Trimmed mesh
R	Radius of curvature of the fold
$\mathcal{S}_0$	$\subset \mathbb{R}^3$; Planar configuration of the net
$\mathcal{S}_f$	$\subset \mathbb{R}^3$; Final configuration of the net
t	Time
w	Fold width
z	$\in \left[-\frac{h}{2}, \frac{h}{2}\right]$; Thickness coordinate
ε_A	Maximum inelastic (actuation) strain across the fold thickness
$\varepsilon_e(z)$	Elastic strain field along the film thickness direction z
$\varepsilon_a(z)$	Inelastic (actuation) strain field along the film thickness direction z
θ	Fold angle
κ	Fold curvature
$\sigma(z)$	Stress field along the film thickness direction z

A.2 Capillary Origami

A.2.1 Theoretical Modeling

Here we are considering the bent profile of a thin one dimensional sheet which is subjected to a surface tension γ along the liquid-liquid-film interface and pressure p on the surface of film due to the liquid-liquid interface curvature. Tangent of the sheet at a point s makes an angle $\theta(s)$ with the x axis. The profile of the sheet can be found by solving this angle. Here we are assuming that the sheet is inextensible.The x coordinate at s is given by

$$x(s) = \int_0^s \cos(\theta(s))ds,$$

and the y coordinate is given by

$$y(s) = \int_0^s \sin(\theta(s))ds.$$

The arc length of from O to s can be expressed as follows.

$$\int_0^s \sqrt{\left(\frac{dx(s)}{ds}\right)^2 + \left(\frac{dy(s)}{ds}\right)^2}ds = \int_0^s \sqrt{\sin^2(\theta(s)) + \cos^2\theta(s)}ds = s.$$

Hence satisfies the assumption.

To find the bending profile of a film of length L after it is subjected to the forces (shown in Fig. A.1) the following steps are followed.

Step A: Find reaction forces and moments

$$\Sigma F_x = 0 \implies f_x + \gamma \cos(\delta + \theta(l)) + \int_0^l p \cos(\tfrac{3\pi}{2} + \theta(s)) ds = 0 \tag{A.1}$$

To simplify, the following short forms are used hereon in the text

$$\gamma \cos(\delta + \theta(l)) = \gamma_x$$

$$p \cos\left(\frac{3\pi}{2} + \theta(s)\right) = p_x(s)$$

Now the equation A.1 can be written as follows.

$$f_x + \gamma_x + \int_0^l p_x(s) ds = 0 \implies f_x = -(\gamma_x + \int_0^l p_x(s) ds) \tag{A.2}$$

Similarly the total force in the y direction is equal to zero.

i. e.

$$\Sigma F_y = 0 \implies f_y + \gamma \sin(\delta + \theta(l)) + \int_0^l p \sin\left(\frac{3\pi}{2} + \theta(s)\right) ds = 0 \tag{A.3}$$

To simplify the expression, the following short forms are used further in the text

$$\gamma \sin(\delta + \theta(l)) = \gamma_y$$

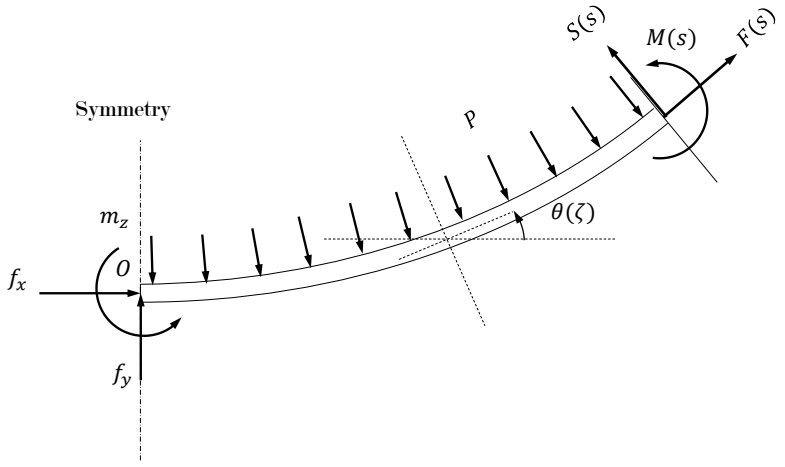

Figure A.1: Free body diagram of a bent sheet at equilibrium.

$$p \sin\left(\frac{3\pi}{2} + \theta(s)\right) = p_y(s)$$

Now the equation A.3 can be written as follows.

$$f_y + \gamma_y + \int_0^l p_y(s)ds = 0 \implies f_y = -(\gamma_y + \int_0^l p_y(s)ds) \tag{A.4}$$

Moment about point O results in the following equation

$$\Sigma M_{z/o} = 0 \implies m_z - y_l\gamma_x + x_l\gamma_y - \int_0^l y(s)p_x(s)ds + \int_0^l x(s)p_y(s)ds = 0$$

where

$$y_l = \int_0^l \sin(\theta(s))ds$$

$$x_l = \int_0^l \cos(\theta(s))ds$$

$$y(s) = \int_0^s \sin(\theta(s))ds$$

and

$$x(s) = \int_0^s \cos(\theta(s))ds$$

$$\implies m_z = y_l\gamma_x - x_l\gamma_y + \int_0^l y(s)p_x(s)ds - \int_0^l x(s)p_y(s)ds \tag{A.5}$$

Step B: make a cut to find the moment at an arbitrary point along the length

The moment acting at an arbitrary point at a distance s from O along the length of the film at the equilibrium is found by taking the total moment about that point and equating it to zero.

$$m(s) + m_z - \int_0^s (y(s) - y(\zeta))p_x(\zeta)d\zeta) + \int_0^s (x(s) - x(\zeta)p_y(\zeta)d\zeta) + x(s)f_y - y(s)f_x = 0$$

Therefore,

$$m(s) = -m_z + \int_0^s (y(s) - y(\zeta))\, p_x(\zeta)d\zeta - \int_0^s (x(s) - x(\zeta))\, p_y(\zeta)d\zeta - x(s)f_y + y(s)f_x \tag{A.6}$$

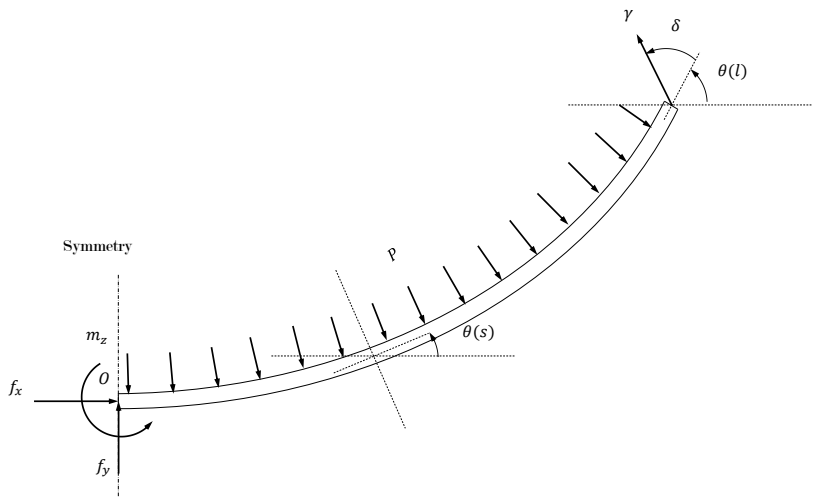

Figure A.2: Free body diagram of a bent sheet at equilibrium after an arbitrary ct was made to find the moment at any point on the sheet

where

$$y(\zeta) = \int_0^s \sin(\zeta) d\zeta$$

and

$$x(\zeta) = \int_0^s \cos(\zeta) d\zeta$$

The relation between curvature at each point and the moment is as follows.

$$M(s) = EI\kappa$$

where E is the Young's modulus of the sheet, I is the area moment of inertia and κ is the curvature defined by $d\theta(s)/ds$. Hence the equation to be solved to find the shape of the thin sheet can be written as follows.

$$-m_z + \int_0^s (y(s) - y(\zeta))\, p_x(\zeta) d\zeta - \int_0^s (x(s) - x(\zeta))\, p_y(\zeta) d\zeta - x(s) f_y + y(s) f_x = EI \frac{d\theta(s)}{ds}$$

A.2.2 Effect of Heat Treatment of the Patterned Sheet on the Folding Response

Heating the patterned sheets for one hour or more prior to placing a droplet on top of them resulted in no discernible folding deformation as shown in Fig. A.3.

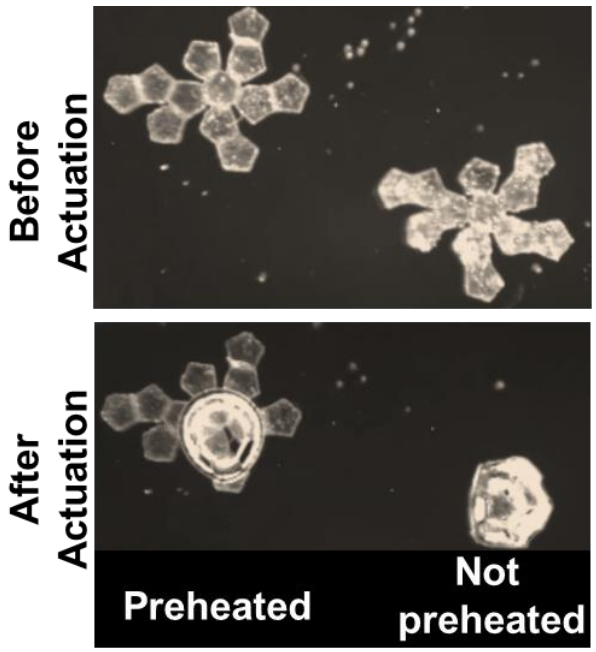

Figure A.3: Effect of preheating on the folding response of the sheets. The precursor flat sheet (left) that was heated at 110°C for one hour after its patterning, prior to the capillary folding procedure, showed little to no folding as compared to a film that was not heated before the capillary folding procedure (right).

A.2.3 Parametric Study of Folding Deformation

Further representative pictures of the parametric study of the single-fold sheet are shown in Fig. A.4.

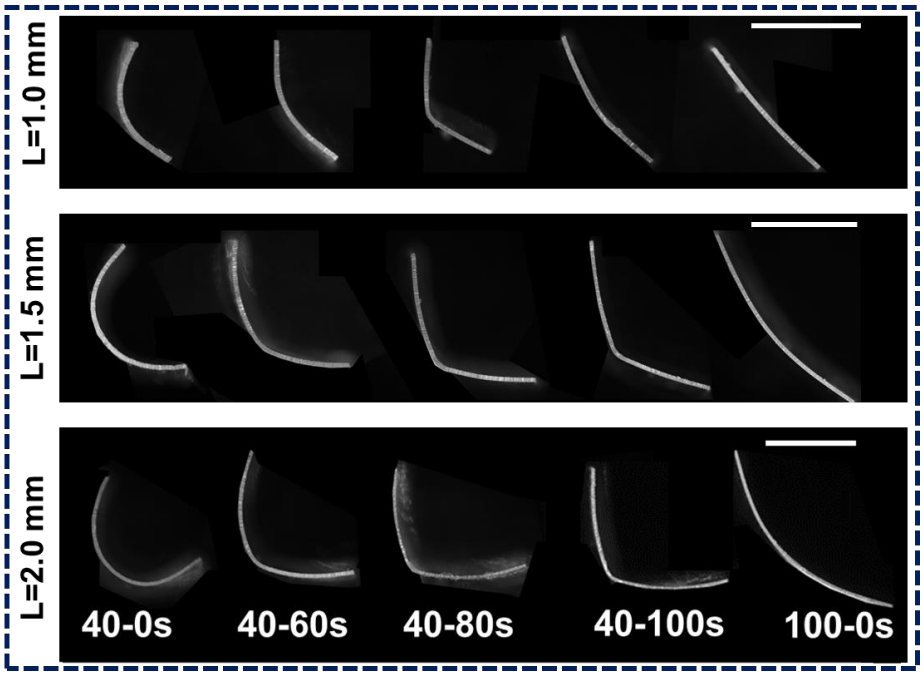

Figure A.4: Experimental analysis of single-fold sheets. Bending of single-fold sheets of three different sizes subjected to distinct exposure times. The first number denotes the total exposure time for the folds and the second number denotes the total exposure time for the faces (e.g., in a 40-60s sample, the folds are exposed for 40 seconds while the faces are exposed for 60 seconds). The exposure intensity was 2 mW/cm2 for all cases. The scale bars are 1.5 mm long.

A.2.4 Data Collected for the Generation of the Results

Table A.2.4. Angle between faces, curvatures of faces, and curvatures of folds of single-fold sheets with L=1mm, L=1.5mm and L=2mm

[h] Size (L in mm)	Exposure 1 (s)	Exposure 2 (s)	D Left	D Center	D Right	κ Left	κ Center	κ Right	Angle
1	40	0	1.960	1.140	1.530	1.020	1.754	1.307	94.710
1	40	0	1.670	1.280	1.930	1.198	1.563	1.036	95.570
1	40	0	1.700	1.120	1.590	1.176	1.786	1.258	93.370
1	40	0	1.590	1.140	1.640	1.258	1.754	1.220	93.530
1	40	0	1.970	1.170	1.780	1.015	1.709	1.124	97.400
Average (L=1mm)	40	0	1.778	1.170	1.694	1.134	1.713	1.189	94.916
STD			0.157	0.057	0.144	0.098	0.079	0.097	1.480
1.5	40	0	1.680	1.360	1.730	1.190	1.471	1.156	58.930
1.5	40	0	2.020	1.470	1.930	0.990	1.361	1.036	45.280
1.5	40	0	1.860	1.490	1.850	1.075	1.342	1.081	60.020
1.5	40	0	1.720	1.500	1.750	1.163	1.333	1.143	59.600
1.5	40	0	2.220	1.490	1.770	0.901	1.342	1.130	58.560
Average (L=1.5mm)	40	0	1.900	1.462	1.806	1.064	1.370	1.109	56.478
STD			0.200	0.052	0.074	0.108	0.051	0.044	5.622

2	40	0	2.580	2.460	3.450	0.775	0.813	0.580	46.450
2	40	0	2.450	1.750	2.160	0.816	1.143	0.926	45.740
2	40	0	1.910	2.340	2.420	1.047	0.855	0.826	33.540
2	40	0	2.890	1.930	2.540	0.692	1.036	0.787	49.880
2	40	0	2.580	1.540	2.500	0.775	1.299	0.800	47.140
Average (L=2mm)	40	0	2.482	2.004	2.614	0.821	1.029	0.784	44.550
STD			0.321	0.348	0.438	0.120	0.180	0.113	5.681
1	40	20	5.580	1.090	5.400	0.358	1.835	0.370	123.160
1	40	20	4.210	1.570	3.430	0.475	1.274	0.583	138.740
1	40	20	6.090	1.520	4.420	0.328	1.316	0.452	128.800
1	40	20	3.350	1.120	3.370	0.597	1.786	0.593	129.420
1	40	20	3.760	1.470	3.350	0.532	1.361	0.597	131.400
Average (L=1mm)	40	20	4.598	1.354	3.994	0.458	1.514	0.519	130.304
STD			1.058	0.206	0.810	0.102	0.244	0.092	5.029
1.5	40	20	5.400	0.590	5.070	0.370	3.390	0.394	84.480
1.5	40	20	4.960	0.790	3.470	0.403	2.532	0.576	88.730
1.5	40	20	4.540	0.520	4.120	0.441	3.846	0.485	85.290
1.5	40	20	4.790	0.650	4.270	0.418	3.077	0.468	95.350

Average (L=1.5mm)	40	20	4.923	0.638	4.233	0.408	3.211	0.481	88.463
STD			0.314	0.099	0.569	0.025	0.478	0.065	4.285
2	40	20	3.880	0.510	5.550	0.515	3.922	0.360	76.260
2	40	20	5.220	0.740	4.510	0.383	2.703	0.443	65.450
2	40	20	5.330	0.780	5.080	0.375	2.564	0.394	79.690
2	40	20	5.030	0.640	3.890	0.398	3.125	0.514	80.470
2	40	20	4.310	0.770	4.580	0.464	2.597	0.437	68.380
Average (L=2mm)	40	20	4.754	0.688	4.722	0.427	2.982	0.430	74.050
STD			0.563	0.102	0.561	0.054	0.511	0.052	6.067
1	40	40	10.640	0.330	6.990	0.188	6.061	0.286	126.600
1	40	40	6.620	0.480	9.170	0.302	4.167	0.218	145.380
1	40	40	7.380	0.480	7.670	0.271	4.167	0.261	114.190
1	40	40	4.190	0.570	6.740	0.477	3.509	0.297	135.430
Average (L=1mm)	40	40	7.488	0.512	7.176	0.294	4.152	0.288	133.014
STD			1.520	0.132	1.386	0.043	1.142	0.058	12.809
1.5	40	40	5.900	0.500	6.150	0.339	4.000	0.325	92.420
1.5	40	40	6.920	0.460	5.390	0.289	4.348	0.371	93.630
1.5	40	40	6.570	0.420	6.590	0.304	4.762	0.303	98.870

1.5	40	40	5.610	0.400	5.300	0.357	5.000	0.377	89.520
1.5	40	40	5.610	0.400	5.940	0.357	5.000	0.337	97.770
Average (L=1.5mm)	40	40	6.122	0.436	5.874	0.329	4.622	0.343	94.442
STD			0.531	0.039	0.481	0.028	0.392	0.028	3.454
2	40	40	6.920	0.440	5.950	0.289	4.545	0.336	72.360
2	40	40	5.960	0.220	6.930	0.336	9.091	0.289	71.120
2	40	40	5.100	0.390	7.010	0.392	5.128	0.285	71.020
2	40	40	5.360	0.440	5.640	0.373	4.545	0.355	70.560
2	40	40	5.010	0.420	5.240	0.399	4.762	0.382	82.300
Average (L=2mm)	40	40	5.670	0.382	6.154	0.358	5.614	0.329	73.472
STD			0.708	0.083	0.704	0.041	1.751	0.037	4.454
1	40	60	6.850	0.520	8.780	0.292	3.846	0.228	147.440
1	40	60	7.760	0.860	8.720	0.258	2.326	0.229	144.470
1	40	60	14.020	1.340	7.960	0.143	1.493	0.251	152.470
1	40	60	8.140	0.840	10.740	0.246	2.381	0.186	153.100
1	40	60	9.750	1.010	8.700	0.205	1.980	0.230	141.690
Average (L=1mm)	40	60	9.304	0.914	8.980	0.229	2.405	0.225	147.834
STD			2.538	0.266	0.930	0.051	0.787	0.021	4.437

1.5	40	60	7.510	0.420	7.290	0.266	4.762	0.274	105.850
1.5	40	60	7.230	0.340	7.010	0.277	5.882	0.285	111.460
1.5	40	60	9.810	0.430	7.370	0.204	4.651	0.271	107.730
1.5	40	60	6.400	0.370	6.010	0.313	5.405	0.333	105.990
1.5	40	60	8.820	0.405	9.480	0.227	4.938	0.211	108.290
Average (L=1.5mm)	40	60	7.954	0.393	7.432	0.257	5.128	0.275	107.864
STD			1.264	0.037	0.542	0.039	0.500	0.025	2.262
2	40	60	6.430	0.460	5.900	0.311	4.348	0.339	65.820
2	40	60	5.650	0.350	8.990	0.354	5.714	0.222	76.490
2	40	60	6.050	0.310	6.310	0.331	6.452	0.317	67.850
2	40	60	15.450	0.330	15.000	0.129	6.061	0.133	71.750
Average (L=2mm)	40	60	5.743	0.405	6.493	0.352	5.128	0.324	70.478
STD			0.590	0.078	1.548	0.038	0.997	0.070	4.073
1	100	0	29.630	7.060	13.430	0.067	0.283	0.149	164.170
1	100	0	15.080	9.370	17.760	0.133	0.213	0.113	167.560
1	100	0	26.210	7.310	19.910	0.076	0.274	0.100	168.790
1	100	0	12.040	6.300	10.450	0.166	0.317	0.191	164.790
Average (L=1mm)	100	0	20.740	7.510	15.388	0.111	0.272	0.138	166.328

STD			7.360	1.136	3.684	0.041	0.037	0.035	1.911
1.5	100	0	7.330	5.070	10.980	0.273	0.394	0.182	154.110
1.5	100	0	10.050	5.350	12.940	0.199	0.374	0.155	146.000
1.5	100	0	11.800	5.940	20.940	0.169	0.337	0.096	139.660
1.5	100	0	9.600	5.230	7.900	0.208	0.382	0.253	140.320
1.5	100	0	11.420	5.700	21.140	0.175	0.351	0.095	155.240
Average (L=1.5mm)	100	0	10.040	5.458	14.780	0.205	0.368	0.156	147.066
STD			1.839	0.363	4.308	0.043	0.024	0.036	5.914
2	100	0	11.350	4.730	11.680	0.176	0.423	0.171	118.820
2	100	0	7.580	4.280	8.980	0.264	0.467	0.223	111.990
2	100	0	8.690	4.310	9.600	0.230	0.464	0.208	116.730
2	100	0	8.180	4.690	9.600	0.244	0.426	0.208	122.050
2	100	0	13.190	4.440	8.880	0.152	0.450	0.225	122.680
Average (L=2mm)	100	0	9.798	4.490	9.748	0.213	0.446	0.207	118.454
STD			2.130	0.188	1.012	0.042	0.019	0.019	3.890

A.2.5 Fabrication of Anchored Folded Shapes

Anchored single-fold sheets are fabricated using a third-step exposure as depicted in Fig. A.5.

A.2.6 DMA Results

SU8 specimens having dimensions 2.5 mm × 25 mm × 55 μm were tested via dynamic mechanical analysis (DMA) using a TA Instruments DMA Q800 by loading them using a sinusoidal force amplitude with frequency of 1 Hz. Tension mode was used for the measurements. A pre-loading force of 0.001 N was applied to avoid initial buckling on the film. A

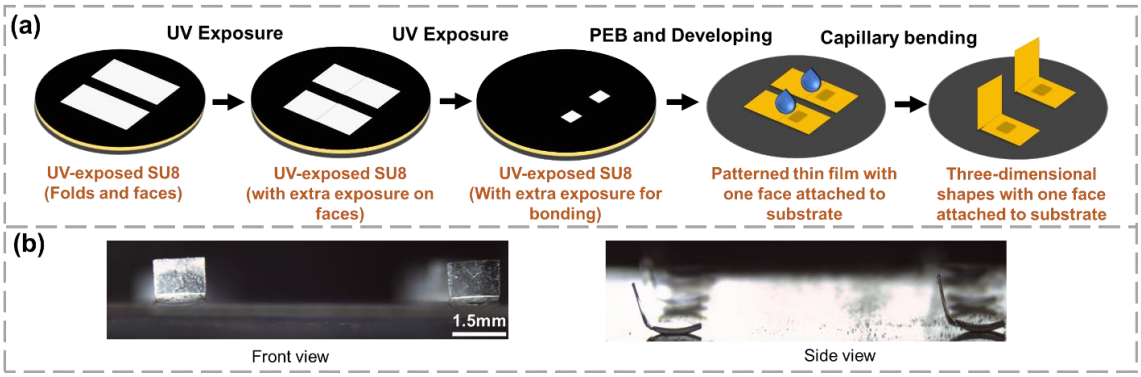

Figure A.5: Fabrication of origami structures with selected faces attached to a supporting structure. (a) Patterning and folding procedure. In addition to the two exposure times required to produce the patterned thin sheets, we perform a third exposure on the regions where bonding to the supporting structure is desired. The sheets are then baked and developed. These anchored sheets are folded to the desired polyhedral shape by using a droplet inside a silicone oil bath at an elevated temperature, just as performed for the free-standing sheets. (b) Images of the resulting folding structures from two different views.

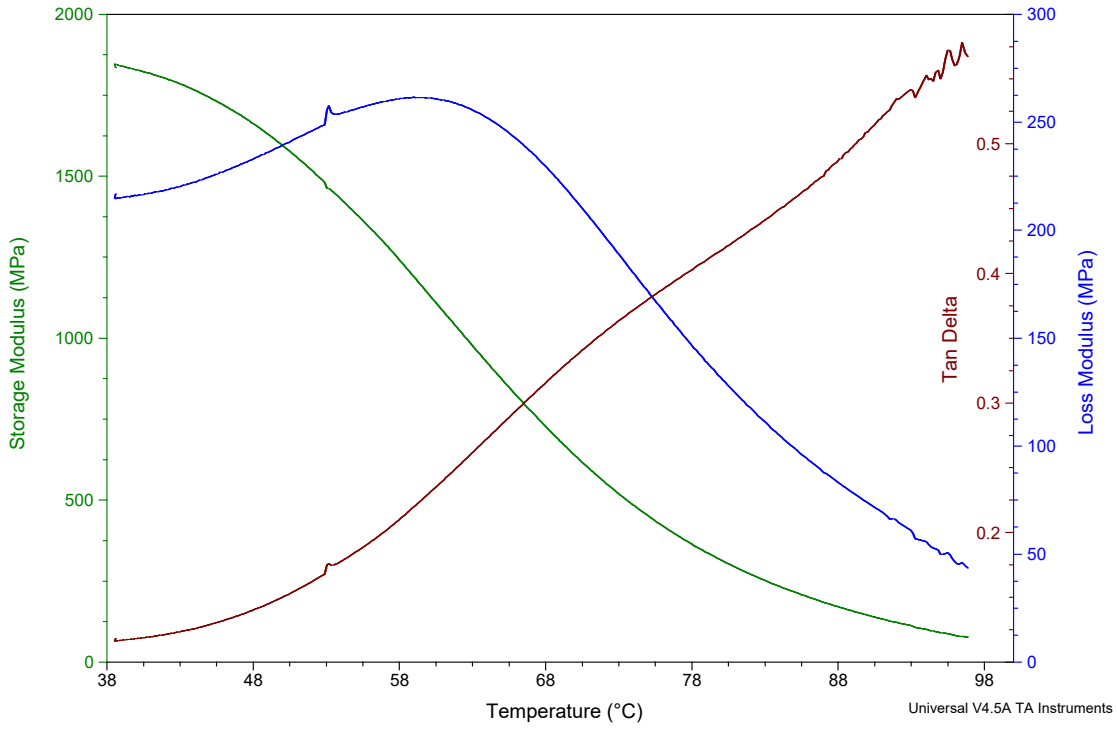

Figure A.6: Dynamic mechanical analysis results of a sheet made by exposing a SU8 film for 180 sec with a 2 mW/cm^2 UV light source followed by an additional hard baking step. These results are associated with specimen 1 of this kind.

temperature ramp of 3°C/min was used for the DMA measurements. Specimens that were exposed to a 2 mW/cm^2 UV light for 40 sec, 60 sec, 80 sec, and 100 sec were used to study the effect of UV exposure time and temperature on the modulus of the material. Completely crosslinked strips were made by subjecting the sheet to 180 sec of UV exposure followed by an additional hard baking step. Hard baking was done at 200°C for 2 hours. DMA analyses were carried out on three SU8 samples of the same nominal size for each exposure energy. The raw data from the analyses are given in this document.

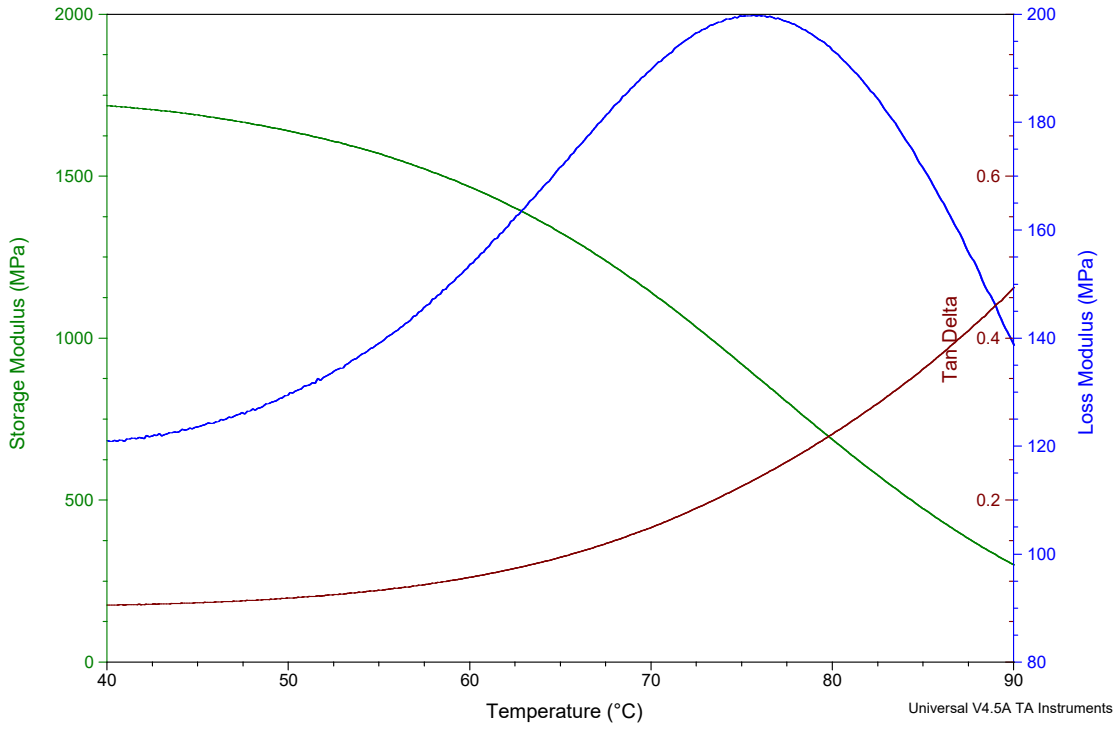

Figure A.7: Dynamic mechanical analysis results of a sheet made by exposing a SU8 film for 180 sec with a 2 mW/cm^2 UV light source followed by an additional hard baking step. These results are associated with specimen 2 of this kind.

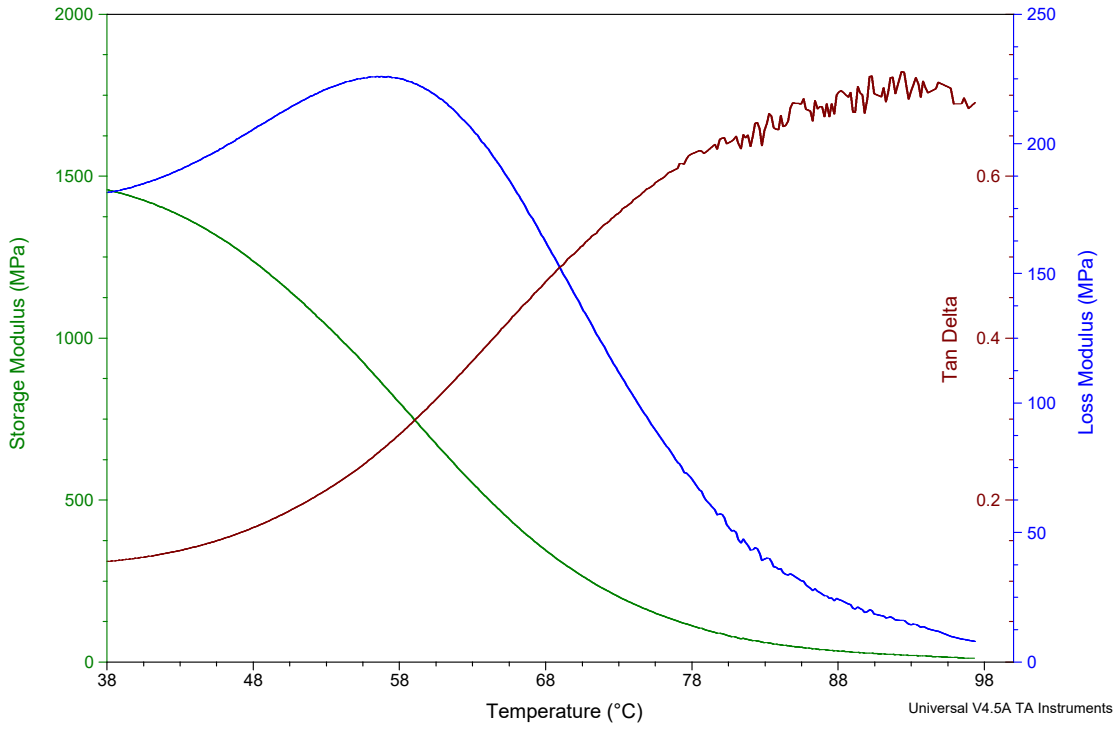

Figure A.8: Dynamic mechanical analysis results of a sheet made by exposing a SU8 film for 180 sec with a 2 mW/cm^2 UV light source followed by an additional hard baking step. These results are associated with specimen 3 of this kind.

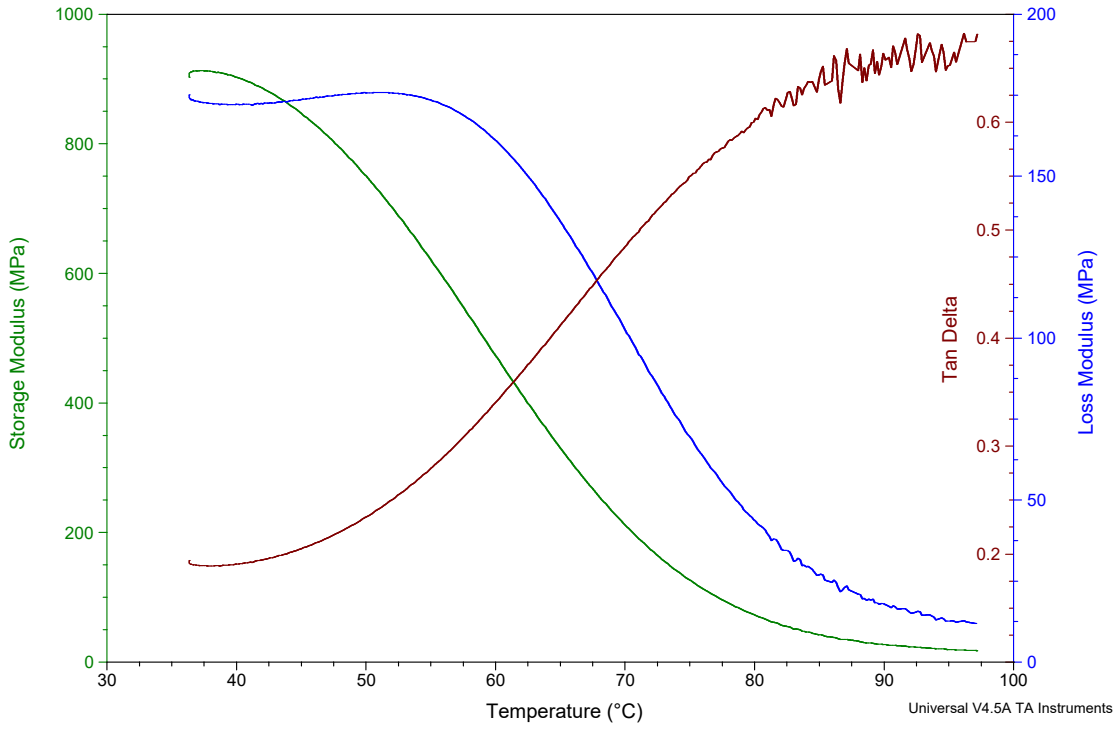

Figure A.9: Dynamic mechanical analysis results of a sheet made by exposing a SU8 film for 100 sec with a 2 mW/cm^2 UV light source. These results are associated with specimen 1 of this kind.

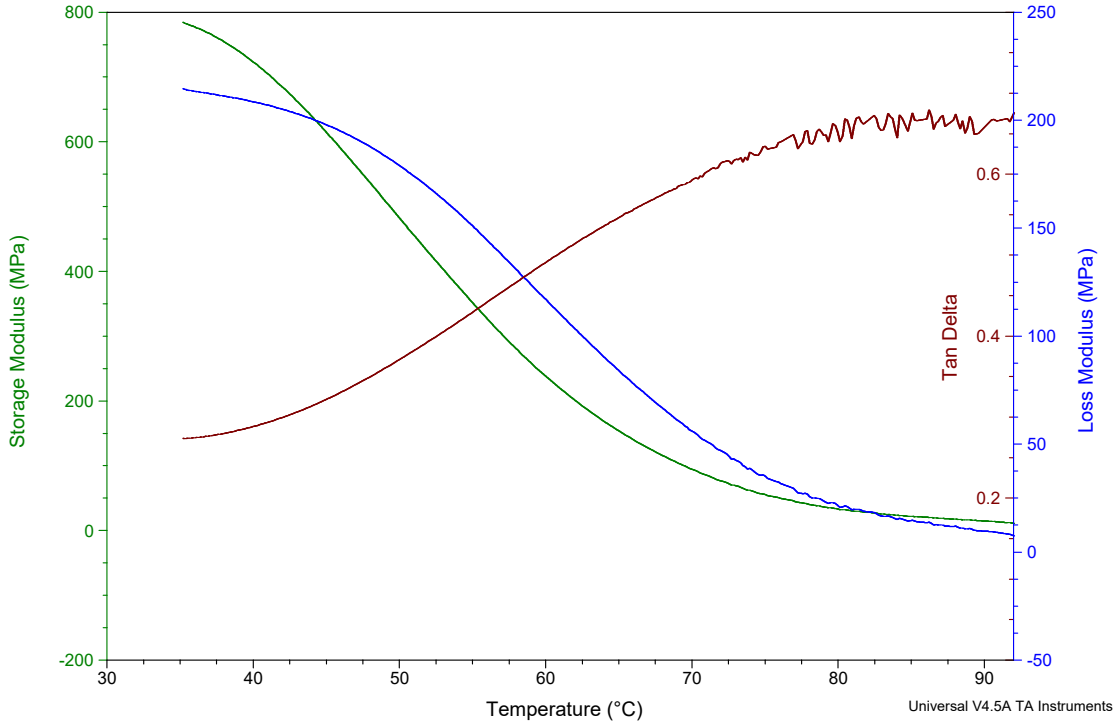

Figure A.10: Dynamic mechanical analysis results of a sheet made by exposing a SU8 film for 100 sec with a 2 mW/cm^2 UV light source. These results are associated with specimen 2 of this kind.

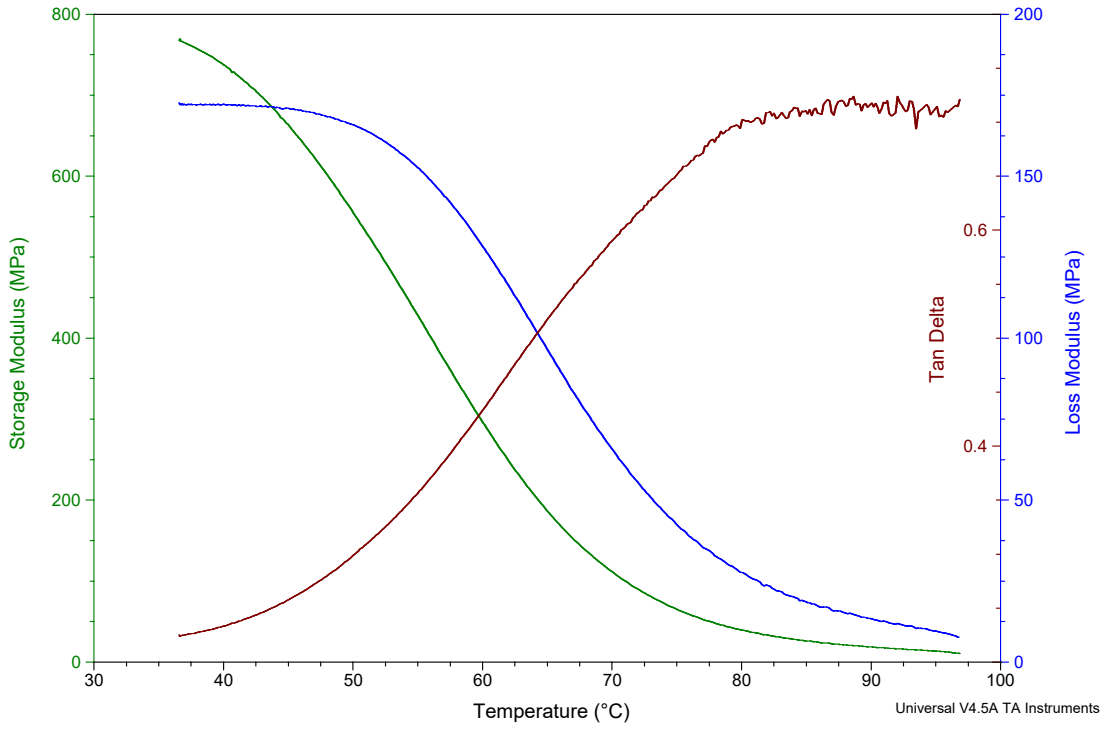

Figure A.11: Dynamic mechanical analysis results of a sheet made by exposing a SU8 film for 100 sec with a 2 mW/cm^2 UV light source. These results are associated with specimen 3 of this kind.

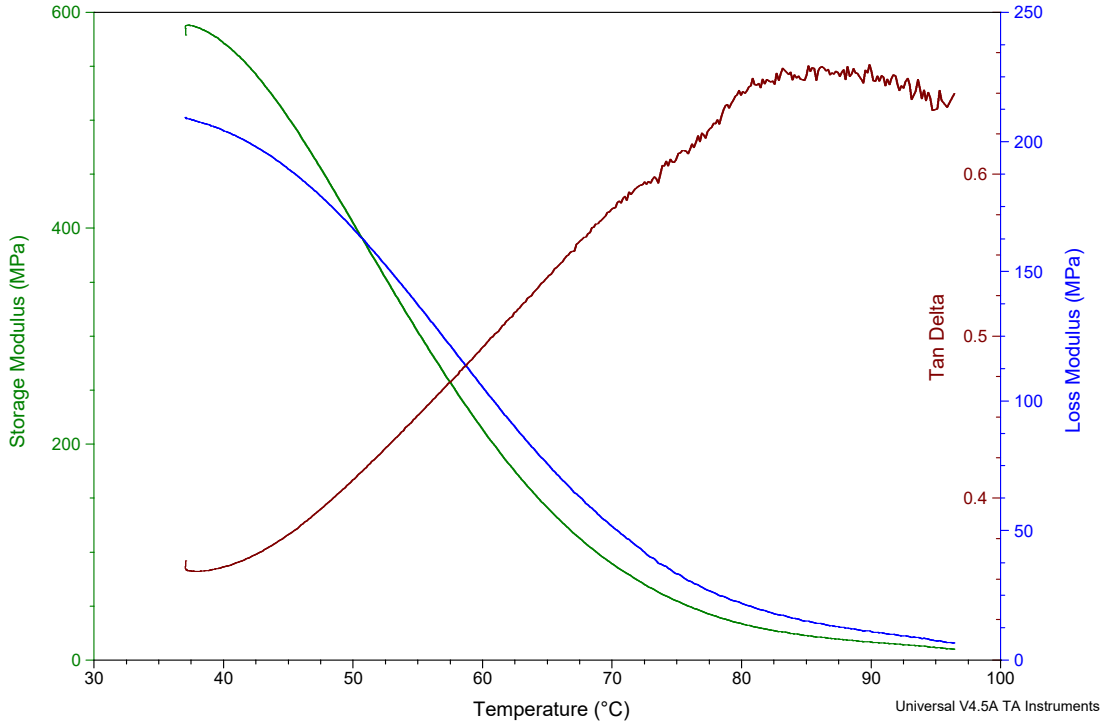

Figure A.12: Dynamic mechanical analysis results of a sheet made by exposing a SU8 film for 80 sec with a 2 mW/cm^2 UV light source. These results are associated with specimen 1 of this kind.

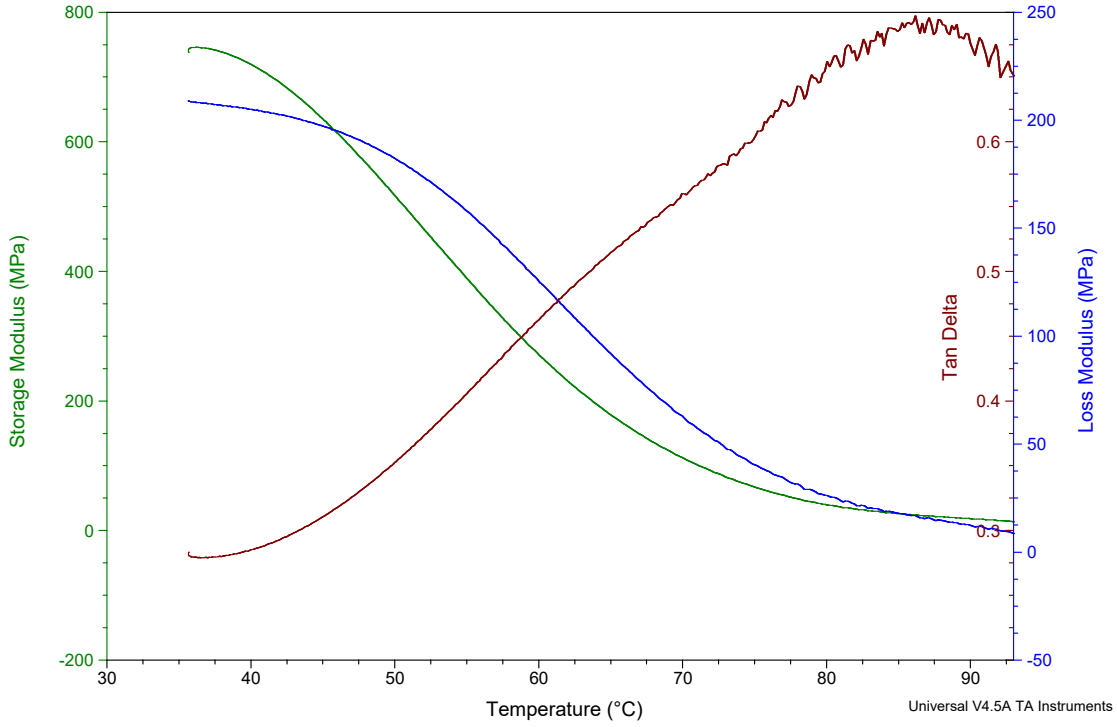

Figure A.13: Dynamic mechanical analysis results of a sheet made by exposing a SU8 film for 80 sec with a 2 mW/cm^2 UV light source. These results are associated with specimen 2 of this kind.

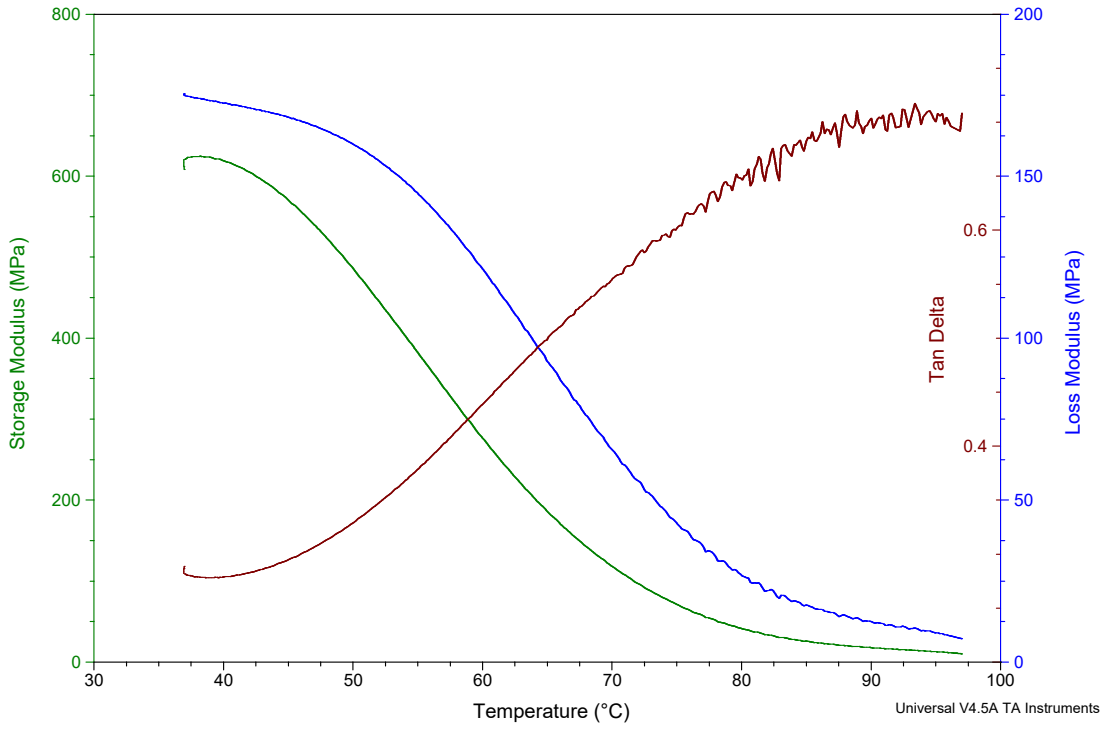

Figure A.14: Dynamic mechanical analysis results of a sheet made by exposing a SU8 film for 80 sec with a 2 mW/cm^2 UV light source. These results are associated with specimen 3 of this kind.

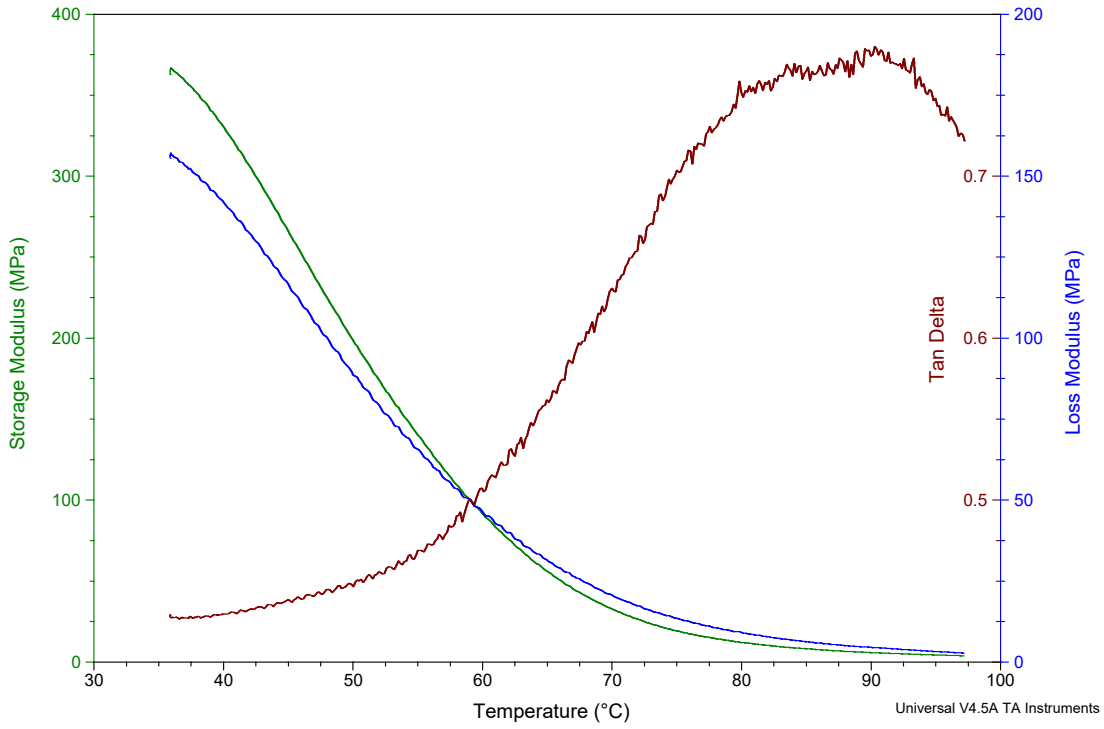

Figure A.15: Dynamic mechanical analysis results of a sheet made by exposing a SU8 film for 60 sec with a 2 mW/cm^2 UV light source. These results are associated with specimen 1 of this kind.

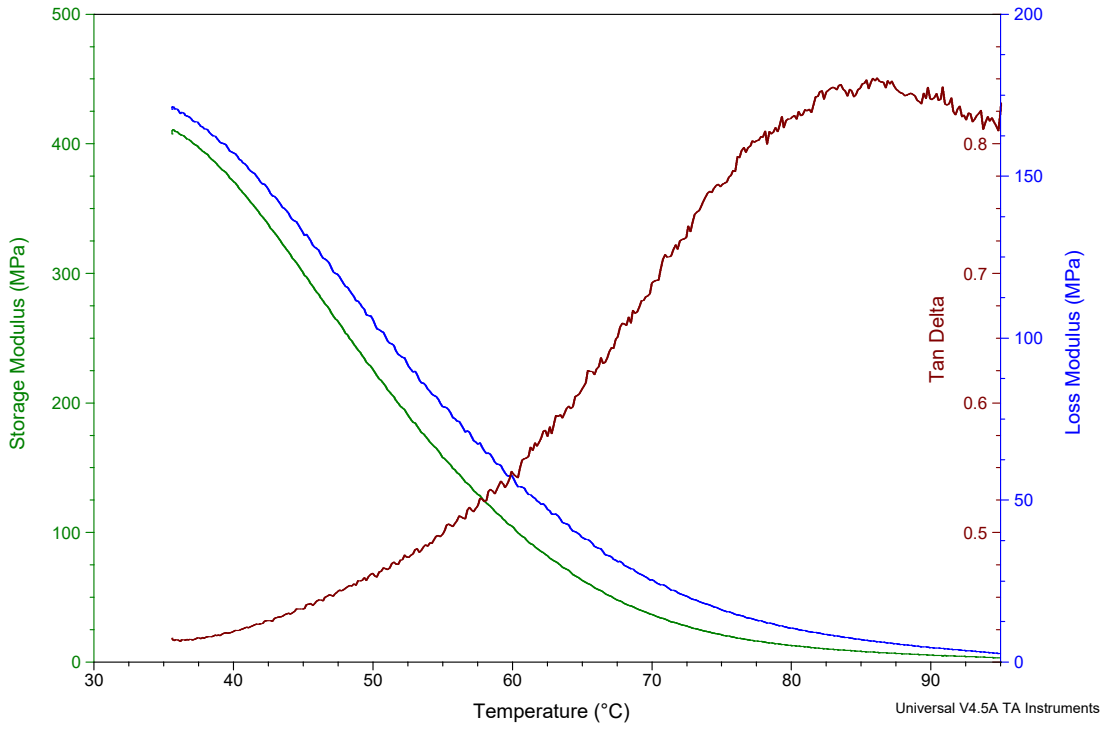

Figure A.16: Dynamic mechanical analysis results of a sheet made by exposing a SU8 film for 60 sec with a 2 mW/cm^2 UV light source. These results are associated with specimen 2 of this kind.

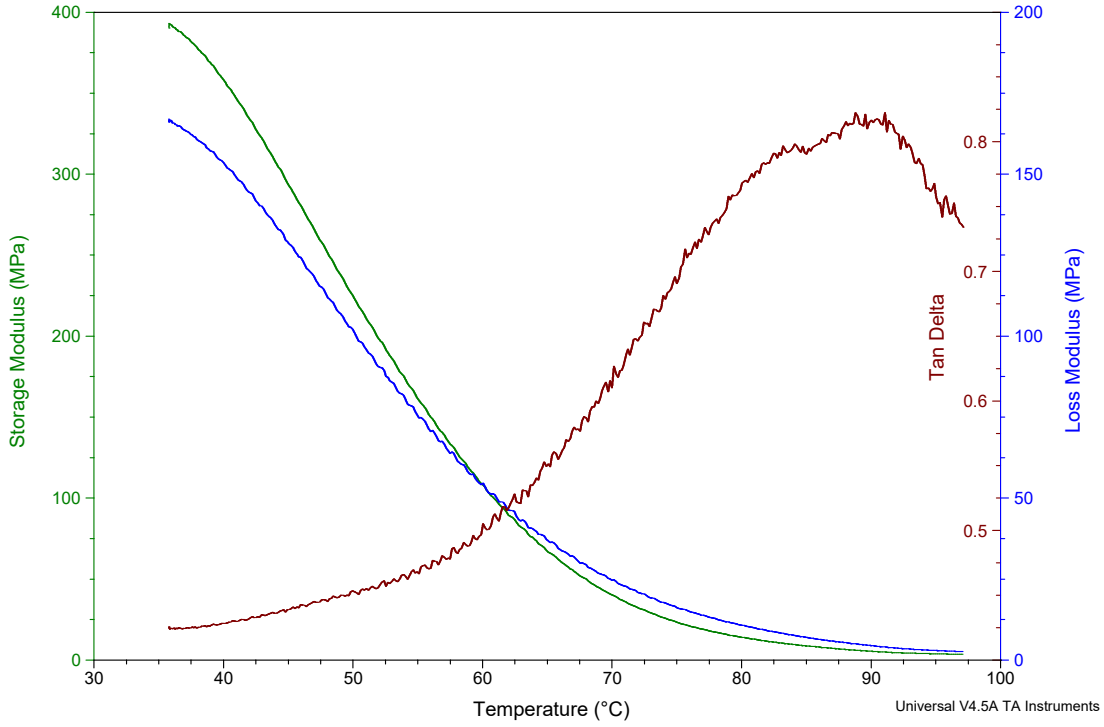

Figure A.17: Dynamic mechanical analysis results of a sheet made by exposing a SU8 film for 60 sec with a 2 mW/cm^2 UV light source. These results are associated with specimen 3 of this kind.

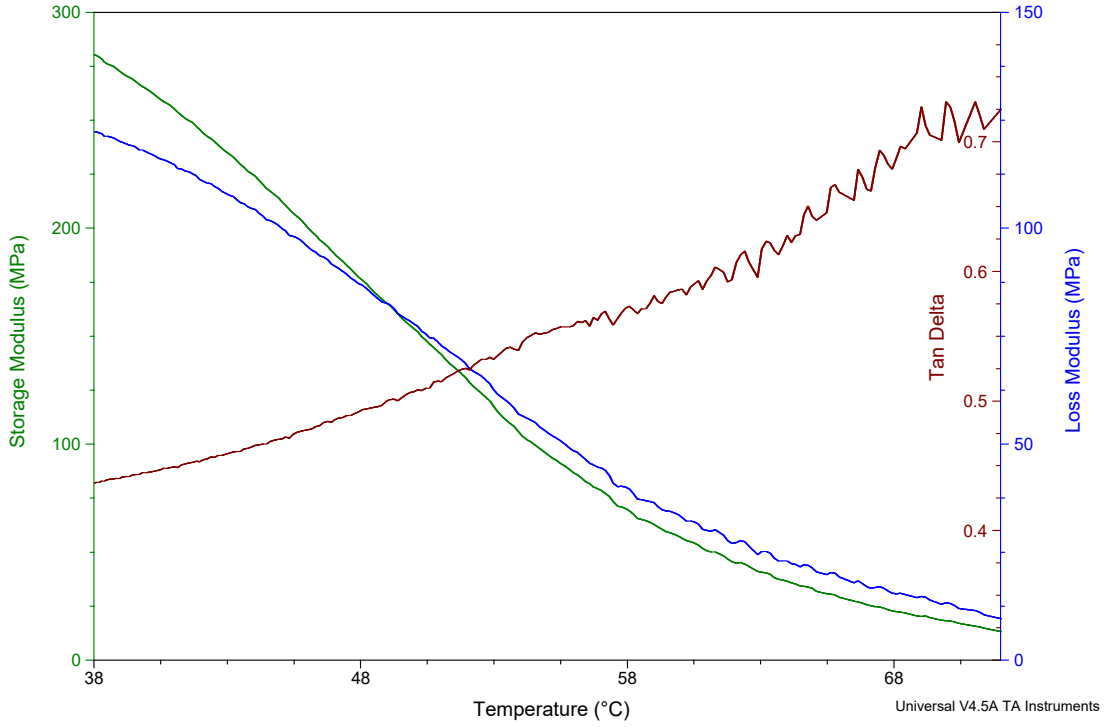

Figure A.18: Dynamic mechanical analysis results of a sheet made by exposing a SU8 film for 40 sec with a 2 mW/cm^2 UV light source. These results are associated with specimen 1 of this kind.

A.3 Nearfield Patterning

A.3.1 Effect of Various Electrospinning Parameters on the Fabrication of Suspended Wires

Voltage, distance and concentration of the polymer affect the fabrication of suspended wires by using electrospinning. High voltage and short distance results in wires being not suspended as shown in Fig. A.21. On the other hand, suspended wires can be fabricated even at high voltage if the concentration of the solution is sufficiently high as shown in Fig. A.22. Long suspended wires can be formed with 500 V and 11% as shown in Fig. A.23.

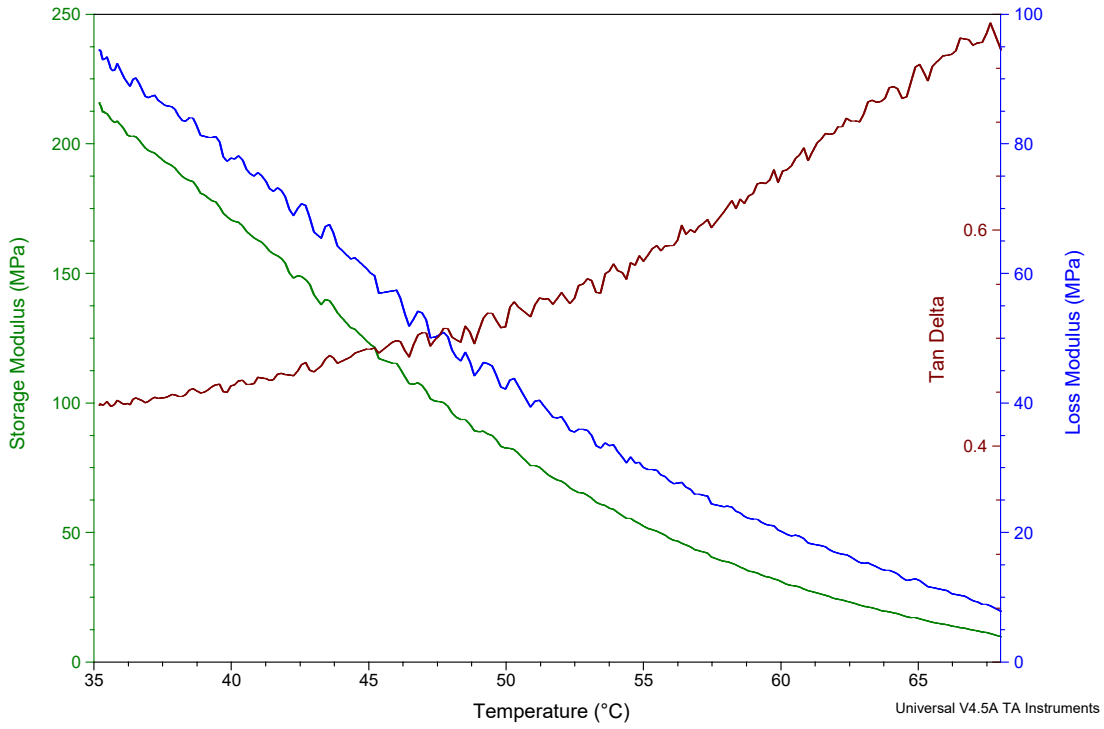

Figure A.19: Dynamic mechanical analysis results of a sheet made by exposing a SU8 film for 40 sec with a 2 mW/cm^2 UV light source. These results are associated with specimen 2 of this kind.

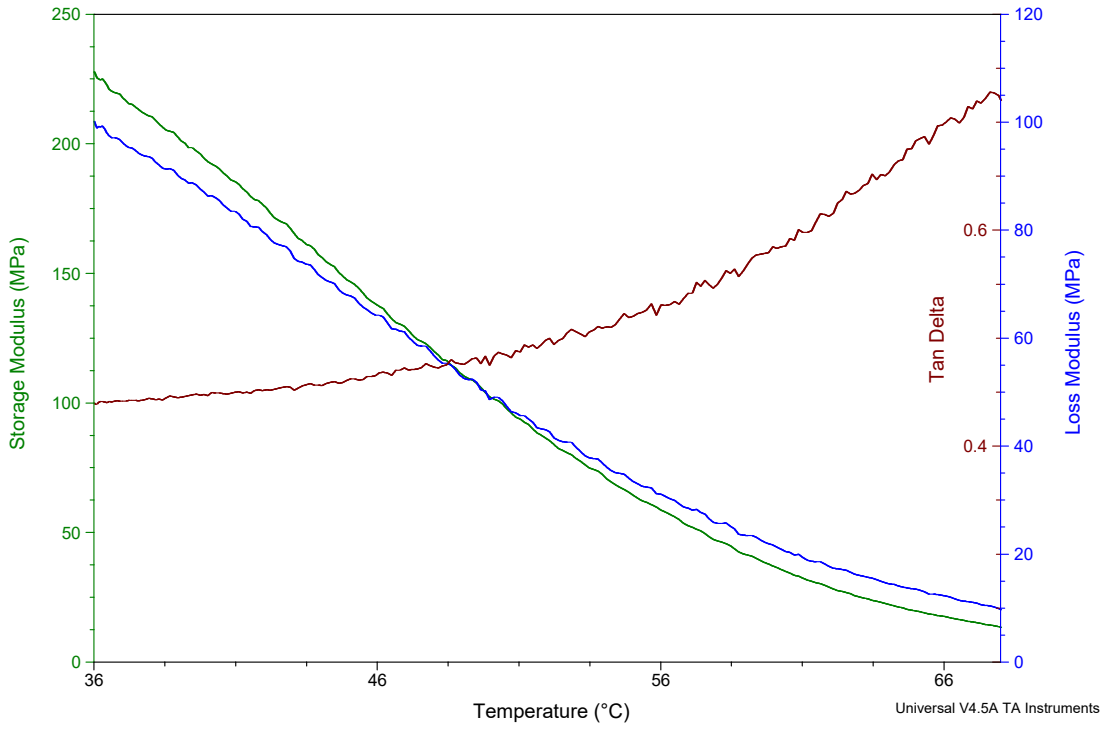

Figure A.20: Dynamic mechanical analysis results of a sheet made by exposing a SU8 film for 40 sec with a 2 mW/cm^2 UV light source. These results are associated with specimen 3 of this kind.

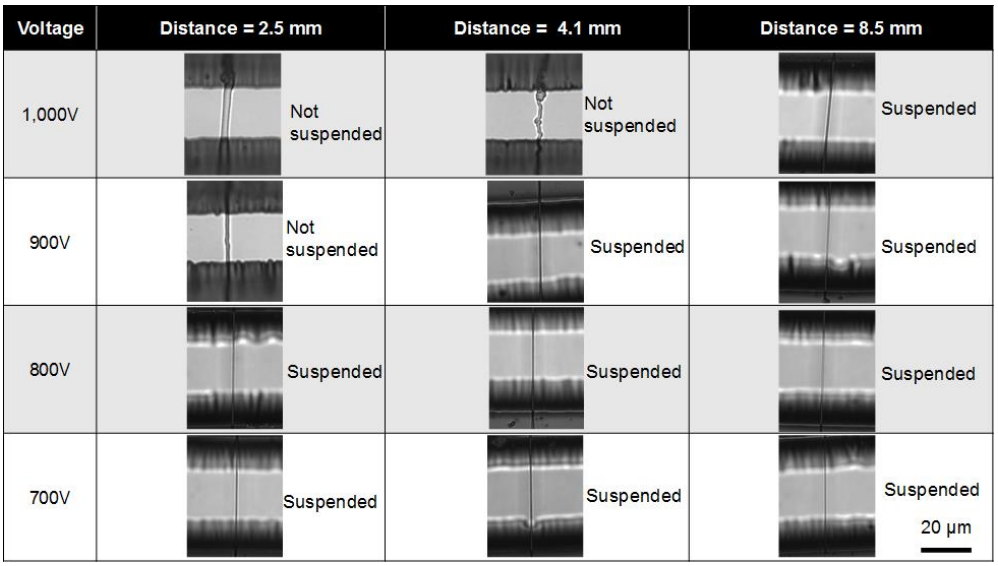

Figure A.21: Array of pictures of wires across a channel depicting the effect of voltage and spinneret-to-collector distance on the ability of the wires to be suspended.

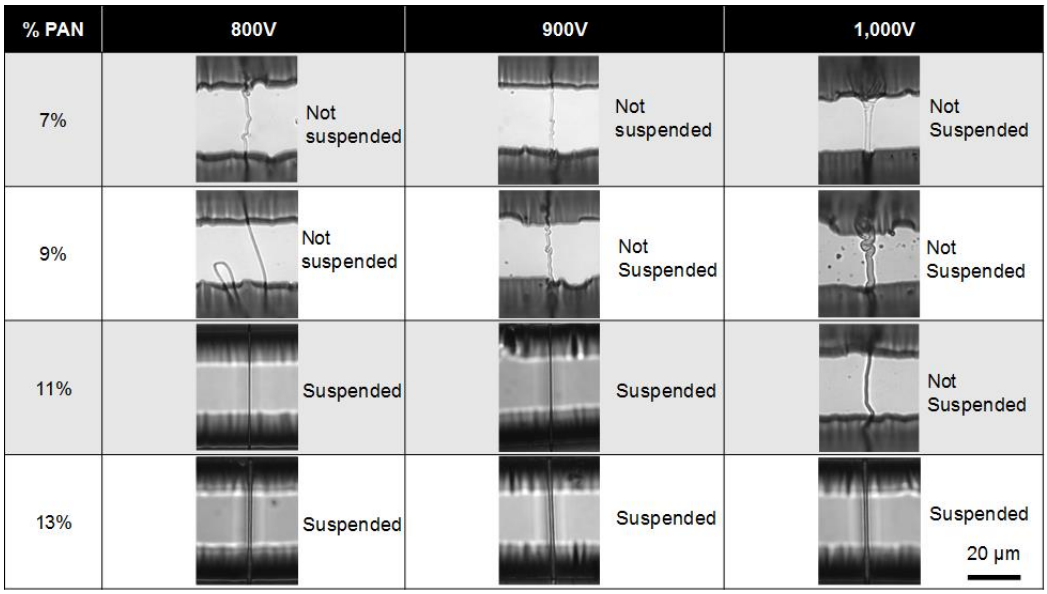

Figure A.22: Array of pictures of wires across a channel depicting the effect of voltage and concentration of PAN solution on the ability of the wires to be suspended.

A.3.2 Effect of Electric Field on the Wire Deposition on Patterned Structures

The effect of the electric field on the deposition was studied by using two different patterns: pillars with circular cross-section and pillars with square cross-section. The simulation carried out using COMSOL Multiphysics showed that the electric field intensities are higher at the edges. This explains the preferential deposition of the incoming wires on the edges of the structures as shown in Fig. A.24.

A.3.3 Effect of Stabilization and Pyrolysis on the Suspended Wires

Effect of the stabilization and the pyrolysis on the suspended wires are studied by using channels having varying width. It has been observed that the wires that are suspended across wider channels sag and eventually touches the floor of the channel. The data is shown

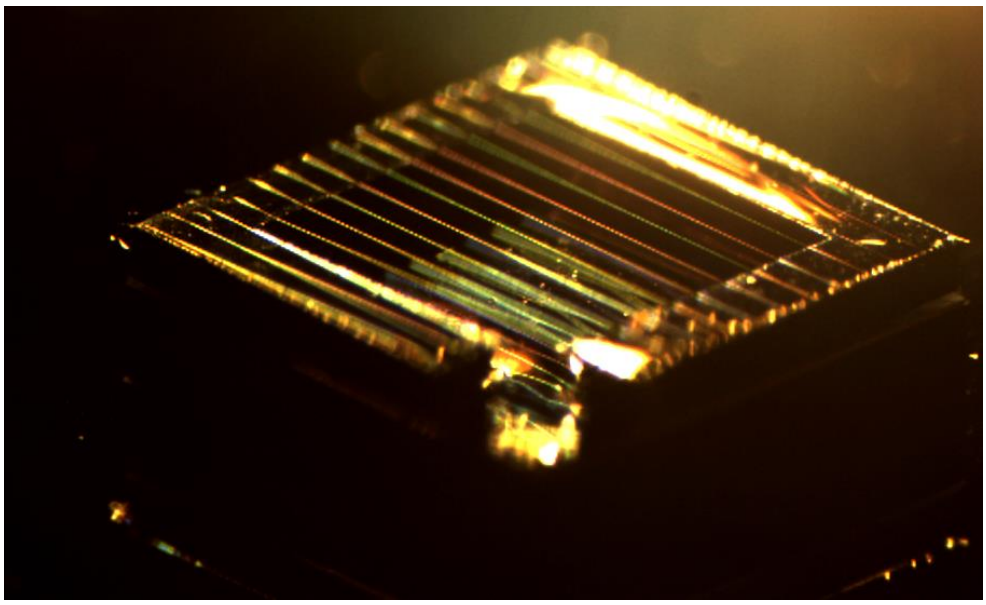

Figure A.23: Wires suspended across a structure of 5mm by 5mm

Channel width	Before stabilization	After stabilization	After pyrolysis
30-40 μm	1	0.97	0.87
40-50 μm	1	0.43	0.40
50-60 μm	1	0.43	0.37

Table A.3: Fraction of the total number of the wires in the zone that are suspended.

in Table. A.3.

A.3.4 Effect of Pyrolysis Temperature on the Shrinkage

The effect of the pyrolysis temperature on the shrinkage was studied by pyrolyzing the wires at different temperature that are otherwise having same fabrication parameters. The study showed an increasing shrinkage with the pyrolysis temperature as shown in Fig. A.25. The shrinkage was observed to be more for the suspended wires in comparison to the wires that

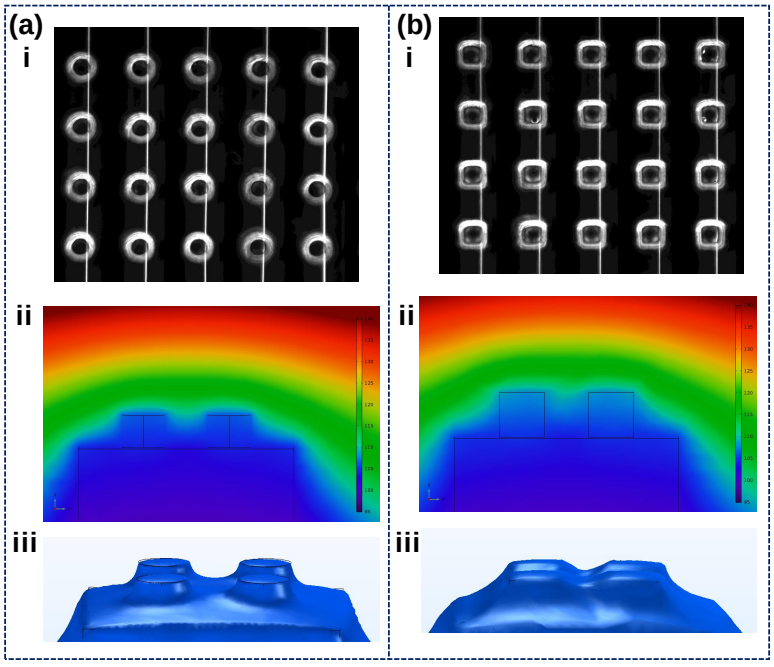

Figure A.24: (a) i. Electrospun PAN wires on pillars with circular cross-section. ii. Electric field intensity on the cross-section of the structures. iii. Isosurface of the electricfield. (b) i. Electrospun PAN wires on pillars with square cross-section. ii. Electric potential at a cross-section of the structures. iii. Iso-surface of the electric potential.

are on the surface.

A.3.5 Controlling the Nickel Thickness

The thickness of the electrodeposited nickel was controlled by the duration of the deposition. The change in the thickness with respect to the electrodeposition duration is shown in Fig. A.26.

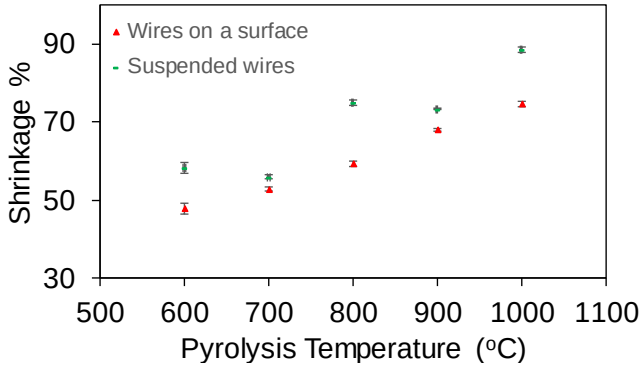

Figure A.25: Variation of the percentage of the shrinkage with the pyrolysis temperature

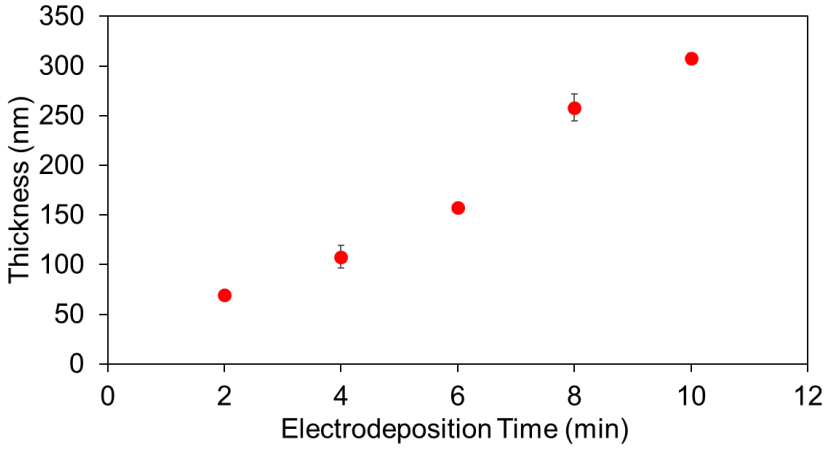

Figure A.26: Nickel Thickness Variation with Electrodeposition Time.